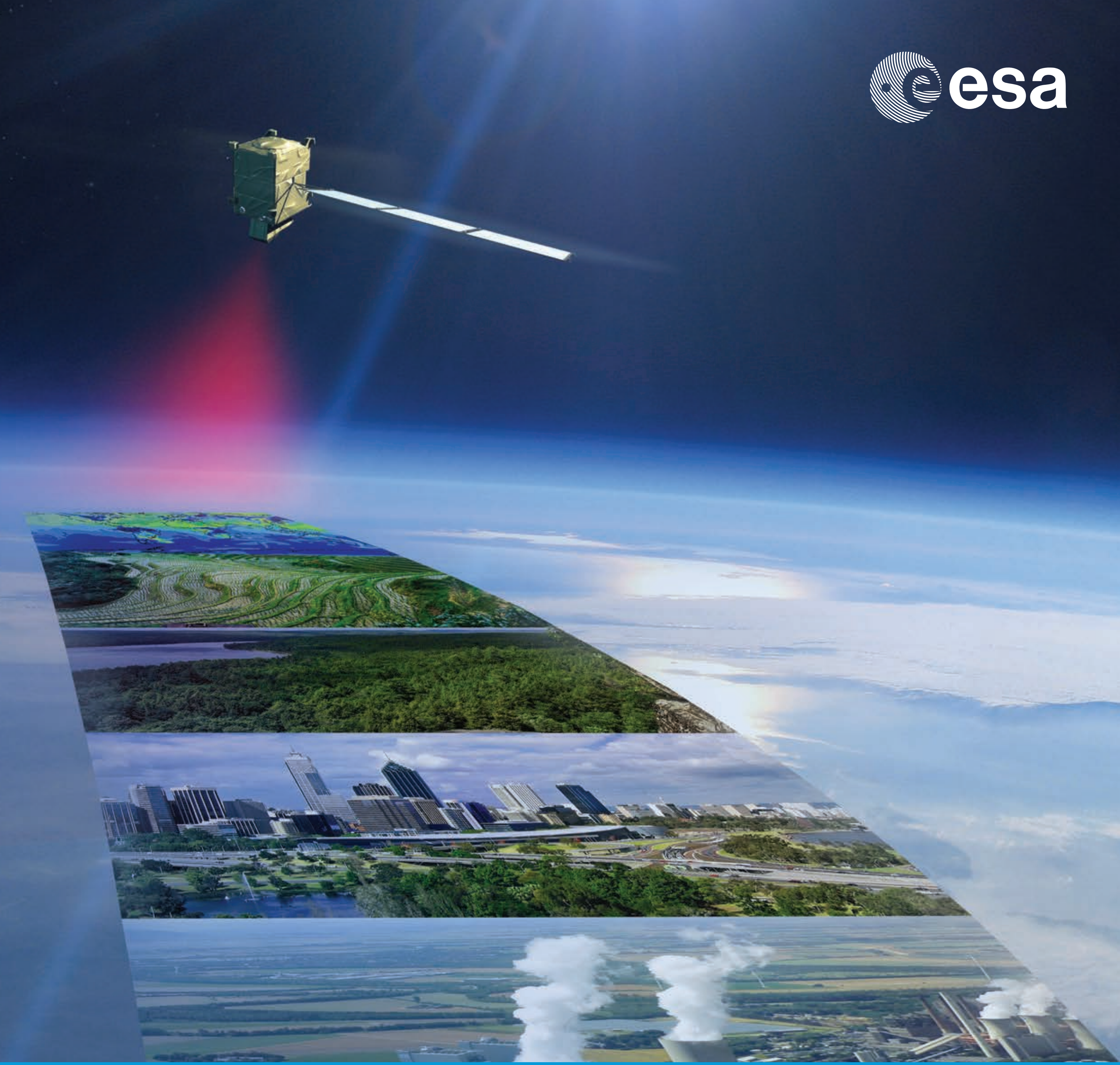

carbonsat flex

→REPORT FOR MISSION SELECTION

An Earth Explorer to observe greenhouse gases

www.esa.int

European Space Agency

SP-1330/1
June 2015

carbonsat flex

→ REPORT FOR MISSION SELECTION

An Earth Explorer to observe greenhouse gases

European Space Agency

Acknowledgements

This report is based on contributions from the CarbonSat Mission Advisory Group (MAG):

Heinrich Bovensmann – MAG Chairman (University of Bremen, DE)
Hartmut Bösch (University of Leicester, GB)
Dominik Brunner (Swiss Federal Laboratories for Materials Science and Technology, CH)
Philippe Ciais (Climate and Environment Sciences Laboratory, FR)
David Crisp (Jet Propulsion Laboratory, US)
Han Dolman (Vrije Universiteit Amsterdam, NL)
Garry Hayman (Centre for Ecology and Hydrology, GB)
Sander Houweling (Netherlands Institute for Space Research, NL)
Günter Lichtenberg (German Aerospace Centre, DE)

Scientific content of the report was compiled by Yasjka Meijer and Paul Ingmann (ESA) with additional contributions, in particular, from Michael Buchwitz (University of Bremen, DE), François-Marie Bréon (Climate and Environment Sciences Laboratory, FR), and Dirk Schüttemeyer (ESA).

Technical content of the report was compiled by Armin Löscher, with contributions from Bernd Sierk, Jean-Loup Bézy, Jerôme Caron, Pedro Jurado (all from ESA), based on inputs derived from the industrial Phase-A/B1 system and technical activities.

Recommended citation: ESA (2015). *Report for Mission Selection: CarbonSat*, ESA SP-1330/1 (2 volume series), European Space Agency, Noordwijk, The Netherlands.

Cover image design: ESA/ATG medialab
Cover photo credits: B. Neininger (power plant)
H. Gerbig – jally.de (city of Perth)
E. Wille (forest)
S. Stalder (rice terraces)
S. Houweling (CO_2 map)

An ESA Communications Production

Publication *Report for Mission Selection: CarbonSat* (ESA SP-1330/1, June 2015)

Production Editor K. Fletcher

Editing H. Rider (EJR-Quartz)

Layout D. Wishart

Publisher ESA Communications
ESTEC, PO Box 299, 2200 AG Noordwijk, the Netherlands
Tel: +31 71 565 3408 www.esa.int

ISBN 978-92-9221-428-9 (2 volumes)

ISSN 0379-6566

Contents

→ EXECUTIVE SUMMARY

Executive Summary

This report forms the basis for the selection of the eighth Earth Explorer mission within ESA's Earth Observation Programme. Two candidates, FLEX and CarbonSat, have undergone extensive feasibility studies. CarbonSat aims to quantify sources and sinks of carbon dioxide (CO_2) and methane (CH_4) by measuring their distribution in the atmosphere. FLEX aims to quantify photosynthetic activity and plant stress by mapping vegetation fluorescence. This report covers the CarbonSat mission.

Atmospheric concentrations of CO_2 and CH_4 have been increasing as a consequence of human activity, as outlined in the most recent assessment by the Intergovernmental Panel on Climate Change. Reducing the emission of these gases is considered one of the most important environmental challenges of the 21st century. A better understanding of sources and sinks at regional and sub-seasonal scales is paramount in addressing this challenge. This will allow identification of the processes that control the rate of increase in atmospheric concentrations of these gases and their potential impact on the future climate.

Since 1750, increased concentrations of greenhouse gases have contributed to an overall positive radiative forcing and warming of the climate system. CO_2 and CH_4 are responsible for approximately 80% of this radiative forcing, and their concentrations have increased by 40% and 150%, respectively, during this period, i.e. CH_4 has more than doubled. Because the anthropogenic emissions of these gases are the primary cause of global warming, the only practical way to mitigate climate change is to reduce these emissions and to manage the carbon cycle. To meet this goal, the internationally agreed target is to keep global warming below 2°C with respect to pre-industrial times.

The rapid growth of the global population has been accompanied by increasing urbanisation, with over 50% of the world's population now living in cities. Urban areas currently contribute 70% of global fossil-fuel CO_2 emissions. By 2013, fossil-fuel combustion, deforestation, and other human activities were adding over 10 billion tonnes of carbon to the atmosphere every year. In response to rice-paddy cultivation, biomass burning, and livestock production, atmospheric CH_4 concentrations also started to rise sharply. Today, emissions of CH_4 associated with agriculture, coal mining, natural-gas extraction, waste treatment, and other human activities significantly contribute to the global budget. An improved understanding of the dynamics of the global carbon cycle, in which CO_2 and CH_4 play an important role, is essential for robust and reliable climate-change prediction.

CarbonSat will provide the first high spatial resolution, global maps of both atmospheric CO_2 and CH_4 and at monthly intervals. This information is needed to advance our understanding of the global carbon cycle and to distinguish emission sources from natural sinks. CarbonSat will allow scientists to improve regional-scale modelling and to derive monthly flux estimates at high accuracy. CarbonSat observations will, for the first time, allow biogenic and anthropogenic fluxes to be separated at the scale of medium-sized countries such as France. With CarbonSat's relatively wide swath and small ground pixel size, it will be possible to image plumes from strong point sources and large cities (local scales) with sufficient accuracy to estimate their emissions.

CarbonSat measurements will quantify atmospheric CO_2 and CH_4 concentrations with precisions of 1–3 ppm (0.25–0.75%) and 6–12 ppb (0.3–0.7%), respectively. This will be provided at spatial scales as small as 6 km^2 at monthly intervals over the globe, with a contiguous sampling over a 200 km-wide swath. Importantly, the instrument has been designed to minimise systematic errors below 0.5 ppm and 5 ppb, respectively, at regional scales such as Western Europe. The high spatial and temporal resolution ensures good coverage in regions prone to cloud cover and allows sources to be discriminated from sinks at various scales. These and other observational requirements reflect the evolution of current greenhouse-gas satellite missions from 1D to 2D sampling.

Previous and current satellite missions have demonstrated the required measurement precision and accuracy requirements for CO_2 and CH_4, but a significant observational gap remains at finer spatial and temporal resolution. Imaging spectrometers provide a solution for spatially mapping their absorption features in the near-infrared (NIR) and shortwave-infrared (SWIR) spectral regions at relatively high spectral resolution. Measurements will be made at 747–773 nm (NIR), at 1590–1675 nm (SWIR-1) and at 1925–2095 nm (SWIR-2), at 0.1, 0.3 and 0.55 nm spectral resolution, respectively. The O_2 column derived from the NIR band, which includes the O_2-A-band, is combined with the CO_2 and CH_4 column measurements to estimate the column-averaged dry-air mole fractions of CO_2 and CH_4. Furthermore, the NIR band is used to correct retrievals for interference by clouds, aerosols, water vapour, and solar-induced chlorophyll fluorescence.

An end-to-end measurement performance simulator has been developed, tested and validated using realistic measurement and instrument implementation scenarios. The performance model has been applied to the relevant range of conditions and addresses the science requirements in an end-to-end manner. Retrieval algorithms applicable for a realistic range of error sources (both geophysical and technical) have been compared against a pre-defined set of performance requirements and validated using existing satellite measurements of CO_2 and CH_4. Consolidated algorithms have been established for retrieving geophysical products. Further processing of these products in flux-inversion models has been assessed using simulated data as well as the data of previous and existing satellites. These assessments confirm the validity of the observational requirements established for CarbonSat.

The principal challenges of the CarbonSat instrument arise from the stringent observational requirements. The technical concepts have been subject to detailed performance analyses and shown to meet the stringent Level-1b requirements. Critical areas have been identified, technology readiness assessed and pre-development activities initiated. Selected technologies build upon heritage of previous and planned atmospheric chemistry missions, and will reach the required maturity level prior to the start of the implementation phase.

The CarbonSat mission covers a wide range of spatio-temporal scales, each of which offers unique opportunities to characterise and quantify the surface-to-atmosphere exchange of CO_2 and CH_4. The overarching scientific objective of the mission is to cover the full range of spatial scales, with particular emphasis on local scales, which is unique to this mission and necessary for separating anthropogenic from natural fluxes. The scale-specific objectives are listed below.

— Regional scale: to provide a breakthrough in the quantification and attribution of regional-scale surface-to-atmosphere fluxes of CO_2 and CH_4

— Country scale: to increase the resolving power of greenhouse-gas-observing satellites to the scale of medium-sized countries

— Local scale: to pioneer the spaceborne detection, characterisation, and quantification of strong local sources of CO_2 and CH_4

CarbonSat will provide a significant step forward in separating anthropogenic emissions from natural fluxes in atmospheric inversions, and prepares for a future global carbon observing system with capabilities to verify emissions, as recently endorsed by the Committee on Earth Observation Satellites (CEOS) Strategy for Carbon Observations from Space. CarbonSat addresses several key scientific challenges of the ESA Living Planet Programme, and it is a natural element in the recently updated Earth Observation Science Strategy. In addition to its immediate scientific impact, this candidate mission can be considered as a demonstrator for a future constellation of greenhouse gas observing satellites. CarbonSat is considered sufficiently mature for implementation as Earth Explorer 8 and could be launched by 2023.

→ INTRODUCTION

1. Introduction

Events marking the current chapter in Earth's natural history provide vivid reminders of our vulnerability and underline the urgency with which we must achieve a sustainable existence on our home planet.

Understanding changes in the Earth system and the impact that humanity is having on its delicate balance is paramount. The ability to acquire new insight into Earth-system processes poses significant scientific and technical challenges. However, it also provides the stimulus and opportunity to develop new measurement capabilities, exploiting the unique vantage point of space to study the ebb and flow of natural processes and the impact human activity is having at local, regional and global scales.

As part of its Earth Observation Programme, the European Space Agency's series of 'Earth Explorer' satellite missions are the epitome of Europe's technical endeavour in realising new Earth-observing capabilities. These missions offer a stream of innovative measurement techniques to explore and understand different aspects of the Earth system. They embody the purpose of the Programme: to address scientific and technical challenges beyond the reach of individual Member States.

Priorities identified by the scientific community are used to guide the development of the Earth Explorer missions. Each has been selected to address and fulfil the strategic objectives of ESA's Living Planet Programme as well as contribute critical new elements to the global Earth-observing system infrastructure.

The guiding principle of defining, developing and operating Earth Explorer missions in close cooperation with the scientific community provides a tool to address the most critical Earth-science questions in as comprehensive and effective a manner as possible. The capability to develop and launch state-of-the-art technologies enables the European science community to achieve substantial scientific advances. It is already evident the extent to which the first Earth Explorers contribute to establishing new frontiers in our scientific knowledge of how the Earth system works, and how humankind influences natural processes.

Since the science and research elements of the Living Planet Programme were established in the mid-1990s, this user-driven strategy has resulted in the selection of seven Earth Explorer missions. Together, they cover a broad range of scientific topics. Importantly, their complementarity further stimulates the development of new applications of their data.

Earth Explorer missions are split into two categories: 'Core' and 'Opportunity'. Core Explorers address complex issues of scientific interest and typically employ substantial elements of new technology. By contrast, Opportunity missions are smaller and more affordable and have more focused scientific goals that can be achieved by novel uses of existing, lower-risk technologies. Through a process of peer review and selection, both types are implemented in separate cycles to ensure a steady flow of missions to address emerging key Earth-science questions.

The first cycle for Core missions resulted in the Gravity field and steady-state Ocean Circulation Explorer, GOCE, which was launched in March 2009, and the Atmospheric Dynamics Mission ADM-Aeolus, scheduled for launch in 2016. The second cycle, initiated in 2000, resulted in the Earth Clouds Aerosols and Radiation Explorer, EarthCARE, due for launch in 2018. The first cycle for Opportunity missions resulted in the ice mission CryoSat, which was rebuilt and launched in April 2010 following a launch failure in 2005, and the Soil Moisture and Ocean Salinity mission, SMOS, also launched in 2009. The second cycle resulted in the magnetic field mission, Swarm, which was launched in November 2013. A third cycle of Core missions, initiated by a Call for Ideas in

2005, led to the selection of the Biomass mission in 2013, since confirmed for full implementation in 2015.

In 2009, a third cycle of Opportunity missions was initiated with a call for mission proposals for the eighth Explorer. In November 2010, two candidates were selected for feasibility study (Phase-A/B1): CarbonSat and FLEX (Fluorescence Explorer).

— CarbonSat aims to quantify sources and sinks of carbon dioxide and methane by measuring their distribution in the atmosphere.

— FLEX aims to quantify photosynthetic activity and plant stress by mapping vegetation fluorescence.

The Reports for Mission Selection capture the status of the respective mission concept at the end of Phase-A/B1 activities. The two volumes will be provided to the Earth-observation community as a basis for the User Consultation Meeting to be held in September 2015, and for the subsequent recommendation for selection of a single Earth Explorer 8 mission.

Each Report for Mission Selection follows a common format and logic. Each identifies the scientific questions and related key societal issues motivating the mission and its research objectives. After establishing the scientific basis and rationale, specific mission objectives are outlined and traced to a set of requirements used for system concept definition. Consolidated descriptions of two competing technical concepts are provided for each candidate mission, the designs of which are optimised to respond to the mission requirements. Based on each design concept, the end-to-end performance is simulated and the maturity of the geophysical data processing is outlined. The results are used to establish the feasibility and maturity of the concept as well as to evaluate the capability to fulfil the mission requirements and scientific objectives.

Each report comprises this introductory first chapter and eight subsequent chapters as follows:

Chapter 2 – identifies the background and scientific issues to be addressed by the mission, considering the contribution of past and present activities in the field. It provides justification for the mission set in the post-2020 timeframe and includes a review of the current scientific understanding of the issue in question while identifying the potential advances in knowledge that the mission could provide.

Chapter 3 – draws on arguments presented in Chapter 2, and summarises specific research objectives and related mission objectives.

Chapter 4 – outlines the mission requirements, including required Level-2 geophysical data products and observational parameters, the need for these observations to be made from space, and aspects of timeliness and timing of the mission.

Chapter 5 – provides an overview of the system elements, including the space and ground segments, operations, calibration and the data processing up to Level-1b.

Chapter 6 – details the scientific data processing and validation concept, including processing and calibration/validation as well as the data processing techniques that need to be implemented to meet the data product requirements.

Chapter 7 – makes a comparison of the expected versus the required performance and ability to fulfil the research/observational objectives based on the documented system concept.

Chapter 8 – documents the readiness of the scientific user community in respect to planned use of the anticipated scientific products, the global context in terms of complementary missions as well as the operational or applications potential of the data products.

Chapter 9 – outlines a programme of implementation. It also addresses the scientific and technical maturity, the development status of key technologies, risks, logistics and schedules.

This Report for Selection covers the CarbonSat mission.

1.1 Definitions

As reference is made to basic definitions throughout the report the requisite background information is below.

Mass Unit Equivalents

The mass units used deviate from the international SI standard as shown in Table 1.1.

SI	Mass Unit Equivalents			
10^{12} kg	1 Pg	1 Gt	10^{15} g	10^{18} mg
10^{9} kg	1 Tg	1 Mt	10^{12} g	10^{15} mg
10^{6} kg	1 kt	10^{9} g	10^{12} mg	

Table 1.1. Conversion of SI to non-SI mass units.

Definition of Spatial Scales and Model Domains

Various spatial scales and model domains are defined as shown in Tables 1.2 and 1.3.

Scale	Definition
Continental scales	Medium-sized continents, such as Europe and large ocean gyres
Regional scales	Sub-continental regions, such as Western Europe
Country scales	Medium sized countries, such as France
Local scales	From points up to large cities

Table 1.2. Definition of spatial scales.

Model	Domain
Global models	Global domain (100–500 km resolution)
Mesoscale models	Regional domain (1–25 km resolution)
Plume models	Local domain (1–100 m resolution)

Table 1.3. Definition of model domains.

Definition of Dry-air Mole Fractions

The dry-air mole fractions of CO_2 and CH_4 are denoted as XCO_2 and XCH_4. They are defined as the total number of CO_2 and CH_4 molecules in a vertical column above a unit surface divided by the corresponding total number of molecules of dry air in that column:

$$XCO_2 = CO_2 \text{ column/dry air column}$$
$$XCH_4 = CH_4 \text{ column/dry air column}$$

The air column is derived from the total number of O_2 molecules. The result is that quantities of XCO_2 and XCH_4 are insensitive to surface topography and

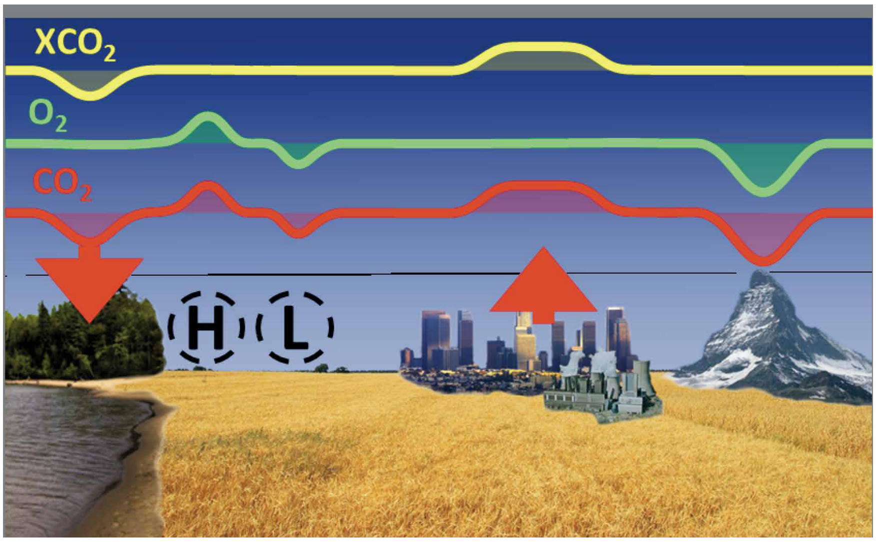

Figure 1.1. Spatial variation of CO_2 (red), O_2 (green) and XCO_2 (yellow) columns. (M. Reuter–IUP)

surface pressure, but sensitive to sources and sinks as illustrated for XCO_2 in Figure 1.1. A similar principle applies to XCH_4.

The O_2 column is used to compute the dry-air column XCO_2, as the O_2 mole fraction of dry air is well known. Variations of XCO_2 result primarily from CO_2 sources and sinks (red arrows) in contrast to the CO_2 column, which also varies with variations in surface pressure and topography.

→ BACKGROUND AND SCIENTIFIC JUSTIFICATION

2. Background and Scientific Justification

2.1 The Carbon Cycle

The latest scientific assessment by the Intergovernmental Panel on Climate Change (IPCC, 2013) states that climate warming is unequivocal. Many recent changes are unprecedented over decades to millennia. The atmosphere and ocean have warmed, snow and ice have diminished and sea level has risen. Changes such as these have resulted from positive radiative forcing caused by increased concentrations of atmospheric greenhouse gases. Carbon dioxide (CO_2) and methane (CH_4) make the largest contributions to radiative forcing (Fig. 2.1, left). With concentrations now the highest for 800 000 years (IPCC, 2013), and continuing to rise (Fig. 2.1, right), reducing the emission of these gases is considered the most important environmental challenge in the 21st century.

Prior to the industrial revolution, global mean atmospheric concentrations of CO_2 were about 280 parts per million (ppm). Since then, concentrations have increased by 40% (Fig. 2.1), and by the end of 2014 several northern-latitude stations measured values exceeding 400 ppm (*www.esrl.noaa.gov/gmd/ccgg/trends*). Over the same period, atmospheric CH_4 concentrations have nearly tripled, from 700 parts per billion (ppb) in pre-industrial times to ~1900 ppb today (Dlugokencky et al., 2011; Ciais et al., 2013). Increased concentrations of greenhouse gases since 1750 have contributed to an overall positive radiative forcing and warming of the climate system. CO_2 and CH_4 are responsible for approximately 80% of radiative forcing (IPCC, 2013).

The global carbon cycle is fundamental to the functioning of the Earth system. It controls the concentration of CO_2 and CH_4 in the atmosphere and the fluxes between the ocean and the land. Fossil-fuel combustion, cement production, and land-use change are the main anthropogenic sources of atmospheric CO_2, while the land and the oceans currently act as net sinks, removing a significant fraction of CO_2 from the atmosphere (Fig. 2.2). Surprisingly and fortunately, as anthropogenic emissions of CO_2 have dramatically increased over the last five decades, the capabilities of the land and ocean to act as sinks have grown in parallel. These two natural carbon reservoirs have continued to absorb, on average, half of the CO_2 emitted from human activities. However, it is not evident that the land and oceans will continue their role as sinks with the same efficiency. Future climate change, rising CO_2 and other human-caused large-scale perturbations, such as land-use change and emissions of nitrogen compounds, will all affect land and

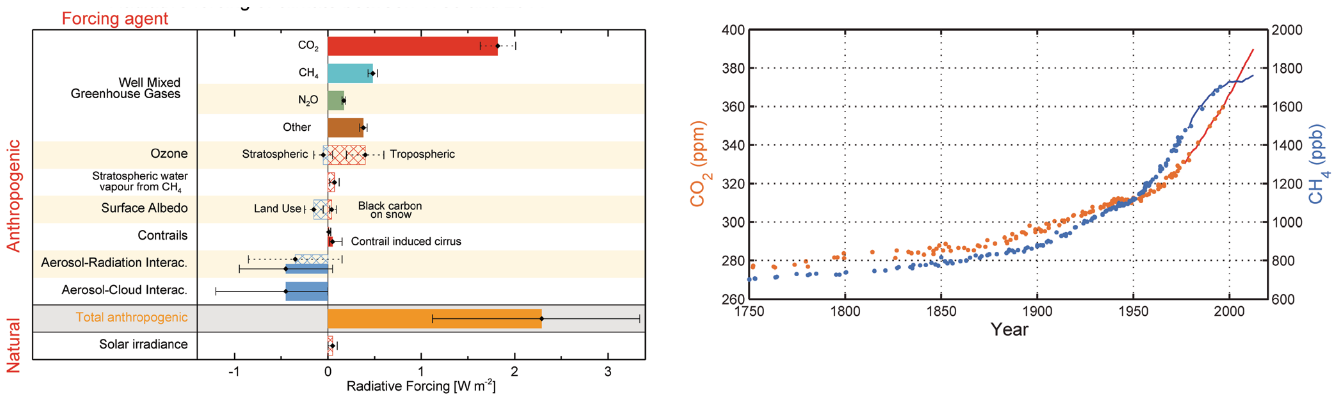

Figure 2.1. Left: Radiative forcing of greenhouse gases and aerosols. Radiative forcing of CO_2 and CH_4 are the main drivers of climate warming. Right: Increase in global atmospheric concentrations of CO_2 and CH_4. This curve is based on ice-core data (dots) and direct atmospheric measurements (solid lines). The increase is caused by human activity and is the main cause of climate change.
Data from IPCC (2013). (Left: F.M. Bréon–LSCE; Right: P. Ciais–LSCE)

Figure 2.2. CO_2 fluxes averaged globally for 2000–2009. Fluxes are in PgC yr^{-1}. (Adapted from Figure 6.1 Errata of Ciais et al. (2013)).

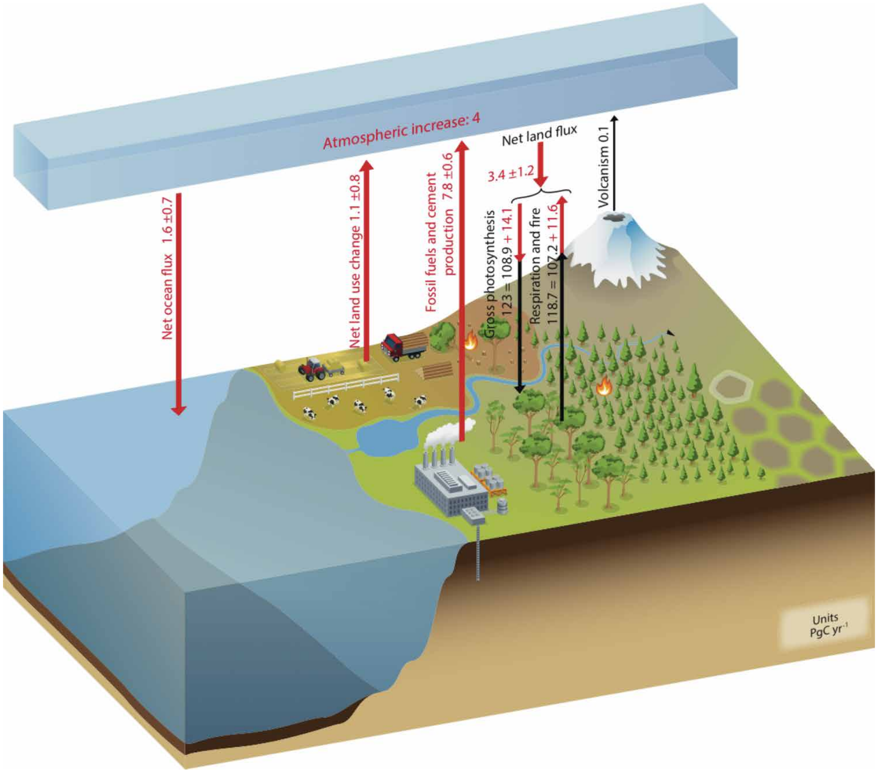

ocean carbon-cycle processes in complex ways, which could amplify or reduce the current increase of atmospheric CO_2 and CH_4.

The most recent IPCC Assessment Report (IPCC, 2013) states: “The future evolution of the land carbon uptake is much more uncertain (compared to the ocean), with a majority of models projecting a continued net carbon uptake under all Representative Concentration Pathways (RCPs), but with some models simulating a net loss of carbon by the land due to the combined effect of climate change and land-use change. In view of the large spread of model results and incomplete process representation, there is low confidence on the magnitude of modelled future land carbon change”. This is illustrated by the spread of Earth System Model results for the projection of future land and ocean carbon fluxes in Fig. 2.3.

An improved understanding of the dynamics of the global carbon cycle is therefore essential for robust and reliable climate change prediction. To meet this objective, ‘natural sinks’ must be identified and quantified. This applies not only at a global scale, but importantly at regional scales so that the processes controlling efficiency and any feedbacks in a changing climate can be understood. This knowledge is essential to improve CO_2 and climate projections on time scales of decades to centuries, so that human societies are better able to predict, mitigate and adapt to the impacts of climate change.

While atmospheric CO_2 has a single, dominant source that is relatively well quantified, that is fossil-fuel combustion, and natural sinks that are less well understood, the situation is different for CH_4. A diverse range of human activities related to livestock production, landfills and waste, fossil-fuel extraction and use, for example, cause emissions of CH_4 to the atmosphere, in addition to that from natural sources (Fig. 2.4). The relative contributions of these anthropogenic CH_4 sources, as well as the main natural emissions from wetlands and fires, for example, are poorly quantified, although it is understood that both types have changed substantially over time. The possibility of additional CH_4 emissions from thawing permafrost, shallow ocean shelves in the Arctic, biomass burning, wetlands and land-use change, have added to these uncertainties. Meanwhile, the principal CH_4 sink – atmospheric oxidation by the hydroxyl radical (OH) – is rather well quantified at the global scale, but the regional distribution and the variability of the OH sink remains poorly understood since it is controlled by complex atmospheric chemistry. An improved understanding of the distribution, variability and intensity of sources of regional CH_4 is an essential precursor to predicting and managing these emissions.

Because anthropogenic emissions of CO_2 and CH_4 are the primary cause of global warming, the only way to attenuate climate change is to reduce these emissions and to manage the carbon cycle by preserving stored carbon and possibly enhancing carbon sinks. The internationally-agreed objective is to

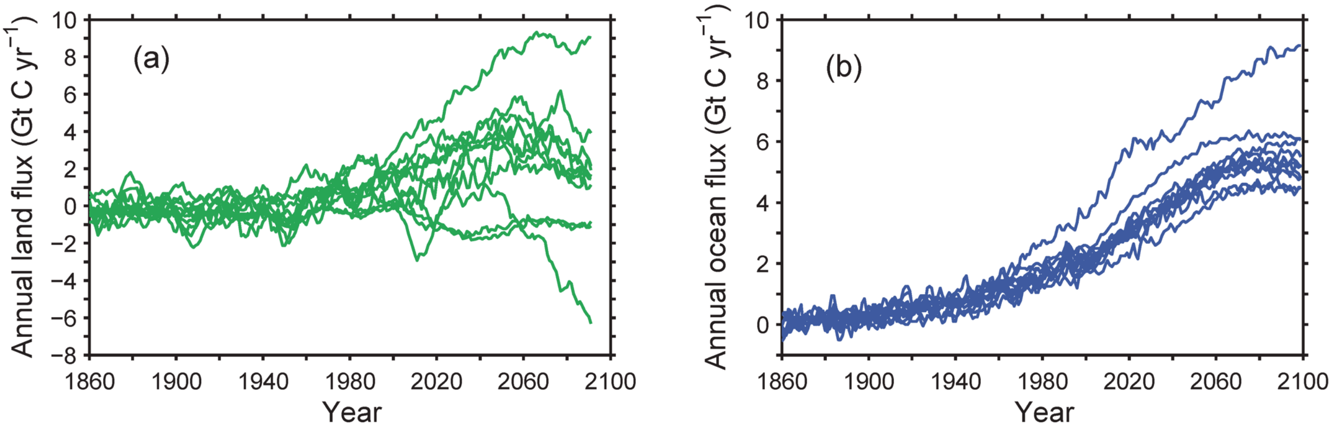

Figure 2.3. Spread of the global annual carbon flux, (a) air to land, and (b) air to ocean, as simulated by coupled carbon–climate models (Earth System Models) and used in the latest IPCC assessment for the same future CO2 concentration pathway (RCP8.5). The spread between models reflects their different responses to climate change and elevated CO2 levels, which illustrates model limitations with respect to uncertainties in understanding the carbon cycle. After Friedlingstein et al. (2014). (P. Ciais–LSCE)

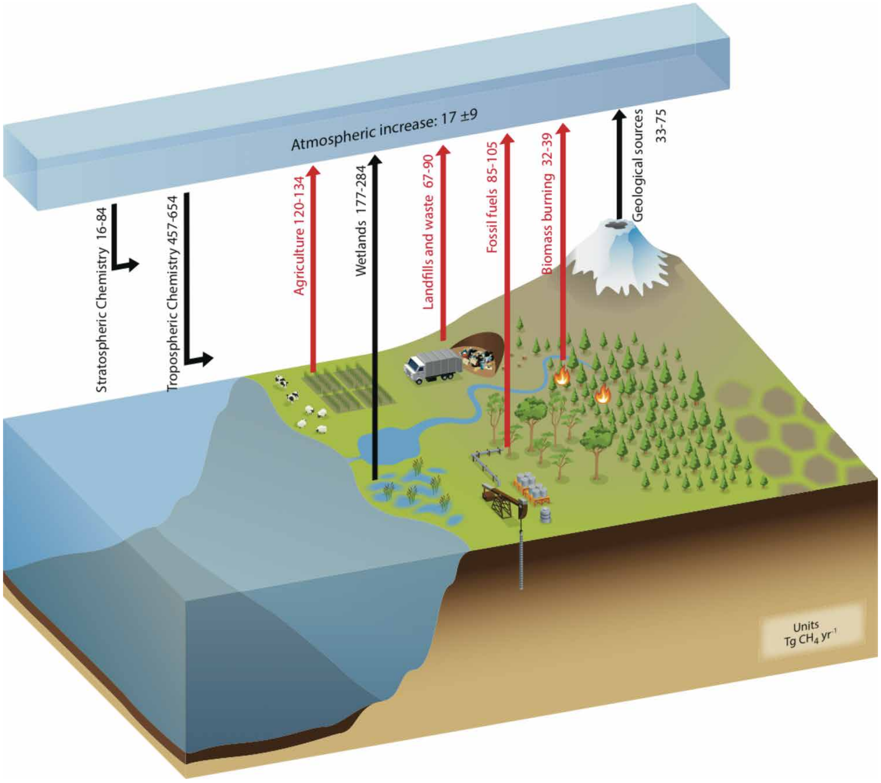

Figure 2.4. The global CH_4 cycle. Numbers represent annual fluxes in $TgCH_4\ yr^{-1}$ for 2000–2009. Black arrows show natural fluxes as well as the chemical removal of CH_4 in the atmosphere by OH radicals. Geological sources include mud volcanoes. There is also a small atmospheric sink of CH_4 in the stratosphere. Red arrows denote anthropogenic emissions of CH_4. (Adapted from Figure 6.2 of Ciais et al. (2013))

keep warming within 2°C with respect to pre-industrial times. As identified by the United Nations Framework Convention on Climate Change (UNFCCC), this will require decisive political action to implement emission mitigation strategies that will need to be sustained over the next century to reduce typical emission rates by 3–5% per year. An accurate knowledge of regional-scale anthropogenic emissions is paramount for designing well-informed mitigation policies. New knowledge can also support the definition of sharing principles for efforts to reduce emissions that are acceptable to all nations, and for monitoring their effectiveness over time.

To quantify and understand the current state of the carbon cycle, to separate natural from anthropogenic contributions, and to reduce uncertainty in the expected evolution of atmospheric concentrations of CO_2 and CH_4, important questions need to be answered:

- What is the magnitude and spatio-temporal distribution of the natural sources and sinks of CO_2 and CH_4?
- What is the magnitude and spatio-temporal distribution of anthropogenic emissions of CO_2 and CH_4 from the use of fossil fuels, land-use change, agriculture and waste treatment?
- What processes drive the uptake of carbon by the land and the ocean in each region, and how are they affected by climate change?
- Will there be positive or negative feedbacks as natural sources and sinks respond to climate change?
- Are large carbon reservoirs at high latitudes (permafrost, methane hydrates) already beginning to respond to dramatic warming in these regions and becoming sources of CH_4 and CO_2 to the atmosphere?

The inability of current observations to quantify carbon fluxes accurately across continental, regional and down to local scales (for the largest sources) is the primary problem in carbon-cycle science today (Fig. 2.1). Limitations in the accuracy, precision, resolution and coverage of atmospheric CO_2 and CH_4 measurements seriously impairs the ability of the scientific community to assess and understand regional fluxes, and to address other terrestrial carbon-cycle science questions.

Sections 2.2–2.6 describe key questions in carbon-cycle research. Section 2.7 details the current global carbon-observing system. Section 2.8 identifies gaps and limitations in this system and Section 2.9 identifies a potential solution.

2.2 Atmospheric CO_2 and CH_4 Increase Related to Human Activity

The increase of CO_2 concentrations in the atmosphere as illustrated in Fig. 2.1 has been driven by the dramatic growth of the global population, from less than one billion in 1800 to over seven billion today. This larger population needs more energy from cheap fossil fuel, more food and more water. The increase in population has also been accompanied by increasing urbanisation, with over 50% of the world's population now living in cities, and this trend will continue in the future (IPCC, 2013). By 2013, fossil-fuel combustion, deforestation, and other human activities were adding over 10.7 Gt of carbon to the atmosphere a year. Urban areas currently contribute 70% of global fossil-fuel CO_2 emissions (Duren and Miller, 2012).

Emissions from fossil fuel dramatically accelerated during the last decade. Between 2002 and 2013, atmospheric CO_2 grew at 2 ppm per year, the highest increase observed since measurements began in 1958 (Fig. 2.5). Although the economic downturn in 2008–2010 temporarily reduced the rate of emission growth, the subsequent economic recovery has led to a continuous increase (Le Quéré et al., 2014). By 2013, fossil-fuel emissions were 55% higher than they had been in 1990. However, according to the International Energy Agency, in 2014 the growth rate in carbon emissions may have stalled at this historically high level, maintaining atmospheric growth rates of 2 ppm per year.

In response to rice-paddy cultivation, biomass burning, and livestock production, atmospheric CH_4 concentrations started to rise slightly before CO_2 (IPCC, 2013). Emissions of CH_4 are now dominated by human activities, mainly from agriculture, coal mining and natural-gas extraction and distribution, as well as waste treatment. After a period of rapid increase, atmospheric CH_4 was quite stable, suggesting a new equilibrium, but then concentrations began to rise suddenly (Fig. 2.6) (Kirschke et al., 2013). The cause of these changes remains hotly debated.

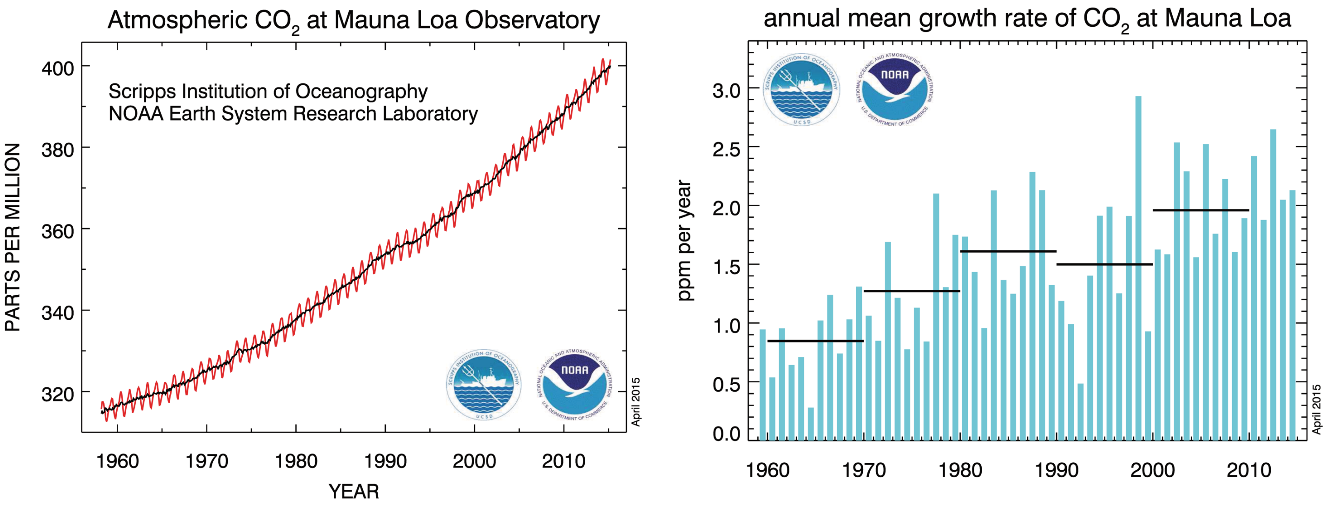

Figure 2.5. Left: Atmospheric CO_2 at Mauna Loa Observatory, Hawaii. The black curve represents seasonally corrected data. Right: Annual mean CO_2 growth rates defined as the first derivative of the seasonally corrected CO_2 curve (blue bars). The decadal average growth-rate values are plotted as horizontal black lines. (P. Tans–NOAA/ESRL and R. Keeling–Scripps Institution of Oceanography)

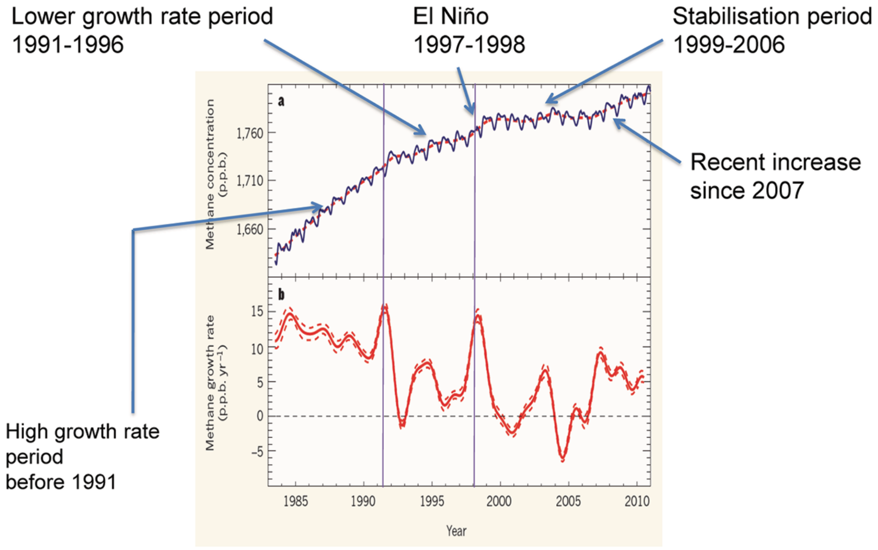

Figure 2.6. Atmospheric CH_4 concentrations (blue) and growth rates (red) since 1983. The arrows indicate growth-rate anomalies over the last three decades. Data from NOAA/ESRL surface network stations. (P. Ciais–LSCE)

2.3 CO_2 Global Budget and Uncertainties

The annual cycle of atmospheric CO_2, seen in the well-known 'Keeling Curve' of *in situ* measurements made at Mauna Loa (Keeling, 1960) (Fig. 2.5), shows that a net CO_2 increase is superimposed on seasonal variations of natural CO_2 fluxes. This is primarily driven by photosynthesis and respiration on land and by air–sea fluxes (Fig. 2.2). Gross natural fluxes to the atmosphere from the land and the oceans emit 120 and 90 GtC yr^{-1}, respectively, but then they also reabsorb a comparable quantity (King et al., 2007; IPCC, 2013). The net effect is that these fluxes are roughly balanced (Fig. 2.7). Fossil-fuel emissions and deforestation result in net fluxes of CO_2 to the atmosphere, which push the natural carbon cycle out of balance. As the primary medium for exchange between the land and oceanic carbon reservoirs, the atmosphere plays a central role in the carbon cycle. Measurements of atmospheric CO_2 can, therefore, be used as a powerful tool to understand and quantify these surface-to-atmosphere fluxes.

The regional distribution and the temporal variability of CO_2 and CH_4 fluxes and their connections with anthropogenic drivers and biogeochemical processes are among the least understood aspects of the carbon cycle (e.g. Keeling and Severinghaus, 2000; Kirschke et al., 2013). Limitations in our understanding of magnitude, trends and mechanisms of regional fluxes translate into large uncertainties in projections of atmospheric greenhouse-gas concentrations made using Earth System Models (Fig. 2.3). An improved understanding of the carbon cycle at regional scales, with coverage of the entire globe so that the sum of regional fluxes can be reconciled with the global growth rates, is the most important goal for the scientific community focusing on the carbon cycle.

Long-term atmospheric CO_2 measurements from surface stations, and known anthropogenic emissions, indicate that less than half of anthropogenic emissions on average stay in the atmosphere. The remainder is taken up by the ocean and the land (Fig. 2.7). The fraction of emissions that accumulates each year in the atmosphere varies greatly from year to year (Fig. 2.8) because climate variability affects CO_2 fluxes from the land (e.g. Bousquet et al., 2000).

Emissions from fossil-fuel burning and cement production are not directly measured, but are estimated using energy data and emission factors for different fuel types. Emissions are reported by countries on an annual basis.

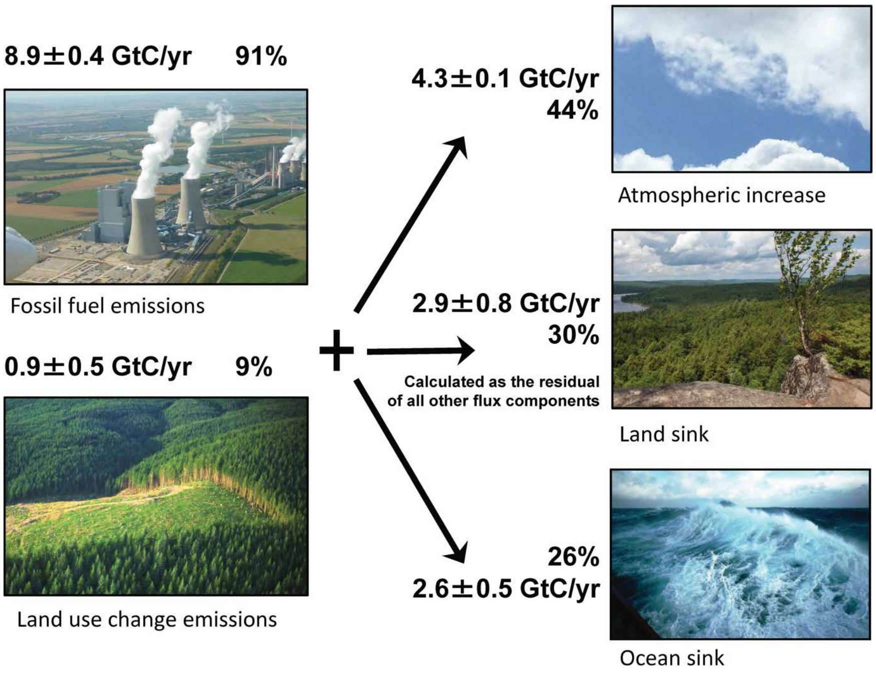

Figure 2.7. Global CO_2 budget for 2004–2013, with anthropogenic emissions (left) causing the increase in atmospheric concentrations, and being partly re-absorbed by the ocean and by land sinks (right). Note that the land sink is calculated as a residual of all other flux components. (Source: Global Carbon Project; *www.globalcarbonproject.org*)

A global emission product is produced and updated each year by the Carbon Dioxide Information Analysis Center and the International Energy Agency (Andres et al., 2014), which serves as a basis for the IPCC assessment and for the annual update of the carbon budget by the Global Carbon Project (Le Quéré et al., 2014). Fossil-fuel emission sources in the developed world are known, to better than 10% at country and annual scales, but emissions over individual cities and regions have much larger uncertainties (Duren and Miller, 2012). In the developing world, which now contributes almost 60% of fossil-fuel CO_2 emissions, uncertainties are substantially higher (Guan et al., 2012; Andres et al., 2014). The lack of data that are independent from numbers reported by countries themselves has been highlighted as a key source of uncertainty in the current carbon budget (Ballantyne et al., 2012).

Emissions of CO_2 from land-use change, mainly deforestation and forest degradation in the Tropics, account for 0.9 GtC yr^{-1} and have an uncertainty of more than 50%. Global deforestation emissions appear to have been rather constant for the last decade. Satellite observations of areas that have lost forest, however, reveal contrasting trends in different countries. For example, rates of deforestation are decreasing in Brazil, but increasing in Indonesia and Malaysia (Hansen et al., 2013), indicating that deforestation is, in fact, far from stable. Forest degradation is more elusive than deforestation and cannot be easily tracked with land-cover measurements. Degradation is estimated to add another 0.2 GtC yr^{-1} to the atmosphere (Pütz et al., 2014).

Estimates of the global CO_2 ocean sink are partly constrained by ocean measurements collected during the 1990s. Ocean biogeochemistry models are used to estimate the associated trend and variability of this sink (Le Quéré et al., 2014). These models, which simulate the annual exchange of carbon between the sea surface and the atmosphere, as well as the transport of carbon through physical mixing and biological processes, are driven by measurement-derived datasets of climate variables. In the carbon budget assessment of the Global Carbon Project (Le Quéré et al., 2014), ocean-model results must be rescaled to the same decadal-mean value that was derived in the 1990s from ocean observations (Fig. 2.7). This is because individual models cannot reproduce the mean observed sink. In 2004–2013, the ocean sink is estimated to have removed 26% of total CO_2 emissions (fossil fuel plus net land-use change), amounting to 2.6 ± 0.5 GtC yr^{-1} . The year-to-year variability of

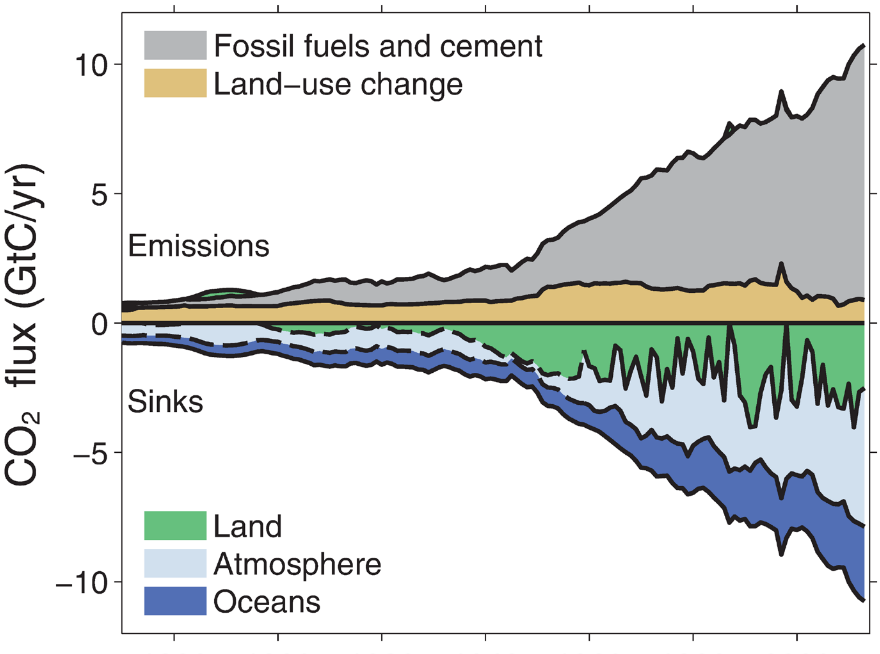

Figure 2.8. Components of the global carbon budget as a function of time (Le Quéré et al., 2014)

the ocean sink is smaller than that of the land, but some regions such as the Eastern-equatorial Pacific and the North Atlantic show evidence of significant interannual fluctuations.

The global CO_2 land sink is not measured directly because of the enormous spatial heterogeneity of ecosystem CO_2 fluxes. Instead, it is calculated as the balance needed to close the global carbon budget –given estimates of anthropogenic emissions, the ocean sink and the atmospheric increase. A rough estimate of the consistency of the residual land sink is provided by results from dynamic global vegetation models, but the spread of these models is too large to trust their results at regional scales (Le Quéré et al., 2014). Using the residual method, the global land sink is estimated to have removed 30% of anthropogenic CO_2 emissions (fossil fuel plus net land-use change) from the atmosphere between 2004 and 2013 (Fig. 2.7).

The evolution of the global carbon budget is shown in Fig. 2.8 and indicates that emissions increase more or less steadily over time and that the ocean sink increases as well, being mainly driven by rising CO_2 in the atmosphere. However, the year-to-year variability of the global land sink is very large. The fluctuations of the land sink reflect the impact of interannual climate variability on ecosystem CO_2 fluxes, predominantly in the Tropics (e.g. Wang et al., 2013b). El Niño years, which are associated with large droughts in tropical regions and that exacerbate fire emissions and decrease ecosystem productivity, result in abnormally high atmospheric CO_2 growth rates. Conversely, during the wetter La Niña years and during years reflecting the cooling effect from large volcanic eruptions, the CO_2 growth rate in the atmosphere is lower than usual. Regional attribution and understanding of the processes of these anomalies in the terrestrial sink remain highly debated. Currently, we do not have sufficient atmospheric observations to determine which continents or biomes absorb or emit abnormal amounts of CO_2 during El Niño and La Niña years, or following volcanic eruptions.

The regional distribution of land and ocean CO_2 fluxes is much more uncertain than their global totals (IPCC, 2013). Some of the most sensitive regions in the carbon cycle are thought to be the Arctic, tropical forests, and the North Atlantic and Southern Ocean. These sensitive regions appear to have either large, climate-sensitive carbon stocks, or large and variable CO_2 fluxes. Currently, however, it is not possible to assess the real magnitude of CO_2 fluxes from these areas owing to the lack of understanding of the key processes that control them. Therefore, their variability and trends remain the subject of scientific controversy.

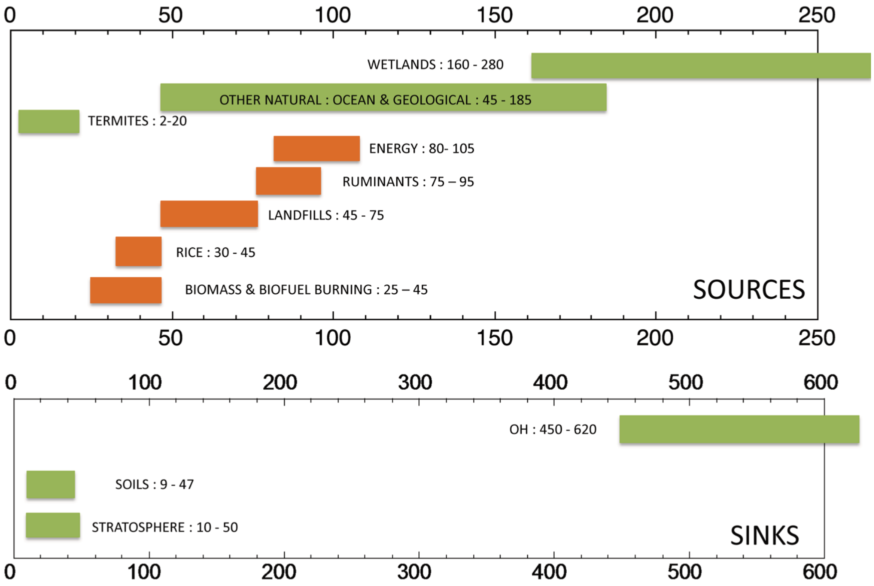

Figure 2.9. Range of bottom-up estimates for natural (green) and anthropogenic (orange) sources and sinks of atmospheric CH_4 (in $TgCH_4$ yr^{-1}). After Kirschke et al. (2013). (P. Ciais–LSCE)

2.4 CH_4 Global Budget and Uncertainties

The global CH_4 budget (Fig. 2.9) is, in some ways, more poorly understood than that of CO_2. Although the global OH sink and the sum of sources is rather well known, the large range of bottom-up emissions estimated illustrates the large uncertainties of each individual source.

Wetland emissions represent the largest and the most uncertain source of the global budget, with published estimates ranging from 90 to 250 Mt yr^{-1} (Kirschke et al., 2013; Fig. 2.9). Wetland emissions are estimated using ecosystem models, which calculate CH_4 emissions given simulations of the height of the water table, the availability of organic carbon in the soil, vegetation cover and climate conditions (Melton et al., 2013). The uncertainties in the wetland emission estimates are important both at high latitudes in summer and all year round in the Tropics. Wetlands in northern latitudes are sensitive to climate change, in particular because of varying hydrological conditions and permafrost decomposition. In the Tropics, CH_4 is also emitted from seasonally inundated floodplains. The representation of small-scale processes that produce CH_4 emissions in models for flooded systems is highly uncertain because of the limited availability of *in situ* flux measurements, difficulties modelling the hydrological dynamics of tropical floodplains, and the balance between CH_4 production (methanogenesis) and destruction (methanotrophy) in the same soil column (Ringeval et al., 2014). Geological natural sources include ocean and land seepage as well as mud volcanoes.

Anthropogenic CH_4 emissions from natural gas and coal extraction, and from the agriculture and waste sectors, can only be estimated from statistical data on livestock, areas of rice-paddies, energy use and emission factors. Significant releases of CH_4 from oil, gas and coal production have recently been observed both from *in situ* measurements and from space (Fig. 2.18 and Fig. 4.2). Our understanding of anthropogenic and natural emissions of CH_4 and the modification of natural emissions caused by human activity (land-use change, agriculture, fire suppression, wetland drainage) is very limited (IPCC, 2013). Compared to CO_2, emissions of CH_4 are from leaks when handling fossil fuels, rather than from fuel burning. There are, therefore, many more uncertainties in emission inventories because leaks can be very local, highly dependent on infrastructure quality and type, and operators are often not even aware that there may be a problem. Fossil CH_4 emissions from rapidly growing Asian economies are estimated to have made a large contribution to the recent increase, but unlike earlier decades, the rate of change of emissions from inventories during the late 2000s does not match the recent observed rate of atmospheric increase (Fig. 2.6).

Unlike CO_2, CH_4 is chemically reactive in the atmosphere. The mean ~10-year residence time of CH_4 in the atmosphere is determined by how it reacts with OH. The concentration of OH, and thus the sum of all the sources, is known to within ±10% based on the decay of methyl-chloroform, but the magnitude of individual sources is much more uncertain. The trend and interannual variations of the OH sink are also less known than the global magnitude (Montzka et al., 2011), even at hemispheric scales (Patra et al., 2014). Because of the uncertainty in the location and magnitude of individual sources and in the magnitude of the atmospheric OH sink, the source apportionment and the regional distribution of CH_4 emissions is challenging. As a result, a clear connection between observed atmospheric CH_4 trends and ongoing policy efforts to reduce emissions of this powerful greenhouse gas cannot be established for specific source sectors.

2.5 Improving Carbon Cycle Predictions

2.5.1 Improving Earth-System Models

The response of the carbon cycle to climate change and to the projected increase of emissions is a critical source of uncertainty in climate predictions (Fig. 2.3). Simulations from Earth-system models that describe the coupling between the carbon cycle and climate change for different emission scenarios indicate consistently that climate change will diminish the ocean and land sinks of CO_2 in some regions during the coming century (IPCC, 2013; Friedlingstein et al., 2006; Jones et al., 2013). Weakened carbon sinks will, in turn, accelerate the growth of atmospheric CO_2 for any given emission scenario, amplifying global warming. Yet, the magnitude of the carbon cycle, climate feedbacks and the underlying mechanisms are poorly understood. Mechanisms that weaken natural CO_2 sinks include increased ocean stratification, more frequent wildfires, and less CO_2 being fixed in land ecosystems because of limited availability of nutrients and water in the Tropics. But other processes, including CO_2 fertilisation, longer high-latitude growing seasons, and enhanced ocean mixing, may increase sinks in other regions. These regional differences and the magnitude of carbon-cycle climate feedbacks related to different biogeochemical processes add even more uncertainty.

The Earth-System Modelling community is actively engaged in benchmarking and evaluation to improve carbon models for land (Randerson et al., 2009) and ocean (Séférian et al., 2013). They evaluate these models using information on fluxes such as satellite vegetation indexes and fluorescence, ocean colour, data from flux towers, and compilations of ocean CO_2 partial pressure data from shipboard measurements. Although helpful, none of these carbon-cycle observations are a direct measurement of regional CO_2 fluxes. Modellers need improved estimates of the spatial distribution and variability of ocean and land CO_2 fluxes to untangle the contributions of climate from other drivers as highlighted by the Group on Earth Observations' *Carbon Strategy Report* (Ciais et al., 2010).

In the previous IPCC assessment, Earth System Models did not include a CH_4-cycle interactive with climate change, but separate studies do point out the existence of CH_4-climate feedbacks, which are related to the sensitivity of wetland and fire emissions to temperature and hydrological changes. The magnitudes and whether these feedbacks are positive or negative are uncertain. For instance, warmer conditions could increase CH_4 production in flooded soils, but increased evapotranspiration could reduce production in wetland areas (e.g. Ringeval et al., 2014).

Carbon cycle data assimilation systems (CCDAS) take the benchmarking of carbon cycle models a step further. The CCDAS approach strengthens the link between atmospheric measurements and biological or oceanic processes by including a biosphere or ocean model in the data-processing chain. In this case, atmospheric measurements are not used to estimate CO_2 fluxes, but to constrain uncertain process model parameters. In other words, measurements of current changes in CO_2 and CH_4 concentrations reduce uncertainty in processes that will determine the evolution of the coupled carbon-climate system. The CCDAS technique (e.g. Scholze et al., 2009) allows the combined use of measurements of different quantities (as well as the combined use of different measurements of the same quantity) including satellite data, reducing uncertainties in parameters of the carbon-cycle component in Earth System Models.

To reliably detect change and develop the understanding of ecosystems that is needed for accurate predictions, more data are required in critical biomes such as the Tropics, the Arctic and boreal zones. This need can best be met with a strategic combination of remote sensing and *in situ* data, with satellite observations providing the dense sampling in space and time required to characterise the heterogeneity of ecosystem structure and function (Schimel et al., 2015). Satellite data, in combination with *in situ* ground-based data of atmospheric CO_2 and CH_4 concentrations, can be transformed into flux maps by atmospheric inversions (Section 2.7). These data can be combined with biomass, burned-area and land-cover change products, vegetation information such as the normalised difference vegetation index (NDVI) or solar-induced vegetation fluorescence (SIF), the latter provided, for example, as a by-product from the Greenhouse Gases Observing satellite, GOSAT, and the Orbiting Carbon Observatory-2 (OCO-2). The joint assimilation of CO_2 and CH_4 concentrations in combination with land-vegetation data is expected to significantly improve the predictive ability of Earth System Models for studies of future terrestrial-surface fluxes and carbon stocks.

2.5.2 Interannual Sensitivity

At the global scale, a strong correlation is observed between land temperatures and yearly CO_2 growth rates. For instance, drier and warmer El Niño years, such as 1982–83, 1986–87 and 1997–98, are associated with high atmospheric CO_2 growth rates (e.g. Wang et al., 2013b) indicating abnormally weak land sinks, (Fig. 2.8). This global property of the land carbon cycle has been used to evaluate carbon cycle models (Cox et al., 2013; Piao et al., 2013). The sensitivity of the carbon cycle to climate variability is not just a global number, but also reflects regionally distinct mechanisms and drivers. For instance, temperature limits carbon uptake in northern ecosystems, whereas tropical forests are limited mostly by precipitation. If there were better coverage than OCO-2, global maps showing regional-scale CO_2 fluxes could be inferred from spaceborne measurements using atmospheric inversions (Section 2.7 and Chapter 3). Maps of fluxes with monthly temporal resolutions would offer carbon-cycle modellers the unique possibility of constraining their modelled sensitivity of carbon fluxes to climate variations per region, per ecosystem and per season.

2.5.3 Detecting Non-Linearities

Of particular concern with respect to climate prediction are non-linear feedbacks of the carbon cycle to climate change that could trigger natural and uncontrolled emissions of CO_2 and CH_4. The main carbon cycle non-linear positive feedbacks, or ‘tipping points’, are related to the following processes: the ongoing thawing of huge stores of permafrost carbon in high latitudes (e.g. Koven et al., 2011); the die-back of carbon-rich tropical forests in response to drying and anthropogenic pressure; the sporadic release of CO_2 during extreme climate events such as droughts and mega-El Niños (Ciais et al., 2005; Reichstein et al., 2013); and the abrupt and potentially massive release of CH_4 hydrates, in particular, from Arctic soils and ocean shelves. A few years of abnormal weather could have triggered large emissions of CO_2 and CH_4 (Khvorostyanov et al., 2008) from sensitive regions, but these are poorly observed. Currently, the sparse observations from surface-based ecosystem and atmospheric *in situ* measurement networks do not allow for the early detection and quantification of tipping points in the carbon cycle.

2.6 Independent Measurements of Anthropogenic Emissions

The transparent and verifiable evaluation of emissions represents a considerable economic and political challenge and underpins the success of international treaties. Currently, anthropogenic carbon emissions are estimated

Figure 2.10. Recent trends in CO_2 emissions of fossil fuel and cement production from the Global Carbon Project energy-use data. (Le Quéré et al., 2014)

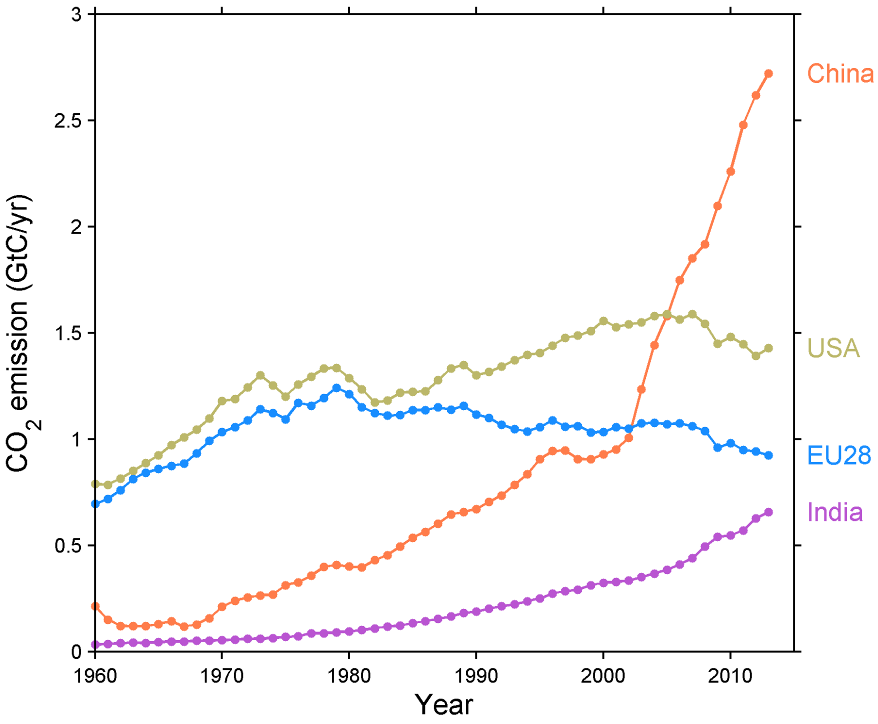

using statistical data on energy use according to agreed methodologies (IPCC, 2006). These methodologies are based on the aggregation of emissions from different sectors and sources – some large, some small.

Countries report emission inventories using fuel consumption data including amount, type, and fuel-specific emission factors. Inventory experts claim uncertainties of 5–10% for Organisation for Economic Cooperation and Development (OECD) countries, rising to 15–20% for China, the world's largest emitter. In fact, inventories are only updated every 3–5 years and are based on emission factors and energy data that sometimes do not mirror technological advances.

Emission inventory estimates for cities are more uncertain as the data required are generally not available or have gaps. Uncertainties are estimated to be in the order of 20–30% for European cities that keep records of their emissions, and it is likely that uncertainties are around 50% for cities in most developing countries as they generally have no inventory in place. Even in Europe or the US where data does exist for some large cities, methods for calculating local emissions differ between cities, making the data unusable at present for upscaling to regional, country and global scales.

At the scale of the largest point sources, emissions of CO_2 are reported by the operators for the largest power plants (www.carma.org), but comparison of different power-plant emission datasets in the US for individual power plants show differences as high as 23%. In many countries, emissions of power plants are not available, the reported locations of sites can be erroneous and sometimes not all power plants are reported.

The evolution of fossil-fuel CO_2 emissions (Fig. 2.10) tracks future scenarios assuming the highest emissions (Peters et al., 2012). Fossil-fuel CO_2 emissions have accelerated since the early 2000s (Raupach et al., 2007) owing to the fast development of emerging economies, in particular China (the top emitter) and India (now the fourth largest emitter), as shown in Fig. 2.10 (Le Quéré et al., 2014). Chinese fossil-fuel CO_2 emissions have increased by ~9% a year over the last decade. This increase was not foreseen by analysts or economic projections during the 1990s and early 2000s. For instance, in their 2002 forecast, the International Energy Agency (IEA) stated: 'Chinese emissions (will) remain well below those of the U.S. in 2030' while, in fact, they had

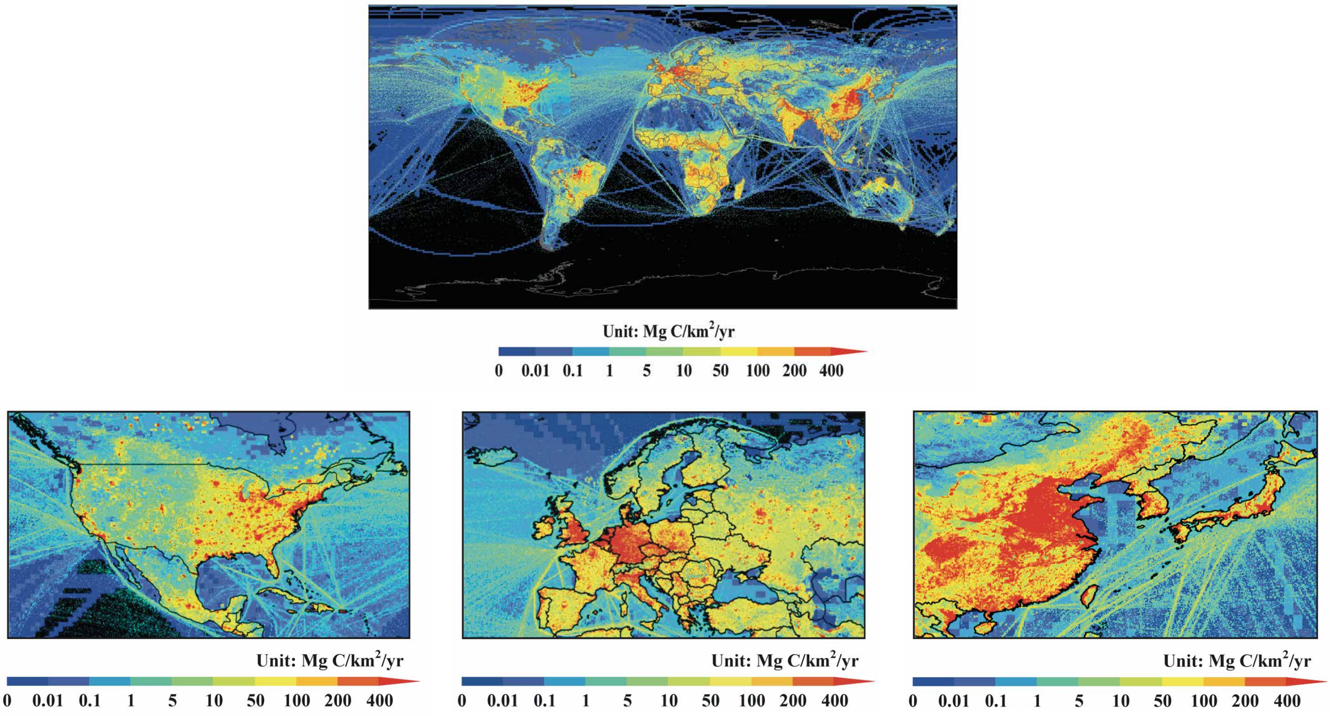

Figure 2.11. Global distribution of fossil-fuel CO_2 emissions (top) and emissions across the US, Western Europe and North-East Asia (bottom). The uncertainty of sub-national scale emissions has been estimated in this dataset to range between 30 and 100%. The lines over oceans are from ship routes. The figure has been redrawn from the 10-km resolution inventory derived from sub-national fuel-use data and detailed emission factors (Wang et al., 2013a).

exceeded US emissions by 2006. However, in 2012–13 there were signs that Chinese emissions were slowing (Fig. 2.10). A preliminary IEA communication[1] in March 2015 announced that global emissions may have levelled out between 2013 and 2014, which was not predicted and remains to be confirmed.

The problem is that the recent growth of emissions has been paralleled by a growth of emission uncertainties. This is because, in emerging economies, statistical data on fuel type, carbon content, and sectorial details are less complete or less regularly updated than in the developed world. For instance, Guan et al. (2012) estimated that the uncertainty of fossil-fuel CO_2 emissions from China is in the order of 15%, based on differences between provincial and national inventories. Therefore, today, the uncertainty of emissions from China is ± 0.4 GtC yr^{-1}, which is actually larger than the carbon sink of North American forests (Ballantyne et al., 2012). Altogether, this reflects an urgent need for independent data to improve emission estimates, both in developed and developing countries.

Emissions of fossil-fuel CO_2 are particularly localised as illustrated by red areas in Fig. 2.11. Although they only take up 2% of the land, urban areas alone account for 70% of fossil-fuel CO_2 emissions (Duren and Miller, 2012). A promising approach to reduce the uncertainty of fossil-fuel CO_2 emissions is to use satellite measurements of CO_2 in the atmosphere above cities (Kort et al., 2012). This approach has, however, not been tested at global or even regional scales because no current satellite has the capability and resolution to regularly observe localised emissions from cities.

Emissions of CH_4 from coal mines, oil industries, landfills, waste-water processing industries, gas-extraction areas and leaking pipelines are also very poorly documented in inventories, given their dispersive nature. For example,

---

[1] *www.iea.org/newsroomandevents/news/2015/march*

uncertainties about CH_4 emissions from shale-gas extraction are receiving a lot of attention and have ignited controversy (Brandt et al., 2014). Unfortunately, at present there is no independent atmospheric observation system capable of monitoring such anthropogenic emissions of CH_4.

The scientific community and policymakers both require independent measurements of fossil-fuel CO_2 and of CH_4 emissions that would help locate and quantify emissions from megacities, power plants, industrial areas and natural-gas extraction regions. The spatial scale at which emission estimates must be monitored is at local scales ranging from points, such as over power plants, to a few tens of kilometres, such as megacities and major shale-gas-extraction areas. Aggregation of data at regional or country scales is then possible for complementing and improving existing national inventories.

2.7 Regional-scale Natural Fluxes

2.7.1 Bottom-up Methods for Upscaling Local Measurements

To quantify and understand the distribution of natural CO_2 fluxes, different types of local observations are available. Flux-tower networks use the 'eddy-covariance' method to measure local fluxes of CO_2, water vapour, and heat between terrestrial ecosystems and the atmosphere. The eddy-covariance method is the main monitoring tool for measuring the net ecosystem exchange (NEE), which is defined as the net flux of CO_2 and equals the balance of ecosystem respiration (release) minus photosynthesis (uptake). The networks have significantly expanded over the last decade (Baldocchi et al., 2001) (Fig. 2.12). Realistic upscaling of regional net CO_2 budgets using flux towers is limited by some systematic errors in NEE measurements, uneven coverage of ecosystems (as shown in Fig. 2.12) and some missed land–atmosphere CO_2 flux components such as erosion (Jung et al., 2011).
Measurements of the difference in CO_2 partial pressure (ΔpCO_2) between the ocean and the atmosphere, collected mainly from ship data (Pfeil et al., 2013), make it possible to scale up the distribution of air–sea CO_2 fluxes to the globe (e.g. Park et al., 2010) using geostatistical methods and data-driven modelling.

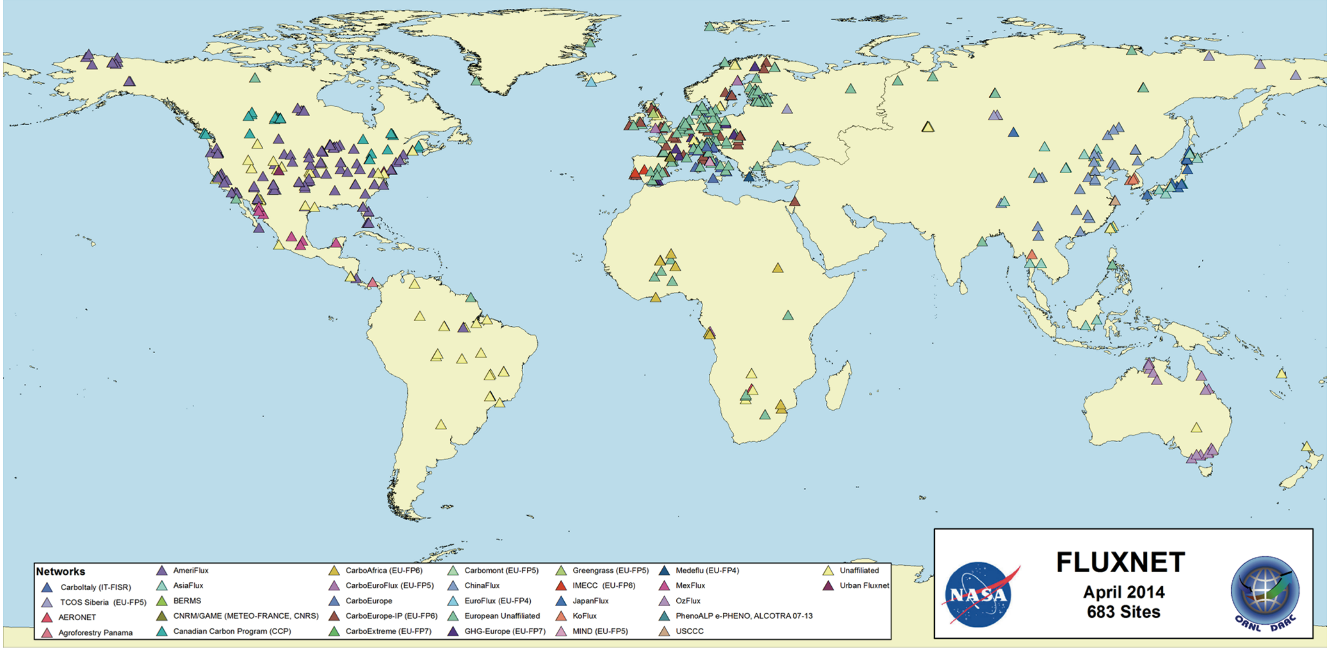

Figure 2.12. Distribution of eddy-covariance flux towers in different ecosystems. (NASA/ORNL DAAC)

This approach is limited mainly by the sparseness of *in situ* data, unknown systematic errors in the sampling (e.g. very poor coverage over the Southern Ocean) and by systematic errors in gas-exchange kinetics.

The upscaling of ocean ΔpCO_2 and eddy-covariance point-scale NEE measurements based on a variety of optimal interpolation techniques, often uses satellite observations of surface properties (e.g. ocean colour, vegetation greenness, sea-surface temperature, soil moisture), as well as gridded climate and weather fields. This data-driven modelling approach is also limited by the sparseness of *in situ* data and unknown systematic sampling errors, for example with data being collected over one region but used to model fluxes over another region.

Observations of natural CH_4 fluxes, mainly from wetlands, are more limited than for fluxes of CO_2, with few sites available and different methods being used (eddy-covariance flux towers or flux chambers). A direct upscaling of wetland ecosystem CH_4-flux measurements from local data has not been produced yet, but wetland ecosystem models use these data for parameter calibration, as well as satellite-derived time-varying maps of the distribution of flooded areas to produce global estimates of emissions. Model intercomparisons reveal large differences between results (Melton et al., 2013).

The strength and value of local bottom-up measurements of CO_2 and CH_4 fluxes is that they provide detailed information to understand site-scale processes. The weakness of bottom-up measurements is they are sparse and uneven, so that assumptions are needed to scale them in space and time into regional fluxes. Generally, regional estimates of terrestrial or air–sea fluxes obtained by upscaling of local observations are prone to systematic errors and can miss key fluxes that were not properly sampled.

2.7.2 Top-down Methods for Down-scaling Atmospheric Measurements

This section describes the top-down method that makes use of spatial and temporal differences in atmospheric concentrations of CO_2 and CH_4 to quantify regional fluxes. This method has the advantage of being 'complete' since the atmosphere is an integrator of all surface fluxes. Therefore, important sources and sinks cannot be missed using this method, which is also called atmospheric inverse modelling. It makes use of atmospheric transport models, which connect surface fluxes to corresponding atmospheric concentrations by accounting for the mixing processes in the atmosphere (Fig. 2.13).

Top-down inverse modelling is a valuable tool, but places significant demands on the accuracy, resolution, and coverage of atmospheric measurements (Enting et al., 1995; Gurney et al. 2002; Baker et al., 2006), and the quality of the atmospheric transport model. Other methods exist that compare independent data streams, either for verifying the consistency of inverse modelling derived estimates, or for investigating the linkage between measurement-derived flux variations and their climatological drivers, such as variations in temperature and precipitation. Surface and satellite atmospheric CO_2 and CH_4 data can also be assimilated to improve model fields of atmospheric concentrations (e.g. Agusti-Panareda et al., 2014; Massart et al., 2014).

So far, atmospheric CO_2 and CH_4 have been measured with high precision from a global network of surface stations. The current network comprises about 100 stations, distributed unevenly around the world. Furthermore, there has been some attrition in the number of sites in recent years (Houweling et al., 2012). Because of the sparse number of monitoring stations and because of the dispersive nature of atmospheric transport, the flux inversion problem is highly underdetermined and contains a much larger number of unknown fluxes than observational constraints. Inversions, thus, make use of additional independent information about the fluxes that are prescribed as *a priori* or first

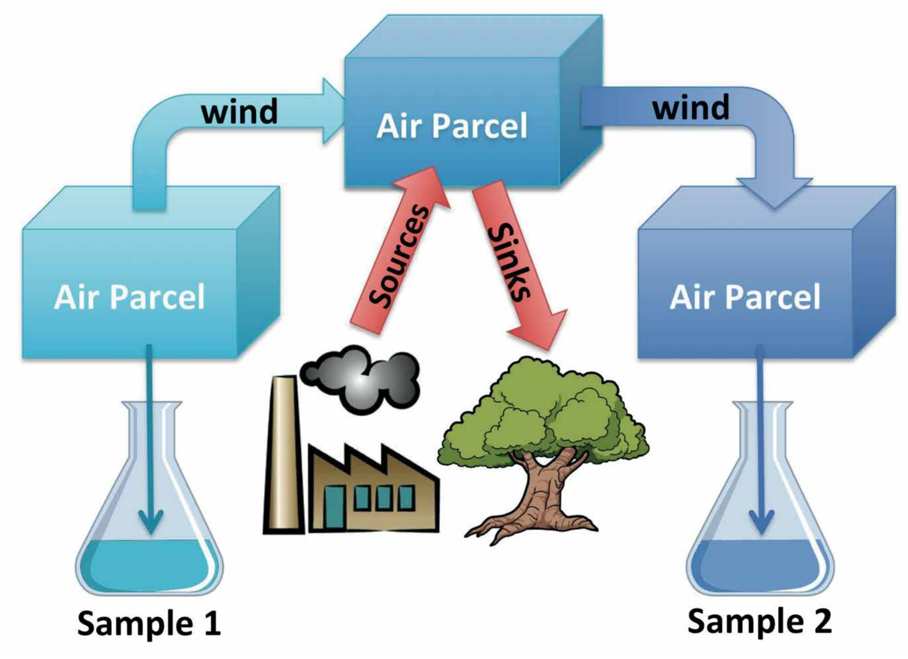

Figure 2.13. Simplified representation of inverse modelling, which is based on CO_2 or CH_4 concentration measurements upwind and downwind of a region emitting or absorbing these gases. A transport model is used to assimilate concentration gradients into surface fluxes. (S. Houweling–SRON)

guess. This information is derived commonly from anthropogenic emission inventories and process model outputs.

The inversion of CO_2 and CH_4 measurements from the current global surface network has enabled a precious, but yet very coarse, diagnostic of the fluxes over the last 20 years. Global inversion results cannot be trusted at scales smaller than large latitude bands, continents or large ocean gyres (Gurney et al., 2002; Peylin et al., 2013). In addition, since there is a lack of measurement stations, CO_2 fluxes from tropical continents and from most ocean gyres are unconstrained by data from the surface network and, thus, bear the largest uncertainties in inversion results. This is illustrated in Fig. 2.14 by the large uncertainties of inverse model results, both for CO_2 and CH_4 fluxes, even when the regional fluxes from inversions are averaged zonally.

Some regions like North America and Western Europe are covered by denser *in situ* surface networks, and inversions using regional transport models have shown the ability to resolve details of CO_2 and CH_4 fluxes within those regions down to the desirable scale of a moderate-sized country in Europe (Broquet et al., 2013) or a group of states in the US (Miller et al., 2013). Yet, the sampling of the atmosphere, even in these best-covered regions, has significant gaps and the number of unknown surface fluxes that inversions attempt to solve remains much larger than the number of *in situ* measurements – meaning that even in these regions the inversions are underdetermined.

Another important limitation of the *in situ* surface network is that fossil-fuel emissions cannot be separated from natural fluxes with these data. The majority of *in situ* stations are located away from urban areas and power plants, but measure air masses that contain a mixture of CO_2 from fossil fuels and from natural reservoirs. Therefore, inversions use emission inventories as if they were perfectly known and subtract their signals from the modelled CO_2 concentrations to solve natural CO_2 fluxes as residuals. In so doing, any systematic error in the assumed field of fossil-fuel CO_2 emissions inevitably translates into a biased diagnostic of natural fluxes. As uncertainties in regional fossil-fuel emissions are increasing over time (Le Quéré et al., 2014) as well as at finer spatial scales, independent constraints on emission estimates appear to be essential for inversions to quantify natural fluxes reliably.

In a data-sparse world, inversions rely on modelled atmospheric transport fields to match observed CO_2 and CH_4 gradients across large distances. Any biases in modelled transport affect the inversion of surface fluxes. Despite

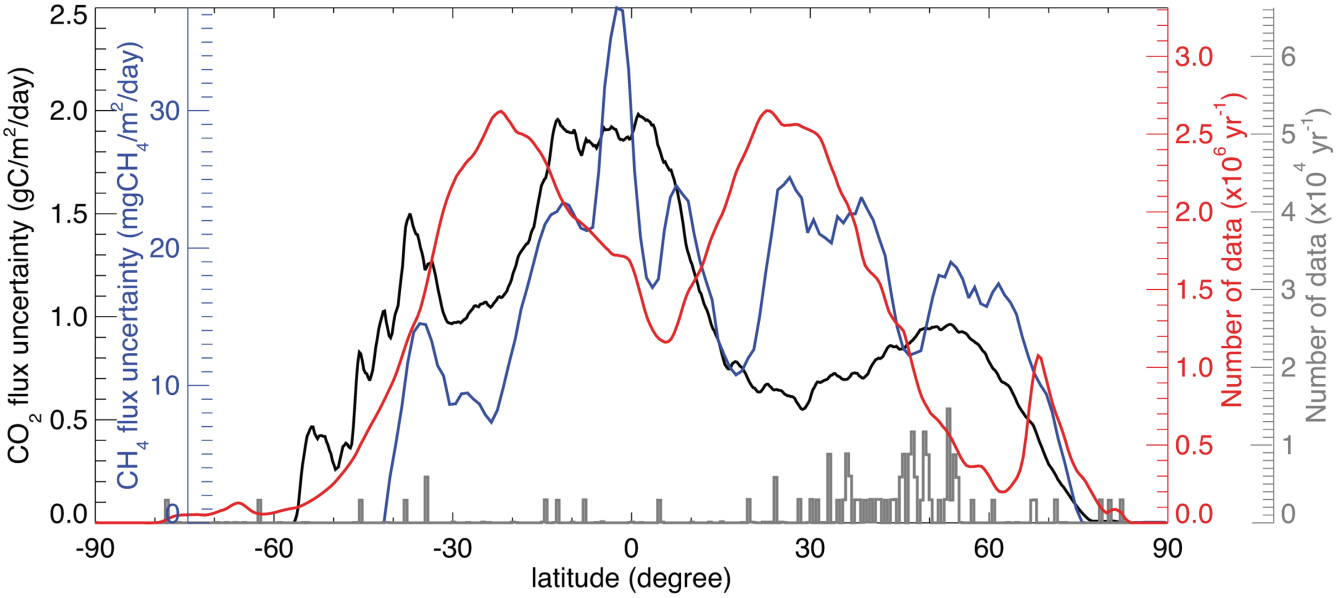

Figure 2.14. Zonal distribution of the uncertainty CO_2 (black) and CH_4 (blue) fluxes from the top-down method or inverse modelling when using sparse in situ data. The number of data is shown in red. The grey lines show the weekly number of data from *in situ* surface sites. (S. Houweling–SRON)

significant progress in numerical weather prediction, recent intercomparisons of atmospheric inversions (Patra et al., 2011) show that the current generation of transport models has significant biases, making evaluation and benchmarking crucial to improve them.

If the coverage, spatial resolution and temporal sampling of atmospheric CO_2 and CH_4 measurements could be substantially improved, without compromising their accuracy, these data would be invaluable in inverse models to strengthen the observational constraints on fluxes and to improve the resolution of the inversion-derived flux estimates. This was noted in the last IPCC report, and was also discussed in the GEO Carbon Strategy (Ciais et al., 2010). Dense ground-based networks measuring atmospheric CO_2 and CH_4 have also demonstrated their potential as a tool for independently verifying emission inventories (Section 2.5). However, this application places high demands on the spatial resolution, coverage of high-emission regions and accuracy of the observations. This cannot be achieved within a decade by simply expanding *in situ* measurement networks.

The most appropriate tool to achieve uniform global coverage and sampling of atmospheric measurements with the required density is to make spaceborne measurements of column-averaged CO_2 and CH_4 dry air mole fraction.

2.7.3 State-of-the-art Satellite Measurements

Spaceborne measurements provide global coverage, enabling the characterisation of regional gradients in the column-averaged CO_2 or CH_4 dry air mole fraction (hereinafter XCO_2 and XCH_4) and from this, allow inverse modelling systems to solve regional surface fluxes.

Satellites provide the unique potential to change the inversion paradigm from current data-poor conditions to a data-rich system in the near future. Yet, monitoring XCO_2 and XCH_4 from space poses stringent requirements on the measurement accuracy if satellite data are be used effectively by inversion modelling systems. In the boundary layer, CO_2 and CH_4 can vary by 30 ppm and several 100 ppb, respectively, in immediate response to surface fluxes. In the less well-mixed free troposphere above, signals of surface fluxes are more

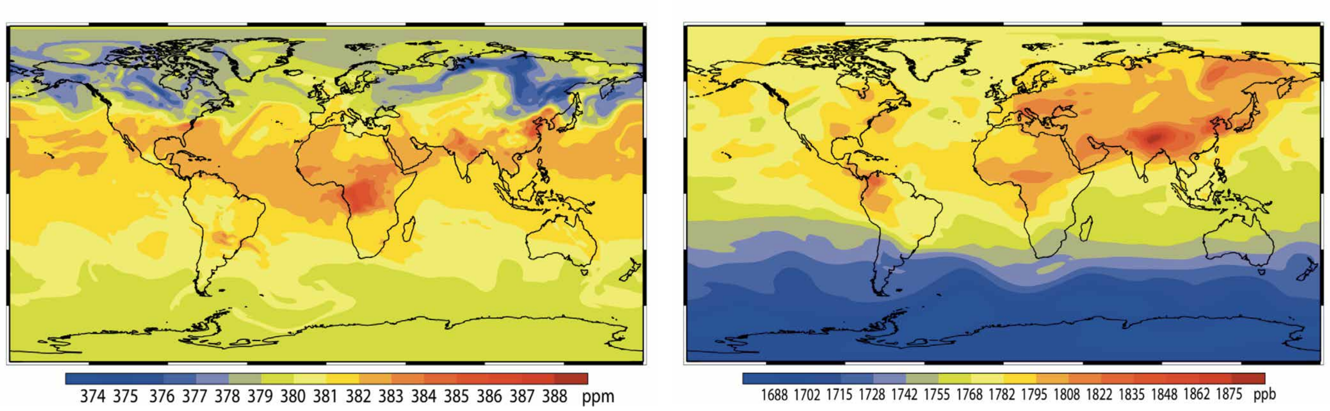

Figure 2.15. Simulations of XCO_2 in ppm (left) and XCH4 in ppb (right) using the TM5 global transport model. Shown are examples of one day in summer 2008 for CO_2 and in summer 2011 for CH_4. (S. Houweling–SRON)

Figure 2.16. XCO_2 time series (Northern Hemisphere average) from SCIAMACHY and GOSAT. (M. Buchwitz–IUP)

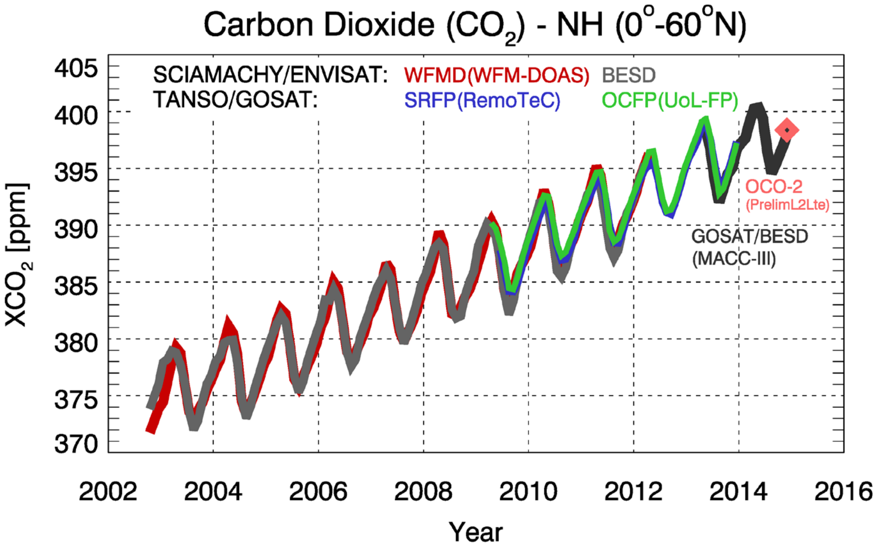

Figure 2.17. Distribution of XCO_2 and XCH_4 for July, August and September from SCIAMACHY (2003) and GOSAT (2013). A continued increase over the last decade is evident. (M. Buchwitz–IUP)

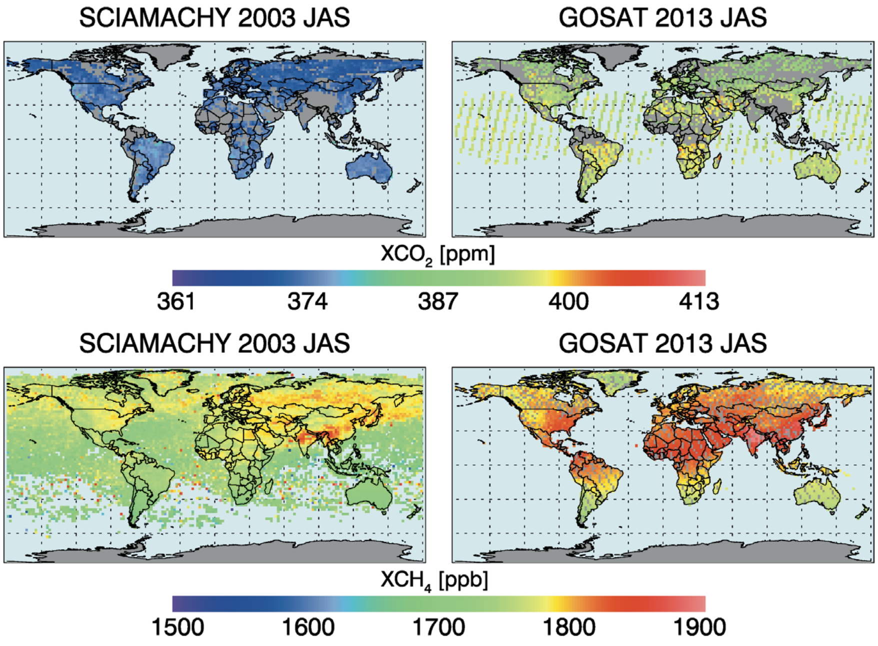

dispersed by rapid atmospheric mixing and transport, and show smoother variations. Therefore spaceborne observations that integrate concentrations over the atmosphere rarely show gradients larger than 8 ppm for XCO_2 and 80 ppb for XCH_4. This is illustrated in Fig. 2.15, which shows XCO_2 and XCH_4 simulated with a transport model. Given fast zonal mixing of the atmosphere in longitude, east–west gradients are even smaller: in the order of 2–3 ppm for XCO_2 and 30 ppb for XCH_4.

Satellite observations of XCO_2 and XCH_4 can, therefore, only improve our understanding of surface fluxes if they have the accuracy, precision, coverage, spatial resolution, and temporal sampling needed to describe gradients with amplitudes of about 3 ppm for CO_2 and 30 ppb for CH_4 on scales ranging from several 100 km over land to ~1000 km over oceans.

Envisat's SCIAMACHY instrument and the GOSAT mission pioneered the ability to remotely sense greenhouse gases with good sensitivity throughout the atmospheric boundary layer. As part of ESA's Climate Change Initiative, extended time series of XCO_2 (Fig. 2.16) and XCH_4 have been produced from SCIAMACHY and GOSAT measurements. As 'essential climate variables' CO_2 and CH_4 data are needed to reduce uncertainties in our knowledge of the climate system (GCOS, 2010). The main scientific achievements of SCIAMACHY and GOSAT are briefly summarised in the following.

SCIAMACHY provided the first measurements of XCO_2 and XCH_4 from space with good sensitivity to the boundary layer. Maps of XCO_2 and XCH_4 distributions obtained from SCIAMACHY (2003) and GOSAT (2013) for July, August and September (Fig. 2.17) show a continued increase over the last decade (Source: Buchwitz et al., 2013c).

SCIAMACHY XCO_2 data products provided insight into how CO_2 fluxes in northern ecosystems respond to interannual surface-temperature variability (Schneising et al., 2014a). In addition, they also showed that large-scale anthropogenic signals could be detected from space (Schneising et al., 2013), and the combination of XCO_2 with NO_2 was used to distinguish between biospheric and anthropogenic signals (Reuter et al., 2014a).

Anomalies in atmospheric XCH_4 were also detected by SCIAMACHY. More recent developments included the first detection and quantification of a localised methane emission hot spot: the Four Corners region in the US (Kort et al., 2014), as shown in Fig. 2.18.

SCIAMACHY's single measurement precision has been assessed against the Total Carbon Column Observing Network (TCCON) and is estimated to be

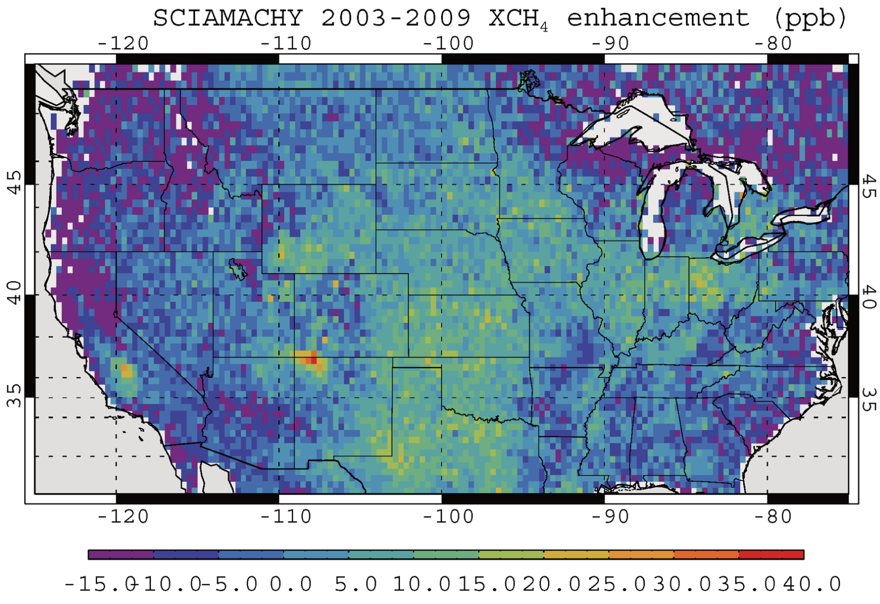

Figure 2.18. A localised methane emission hot spot detected using SCIAMACHY XCH_4 data. The red dot in the centre is the Four Corners area in the US, a major source of anthropogenic methane emissions that was significantly underestimated in inventories. After Kort et al. (2014). (C. Frankenberg–JPL)

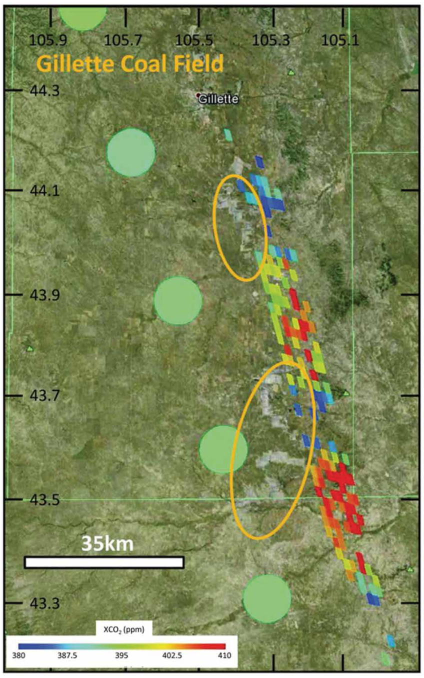

Figure 2.19. GOSAT and preliminary OCO-2 data showing XCO_2 enhancements over Gillette Wyoming, US, a large coal-mining operation that provides 35% of the US coal. Targeted GOSAT soundings from 27 June 2014 (circular footprints) indicate uniform XCO_2 emissions of around 391 ppm, with little contrast. Observations from a single OCO-2 orbit track on 18 November 2014 (parallelograms) appear to show an XCO_2 plume with values more than 20 ppm over the ambient values. (F. Schwandner–JPL)

2–5 ppm for XCO_2 and 30 ppb for XCH_4. The estimated relative bias is around 1 ppm for XCO_2 and 4–12 ppb for XCH_4 at regional scales (Buchwitz et al., 2013c).

Measurements from GOSAT have been acquired since 2009 (Figs. 2.16 and 2.17). The instrument's high spectral resolution and good signal-to-noise ratio result in XCO_2 measurements with minimal systematic errors. However, the drawback is reduced spatial coverage and resolution. This limits the use of the data, only constraining the variability of terrestrial CO_2 fluxes, and only at continental scales. Detection of point sources from GOSAT is limited to the detection of an excess of CO_2 over the megacity of Los Angeles to a few ppm (Kort et al., 2012).

GOSAT single measurement precision assessed against TCCON is 2–3 ppm for XCO_2 and 15 ppb for XCH_4. The estimated relative bias is lower than 1 ppm for XCO_2 and 3–8 ppb for XCH_4 at regional scales (Buchwitz et al. 2013c).

The OCO-2 mission is making important steps in improving spatial resolution and accuracy for XCO_2 measurements (Frankenberg et al., 2014). OCO-2 detects point sources (Fig. 2.19), which shows the importance of a small footprint (a few square km), but also the need for a wider swath (a few hundred km) to resolve sources such as big cities and power plants within the context of the surroundings. The sparse sampling of GOSAT misses large point sources.

OCO-2 single measurement precision is expected to be 0.5 ppm for XCO_2. The OCO-2 satellite aims to limit biases at regional scales in XCO_2 data to below 0.5 ppm.

From SCIAMACHY and GOSAT data around the O_2-A-band, SIF was derived for corrections and can serve as a by-product (Joiner et al., 2011, Frankenberg et al., 2011b). For OCO-2, SIF will be an official data product (Frankenberg et al., 2014).

2.8 Limitations in the Observing System

2.8.1 Knowledge Challenges: Quantification of Sources and Sinks

Most current greenhouse-gas budget estimates, based on *in situ* and satellite measurements, range from global to no better than continental scales. Ocean fluxes are very weakly improved by inversions. For continental-scale fluxes of CO_2 and CH_4, the uncertainties in *a priori* estimates (i.e. before using atmospheric data in an inversion) are currently roughly 50–100% of their mean value. After inversion, the uncertainty in these fluxes remains high at roughly 30–90% of their mean (e.g. Reuter et al., 2014b). Over regions where *in situ* and satellite data are very sparse or do not exist, the uncertainty reduction after inversion is close to zero.

There is a clear need for new observations that can be used to reduce uncertainties of terrestrial CO_2 and CH_4 fluxes at continental scales with monthly resolutions. The carbon-cycle community requires CO_2 and CH_4 budgets for all the continents with an uncertainty of a few hundred MtC yr $^{-1}$ and a few MtC yr^{-1}, respectively, and with interannual variations. This calls for a satellite mission with sufficient measurement coverage, even in regions that are often covered by cloud such as in the mid-latitudes and the Tropics. This would tighten the observational constraints in these poorly-sampled regions.

Ocean fluxes are more diffuse and also slightly better known from existing bottom-up data than terrestrial fluxes. Yet, the ocean CO_2 sink differs between regions and varies across seasons. Inversion results would be useful for ocean carbon cycle researchers if they could provide CO_2 flux estimates at the scale of large ocean gyres, with typical monthly resolutions. This also requires having sufficient measurement coverage in ocean regions that are often covered by cloud.

An important challenge is to provide a breakthrough in the quantification and attribution of regional-scale surface-to-atmosphere fluxes of CO_2 and CH_4.

Current *in situ* and satellite observations are too sparse to provide flux estimates at the scale of middle-sized countries and biomes of similar spatial scales. This limits the possibility of helping countries assess the effectiveness of their efforts to reduce emissions and increase sinks. An example of the scientific need at this scale is to separate CO_2 fluxes between regions covered by ecosystems that have different biogeochemistry; for example, crops in the US Great Plains versus forests in the southeast of the country. A second example is the need to better quantify how climate-induced disturbances impact country-scale CO_2 fluxes, such as the heatwaves and droughts that struck Western Europe in 2003 and Western Russia in 2010. Such extreme climate events appear to be systematically accompanied by releases of CO_2 (few hundred MtC), both during and after spells of drought, suggesting a lagged response from ecosystems. The science gap is in the ability to quantify even small and moderate regional CO_2 and CH_4 flux anomalies, as related to events such as drought, spring frost, large-scale insect attacks and flooding (Kurz et al., 2008).

The goal is to increase the resolving power of greenhouse-gas observing satellites to the scale of flux estimates for medium-sized countries.

The gap in observing capabilities for emissions of fossil CO_2 at local scales is even more salient than for land or ocean fluxes, because there is no observation today that brings an independent constraint on self-reported emission inventories. At national scales, emission totals obtained from energy-use statistics are reported to have a small relative uncertainty, but in some countries emissions are so large in magnitude that their absolute uncertainty is, in fact, larger than those of continental fluxes. In countries that have intense emissions in some regions and productive ecosystems in others, like US, China and India, inversions cannot separate natural CO_2 fluxes from fossil emissions. The distribution and magnitude of emissions within a country are less accurate than national totals, which complicates inversions for their retrieval of terrestrial CO_2 fluxes.

Monitoring emissions from cities and large power plants for CO_2 requires high spatial resolution, dense coverage and frequent revisits, supplemented by *in situ* data and better city-scale inventories (Ciais et al., 2014). Building a global carbon-observing system capable of verifying emissions would require a constellation of satellites, which would need large investment and strong international cooperation. The current challenge for the scientific community is to demonstrate the first suitable XCO_2 and XCH_4 data with high spatial-resolution and imaging capabilities to learn how to quantify such emissions. This knowledge will be crucial for making the most cost-effect choices in the context of a potential future operational global carbon-observing system.

Measuring strong, but poorly known, anthropogenic sources of CH_4, for example from coal mining (Kort et al., 2014) and oil and gas production fields (Karion et al., 2013), is a new challenge for spaceborne measurements at the local scale. These sources result in dispersive CH_4 emissions over areas from several up to 1 000 km^2 for large oil and gas production via hydraulic fracturing (fracking) and can reach CH_4 emissions of about 500 kt yr^{-1} (Karion et al., 2013, Schneising et al., 2014b). The US Environmental Protection Agency (EPA) bottom-up CH_4 emission inventories for these oil and gas fields are in the range of 100–200 kt yr^{-1} , with error bars of 20–50% (Schneising et al., 2014b). The official EPA estimates consistently underestimate the measured dispersive emissions from these sources over all spatial scales (Brandt et al., 2014).

In order to pioneer the detection, characterisation and quantification of strong local sources of CO_2 and CH_4 from space, the challenge is to increase the spatial resolution and coverage of greenhouse-gas observing satellites while maintaining high data accuracy to map local gradients in XCO_2 and XCH_4 introduced by these sources.

2.8.2 Gaps in Satellite Measurements

The SCIAMACHY and GOSAT instruments already provided some information about total column XCO_2 and XCH_4, which stimulated the development of retrieval and validation techniques and flux inversions. GOSAT allowed an important step forward in measurement accuracy compared to SCIAMACHY, however, at the cost of rather sparse coverage. To increase the flux resolving power of inversion using satellite data, there is a need for new systems that combine high accuracy with excellent coverage.

In specific biomes, such as tropical rainforest, measurement coverage of both existing satellites and *in situ* networks remains very limited owing to high cloud cover. Over the Amazon basin, for instance, GOSAT acquires too few data, so that the CO_2 and CH_4 budget of this region is constrained by remote downwind XCO_2 and XCH_4 data southeast and northwest of the Amazon. This insufficient data coverage compounds the CO_2 source in the 'arc of deforestation' (Hansen et al., 2013) of the southeast Amazon with the CO_2 uptake by undisturbed forest in the central and northern areas. More frequent (i.e. monthly) and improved spatial coverage of CO_2 and CH_4 measurements is needed over tropical continents, which are key regions of biological feedbacks to climate change.

At latitudes polewards of 45°, SCIAMACHY and GOSAT showed strong seasonal variations, which reflect the greater amount of useful data during the northern hemisphere summer. Since the annual CO_2 exchange is a net balance between two large opposite fluxes, respiration and photosynthesis, much better coverage throughout the year is needed, ideally with monthly coverage. Thermal-infrared sounders like the Atmospheric Infrared Sounder (AIRS) and the Infrared Atmospheric Sounding Interferometer (IASI) do not solve this coverage problem because they do not offer a sufficient sensitivity down to the surface for accurate inversion of surface fluxes. Improved coverage of XCO_2 and XCH_4 measurements in the northern latitudes is needed, in particular to overcome the presence of clouds in many areas.

Figure 2.20 compares the spatial resolution and coverage of the recent satellites. The low spatial resolution and large uncertainties of SCIAMACHY limited the use of this dataset for understanding regional carbon fluxes. GOSAT improved on data quality but has much sparser sampling, collecting only 300–1000 cloud-free XCO_2 and XCH_4 soundings a day. OCO-2 measures only XCO_2, but with better sensitivity, better sampling (>100 000 cloud-free soundings a day) and better spatial resolution than GOSAT. There is significant spatial variability in XCO_2 on spatial scales of <10 km along OCO-2 measurement tracks, but these tracks are separated by more than 1.5° of longitude and sample less than 7% of Earth's surface each month. Between

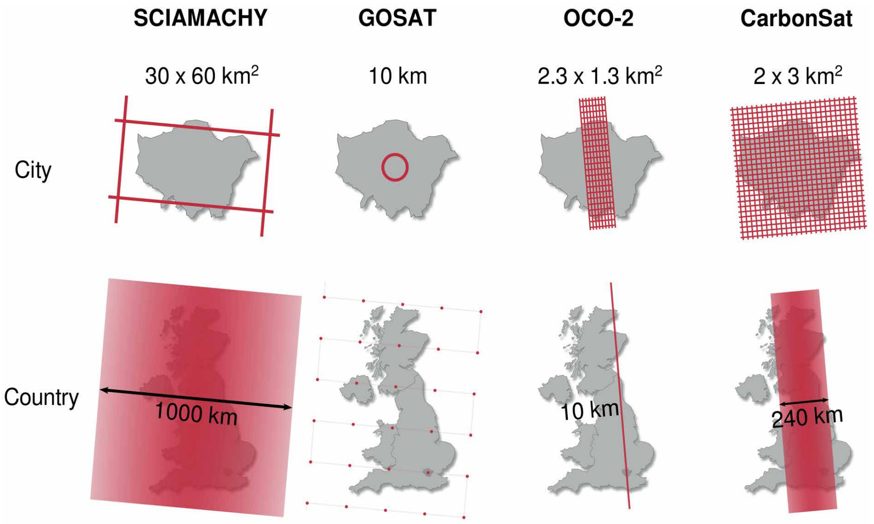

Figure 2.20. Comparison of the spatial resolution and coverage of SCIAMACHY, GOSAT, OCO-2 and CarbonSat. (O. Schneising–IUP)

two OCO-2 tracks, regional fluxes remain loosely quantified by modellers as atmospheric transport models are used to infer them.

To resolve regional CO_2 and CH_4 fluxes and their variability, further improvements are needed for space-based measurements of XCO_2 and XCH_4, not only in coverage but also in the spatial resolution of the measurements, which calls for imagers instead of samplers.

2.9 CarbonSat: Towards a Future Global Carbon-Observing System

The next step in greenhouse gas observations is to evolve, beyond the point- and the line-sampling of former and current satellites, to globally map concentrations of CO_2 and CH_4. The CarbonSat mission will image XCO_2 and XCH_4 from space (Fig. 2.20) at high spatial resolution. This contiguous coverage of high accuracy measurements will fill the gap in carbon observations for regional to national scales. At regional scales this should allow separating the natural fluxes from anthropogenic emissions. The imaging capability and improved detection limit should also allow access to a much wider range of applications, down to the scale of large cities and strong point sources.

CarbonSat could pioneer the spaceborne detection, characterisation, and quantification of strong local sources of CO_2 and CH_4, which has been identified by the Group on Earth Observations (GEO) and the Committee on Earth Observation Satellites (CEOS) Carbon Observing Strategy documents (Ciais et al., 2010; CEOS, 2014). Such a mission would have the dual advantage of delivering independent information on emissions and improving the knowledge of natural fluxes.

CarbonSat targets the following key advantages:

- An accuracy of individual XCO_2 measurements is as good as those expected from OCO-2 and the accuracy of individual XCH_4 measurements are comparable to those of GOSAT

- A small footprint for both XCO_2 and XCH_4, which would allow the identification of natural fluxes at scales ranging from 100 to ~500 km

- A wide swath would the observation of plumes of local-scale sources, such as megacities and strong point sources, in their background context for estimating emissions

- A dense contiguous global coverage of cloud-free soundings which is an order of magnitude larger than OCO-2 and several orders of magnitude larger than GOSAT. Even in regions that are often covered by cloud, such as tropical forests and northern mid-latitudes, CarbonSat would deliver enough cloud-free data for inversions to determine regional fluxes on monthly scales.

The delta with respect to previous missions is that this mission would enable the quantification of time-varying regional-scale CO_2 and CH_4 fluxes. It would provide a significant step forward separating anthropogenic emissions from natural fluxes in atmospheric inversions, and prepares for a future global carbon observing system with capabilities to verify emissions.

→ RESEARCH OBJECTIVES

3. Research Objectives

The CarbonSat mission will provide a new and enhanced capability of measuring CO_2 and CH_4 from space so that surface-to-atmosphere fluxes can be determined. The mission will pioneer a way of detecting and quantifying local-scale (up to the scale of a large city) greenhouse-gas emissions as well as quantifying country-scale fluxes. As outlined in Chapter 2, its predecessors, SCIAMACHY on Envisat and the Greenhouse-gases Observing Satellite (GOSAT), confirmed the presence of signals from strong local emission sources, but those could only be resolved by averaging multiyear data, which limits the analysis of changes over time. The Orbiting Carbon Observatory-2 (OCO-2) satellite, launched in 2014, records clearly the variability of CO_2 along its narrow (<10-km wide) measurement track, but it lacks the imaging capabilities needed to map greenhouse-gas plumes and to quantify emissions.

CarbonSat will be the first mission dedicated to the systematic exploration of CO_2 and CH_4 local-scale signals by extending the conventional measurement approach with imaging capabilities. As noted in Section 2.7.3, XCO_2 and XCH_4 variations associated with surface sources and sinks rarely exceed 2% (8 ppm XCO_2) and 4% (80 ppb XCH_4), respectively. However, typical variations are generally a factor of 5–10 smaller, so a precision of 1–3 ppm for XCO_2 and 6–12 ppb for XCH_4 is needed to resolve the most important fluxes at local to regional scales. To resolve the relative roles of processes at these scales, measurements must have this high precision plus high resolution and cover the entire globe. Specific measurement requirements are described in more detail in Chapter 4.

3.1 Mission Objectives

The CarbonSat mission covers a wide range of spatio-temporal scales, each of which offers unique opportunities to characterise and quantify the surface-to-atmosphere exchange of CO_2 and CH_4. The overarching scientific objective of the mission is to cover the full range of spatial scales, with particular emphasis on local scales, which is unique to the mission and necessary for separating anthropogenic and natural fluxes. The scale-specific objectives are listed below and explained in more detail in the remainder of this chapter.

- **Regional scale:** To provide a breakthrough in the quantification and attribution of regional-scale surface-to-atmosphere fluxes of CO_2 and CH_4.

- **Country scale:** To increase the flux-resolving power of greenhouse-gas-observing satellites to the scale of medium-sized countries.

- **Local scale:** To pioneer the spaceborne detection, characterisation and quantification of strong local sources of CO_2 and CH_4.

These objectives should enable addressing the questions posed in the bullet list in Section 2.1.

3.1.1 Regional-scale Fluxes

The combination of a wide swath and small footprint will deliver substantially more data than previous missions. This will be achieved without compromising on the precision or accuracy of single soundings. CarbonSat is the first mission to combine excellent measurement quality with excellent measurement coverage, both of which are crucial to advance spaceborne greenhouse-gas monitoring. The combination of coverage and quality is particularly important for:

- improving the observational constraints on surface fluxes in regions prone to cloud cover, such as the mid-latitudes and the Tropics, thereby strengthening the observational constraints in these poorly-sampled regions and minimising the impact of clear-sky sampling biases

- providing the spatial and temporal detail needed to increase the resolution of surface fluxes derived from current inversion approaches

An important aim of carbon-cycle research is to understand and quantify the response of land to changing environmental conditions, as discussed in Chapter 2. Signals have been found in GOSAT data that indicate the carbon-cycle response to large climatological anomalies, such as major droughts in the Amazon (Parazoo et al., 2013) and heat waves in Europe and Russia (Guerlet et al., 2013). Such events yield valuable information about the functioning of ecosystems. The CarbonSat mission will use the same concept to investigate the impact of more frequently occurring, smaller anomalies in precipitation and temperature, improving our understanding of how these factors influence specific ecosystem types in different climatic zones (e.g. the difference in biomass burning in tropical and boreal ecosystems). This information will strengthen the link between spaceborne CO_2 and CH_4 measurements and the development and evaluation of ecosystem models. For GOSAT, regional-scale flux anomalies of about 0.5 PgC are detectable over seasonal and subseasonal time scales. CarbonSat is expected to improve this performance by a factor of five.

The use of CarbonSat data can go beyond estimating emissions, which is often the final outcome of inverse-modelling studies. The mission will also contribute to process attribution and improved understanding of the feedback to human-induced perturbations of the climate. A very promising application area is in carbon-cycle data assimilation systems, in which key processes driving the global carbon cycle are constrained by combining complementary data streams.

3.1.2 Country-scale Fluxes

So far, the spatial resolution and coverage of spaceborne greenhouse-gas measurements has limited their application to the estimation of regional and continental-scale surface fluxes by using global inverse-modelling techniques. The current state-of-the-art method for estimating country-scale fluxes is to use inverse-modelling techniques with measurements from regional networks of flux towers that measure the local vertical exchange (flux) of CO_2. As a consequence, this approach is limited to the few regions where such networks exist. The availability of CarbonSat data at higher spatial resolution will allow the estimation of country-scale surface fluxes across much of the world. In addition, the data will be of interest to the mesoscale modelling community. Their models are better suited for extracting high-resolution information from the data, which would be needed for the quantification of greenhouse-gas fluxes at country scales.

The improved coverage and resolution of CarbonSat measurements will bring country-scale emission estimation and verification within reach for medium-sized countries such as France. Even in Europe, the performance of the Integrated Carbon Observing System network is expected to be enhanced by the inclusion of a fully independent source of high-quality satellite data. Outside Europe and the US, independent verification of national greenhouse-gas budgets is currently not feasible as GOSAT measurements do not provide sufficient coverage. Initial attempts can be made using OCO-2 data, but only for CO_2. CarbonSat will make an important step forward by measuring CH_4 in addition to CO_2. Improving on the performance of OCO-2 by at least a factor of two will make a step towards discriminating biospheric and anthropogenic fluxes at country scales. Tall-tower networks, such as the European Integrated Carbon Observing System, provide an excellent opportunity to test the performance of regional-scale inversions driven by CarbonSat data.

3.1.3 Local-scale Fluxes

CarbonSat will provide a new view on Earth's atmosphere, which will allow the exploration and mapping of strong local sources of CO_2 and CH_4 from large power plants, oil and gas extraction fields, to large cities. Although the nature and location of many such targets are known, quantification of fluxes remains largely unverified. To improve this situation, the atmospheric component of the monitoring system needs to be extended so that scales of a few square kilometres can be resolved and so that they can be understood with respect to their background context. The global mapping of local sources will provide essential information for verifying relevant processes and for testing the spatial disaggregation of country-scale statistics in anthropogenic emission inventories. This information is needed to improve *a priori* information on anthropogenic emissions used in inverse modelling of CO_2 and CH_4 fluxes. CarbonSat has the potential to explore unexpected local sources, both anthropogenic and natural, yielding systematic investigation of this, so far, unexplored dimension of greenhouse-gas research.

For many urban and industrial sources, estimated CO_2 and CH_4 emissions are far from certain. This is particularly true in the developing world, where inventories are limited, poorly maintained or non-existent. Sources for which accurate greenhouse-gas emission estimates do exist, such as power plants in developed countries, can be used to further develop and test emission quantification methods. The CarbonSat mission makes use of these known sources to demonstrate its capabilities as a proof of concept, and then apply the method to unknown sources which are scientifically more relevant targets. Using SCIAMACHY, CH_4 emissions from the Four Corners mining area in the US could be quantified after averaging five years of data (Kort et al., 2014). It is expected that a single overpass of CarbonSat can be used to quantify emissions 75 times smaller.

Dedicated efforts have been made to assess greenhouse budgets of cities such as Indianapolis in the US and Paris in France (Turnbull et al, 2014; Bréon et al, 2015). To extend this concept to many other cities in the world requires the current observing system to be complemented with an adequate space segment. The aim of the CarbonSat mission is to explore the potential of satellites to deliver city-scale surface fluxes of CO_2 and CH_4. The imaging capability delivers emissions under varying conditions, yielding information about source, strength and variability over seasonal time scales. Such information provides essential input for the development of fossil-fuel data assimilation systems (Asefi-Najafabady, 2014), and improves the capability of inversions to separate anthropogenic emissions from biological fluxes.

The quantification of local emissions is also important for studying land-use change, in particular tropical deforestation and biomass burning. GOSAT measurements have shown that it is possible to detect interannual variability in CO_2 emissions from biomass burning, despite its limited coverage. However, a regional-scale attribution of these signals is beyond its capabilities. As a result, it remains difficult to distinguish between direct emissions from fires and respiration fluxes from ecosystems affected by fire or by drought. With CarbonSat it will be possible to detect burning plumes and to quantify the emission from large local fires. The ratio between CH_4 and CO_2 emissions provides additional information on the burning conditions. Such information is also needed to improve the attribution of country- to regional-scale carbon fluxes from land use and land-use change.

3.2 International Monitoring Context

The targets and objectives discussed above are achieved with the CarbonSat mission as an integral component of the emerging global carbon-cycle and greenhouse-gas observing system. This system includes a modelling component to infer emissions from greenhouse-gas measurements using inverse-modelling techniques. The CarbonSat mission will stimulate the development of new models with a rich dataset to support their evaluation. CarbonSat's novel component of high-resolution mapping of strong local sources makes it highly complementary to the existing, predominantly ground-based, measurement infrastructure. However, the mission objectives discussed in this section would not be feasible without CarbonSat.

CarbonSat will explore new scales and applications of a future operational greenhouse-gas monitoring system of CO_2 and CH_4 from space, as highlighted in the Group on Earth Observations (GEO) Carbon Strategy and the Committee on Earth Observation Satellites (CEOS) strategy response. The long-term aim of this extension is to allow the detection of trends in anthropogenic emissions and contribute to the verification of anthropogenic emission targets. The results of the supporting scientific studies, discussed in Chapter 7, confirm that CarbonSat, indeed, has the potential to make significant steps forward across the full application range and justifies the requirements on instrument performance presented in Chapter 4.

The process knowledge that will be gained through the CarbonSat measurements has an important application in Earth-system modelling. This links the CarbonSat mission to climate-change prediction. Reducing the uncertainty in critical process parameters describing the natural carbon cycle in these models narrows uncertainties in climate-change predictions. It makes CarbonSat an essential and indispensable component of the international Earth observing programme.

CarbonSat addresses the key scientific challenges of the ESA Living Planet Programme relevant at the time of selection as a candidate mission (ESA, 2006). In particular:

- **Atmosphere challenge 1:** To understand and quantify the natural variability and human-induced changes in Earth's climate system.

- **Land challenge 1:** To understand the role of terrestrial ecosystems and their interaction with other components of the Earth system for the exchange of water, carbon and energy, including the quantification of the ecological, atmospheric, chemical and anthropogenic processes that control these biochemical fluxes.

- **Land challenge 3:** To understand the pressure caused by anthropogenic dynamics on land surfaces (use of natural resources, and land-use and land-cover change) and their impact on the functioning of terrestrial ecosystems.

The Scientific Achievements and Future Challenges document (ESA, 2015b) sets a bold and clear vision for measuring greenhouse-gas concentrations from space to improve the knowledge of fluxes: "*Knowledge of today's carbon sources and sinks, their spatial distribution and their variability in time is one of the essential ingredients for predicting their atmospheric concentration levels, and, in turn, the radiative forcing of climate change by greenhouse gases. With dense spatial and temporal sampling, satellite measurements of the distribution of* *global atmospheric greenhouse gas concentrations could improve our knowledge of both natural and anthropogenic surface fluxes. The required precision is nonetheless very high since the trends, as well as the diurnal, synoptic, seasonal and inter-annual variations, are two orders of magnitude lower than the background levels.*"

The objectives of the CarbonSat mission also address several of the challenges outlined in the recently published Earth Observation Science Strategy (ESA, 2015a), in particular, those dealing with surface-atmosphere interactions (challenge A2), atmospheric composition and climate (challenge A3), natural processes on land and human activity (challenge L1), and interactions between global change and biogeochemical cycles and productivity (challenge L2). CarbonSat is a natural element in the strategy and provides a demonstration for the future operational system recently endorsed by CEOS (CEOS, 2014).

→ OBSERVATIONAL REQUIREMENTS

4. Observational Requirements

Chapters 2 and 3 established the need for improved measurements of atmospheric CO_2 and CH_4 at the spatial and temporal scales required to substantially improve our knowledge of natural and anthropogenic fluxes from local to global scales. They also outlined the limitations of the current observing system.

This chapter describes the main measurement requirements to fulfil the science objectives summarised in Chapter 3. CarbonSat's primary geophysical products, global high-spatial-resolution maps of accurate XCO_2 and XCH_4 data, are introduced and specified. The need for improved surface-to-atmosphere fluxes in relation to the mission objectives is summarised in Section 4.1. The overall observational approach is given in Section 4.2. This provides the conceptual framework required to retrieve surface flux information from the atmospheric concentration measurements, as well as the general framework used to invert Level-1 solar backscatter data (radiances, solar irradiance, and reflectance) in the near- and shortwave-infrared into the geophysical data products (Level-2) using state-of-the-art absorption spectroscopy combined with radiative transfer forward modelling. In Section 4.3, CarbonSat's primary geophysical products and their key requirements to meet the mission objectives are detailed. Section 4.4 establishes the link between the Level-1 requirements and the required geophysical products, which form the basis for defining the CarbonSat system in Chapter 5.

4.1 The Need for Improved Flux Estimates

This section presents and discusses key numbers specifying the performance of the greenhouse-gas observing system that is needed to reach the mission objectives formulated in Chapter 3. These performance specifications have been used as guidance for the requirements of the primary geophysical products, and hence the design of CarbonSat. The specifications have also been used in the supporting scientific studies to verify that the Level-2 requirements ensure the performance needed to achieve the mission objectives. As demonstrated by the results, which are presented and discussed in Chapter 7, this is, indeed, the case. Here, the higher level performance needs are outlined, specified for the different spatial scales addressed by CarbonSat. The key numbers are summarised in Table 4.1.

4.1.1 Country, Regional and Global Scales

As discussed in Chapter 2, the uncertainties in *a priori* estimates of CO_2 and CH_4 (i.e. independent of atmospheric measurements) are roughly 50–100% of the actual fluxes, apart from anthropogenic sources of CO_2, which are believed to be substantially more accurate (about 10% of the flux). For regional to global scale applications of satellite-observed CO_2, the primary goal is to improve our understanding of the natural components of the terrestrial carbon cycle, including managed ecosystems, which are less well quantified. The aim of a global greenhouse-gas observing system augmented with CarbonSat is to obtain a substantial reduction in uncertainty to roughly 25% of the flux, which translates to about 0.5 gC m^{-2} day^{-1} of CO_2 and 10 mg m^{-2} day^{-1} of CH_4 on the scale of monthly fluxes at 500×500 km^2. To estimate CO_2 fluxes at annual scales, the seasonally varying natural sources and sinks (i.e. photosynthesis and respiration fluxes) must be estimated more precisely. For sub-continental scales, net ecosystem exchanges are typically a few tenths of a PgC yr^{-1}. With

Table 4.1. Uncertainty levels to be achieved using CarbonSat data in the greenhouse-gas observing system.

Flux Estimate	Temporal Resolution	Spatial scale source area (N–S) km × (W–E) km	Uncertainty	Unit	Comment
CO_2 over land at country, regional to continental scales	Monthly Annual	500×500	0.5 0.1	gC m^{-2} day^{-1}	Corresponds to 14 Mt $CO_2$$^\$$ Corresponds to 33 Mt $CO_2$$^\$$
CO_2 local-scale city source	Instantaneous (at overpass time)	>10×10	7	Mt CO_2 yr^{-1} $^\#$	For targets >35 Mt CO_2 yr^{-1} $^\#$
CO_2 local-scale point source	Instantaneous (at overpass time)	<2×2	4	Mt CO_2 yr^{-1} $^\#$	For targets >20 Mt CO_2 yr^{-1} $^\#$
CH_4 over land at country, regional to continental scales	Monthly	500×500	10	mg CH_4 m^{-2} day^{-1}	Corresponds to 75 kt $CH_4$$^\$$
CH_4 local scale strong sources (oil/gas/coal)	Instantaneous (at overpass time)	>10×10	40	kt CH_4 yr^{-1} $^\#$	For targets >200 kt CH_4 yr^{-1} $^\#$
CH_4 local scale other sources	Instantaneous (at overpass time)	<2×2	8	kt CH_4 yr^{-1} $^\#$	For targets 20–40 kt CH_4 yr^{-1} $^\#$

$^\$$Flux uncertainty integrated over the specified spatio-temporal scale.
$^\#$Instantaneous flux expressed as an annual timescale.

the help of CarbonSat, the aim is to reduce the uncertainty to well below 0.1 PgC yr^{-1}, which translates to an average flux uncertainty of 0.1 gC m^{-2} day^{-1} at scales of 500×500 km^2. A spatial scale of 500 km is chosen as it represents the flux resolving power required for country-scale flux estimation. Extreme events, such as the summer heatwaves that struck Western Europe in 2003 and the Moscow region in 2010 were accompanied by a release of carbon of about 0.5 Pg. CarbonSat aims to quantify anomalies five times smaller, to an accuracy of 25%. The spatial-temporal resolution of 500×500 km^2 and one month will obtain important information to localise the origin of emission anomalies.

4.1.2 Local Scales

The aim of the CarbonSat mission is to demonstrate that it is possible to quantify emissions of CO_2 from large cities in a way that allows existing emission inventories to be evaluated at the time of the overpass. This requires accuracies of the inferred emissions in the order of 10% of the total on the basis of a single cloud-free overpass for large cities where emission inventories exist. For large cities that do not have inventories, an accuracy of 20% is already an important gain in information. The seasonal variation can be established with several overpasses per season. This approach should also allow trends to be assessed for large cities that are expanding rapidly, once several years of data have been collected. CarbonSat aims to quantify emissions from large cities that emit >35 Mt CO_2 yr^{-1}. This applies currently to the six largest cities in Europe, and to about 20 comparable cities on other continents. It is expected that by 2025 the number of large cities will increase by at least 30% (United Nations, 2012). Among these targeted cities, there are several cities for which robust emission inventories do not exist. Therefore, once the capability has been demonstrated on large and well-defined target cities, the approach can be applied to more uncertain sources.

For point sources at local scales, the objective of CarbonSat is to demonstrate the feasibility of spaceborne detection and quantification of fossil-fuel emissions from sources such as large power plants. Globally, power plants account for about 30% of the total emissions of CO_2 from fossil-fuel use. The aim of CarbonSat is to demonstrate the detection and quantification of large power plants (~20 Mt CO_2 yr^{-1}). Assuming a typical uncertainty of 10% per power plant, the emission data from a single CarbonSat overpass should be accurate to about 2 Mt CO_2 yr^{-1}. For CO_2 point sources with larger uncertainties (including volcanoes), even an accuracy of 4 Mt CO_2 yr^{-1} will be an important gain in information.

Comparisons between different CH_4 emission inventories for large cities like Paris highlight the uncertainties in the existing bottom-up emission quantification methods, uncertainties which are generally much larger for CH_4 than for CO_2. Estimated emissions of CH_4 from large cities may vary by factor two. Strong anthropogenic sources of CH_4 are, for example, coal mining and oil- and gas-production fields, and these have a large uncertainty. Emissions result from dispersive CH_4 emissions in areas (from a few km up to approximately 30 km) of unconventional oil and gas production and can reach about 500 kt CH_4 yr^{-1} (Karion et al., 2013; Schneising et al., 2014b, see also Fig. 4.2). CH_4 emissions from coal mining can reach similar source strengths (Kort et al., 2014, see Fig. 2.18). Bottom-up emission inventories, from the US Environmental Protection Agency (EPA) for the oil and gas fields mentioned above (Fig. 4.2), are in the 100–200 kt CH_4 yr^{-1} range with error bars of 20–50% (Schneising et al., 2014b). Discrepancies between EPA and measured emissions are large at various scales (Brandt et al., 2014). Also current error bars are large (20–50%) in emission estimates derived from satellite-and *in situ* data. A quantification of such sources (200 kt CH_4 $yr^{-1)}$ with an uncertainty of 20% or better would therefore be a major breakthrough. At the point-source scale, CH_4 emissions from coal-mine ventilation (20–30 kt CH_4 yr^{-1}), landfill sites (10–20 kt CH_4 yr^{-1}) and smaller oil- and-gas production areas (20–40 kt CH_4 yr^{-1}) have large uncertainties in their estimates (>50%). Mud volcanoes are an important and highly uncertain source of CH_4, contributing up to 5% to global emissions. Although outgassing mud-volcanoes are probably too small to detect (0.2–1.6 kt CH_4 yr^{-1}), erupting mud-volcanoes are estimated to emit orders of magnitude more. CarbonSat is likely to catch and quantify at least a few such eruptions during its life in orbit. To demonstrate the capability of CarbonSat, and to detect and quantify strong local sources of CH_4 from space, the aim is to reach an accuracy of 8 kt CH_4 yr^{-1}.

4.2 Observational Approach

4.2.1 Inferring Fluxes from Geophysical Products

Inferring surface fluxes from space-based measurements of top-of-the-atmosphere radiances involves two steps. First, from spectrally resolved observations we retrieve the column-averaged dry-air mole fraction of CO_2 or CH_4, and secondly we perform the ‘flux inversion’. Column retrieval uses the method of absorption spectroscopy with the measured upwelling radiance and solar irradiance as input, as detailed in Chapter 6. This gives the primary Level-2 data products of CarbonSat: the column mean dry mole fractions of CO_2 and CH_4, denoted as XCO_2 and XCH_4, respectively (Section 1.1).

The flux inversion then uses as input the spatially resolved Level-2 data products XCO_2 and XCH_4, along with information about meteorological conditions (wind, pressure, temperature) and *a priori* assumptions on surface-to-atmosphere fluxes (for example, magnitude, distribution, uncertainty). These quantities are then assimilated into a flux inversion model, which delivers updated information on surface-to-atmosphere fluxes to reproduce the observed distribution of trace gas (detailed in Chapters 6 and 7). There are several methods in place today that make use of observations of atmospheric CO_2 and CH_4 to improve our knowledge of the sources and sinks of greenhouse

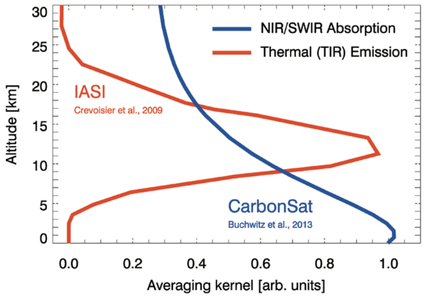

Figure 4.1. Height sensitivity of IR thermal emission and NIR/SWIR solar absorption spectroscopy (higher numbers indicate higher sensitivity) as determined by the averaging kernel for CO_2 (sensitivity for CH_4 is similar). Note that solar absorption spectroscopy has a much higher sensitivity to the planetary boundary layer, where the impact of sources and sinks is largest. (M. Buchwitz–IUP)

gases and their interactions with the climate system. While originally developed for surface *in situ* observations, these methods have been adapted and further developed for satellite observations of XCO_2 and XCH_4 (Chapter 2 and 6).

Concentrations of CO_2 and CH_4 change owing to sources and sinks, i.e. generation and loss and due to atmospheric transport. Thus sources and sinks lead to gradients in the atmospheric concentration of those gases. Variation in concentration gradients in space and time can be measured with satellite instruments. Since the observed gradients are small, accurate measurements as well as accurate retrieval algorithms (Chapter 6) are required. Furthermore, in order to derive sources and sinks from the determined gradients, accurate inverse modelling is needed (Chapter 6).

As most sources and sinks are located at or near to the surface, high measurement sensitivity down to the lowest atmospheric layer, the planetary boundary layer, is needed. CarbonSat will use absorption spectroscopy of high-resolution spectra of backscattered solar light in the near- and shortwave infrared absorption bands of CO_2, CH_4, and O_2, which gives a much higher sensitivity to the boundary layer than thermal-infrared emission spectroscopy (Fig. 4.1).

In addition, high spatial resolution and good spatial coverage are needed to characterise the variability of XCO_2 and XCH_4 on scales that enable observing the influence of sources, sinks and weather patterns on their atmospheric concentrations. As the information on greenhouse-gas sources and sinks is needed to determine global budgets and to study ecosystem processes in different climatic regions in a comparable way, a satellite is the most suitable platform to obtain this information.

Sources of CO_2 and CH_4 from fossil fuel combustion and energy production result in a local enhancement in XCO_2 and XCH_4 as already seen in multiyear data averages of SCIAMACHY data (Chapter 2) and in airborne remote-sensing data (Section 4.2.1). High spatial resolution is needed to distinguish between signals from strong source areas and background variations of XCO_2 and XCH_4. However, high spatial resolution alone as provided by OCO-2 is not sufficient because of the temporal variability of greenhouse-gas concentrations. Only the combination of high spatial resolution with a wide swath will capture their variability while separating natural and anthropogenic sources even within individual measurements.

Therefore, XCO_2 and XCH_4 need to be contiguously measured across a broad track (compare Fig. 2.20), as well as along-track, producing accurate 2D images. This at a spatial scale adequate to resolve sources and sinks at the surface, since gradients in atmospheric column concentrations are mainly produced there, and discriminate them from the variability in XCO_2 and XCH_4 introduced by meteorology.

4.2.2 Detecting Sources from Images

In addition to the assimilation of individual measurements of XCO_2 or XCH_4 into surface-flux inversion models, analysis of images of XCO_2 and XCH_4 provides direct information on the sources of these greenhouse gases. The current state-of-the-art using SCIAMACHY or GOSAT data is to generate maps of multiyear averages and/or differences of multiyear averages of XCO_2 or XCH_4, typically with a grid spacing of a few hundred kilometres, to detect sources as areas identified by increased (average) concentrations. Figure 4.2 shows an example of multiyear analysis of SCIAMACHY XCH_4 used to detect local column enhancements correlating to areas of unconventional oil/gas production (i.e. by fracking), (Schneising et al., 2014b). Other examples in the literature show an enhanced CO_2 concentration over the Los Angeles megacity area (Kort et al. 2012) and enhanced CH_4 concentrations over the Four Corners region in the US (Kort et al., 2014).

This type of analysis is currently very limited with respect to either temporal resolution (multiyear averages) or spatial resolution (one degree latitude/longitude at best) or both, owing to the sparse data coverage of existing satellite sensors. With current datasets, the analysis will only reveal extremely large sources with relatively constant emissions over time.

Results from airborne measurements demonstrated that, with XCO_2 and XCH_4 data of sufficiently high quality, quantitative information on individual strong sources can be obtained even from a single image (Krings et al., 2011, 2013), which could be from a single satellite overpass (Bovensmann et al. 2014a).

Figure 4.3 shows examples of a CO_2 plume from a power plant and a CH_4 plume from an oil/gas production field. Measurements were made by the airborne spectrometer MAMAP, which is based on the same measurement principle as CarbonSat (Krings et al 2011, 2013). The CO_2 source is a power plant emitting approximately 16 Mt CO_2 yr^{-1}. The CH_4 localised source is from dispersive emissions from an oil/gas field in California with unknown emissions. From the measured signal, emission strength can be estimated at 20–40 kt CH_4 yr^{-1}, which is similar to the emission strength of the coal-mine

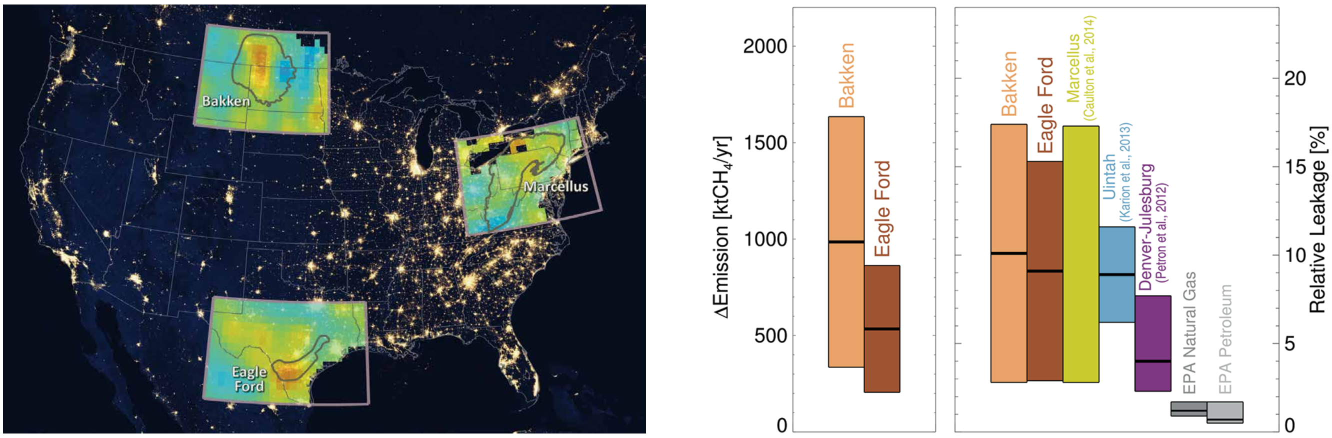

Figure 4.2. Methane emissions from hydraulic fracturing (fracking) as detected by satellite observations. Left: SCIAMACHY XCH_4 over three major fracking areas (Bakken, Eagle Ford and Marcellus) in North America overlying a background image of night lights (NASA). Right: estimated methane emissions and methane leakage rates from six years of SCIAMACHY data. (Schneising et al., 2014b)

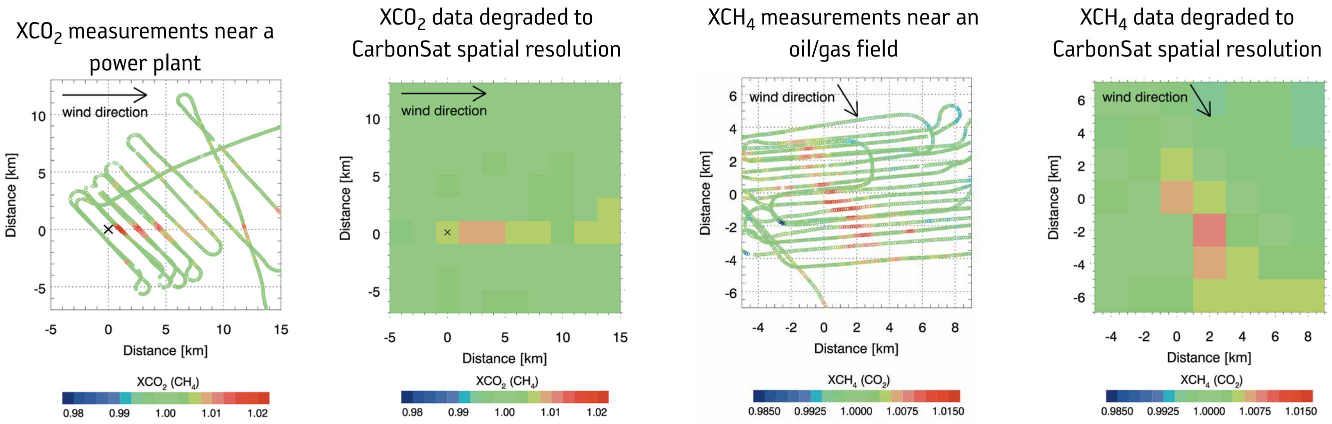
XCO_2 measurements near a power plant

XCO_2 data degraded to CarbonSat spatial resolution

XCH_4 measurements near an oil/gas field

XCH_4 data degraded to CarbonSat spatial resolution

Figure 4.3. Airborne measurements of XCO_2 and XCH_4 around strong local-scale emission areas. The data have also been degraded to CarbonSat spatial resolution for comparison. The CO_2 local-scale source is a power plant emitting approximately 16 Mt CO_2 yr^{-1}. The CH_4 local-scale source is dispersive emissions from an oil/gas field in California. (T. Krings–IUP)

ventilation shafts studied by Krings et al. (2013). Note that these estimated fluxes are an order of magnitude smaller than the emissions from oil/gas fields as reported in Karion et al. 2013.

CarbonSat, with its high spatial resolution and good across-track imaging capabilities, will greatly enhance the capabilities for greenhouse-gas observations by providing orders of magnitude more data, allowing monthly to seasonal temporal coverage with spatial resolution down to the sub-city scale (few km).

4.3 Geophysical Product Requirements

4.3.1 Main Level-2 Products and Key Mission Requirements

CO_2 and CH_4 are essential climate variables. Several documents recommending Level-2 product requirements are available (e.g. GCOS, 2011 and Chevallier et al., 2014b). These documents have been reviewed with respect to how far they already address CarbonSat mission scientific goals. These requirements were then refined or extended to fully cover the CarbonSat mission goals. Table 4.2 summarises the main mission and Level-2 requirements, which are detailed and justified in the following sections.

4.3.2 Observational Requirements for Atmospheric CO_2

Of the two targeted species, CO_2 has the longest atmospheric lifetime, for which estimates range between 300 and 1000 years. With the current emission rates, concentrations are increasing by approximately 2 ppm per year. Because of its long lifetime, background concentrations are high (expected to soon exceed 400 ppm). Perturbations by current emissions and biogenic fluxes are only a small signal on top of this background level.

Both human activities and natural processes modify the atmospheric concentration of CO_2 at various spatial and temporal scales. Figure 4.4 summarises the processes, the scales and the order of magnitude of change in XCO_2. They include annual growth rate, interhemispheric gradient, inter-annual variations, seasonal cycle, synoptic weather systems, biomass burning as well as anthropogenic perturbations at city and local scales.

In the last decade, starting with the pioneering paper from Rayner at al. (2001), numerous inverse modelling studies of relevance have been performed.

Table 4.2. Summary of mission and product requirements for the primary products XCO_2 and XCH_4.

	XCO_2	XCH_4
Random error (G/T)	1/3 ppm	6/12 ppb
Systematic error (G/T)	0.2/0.5 ppm	2.5/5 ppb
Horizontal resolution grid size (G/T)	2×2 /2×3 km^2	2×2/2×3 km^2
Vertical resolution	total column	total column
Spatial coverage	global	global
Temporal coverage (poleward of 40° latitude)	<12 days	<12 days
Temporal coverage (at equator)	30 days	30 days
Local overpass time	10:00–14:00	10:00–14:00
Mission lifetime (T/G)	3/5 years	3/5 years
Data latency	48 hours (Level-1) 2 weeks (Level-2)	48 hours (Level-1) 2 weeks (Level-2)

Threshold (T): expresses the minimum acceptable capability and level of performance. Goal (G): denotes a non-mandatory requirement.

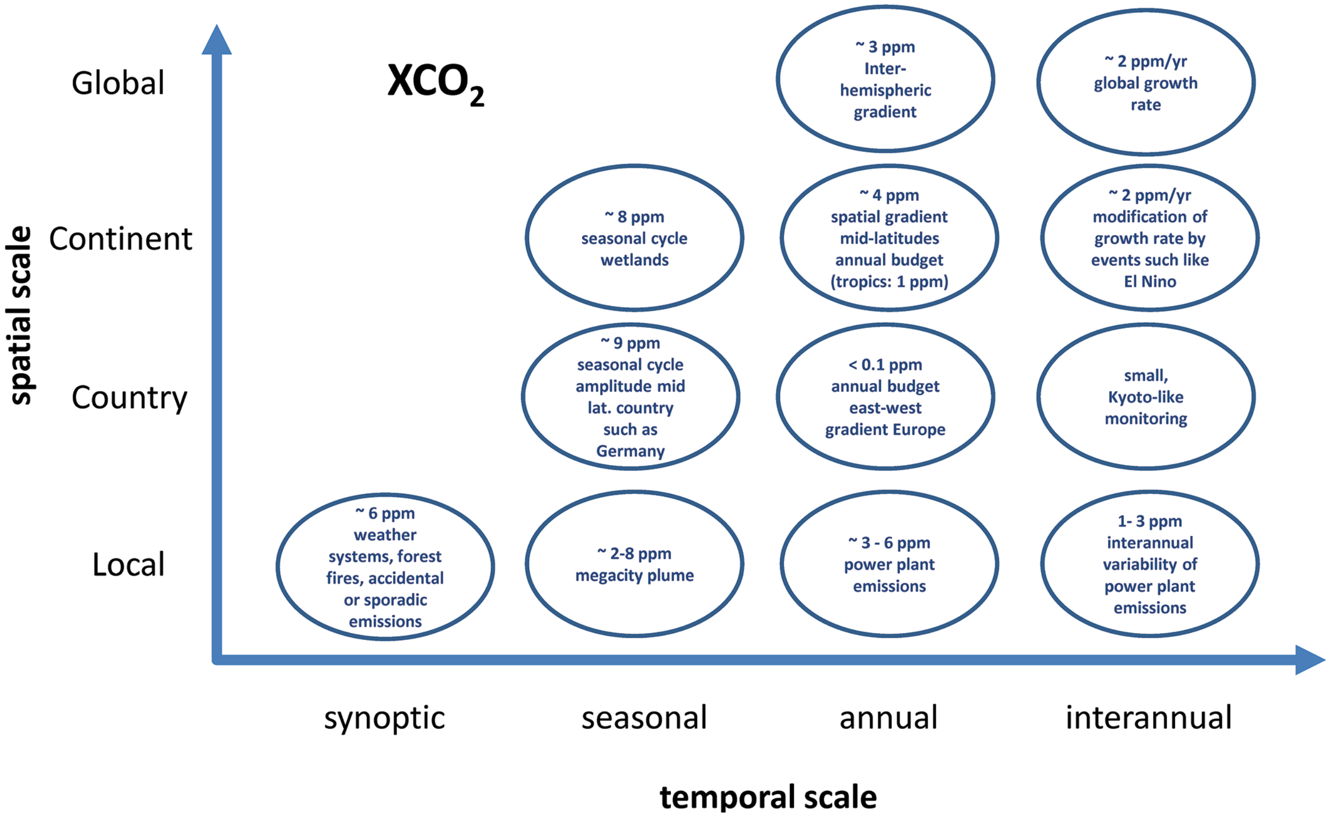

Figure 4.4. Variability of XCO_2 owing to different processes at different spatial and temporal scales. Adapted from material provided by J. Marshall–MPI BGC. (H. Bovensmann–IUP)

Previously reported requirements on the precision of XCO_2 were in the order of ~1 ppm or better for regional averages and monthly means (Chevallier et al., 2007). This is also confirmed by the investigations on user requirements within the ESA greenhouse-gas Climate Change Initiative project (Chevallier et al., 2014b) and the most recent Global Climate Observing System (GCOS) requirements on greenhouse-gas measurements from space (GCOS, 2011).

For CarbonSat these requirements were revisited in dedicated inverse modelling studies (Chapter 7) which confirmed that a 1–3 ppm single-measurement precision is needed for global- to regional-scale applications. At these scales, the precision per grid box of the model achieved with the above mentioned precision can be much better than 1 ppm owing to the aggregation of a large number of measurements in one grid box. Details of this aggregation advantage will depend on the detailed error characteristic and error correlations. Nevertheless, also in the context of systematic error characterisation, the 1 ppm precision requirement has high priority.

For the city and point sources at the local scale, it was established with simulations that a single-measurement precision towards 1 ppm is needed to constrain strong point sources (Chimot et al., 2014, Buchwitz et al., 2015b). Figure 4.5 demonstrates this for strong CO_2 point sources. The inversion uncertainty (error in the derived emissions) depends mainly on wind speed, spatial resolution, source strength and single-measurement precision. City-scale simulations were performed for Berlin and surrounding areas, including two strongly emitting power plants. Figure 4.6 shows how the Berlin XCO_2 city plume is affected by noise in XCO_2 data. Again, a precision of at least 1–1.5 ppm is needed. This is consistent with remote-sensing studies of urban domes indicating that column-averaged observations with single-measurement precisions of 1.5 ppm at spatial scales of 2–4 km would be sufficient to detect enhancements typically associated with megacities (Wunch et al., 2009).

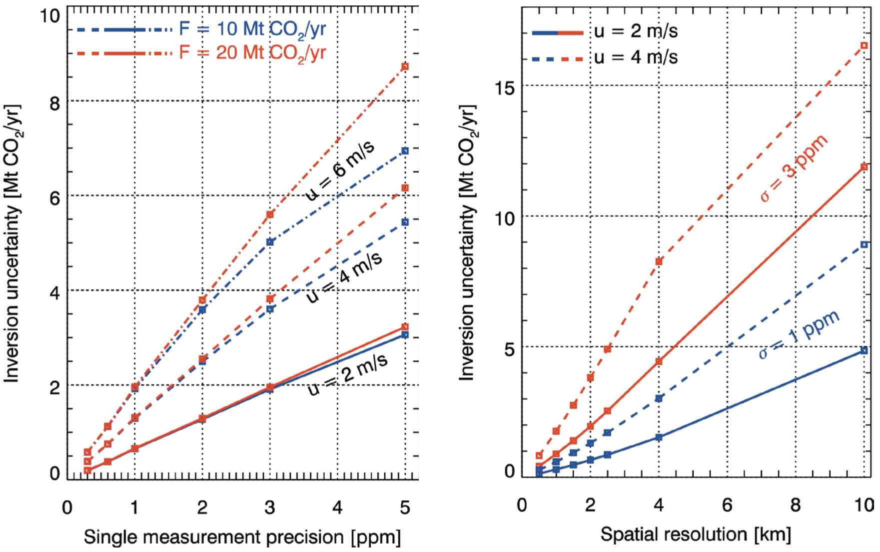

Figure 4.5. Left: inversion uncertainty for localised CO$_2$ sources as a function of single-measurement precision, wind speed (u) and emission rate (F) for a fixed spatial resolution of 2 km. Right: inversion uncertainty for localised sources as a function of the spatial resolution, single-measurement precision, the wind speed (u) for a fixed emission rate of 20 Mt CO$_2$ yr^{-1}. The uncertainty requirement is 4 Mt CO$_2$ yr^{-1}. (T. Krings–IUP)

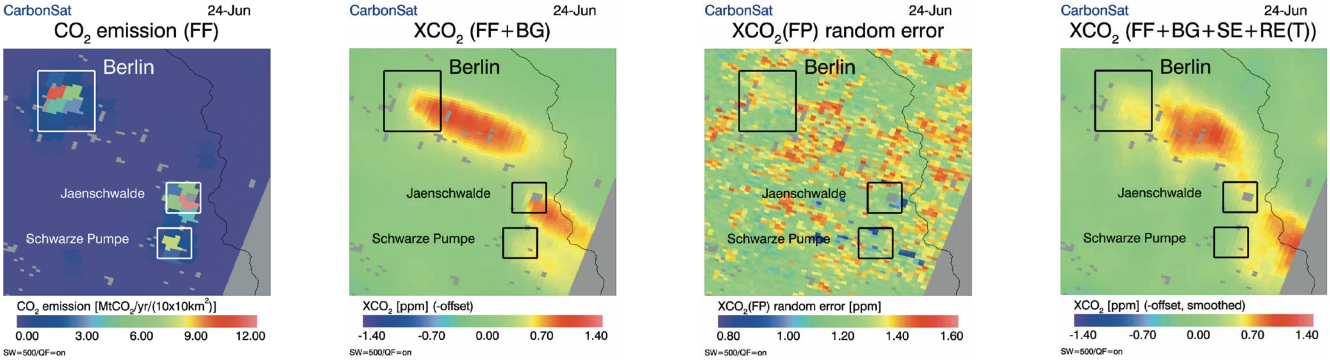

Figure 4.6. Sensitivity study on city scales. From left to right: map of fossil-fuel emissions from a database; modelled enhancement in XCO$_2$ owing to fossil-fuel emissions and variations in biogenic fluxes; map of random errors (threshold signal-to-noise ratio (SNR) of CarbonSat); simulated CarbonSat result including variability in fossil-fuel emissions, biogenic fluxes, random and systematic errors. Boxes indicate the major source areas of Berlin (43 Mt CO$_2$ yr^{-1}), Jaenschwalde (power plant, 30 Mt CO$_2$ yr^{-1}) and Schwarze Pumpe (power plant, 16 Mt CO$_2$ yr^{-1}). (M. Buchwitz–IUP)

Tapping XCO$_2$ plumes from power plants with airborne instruments has shown that a single-measurement precision of 1 ppm is sufficient to detect a local XCO$_2$ enhancement with a quality that allows the determination of strong point-source emissions (Bovensmann et al., 2014a, see also Fig. 4.3).

Inverse modelling studies using modelled and/or real data show a critical sensitivity to systematic errors in the measured concentrations (Miller et al., 2007; Chevallier et al., 2007). Therefore, a strict requirement on biases is needed. This is also highlighted in Chevallier et al. (2014b) and GCOS (2011). It is therefore required that systematic errors will be smaller than 0.2 ppm (G) and 0.5 ppm (T) after global background correction.

The overall aim is to achieve small systematic errors by the combination of system design and accurate retrieval models. Schemes to correct biases including ground-based networks are commonly accepted, which are presented in Chapter 6.

4.3.3 Observational Requirements for Atmospheric CH_4

The chemical lifetime of CH_4 is about 10 years, which is much shorter than that of CO_2 (300–1000 years). The background concentration of about 1750 ppb (1.75 ppm) is therefore lower than CO_2, and signals of strong sources (wetlands, large fossil-fuel production areas) can be detected above these background concentrations even by SCIAMACHY (Bloom et al., 2010, Kort et al., 2014, Schneising et al., 2014b).

As with CO_2, human activities and natural processes modify the atmospheric concentration of CH_4 at various spatial and temporal scales. Figure 4.7 summarises the related processes, scales and order of magnitude of gradients. They include annual global growth rates, interhemispheric gradients, inter-annual variations, seasonal cycle, synoptic weather systems, biomass burning as well as anthropogenic perturbations at city and local scales.

In the last decade numerous inverse modelling studies of relevance were performed using simulated and real XCH_4 data (Alexe et al., 2015, Bergamaschi et al., 2013, and references therein). In these studies and in Chevallier et al. (2014b), the required precision of XCH_4 was determined to be in the order of ~5–10 ppb or better for regional and monthly averages. For CarbonSat, the precision for XCH_4 was established by dedicated inverse modelling studies Chapter 7). These studies showed that a single-measurement precision better than 12 ppb as threshold (6 ppb as goal) is needed to adequately constrain fluxes at monthly to seasonal scales.

In addition, the CarbonSat science studies showed that this single-measurement precision is sufficient to constrain local scale sources (Fig. 4.8), as determined from multiple overpasses. Note that at larger scales, the precision per model grid box can be much better than 12 ppb owing to the aggregation

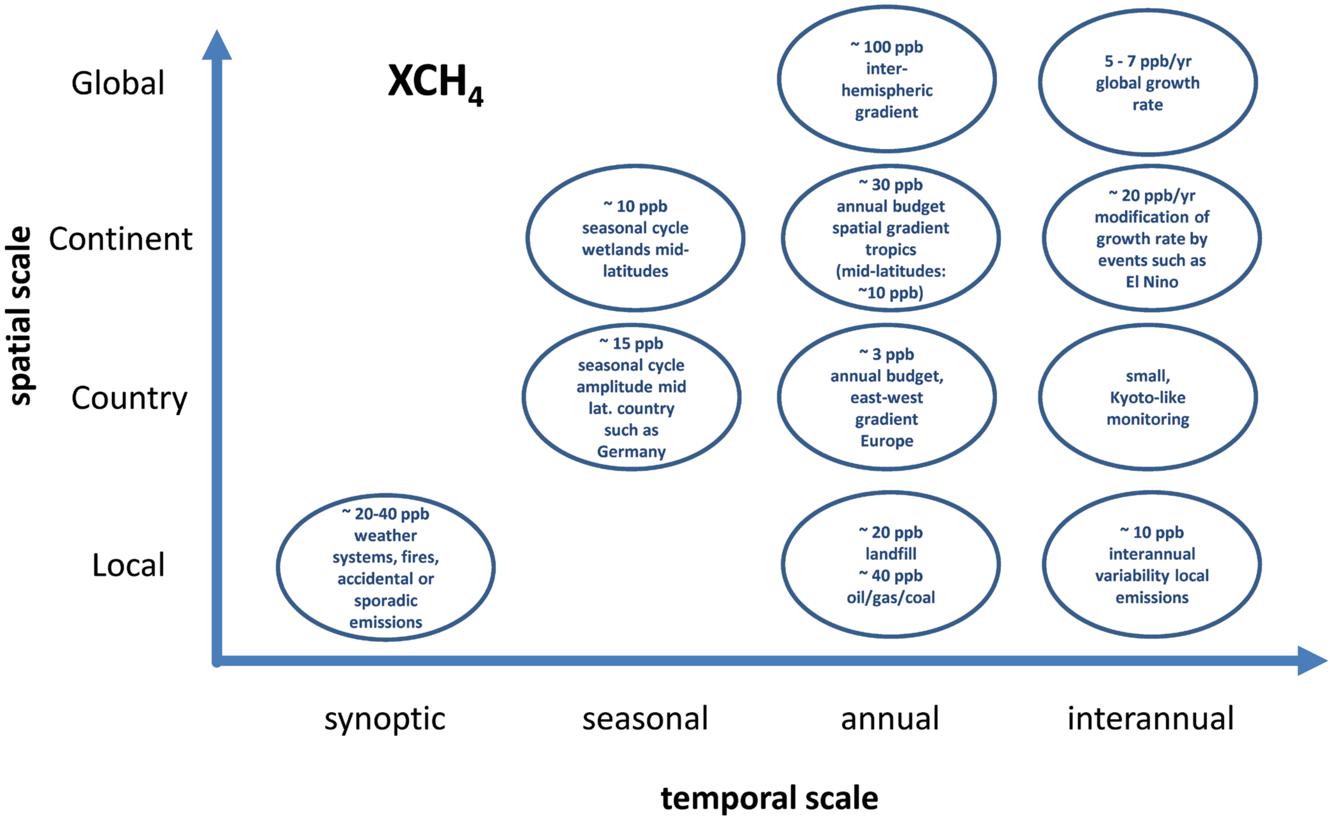

Figure 4.7. Variability of XCH_4 due to different processes at different spatial and temporal scales. Adapted from material provided by J. Marshall–MPI BGC. (H. Bovensmann–IUP)

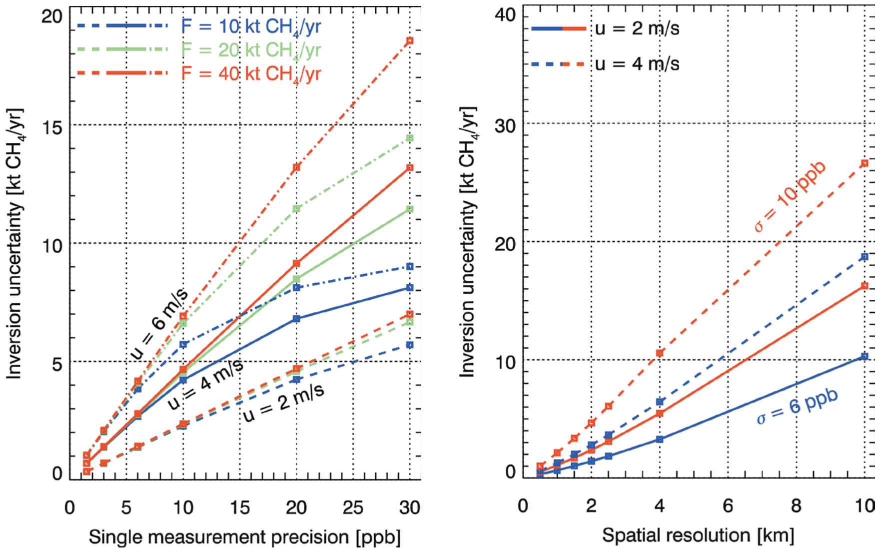

Figure 4.8. Left: inversion uncertainty for localised CH_4 sources as a function of single-measurement precision, wind speed (u) and emission rate (F) for a fixed spatial resolution of 2 km. Right: inversion uncertainty for localised sources as a function of the spatial resolution, single-measurement precision, the wind speed (u) for a fixed emission rate of 40 kt CH_4 yr^{-1} yr. The uncertainty requirement is 8 kt CH_4 yr^{-1}. (T. Krings–IUP)

of a large number of measurements per grid box. As for XCO_2, this aggregation advantage will depend on detailed error characteristics and error correlations, which for larger areas leads to a threshold precision requirement of 12 ppb. Nevertheless, also in the context of systematic error characterisation, the 6 ppb precision requirement has high priority.

Airborne mapping of XCH_4 plumes from coal-mine ventilating shafts, oil/gas production areas and landfills has demonstrated that a single-measurement precision of better than 10 ppb is feasible (Fig. 4.3).

A strict requirement on minimising systematic biases is also needed for XCH_4 (Chevallier et al., 2014b, GCOS, 2011). It is therefore required that systematic errors will be smaller than 2.5 ppb (goal) and 5 ppb (threshold) after a global background correction. The overall aim is to achieve small systematic errors by the combination of system design and accurate retrieval models. Schemes to correct biases including ground-based networks are commonly accepted practices which are presented in Chapter 6.

4.3.4 Spatio-temporal Sampling Requirements

Space-based measurements of XCO_2 would make their most significant contribution to understanding the carbon cycle in tropical and boreal regions. XCO_2 estimates over the oceans are needed to quantify CO_2 fluxes and to facilitate the tracking of land fluxes transported over the ocean. Global XCH_4 measurements are expected to dramatically reduce emission uncertainties, and allow the separation of wetland and anthropogenic sources. This is currently not possible, because these regions are poorly sampled by existing surface networks. XCO_2 and XCH_4 measurements must also be collected over almost the full range of latitudes to avoid uncertainties introduced by inversions owing to limitations in transport models. There are negligible emissions of CH_4, over oceans, but there are sources on land, from the Tropics to the high latitudes making it important to cover all the continents.

As the mission will use absorption spectroscopy of solar backscattered light, the coverage of the solar illuminated part of Earth is the target area: good data quality requires high illumination. For CarbonSat applications, a late morning orbit (10:00–12:00, local time descending node) is slightly preferred over an early afternoon orbit (12:00–14:00, local time ascending node), as in the morning there are on average fewer clouds, the average wind speed is lower and anthropogenic emissions peak. As CarbonSat aims to better quantify sources and sinks, coverage of the mid to high-latitude land areas

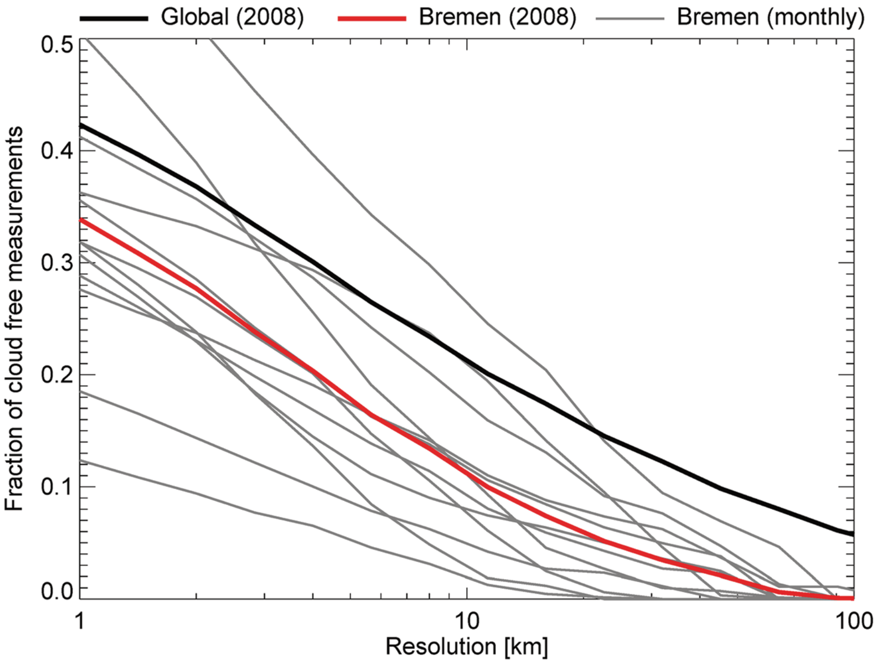

Figure 4.9. Example of the dependence of the fraction of cloud-free observations on the spatial resolution. The figure shows a global average for 2008 (black), an average for 2008 for Bremen (red) and the monthly variability for Bremen (grey). (M. Reuter–IUP)

in the northern hemisphere is more important than coverage of the southern hemisphere high latitudes, hence the slight preference for the morning orbit.

Most of the finer-structured source regions are over land, coverage of land with high spatial resolution is more important than coverage of the oceans. It has to be noted that, as the signal in the shortwave infrared over ocean is low (owing to low surface albedo), measurements over the ocean need to be performed in a special mode, viewing glint/glitter reflections. This has proven to be valuable for GOSAT and OCO-2.

Natural CO_2 and CH_4 fluxes vary on diurnal, synoptic, seasonal and interannual time scales. Point-source and city emissions also vary on diurnal and seasonal time scales. Existing ground-based measurements indicate that while diurnal CO_2 variations in the vicinity of local sources and sinks can be large (>10 ppm), these variations are confined to near the surface, contributing small XCO_2 variations (< a few ppm). Measurements acquired at the same time of day everywhere on Earth have a better inter-comparability for inferring fluxes.

CarbonSat aims to improve the carbon budget at monthly scales, thus allowing research into seasonal dependence of climate feedbacks in the carbon cycle. Therefore, monthly global coverage needs to be achieved at the equator. Polewards of 40°N, where biosphere and anthropogenic emissions from fossil-fuel combustion are often strongly interwoven, complete longitudinal coverage needs to be achieved every 12 days.

Local-scale emission areas need to be observed within their context, to distinguish gradients introduced by mesoscale meteorology and local scale sources from natural background levels. Therefore, a minimum swath is required, which is larger than these typical source areas and includes their cleaner surroundings (compare Fig. 4.6). Ideally, the contiguously sampled across-track swath width should therefore be 500 km with a breakthrough requirement of 240 km and a threshold of 160 km. It is noted that the previously described global coverage requirement results in a minimum swath width of 180 km.

While natural CO_2 fluxes produce XCO_2 variations at scales ranging from 100 to ~1000 km, cities and point sources cause XCO_2 variations at smaller scales, typically from a few km to 100 km. Similarly, the spatial extent of XCH_4 gradients varies depending on the source between large areas (wetlands;

~50–1000 km) and point sources (landfills, gas extraction sites; a few km to 100 km). The combination of high spatial resolution and good spatial coverage helps to ensure that cloud-free soundings can be obtained even in partially cloudy conditions. For cities and point sources, only imagery at high spatial resolution around the zone of interest allows the detection of plumes usable for emission quantification.

The spatial resolution requirement for CarbonSat is driven by the science requirement to measure XCO_2 and XCH_4 very accurately at the spatial scale of the most relevant processes affecting the sources and sinks as well as processes impacting XCO_2 and XCH_4 such as clouds and weather systems.

For the global to regional applications the spatial resolution requirement is driven by the need to observe a large number of cloud-free measurements each month and for each model grid box (typically 3–5° depending on the model). This is especially applicable in regions like the Tropics, which are important for the global carbon budget and currently sparsely sampled. The fraction of cloud-free observations is dependent on the spatial resolution of the instrument (Fig. 4.9). In particular, for partially cloudy regions, like the Tropics, the number of cloud-free scenes decreases rapidly with spatial resolution.

Taking into account that an across-track imaging concept such as CarbonSat provides more than one order of magnitude more data points than a system like OCO-2 with a spatial resolution grid size of ~3 km^2, a spatial resolution grid size of 6 km^2 as threshold (goal: 4 km^2) is sufficient. This will allow critical regions like the Tropics to be covered with approximately an order of magnitude more data points than by OCO-2. This significant increase in data will provide the basis for an improved flux determination at better spatial and temporal scale (monthly) with reduced uncertainties, which will be further detailed in Chapter 7.

Spatial resolution directly affects the sensitivity to strong localised point sources, as illustrated in Figs. 4.5 for CO_2 and 4.8 for CH_4. While a higher than 2×3 km^2 spatial resolution sampling size would be preferred, this threshold value still allows the detection of strong point sources. Under favourable conditions (e.g. low wind speed, no nearby clouds) their emissions can be estimated with an uncertainty better than 4 Mt CO_2 yr^{-1} (assuming single-measurement precision of approximately 1.5 ppm and 6 ms^{-1} wind speed, see Fig. 4.5) and better than 8 kt CH_4 yr^{-1} (assuming precision of approx. 10 ppb and 3 ms^{-1} wind speed, see Fig. 4.8). In less favourable conditions, averaging might be needed to quantify emissions.

Inverse modelling studies were also performed for assessing the fidelity of constraining greenhouse gas fluxes at the sub-continental scale and at monthly resolution (Chapter 7).

4.3.5 Mission Duration and Data Latency

Ideally, greenhouse-gas fluxes need to be measured over time scales relevant for climate, which means continuous observations over several solar cycles. As CarbonSat is an Explorer mission delivering data for process studies and exploration into new spatial scales for surface flux estimates, the mission duration will at least allow the characterisation of the impact of interannual variations on the carbon cycle. In addition, the mission will have the potential to detect changes in sources and sinks over the annual cycle. As a result, a minimum mission of three years is required, with the goal of a longer than five years.

The mission objectives do not impose a strong requirement on Level-2 data timeliness and near-realtime data access. Processing and the data assimilation to derive sources and sinks from the CarbonSat Level-2 dataset is assumed to be the most time consuming step; the Level-0 to Level-1 processing is assumed to be faster. Therefore calibrated and geolocated Level-1 data (Level-1b) will be available within two days after acquisition. Accurate Level-2 data will be available after two weeks.

4.4 Level-1 Data Requirements

The main Level-1 data products required from CarbonSat are the spectral radiance L in nadir and sunglint mode and the solar irradiance E from direct Sun measurements. Together they can be used to compute the reflectance R, defined as follows:

$$R(\lambda) = \frac{\pi \cdot L(\lambda)}{E(\lambda) \cdot \cos(\theta)} . \tag{4.1}$$

Here θ is the solar zenith angle (SZA) and λ is the sampled wavelength. The reflectance is the main input for the Level-2 retrieval and needs to fulfil a set of spectral, radiometric and geometric requirements, as described in the following sections. The full set of Level-1 requirements, including those discussed below, was established using retrieval simulations, which include varying spectral ranges, spectral resolution, SNR, radiometric errors (relative and absolute, spectral and spatial, zero-level offset), spectral calibration errors, spatial and temporal coregistration, additive offsets, and polarisation related errors.

As CarbonSat has to deliver accurate Level-2 data over a large range of illuminated conditions, it has to be ensured that the Level-1 performance is met, not only in favourable illumination conditions (e.g. in the Tropics), but also where there is less illumination such as in high-northern latitudes (boreal forest). For defining the dynamic range of the instrument, several reference scenarios were simulated, covering a representative range of bright as well as dark illumination conditions. The dynamic range for each spectral band derived from these simulations is listed in Table 4.3. In the following subsections, radiances are given in units of photons s^{-1} cm^{-2} nm^{-1} sr^{-1}, as is common practice for this type of instrument specifications (e.g. for Sentinel-4 and Sentinel-5). Conversion into the SI standard unit W^{-1} cm^{-2} sr^{-1} nm^{-1} is described in, for example, Boreman (1997).

4.4.1 Requirements Driven by their Influence on Retrieval

The approach to obtain accurate information on the distribution of atmospheric CO_2 and CH_4 from CarbonSat radiance and irradiance observations makes use of well-established principles of atmospheric absorption spectroscopy and

Table 4.3. Dynamic ranges for CarbonSat derived from geophysical reference scenarios. See Table 4.4 for band definitions.

Dynamic range definition	Scenario	SZA	Albedo NIR/ SWIR-1/ SWIR-2	NIR [photons s^{-1} cm^{-2} nm^{-1} sr^{-1}]	SWIR-1 [photons s^{-1} cm^{-2} nm^{-1} sr^{-1}]	SWIR-2 [photons s^{-1} cm^{-2} nm^{-1} sr^{-1}]
Maximum for saturation recovery	Maximum radiance of bright desert scenario	0°	0.8/0.7/0.6	1.3×10^{14}	4.5×10^{13}	2.1×10^{13}
Maximum for Level-1b requirements	Maximum radiance of bright vegetation/soil scenario	0°	0.5/0.4/0.4	8.2×10^{13}	2.6×10^{13}	1.4×10^{13}
Minimum for Level-1b requirements	Maximum radiance of dark vegetation/soil scenario	75°	0.1/0.05/0.05	5.0×10^{12}	9×10^{11}	4.3×10^{11}
Minimum for SNR	Minimum radiance of dark vegetation/soil scenario	75°	0.1/0.05/0.05	2.5×10^{11}	4.5×10^{11}	8×10^{10}

radiative transfer modelling. These methods have been developed for previous and current satellite missions (SCIAMACHY, GOSAT and OCO-2) and have demonstrated to be capable of delivering accurate XCO_2 and XCH_4 data products (Chapter 6). High spectral resolution atmospheric spectra are taken in regions where these gases show characteristic spectral absorption features. The depth of the absorption lines depends on the amount of the absorber in the atmosphere (the number density), the absorption cross-section of the absorber and length of the path of the measured photons through the atmosphere.

The light path is modified by atmospheric scattering, by aerosols and clouds, and surface reflectivity. Aerosols and clouds are highly variable in space and time. Therefore, in general, the Level-1 requirements on signal-to-noise, spectral resolution and spectral coverage need to be optimised not only with respect to determining the total column CO_2 and CH_4, but also for deriving the relevant information on scattering. In the 'weak CO_2 band' around 1.6 µm, where the atmosphere is relatively transparent, the measurements are sensitive to gas concentrations down to the ground (this is important because most sources and sinks are on the surface), but only little information can be derived on scattering parameters. In order to obtain information on scattering parameters, additional spectral regions with strong absorption lines are needed. The light in these spectral regions is only weakly influenced by the surface signal and allows a separation from surface and atmospheric effects and the identification of aerosol and cloud effects. These could be regions containing strong absorption lines of CO_2 but also spectral regions with strong absorptions by O_2 and H_2O. CarbonSat measures O_2 to determine the number of (dry) air molecules, which is required to convert the columns of CO_2 and CH_4 into the respective dry-mole fractions.

The retrieval approach chosen for CarbonSat takes into account lessons learned from the SCIAMACHY, GOSAT and OCO-2 missions. One lesson learned is that spectral regions with saturated water absorption lines provide cirrus information as shown in, for example, Heymann et al. (2012). Another lesson learned is the need for an efficient correction of the impact of solar-induced fluorescence (SIF) (Frankenberg et al., 2011a) on the O_2-A-band, to make full use of this band for characterising atmospheric scattering, notably from scattering by aerosols. This can be achieved by determining SIF from isolated solar Fraunhofer lines located in the vicinity of the O_2-A-band near 755 nm (Frankenberg et al., 2012) which are not influenced by atmospheric absorption. This approach will effectively avoid biases in the radiative transfer in the O_2-A-band, which would otherwise be introduced by SIF. Taking SIF into account allows the accurate correction of scattering by aerosols from the O_2-A-band spectra (Chapter 6). All these corrections will – as a by-product – also yield geophysical information on cirrus clouds, aerosol and SIF. As they will not drive the mission concept, they are called spin-off products throughout this report (Chapter 8). Further details on retrieval algorithms are presented in Chapter 6.

4.4.2 Spectral Ranges

Taking into account the lessons learned from previous missions, the spectral bands as depicted in Fig. 4.10 are required to retrieve the key quantities XCO_2 and XCH_4 including the correction for interferences with SIF and water vapour as well as taking into account the scattering light path accurately by simultaneously retrieving aerosol and cirrus cloud parameters.

As shown in Frankenberg et al. (2012), corrections for SIF need to be considered for accurate XCO_2 retrieval, otherwise errors of up to 1 ppm can

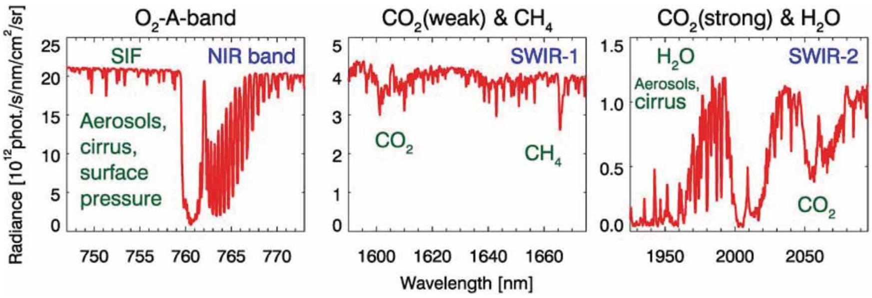

Figure 4.10. Spectral ranges used to derive accurate dry-column concentrations of CO_2 and CH_4. Parameters such as aerosol, cirrus clouds and SIF are also indicated. (M. Buchwitz–IUP)

Band ID	Spectral range [nm]	Related Level-2 product (interfering parameters)
NIR	747–773	XCO_2, XCH_4, (SIF, aerosol, clouds, surface pressure, surface albedo, temperature)
SWIR-1	1590–1675	XCO_2, XCH_4 (aerosol, clouds, H_2O, surface albedo)
SWIR-2	1925–2095	XCO_2, XCH_4 (cirrus, aerosol, clouds, H_2O, surface albedo)

Table 4.4. Spectral band IDs, spectral ranges and relation to Level-2 products.

be expected. This has been tackled for CarbonSat by including the 747–759 nm spectral range, which contains a number of distinct solar Fraunhofer lines (Fig. 4.10). The spectral resolution in the NIR band is driven by the need to adequately resolve detail of the O_2-A-band to correct for atmospheric scattering and radiance contribution from SIF. Table 4.4 identifies the spectral band (IDs) together with spectral ranges, the related Level-2 products and the interfering parameters.

4.4.3 Spectral Requirements

During the Phase-A activities, a systematic trade study was performed (Bovensmann et al., 2014b) to consolidate the requirements on spectral ranges, spectral sampling, spectral resolution and SNR, with the goal of meeting the stringent Level-2 requirements for XCO_2 and XCH_4. The main conclusion of this trade study was that a relaxation of the spectral resolution can be compensated by an increase in the spectral range in the NIR (more Fraunhofer lines to better disentangle the SIF from the O_2-A-band) and SWIR-2 (inclusion of strong water vapour bands for cirrus detection) and by moderately increasing the SNR. From this study, the baseline set of Level-1 requirements as summarised in Table 4.3 and Table 4.5 were derived. A separate analysis using high spectral resolution GOSAT data to investigate the impact of reduced spectral resolution on XCO_2 and XCH_4 Level-2 supported the above findings (Galli et al., 2014).

Band ID	Spectral resolution [nm]	Spectral sampling ratio	SNR @ L_{ref}	Lref [photons s^{-1} cm^{-2} nm^{-1} sr^{-1}]
NIR	0.1	3	300 (G) / 150 (T)	4.2×10^{12}
SWIR-1	0.3	3	320 (G) / 160 (T)	1.5×10^{12}
SWIR-2	0.55	3	260 (G) / 130 (T)	3.8×10^{11}

Table 4.5. Requirements for spectral resolution, spectral sampling and SNR. The SNR requirements are expressed at a specific reference radiance (L_{ref}).

Concerning the SNR, as it has a direct impact on the precision of the XCO_2 and XCH_4, it was identified that when requiring a spatial resolution grid size of 2×3 km^2, an SNR higher than the threshold requirement would be favourable, as it (via higher precision in XCO_2 and XCH_4) increases the sensitivity to detect point source emissions (Figs. 4.4 and 4.6). Therefore, an SNR goal requirement is also indicated. Note that the SNR requirements are valid per spectral detector element assuming the required spectral sampling ratio is met. The required SNR at other radiance levels is computed by applying a scaling law.

The spectral performance requirements for CarbonSat are parameterised in terms of the Instrument Spectral Response Function (ISRF), sometimes referred to as the Instrument Line Shape (ILS). The ISRF of a given spectral channel can be defined as the instrument spectral response to a monochromatic stimulus, normalised such that its spectral integral is unity. It characterises the spectral response of the instrument to the monochromatic spectral radiance and irradiance incident at the entrance of the telescope. The ISRFs of the spectral channels provide the link between the forward radiative transfer model and the spectra measured by the instrument. Therefore, the ISRF must be accurately known for Level-2 processing.

Since the ISRF fully describes the spectral response of the instrument, parameters derived from it are used for the definition of spectral requirements: the spectral resolution is Full Width at Half Maximum (FWHM). The spectral sampling ratio corresponds to the number of detector pixels within such FWHM. The requirement for the spectral sampling ratio is three, which ensures that aliasing is avoided when interpolating measurements on different wavelength grids, which is needed to derive reflectance, since solar spectra are Doppler-shifted. The barycentres of the ISRFs define the wavelengths λ_0, to which the spectral channels (detector pixels) of the measured radiance and irradiance spectra are associated. Systematic uncertainties in ISRF will introduce biases in XCO_2 and XCH_4. Distortion of the ISRF owing to non-uniform scenes will degrade the precision of the Level-2 retrievals. Because the ISRF is fundamental, it needs to be characterised on-ground and known in-orbit to better than 2% of its peak value over the full width (down to 1% of the peak). In-orbit stability, including effects from non-uniform scenes, needs to be better than 2%.

Information on scene heterogeneity, owing to spatial sub-pixel variations in surface properties, clouds and aerosols, as well as strong XCO_2 or XCH_4 gradients in parts of the field-of-view, can be obtained by using high spatial resolution data for dedicated spectral intervals (high spatial sampling channels). They can be used to derive the effective ISRF owing to inhomogeneous slit illumination as a consequence of scene heterogeneity. It requires that some specific spectral intervals will also have to be downloaded at higher spatial resolution, but not necessarily at the same high spectral resolution as the nominal Level-1b data. The proposed spectral windows (about 20) are driven by their information objectives (sub-pixel properties, CO_2, CH_4 cloud and aerosol characterisation).

4.4.4 Geometric Requirements

The geophysical products derived from the observed spectra are associated with spatial samples, which are the areas on Earth's surface over which the radiance spectra are acquired. To allow appropriate imaging of source areas like cities or strong point sources, both the spatial sampling and resolution must be sufficient to resolve their features. The spatial sampling distance (SSD) in along-track (SSD_{ALT}) and across-track (SSD_{ACT}) will not be too different. The SSD will not exceed 3 km in one direction and the covered area by each sample (product of SSD_{ALT} and SSD_{ACT}) will be smaller than or equal to 6 km^2. This implies that the allowed aspect ratio between SSD_{ALT} and SSD_{ACT} is between

1.5 and 0.66. The spatial resolution of the measurement is expressed by the fraction of the detected energy, which actually originates from the sampled rectangular area of 6 km^2. This figure of merit, referred to as System Integrated Energy (SIE), is computed from the System Energy Distribution Function (SEDF), which describes the spatial distribution of the detected photons. The aerial integral of the SEDF over the spatial sample (SSD_{ALT} by SSD_{ACT}) yields the SIE. To allow for an appropriate image interpretation of the Level-2 products, the SIE is required to be larger than 70%.

As accurate retrieval algorithms, especially for XCO_2, rely on the three-band retrieval approach, which simultaneously uses spectral information from the three spectral bands, the spectral information from all three bands needs to originate from the same spatial area, i.e. needs to be spatially co-registered. Different error contributors were assessed which could be the consequence of spatially imperfect co-registration, for example effects of gradients in cirrus clouds, topography and surface albedo. It was found that changing cirrus cloud optical depth is a major driver for the co-registration. Using lidar observations in presence of a cirrus optical depth between 0.1 and 0.15, it was shown that the interband spatial co-registration requirement is driven by the XCO_2 error budget and that a spatial co-registration between the SWIR and the O_2-A-band (NIR) must be better than 10–15 % of the SSD in the across-track direction (Bovensmann et al., 2014b). This leads to a requirement of 15% between the SWIR bands and the O_2-A-band. A spatial mis-registration between the SWIR-1 and SWIR-2 has a lower impact, so that up to 30% mis-registration is still acceptable.

4.4.5 Radiometric Requirements

The absolute radiometric accuracy required for CarbonSat measurements is driven by the necessity to determine the surface albedo of the measured spatial sample, which is an important contributor to the effective photon path length. In order to retrieve this important parameter, uncertainty in the measured reflectance has to be better than 3% in all spectral bands.

As the information on XCO_2 and XCH_4 is derived from spectral absorption structures, any spectral structure interfering with the absorbers of interest needs to be minimised. Such spurious ‘spectral features’ can be induced by stray light, diffuser speckles, polarisation sensitivity and non-linearity effects. Their impact on the retrieved Level-2 products strongly depends on the spectral structure of the measurement error in reflectance. The higher the correlation with the spectral signature of the absorbing molecular species at instrument resolution, the larger is the expected error in the retrieved column amount. To minimise these correlated radiometric errors and the resulting retrieval error, a new figure of merit and corresponding requirement was introduced: The Effective Spectral Radiometric Accuracy (ESRA), which is defined as the scalar product of the reflectance error spectrum ΔR and a given gain vector G, is defined at the spectral samples i measured at wavelength λ_i:

$$\mathrm{ESRA} = \sum_i \Delta R_i \cdot G_i \tag{4.2}$$

The gain vector elements G_i can be interpreted as the weights of the individual reflectance measurements R_i in the product retrieval. R is derived from instrument and residual calibration errors, such as stray light, polarisation sensitivity, diffuser features and detector non-linearity. The requirement on ESRA constrains the impact of residual spectral features on the Level-2 retrieval. The gains, plotted in Fig. 4.11, are provided for each of the two target gas species and are derived from the baseline retrieval algorithm (Level-2 processor). Details of gain vectors used in the ESRA requirement are described in more detail in Sierk et al. (2014).

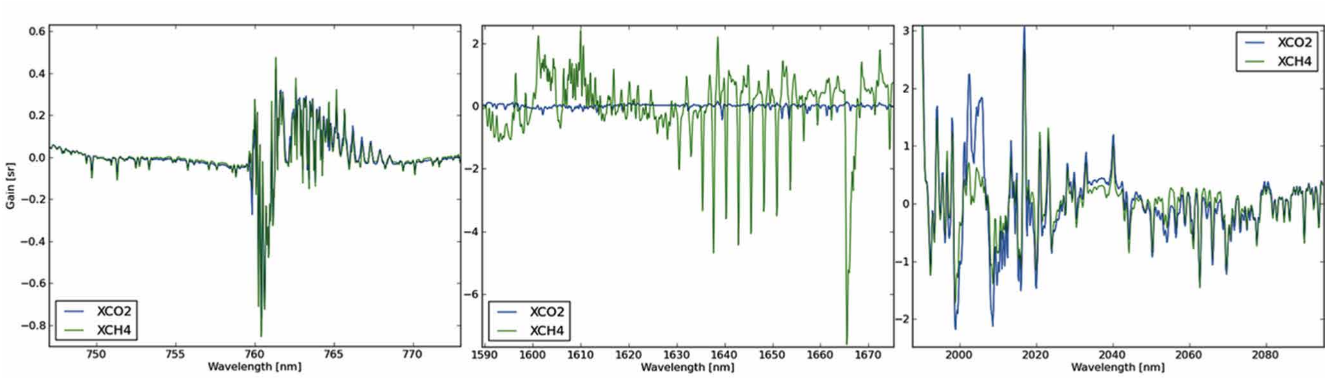

Figure 4.11. Gain vectors for XCO_2 and XCH_4 in the NIR, SWIR-1 and SWIR-2 spectral bands. The scalar product of the gain vectors with the reflectance error spectrum yields the dimensionless ESRA value, which is a measure for the impact on the retrieval accuracy. (Sierk et al., 2014)

The radiation detected has been scattered by molecules and aerosol and/or reflection at the ground. The degree of polarisation (DOP) of the measured spectral radiance depends on the observation geometry as well as on the penetration depth into the atmosphere. The steep absorption pattern of the O_2-A-band as well as the saturated absorptions of water vapour in the SWIR-2 band induces a strong variation in DOP in these bands, which is low in the continuum region and high in the centre of the band, where most of the photons have been Rayleigh-scattered. In the SWIR bands outside strongly saturated absorption bands, Rayleigh scattering is almost negligible, but Mie scattering is more significant and the polarisation state is mostly dominated by the surface reflection. Although the expected maximum DOP from surface reflections is lower than in the NIR band, the detected SWIR signal can be polarised up to 30%. Within the saturated absorption bands, the light over land is polarised up to 100%. For sunglint observations, due to the detection in specular reflection, the DOP can reach values close to 100%, but these can be easier predicted from the reflection geometry.

Spectrometers are known to feature polarisation-dependent throughput, and the polarisation of the Earth spectral radiance therefore induces a relative radiometric error in the measured radiance. This radiometric error varies with the ground scene and geometry and does not cancel out in the Earth reflectance, as the Sun irradiance is unpolarised. The polarisation sensitivity (PS) is defined via the maximum and minimum signals ($L_{\max}$ and $L_{\min}$) measuring 100% linearly polarised radiance as the polarisation angle is rotated over 180°:

$$\mathrm{PS}(\lambda_i) = \frac{L_{\max}(\lambda_i) - L_{\min}(\lambda_i)}{L_{\max}(\lambda_i) + L_{\min}(\lambda_i)} \tag{4.3}$$

From retrieval simulations with standard assumptions it was established that the maximum PS of the instrument will be smaller than 0.5% for each band, assuming a spectrally constant polarisation angle.

Multiplicative radiometric gain errors (Fig. 4.12) need to be known to within 0.5%, to reduce related errors in XCO_2 and XCH_4, below 0.1 ppm for XCO_2 and below 0.5 ppb for XCH_4.

From the experience with retrievals of XCO_2 and XCH_4 from SCIAMACHY and GOSAT, it has been established that unknown additive offsets can have a severe impact on Level-2 product quality. Therefore, XCO_2 and XCH_4 errors due to additive radiance offsets for various scenarios have been investigated using linear error analysis based on the gain matrix approach (see above) as well as using full iterative retrievals for various aerosol and cloud contaminated scenes (Chapter 6). For example, for a typical scene (vegetation albedo and SZA 50°) the amount of aerosol and cirrus has been varied within a typical range (from zero to an aerosol optical depth of 0.3 and a cirrus optical depth of 0.4 (Fig. 7.14)) and radiance spectra with and without radiance offsets

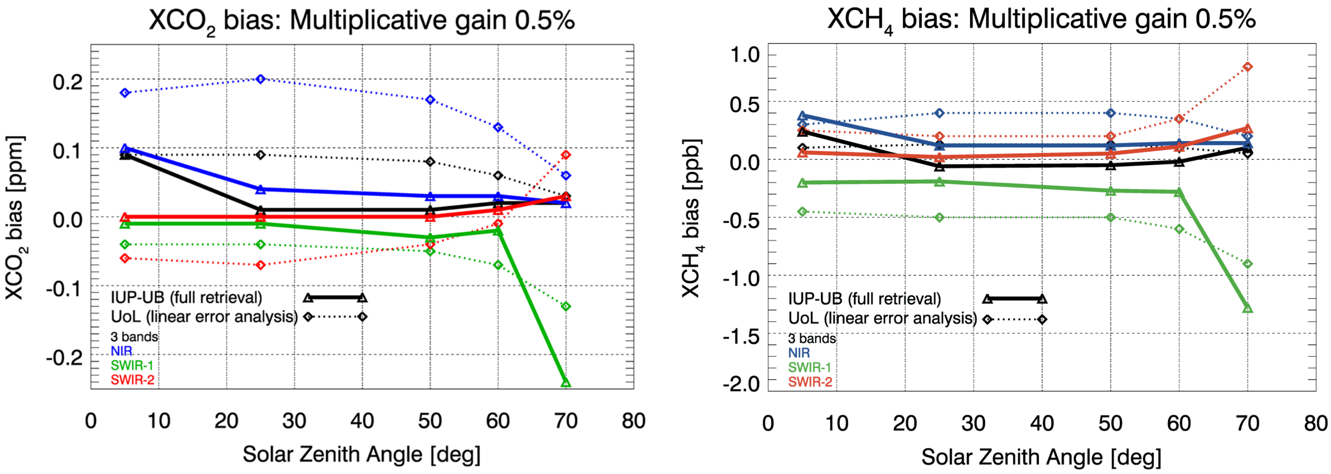

Figure 4.12. Systematic errors for XCO$_2$ (left) and XCH$_4$ (right) expected to be the results of multiplicative radiometric gain errors. (M. Buchwitz–IUP)

have been generated as input for the Level-2 retrieval algorithm. For an additive radiance offset of 8.4×10^9 photons s^{-1} nm^{-1} cm^{-2} sr^{-1} in the NIR band, 8.6×10^9 photons s^{-1} nm^{-1} cm^{-2} sr^{-1} in SWIR-1 and 2×10^9 photons s^{-1} nm^{-1} cm^{-2} sr^{-1} in SWIR-2, the bias in XCO$_2$ increases from 0.25 ppm to 0.34 ppm (XCH$_4$ 0.4 ppb to 1.2 ppb). As expected, the random error (precision) of the XCO$_2$ and XCH$_4$ retrievals is essentially identical. The offset related errors for this case are therefore approximately 0.1 ppm for XCO$_2$ and 0.8 ppb for XCH$_4$. For large SZAs (e.g. 75°) the errors will become even larger (e.g. 0.2 ppm for XCO$_2$ and 2 ppb for XCH$_4$). Overall, it is concluded that the additional errors due to additive radiance offsets should not exceed the values given above.

The observational requirements relevant for the instrument design are listed in Chapter 5 (Table 5.3). The expected performance of the system concepts is compared with the observational requirements in Chapter 7.

→ MISSION ELEMENTS

5. Mission Elements

This chapter provides the technical description of the CarbonSat mission as derived from the preparatory activities during Phase-A/B1. It shows how two candidate concepts can respond to the scientific mission requirements defined in the previous chapters.

The system description is based on the results of the work performed during parallel Phase-A/B1 system studies by two industrial consortia (led by Airbus Defence and Space and by OHB System AG, respectively). Where necessary, both implementation concepts (A and B) are described in order to present significantly different approaches that are capable of meeting the mission requirements.

An overview of the mission architectures and proposed orbits are given subsequently (Sections 5.1 & 5.2), then the space segment is described in detail (Section 5.3), followed by launcher selection (Section 5.4), ground segment (Section 5.5) and operations concepts (Section 5.6). The overall mission performance is summarised in Chapter 7.

5.1 Mission Architecture Overview

The key architectural mission elements of the CarbonSat mission are illustrated in Fig. 5.1.

The CarbonSat space segment is implemented with a single satellite carrying one payload: the Greenhouse Gas Imaging Spectrometer (GHGIS), a pushbroom optical instrument operating in three spectral bands: one in the near-infrared (NIR) spectral range and two in the shortwave infrared (SWIR)

Figure 5.1. CarbonSat mission elements. (ESA)

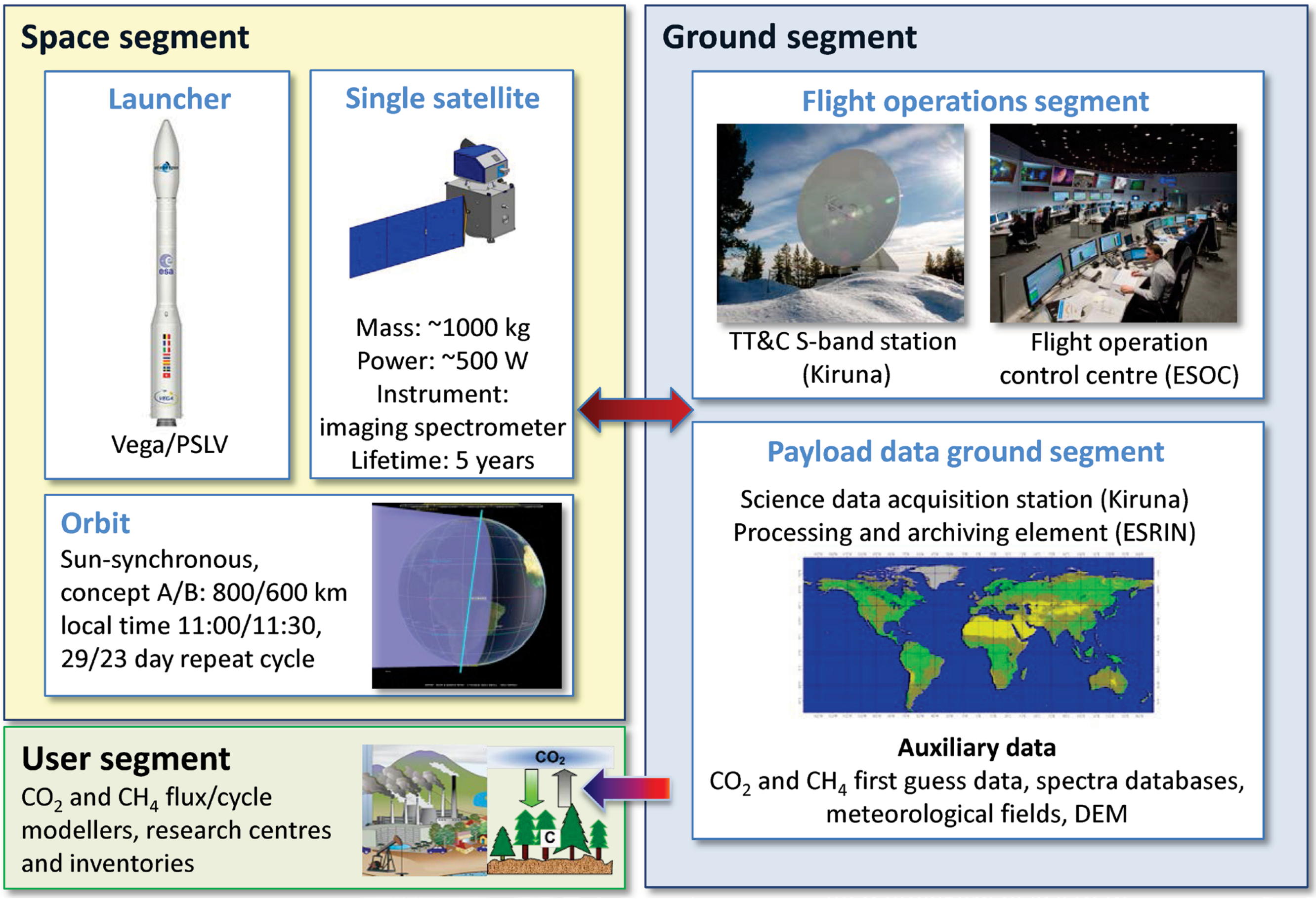

Table 5.1. Selected CarbonSat orbits for Concepts A and B.

	Concept A	Concept B
Orbit type	Repeating frozen Sun-synchronous	Repeating frozen Sun-synchronous
Orbits per day	14+8/29	14+21/23
Orbit average altitude [km]	794	594
Local time	11:00 descending node	11:30 descending node
Nadir to sunglint ratio	2:1	4:1–4:1–5:1 pattern repeats
Repeat Cycle (RC) length [days]	29	23

Table 5.2. Geometrical and temporal coverage of Concepts A and B.

Requirement	Concept A	Concept B
Swath derived from coverage requirement and orbit selection	Instrument FOV: 17.3° Resulting swath: 240 km	Instrument FOV: 18.6° Resulting swath: 185 km
95% geometrical coverage over land at the equator in 30 days, nadir only	100% in 29 days	97%
95% geometrical coverage over land at the equator in 30 days, nadir & sunglint	100% in 18 days	100% in 23 days
95% geometrical coverage over land polewards of 40° latitude in 12 days, nadir only	84%	91%
95% geometrical coverage over land polewards of 40° latitude in 12 days, nadir & sunglint	100% in 11 days	100%
Average ocean coverage as absolute area within 30 days	94%	66%
Average ocean coverage as defined below within 30 days	100% in 24 days	98% in 30 days

spectral range. The satellite flies in a near-polar, Sun-synchronous (SSO) quasi-circular frozen Low Earth Orbit (LEO) at an altitude of ~800 km or ~600 km with a swath width of ~240 km or ~185 km, depending on the implementation concept (A and B, respectively). The orbits are designed to meet the observation requirements (detailed in Chapter 4) at nadir over land and to observe sunglint over the oceans. The equator crossing Local Time of the Descending Node is required to be between 10:00 and 14:00 hrs. The two different orbit selections are driven by the resulting repeat cycle and orbit height. The latter defines, in combination with the instrument field-of-view (FOV), the swath width. The strategy for Concept A is to achieve coverage at the equator in one repeat cycle whereas Concepts B needs more than one cycle (Table 5.2).

The science data and stored housekeeping and telemetry (HKTM) data are transmitted nominally to the Kiruna ground station in Sweden (the sizing case) via X-band, while realtime telemetry data is transmitted via S-band.

The required mission lifetime is nominally three years with fuel for five years. The standard operation scenario foresees a fixed number of orbits with the instrument looking towards nadir (nominal land-observation mode) followed by one orbit with the instrument pointed towards the spot of specular reflection of the incident sunlight (sunglint mode over the oceans and over snow and ice-covered surfaces); solar calibration takes place before entering into eclipse in anti-flight direction. The ratio between nadir and glint orbits is two nadir orbits followed by one sunglint orbit (2:1) for Concept A and periods

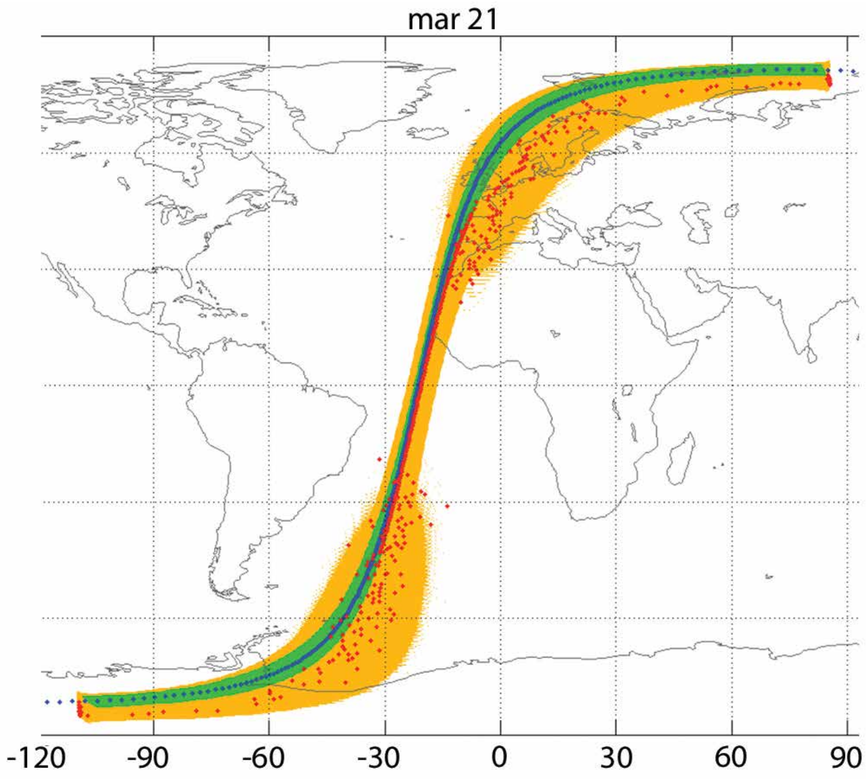

Figure 5.2. The effective swath (green) obtainable in sunglint mode at equinox is shown. The spot of specular reflection is tracked by pitch steering. Spot of specular reflection (red dots), sub-satellite point (blue dots), sunglint trail (orange) for Concept A. (Airbus Defence and Space/ Deimos)

of four/four/five nadir orbits, each one followed by one sunglint orbit (4:1–4:1–5:1) for Concept B. The optimal ratio for glint to nadir orbits is driven by the repeat pattern and swath width. It is tuned to give priority to land observations but maximise the return over oceans, resulting in different solutions for the two concepts.

The ground segment supports mission operations, data processing including calibration of Level-1 products, product distribution and archiving.

5.2 Mission Analysis and Orbit Selection

The CarbonSat mission includes two different observation modes, which are driven by the surface reflectivity at the observational bands. The nominal mode aims at radiance observation over land areas in a nadir-looking geometry. Over water bodies, the reflected signal strength in the observed SWIR bands is too low to reach the necessary Signal-to-Noise Ratio (SNR), thus the Line of Sight (LOS) of the instrument is tilted towards the spot of the specular solar reflection over the oceans, the sunglint mode. This mode also ensures the necessary SNR over snow and ice covered regions. The pointing is achieved by pitching the platform, hence keeping the LOS of the instrument fixed with respect to the platform in both concepts. The baseline orbits of Concept A and Concept B are stated in Table 5.1.

5.2.1 Mission Coverage

Although they are quite different, the orbits selected by the two consortia fulfil most temporal and spatial coverage requirements, which are:

- Solar Zenith Angle (SZA) at the observed ground sample to be less than 75° in the northern hemisphere and 60° southern hemisphere

- 95% geometric coverage at the equator in 30 days

- 95% geometric coverage over land polewards of 40° latitude within 12 days

- over oceans, grid box of size 1° in latitude by 5° in longitude to include one spatial sample on average over 30 days

The achieved coverage (cloud-free conditions assumed) of the two concepts is stated in Table 5.2, reported as a percentage of the observable area for nadir and grid boxes for sunglint. Sunglint observations over land are also downlinked. To derive the sunglint affected area of the oceans, the Cox-Munk model is used, assuming a surface wind speed of 4 ms^{-1}. The pointing law proposed for both

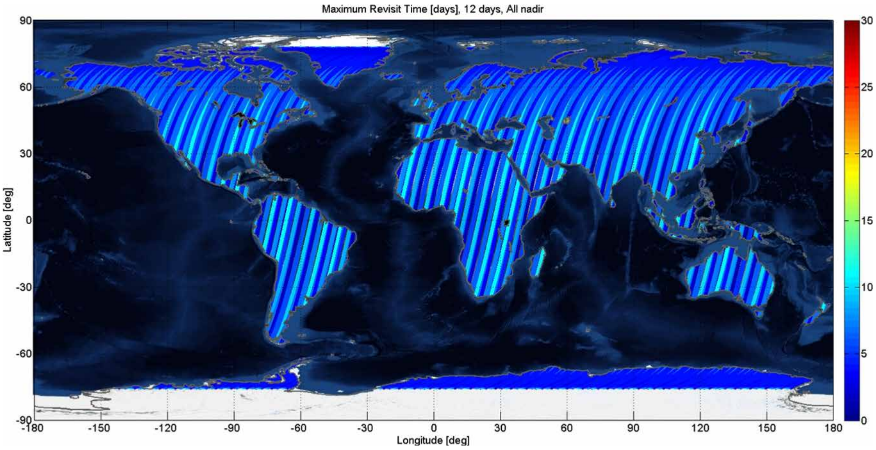

Figure 5.3. Concept A: global coverage of accumulated nadir and sunglint orbits over land after 12 days. (Airbus Defence and Space/Deimos)

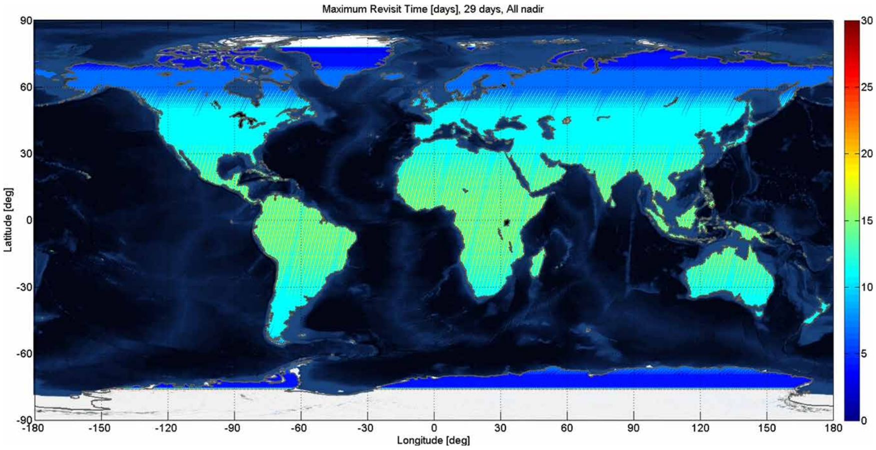

Figure 5.4. Concept A: global coverage of accumulated nadir and sunglint orbits over land after 30 days. (Airbus Defence and Space/Deimos)

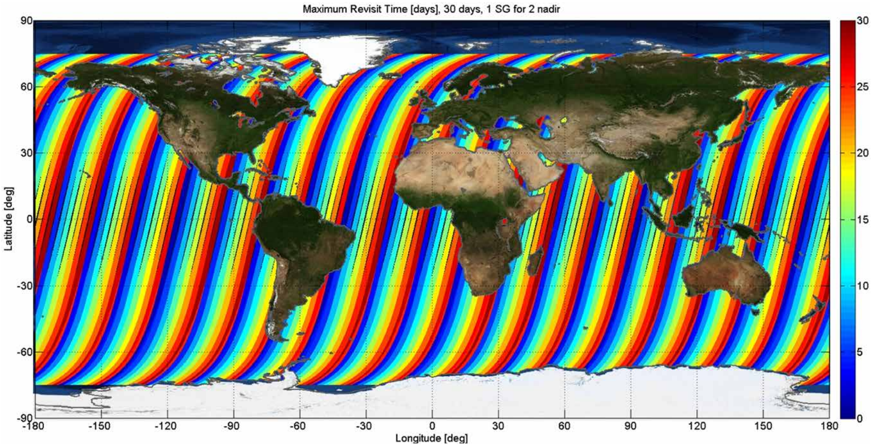

Figure 5.5. Concept A: ocean coverage of sunglint orbits after 30 days. (Airbus Defence and Space/Deimos)

concepts to follow the glint spot is based on a continuous steering covering a range of ±40°.

Orbit maintenance does not present specific challenges. Owing to different drag conditions inherent to the selected orbits, Concept B requires more orbit maintenance manoeuvres; in any case, a mean availability above 90% over one month is ensured by both concepts. At end-of-life (EOL), Concept A requires a deorbiting manoeuvre to ensure (uncontrolled) reentry within 25 years, whereas the orbit selected in Concept B results in an uncontrolled reentry within 25 years (~16 years estimated) without any manoeuvring.

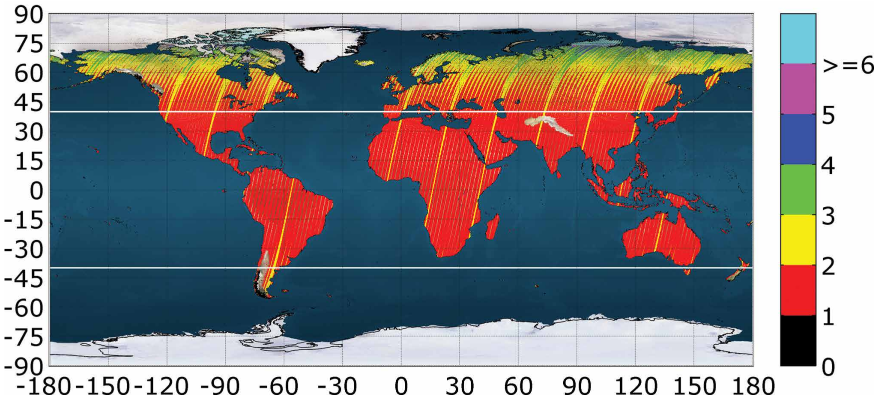

Figure 5.6. Concept B: global coverage of accumulated nadir and sunglint orbits over land after 12 days. 40° latitudes indicated by white lines. (OHB/GMV)

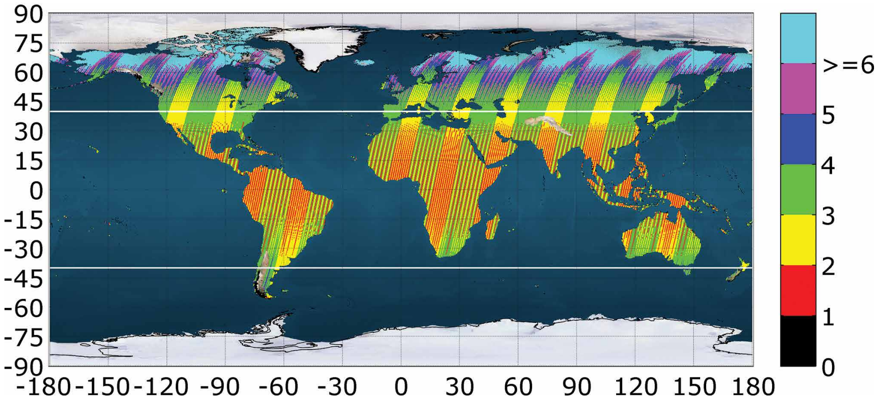

Figure 5.7. Concept B: global coverage of accumulated nadir and sunglint orbits over land after 30 days. OHB/GMV)

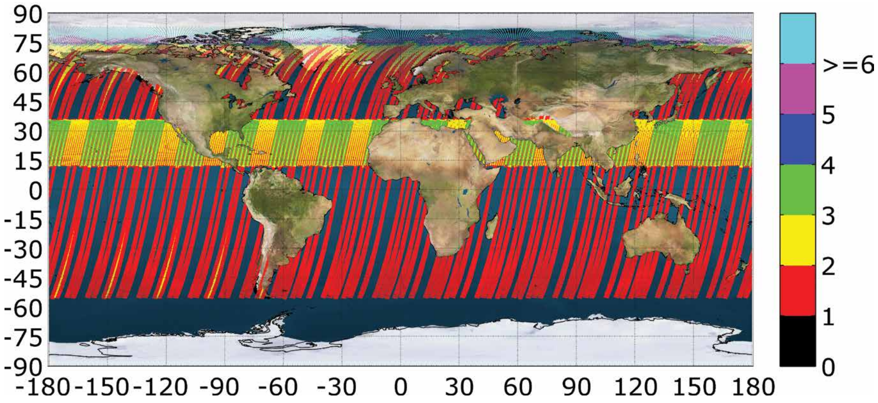

Figure 5.8. Concept B: ocean coverage of sunglint orbits after 30 days. (OHB/GMV)

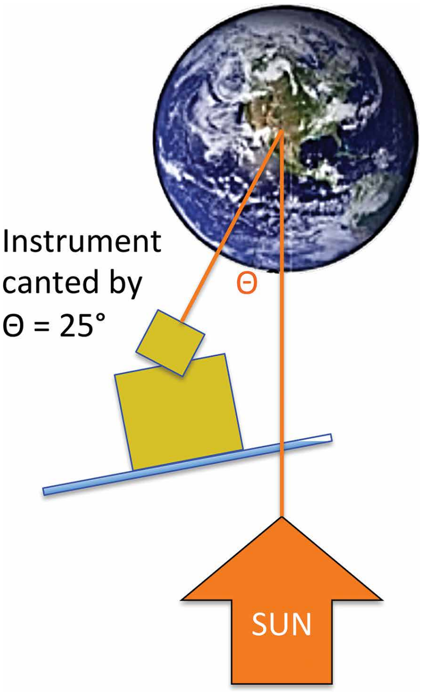

Figure 5.9. Illustration of instrument cant angle for Concept A. (Airbus Defence and Space)

Both selected orbits are adequate to fulfil the mission needs. Concept A is currently non-compliant with the 12-day coverage requirement polewards of 40° latitude. This can be corrected by switching to an observation pattern favouring nadir observations over land (5 nadir, 1 sunglint = 5:1), which is still compliant with the ocean coverage requirements. The selected pattern of 2:1 represents a worst case in terms of power; switching to a 5:1 pattern has no system impacts.

Concept B is slightly non-compliant with the 30-day global coverage at the equator (small coverage gaps, which are closed during the next RC) and with the ocean coverage.

The selected orbits differ significantly in altitude. The ΔV budget for the lower one is dominated by orbit maintenance manoeuvres owing to drag, whereas for the higher one it is dominated by the EOL deorbit burn.

The instrument viewing angles and pupils are very similar in both concepts, resulting in a wider swath for Concept A (the higher orbit), which however reduces the spatial oversampling compared to Concept B (the lower orbit). Both concepts can measure up to 80° SZA in both hemispheres.

5.3 Space Segment

5.3.1 Overview

The space segment consists of a single satellite carrying the GHGIS instrument. The satellite configuration is strongly constrained by the fully passive cooling concept of the GHGIS in conjunction with the two observation geometries (nadir and sunglint). In any observation geometry, the radiative fluxes onto the instrument radiator must be minimised by appropriate radiator accommodation and baffling. In particular, the pitch manoeuvre drives the accommodation and optimal thermal design of the instrument as well as the respective baffle sizing. The two consortia investigated a number of options, with an emphasis on maximum reuse of either the whole platform or its subsystems. This is reflected in the resulting satellite configurations.

Following the description of the configuration in Subsection 5.3.2, the payload concept is described in Subsection 5.3.2, platform and subsystems in Subsection 5.3.4, complemented with the overall budgets in Subsection 5.3.5.

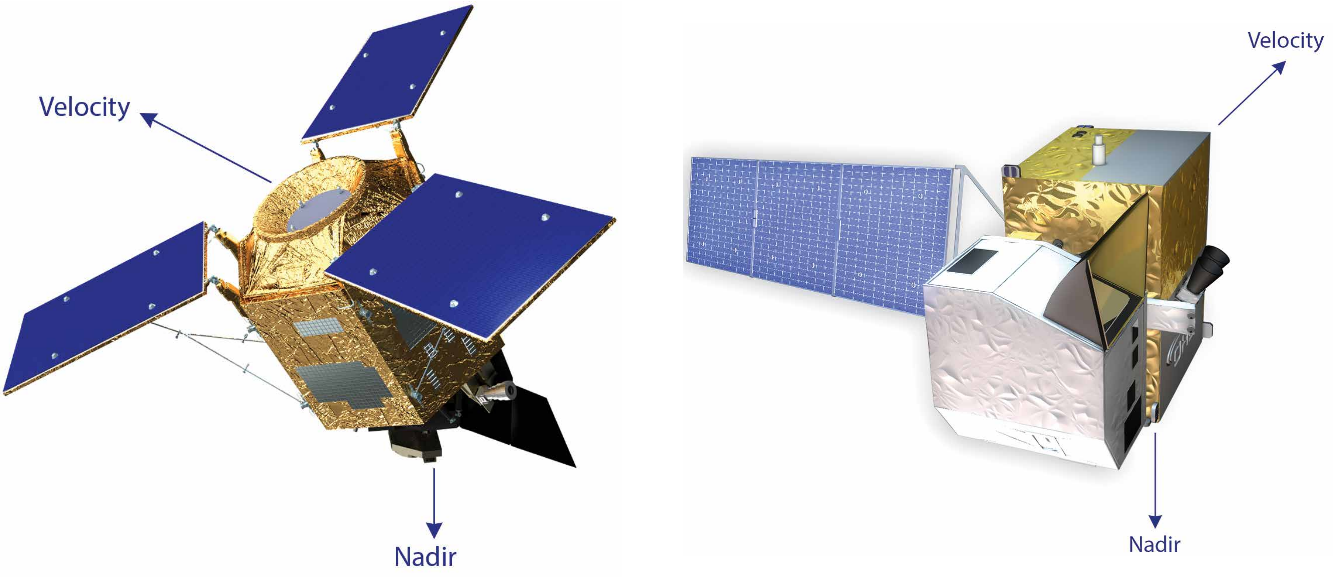

Figure 5.10. Satellite configuration, left: Concept A (Airbus Defence and Space), right: Concept B. (OHB)

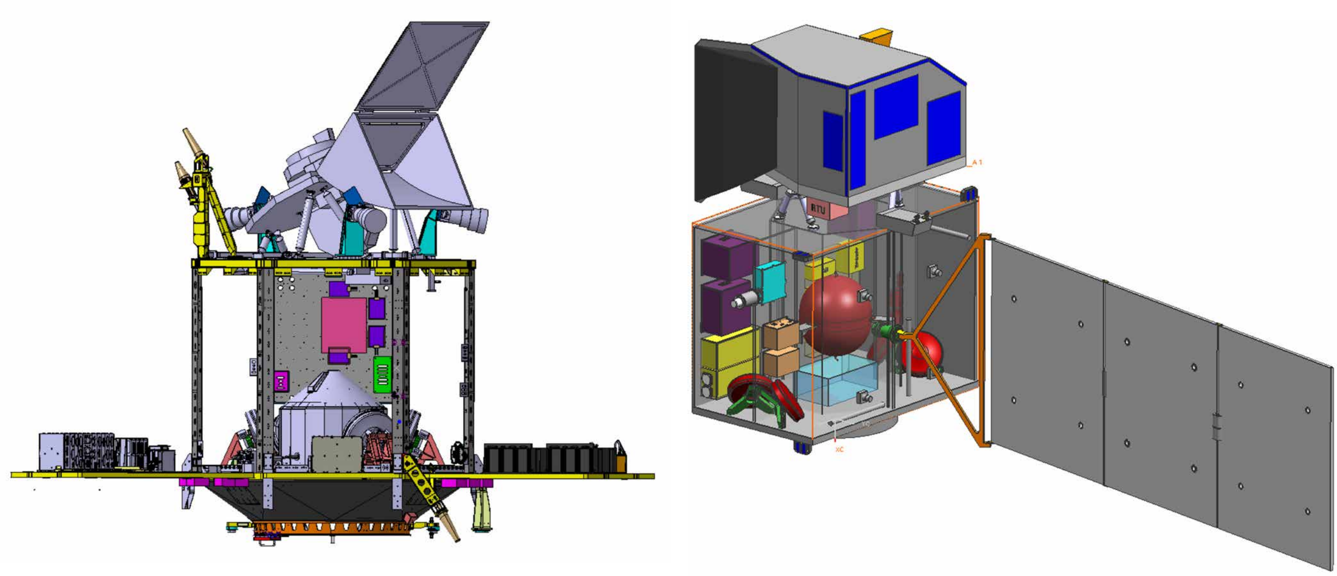

Figure 5.11. Overview of satellite layout. Left: Concept A (Airbus Defence and Space), right: Concept B (OHB).

5.3.2 Satellite Configuration

Concept A is based on a recurring platform, the AstroBus 250 (AS250) from the Airbus Defence and Space group, with the payload mounted on the top panel. This requires an instrument optimised to be compatible with the specific accommodation constraints of the AS250. In particular, the passive cooling concept requires a careful radiator design with respect to fluxes from Earth, the Sun and the platform itself during the pitch manoeuvre.

An instrument cant angle is implemented to point the three solar arrays towards the Sun, rather than the Z-axis towards nadir, Fig. 5.9. This geometry optimises the solar aspect angles on the solar arrays, as well as the radiator view factor to cold space as the solar arrays are effectively ‘tilted away’ from the instrument. As the baseline, an instrument cant angle θ of 25° from Z was chosen, representing a compromise between optimal solar aspect angle and radiator view factor at a LTDN of 11:00.

Concept B is based on a bespoke platform tailored to the instrument needs. Sunglint pointing is implemented by pitching the whole platform while maintaining the orientation of the instrument radiator to cold space and having sufficient power generated by the articulated solar array.

The instrument is mounted on the top panel (that opposite the panel that accommodates the launch adapter), which is oriented in anti-flight direction. To allow manoeuvres without the need to turn the platform 180°, thrusters are mounted on brackets protruding from the bottom panel, firing in anti-flight direction; plume simulations have excluded any contamination issues.

In both concepts the instrument is mounted isostatically on the platform to minimise thermoelastic coupling, whereas startrackers are mounted directly on the platform. Platform and payload are thermally de-coupled as far as possible, and the accommodation of the S- and X-band antennae in both concepts allows an unobstructed FOV.

5.3.3 Payload

5.3.3.1 Overview

The GHGIS measures spectral radiance in the two observation modes, as well as irradiance spectra in Sun-calibration mode. From these measurements, the Earth reflectance is derived.

Figure 5.12. Principle of a pushbroom imaging spectrometer. The entrance slit of the spectrometer is imaged onto Earth's surface, defining the swath width in across-track direction. The instrument spectrally disperses the slit image in along-track direction, which is sampled by the satellite motion during integration time. The products for each spatial sample are inferred from radiance spectra imaged onto the 2D array detector. (ESA)

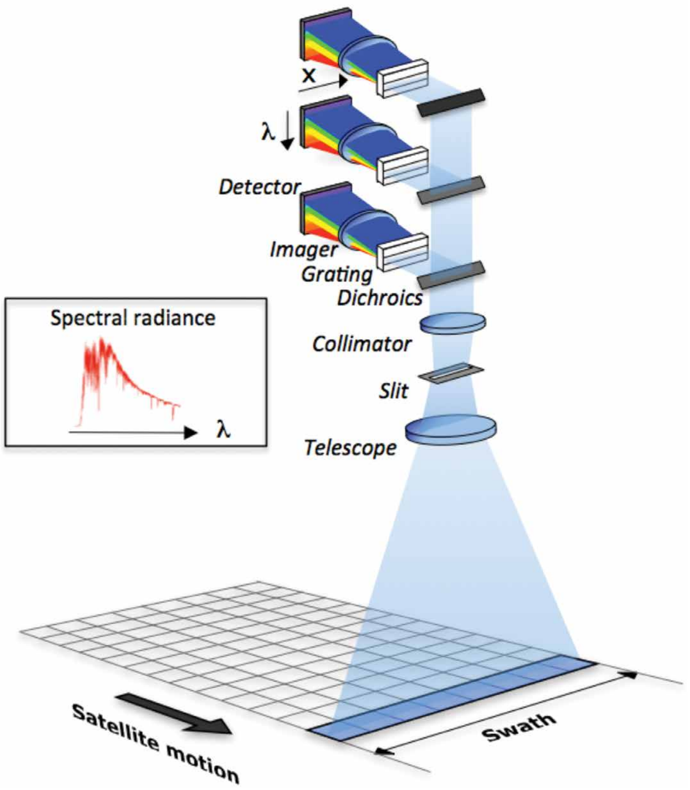

The following sections address the observation principles and the description of the instrument, starting with an overview of the instrument concepts. Then the impact of key requirements at Level-1b (as derived from the scientific needs) on the detailed definition of the instrument is discussed and presented by describing the main subsystems and the calibration strategy.

5.3.3.2 Observation principle

The GHGIS instrument performs simultaneous, spatially co-aligned observations of spectrally resolved Earth reflectance in three separated spectral regions: one in NIR and two in SWIR (SWIR-1 and SWIR-2), using three pushbroom imaging spectrometers (Table 5.3 on page 80).

The measurement principle is illustrated in Fig. 5.12. A nadir-pointing telescope images the ground scene on the entrance slit of the spectrometer, projecting the slit onto Earth's surface perpendicular to the ground trajectory of the sub-satellite point (spacecraft motion vector). The projected slit length in across-track (ACT) direction defines the swath width. As the satellite moves along its orbit, the projected slit continuously scans the ground in the along-track (ALT) direction and the diffraction gratings spectrally disperse the slit image perpendicular to the ACT direction. The spectrometer cameras focus the 2D images onto the array detectors. The distance travelled during integration time (exposure time between two successive read-outs) provides the spatial sampling in the ALT direction during acquisition. At any instant, the detector pixels represent elements of the image sampled spatially in the ACT direction and spectrally in the ALT direction.

Figures 5.13 and 5.14 illustrate an example of the simultaneous spatial-spectral imaging of the GHGIS instrument. Figure 5.13 depicts an aerial image obtained from airborne measurements of reflectance performed by the Airborne Visible Infrared Spectrometer (AVIRIS) over the San Francisco Bay area. Some terrain types, which are characterised by different albedo regimes, are indicated in the true-colour image on the left. The white box highlights a section of 30 km in north–south and 2 km in east–west direction, which corresponds to ten ACT and one ALT spatial samples of the GHGIS instrument. The three images on the right side of Fig. 5.13 show the reflectance measurements over the highlighted area in three AVIRIS channels (763 nm, 1602 nm, 1998 nm), which are close to the CarbonSat spectral bands. The sharp radiometric contrast between the different terrain types is clearly visible. On the basis of these data, CarbonSat measurements for this scene were simulated, and are plotted in Fig. 5.14. The three plots represent the signal (number of electrons) detected at the three focal planes of the GHGIS instrument after an integration time of 300 ms (corresponding to the ALT spatial sampling distance). The spatial (vertical) axis covers a 30-km wide section of the swath width, and the spectral (horizontal) axis covers the complete spectral range of each band. The signal structure in the spectral direction is characterised by the absorption features of the CO_2, CH_4, H_2O and O_2 molecules, which are indicated on the spectral axis. In the spatial direction, the ground albedo variations corresponding to the indicated terrain types are clearly visible, e.g. the sharp transition between land and water. The 2D plots in Fig. 5.14 illustrate the principle of spatio-spectral imaging, and indicate the spatial and spectral resolution of the GHGIS instrument before binning.

After detector read-out, these data are spatially binned on board by co-adding 14 pixels in spatial (ACT) direction (spatial oversampling factor of Concept B). The horizontal white lines indicate the binning windows for this co-addition to form 10 spatial samples each of 3 km in ACT by 2 km in ALT direction. In addition to these spectra, high spatial sampling (HSS) data are

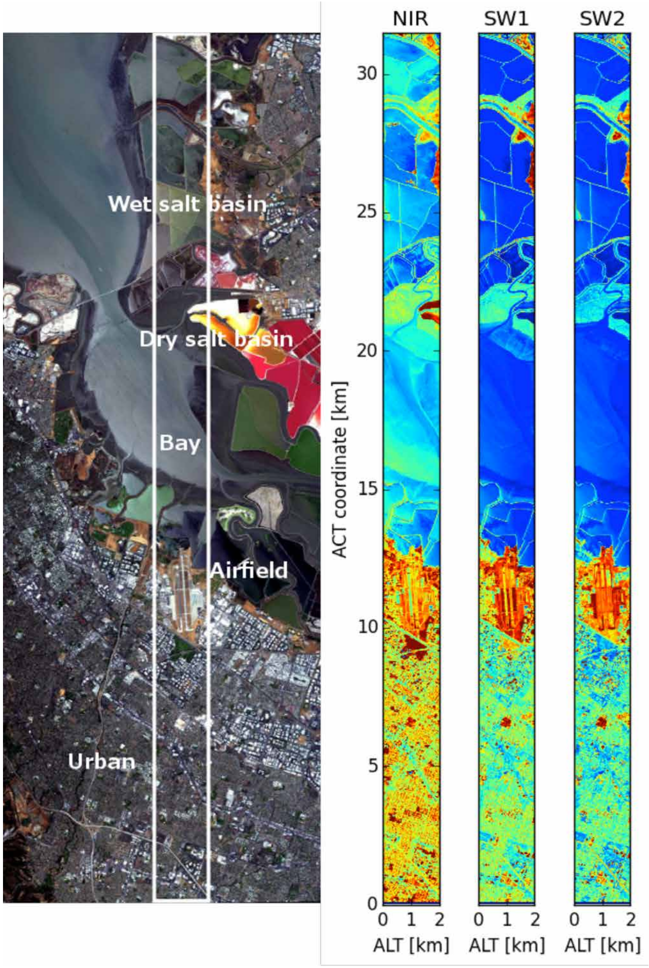

Figure 5.13. Aerial images of reflectance from the AVIRIS instrument. The image on the left shows part of the San Francisco Bay area covering various terrain types with different albedos, over which the measurements were acquired. On the right, AVIRIS observations in three channels close to the GHGIS spectral bands are depicted, which correspond to the area between the white lines in the left image. These data illustrate the radiometric contrast in the GHGIS spectral bands at high spatial resolution. They were used to simulate the GHGIS measurements shown in Fig. 5.14. (NASA/JPL)

Table 5.3. GHGIS-related main Level-1b requirements.

Requirement	Value	Driver	Impact
Geometric			
Swath	180 km	Coverage	Telescope, ACT FOV
Spatial sampling distance (SSD)	2 km (ALT)×3 km (ACT)	Spatial resolution	Detector size, SNR, ACT oversampling, integration time
Integrated energy	>70% in 1.0×1.0 SSD >90% in 1.5×1.5 SSD	Spatial resolution	Optical quality, slit width, polarisation scrambler
Spatial coregistration - Intra-band (NIR, SWIR) - Inter-band (NIR vs. SWIR)	15% of ACT SSD 30% of ACT SSD	Scene topography, non-uniform scenes	Optical quality (keystone), ACT oversampling
Radiometric			
SNR@ L_{ref}	NIR: >150 SWIR1: >160 SWIR2: >130	Retrieval precision	Pupil size, mass and volume
Absolute radiometric accuracy	<3% (all bands)	Retrieval accuracy (surface albedo)	On-ground and inflight radiometric calibration
Relative spatial radiometric accuracy (RxRA)	<0.5%	Retrieval accuracy (bias) and precision	Straylight, Sun diffusor, detection linearity
Relative spectral radiometric accuracy (RlRA)	<0.5%	Retrieval accuracy (bias) and precision	Straylight, polarisation scrambler, Sun diffuser, detection linearity
Effective spectral radiometric accuracy	<0.1% (CO_2) <0.14% (CH_4)	Retrieval accuracy (bias) and precision	Straylight, polarisation scrambler, Sun diffuser, detection linearity
Zero-level offset	NIR: <0.15% SWIR1: <0.50% SWIR2: <0.30%	Retrieval accuracy (bias)	Detector temperature, thermal stability
Polarisation sensitivity	<0.5% (all bands)	Retrieval accuracy (bias) and precision	Polarisation scrambler, diffraction grating
Straylight sensitivity at 5 SSD from contrast transition after correction	1% over cloud contrast scene	Retrieval accuracy (bias) and precision	Surface roughness, cleanliness, baffling
Spectral			
Spectral range	NIR: 747–773 nm SWIR1: 1590–1675 nm SWIR2: 1925–2095 nm	Product coverage	Detector size, spectral FOV
Spectral resolution (SR)	NIR: <0.10 nm SWIR1: <0.30 nm SWIR2: <0.55 nm	Retrieval accuracy, spectral re-sampling	Diffraction grating (dispersion), focal length
Spectral Sampling Ratio	>3 in all bands	Spectral re-sampling	Diffraction grating (dispersion), pixel size
Instrument Spectral Response Function (ISRF) shape knowledge	<2% in flight	Retrieval accuracy, non-uniform scenes	On-ground calibration, mechanical stability, slit homogeniser
Spectral channel knowledge	NIR: <0.002 nm SWIR-1: <0.005 nm SWIR-2: <0.009 nm (<5% of spectral sampling interval)	Retrieval accuracy	On-ground calibration, Level-1b processor

Requirement	Value	Driver	Impact
Spectral continued			
Spectral channel stability over one orbit	NIR: <0.010 nm SWIR-1: <0.025 nm SWOR-2: <0.045 nm	Retrieval accuracy	Mechanical stability
Spectral coregistration	NIR: <10% SSI SW1: <30% SSI SW1: <10% SSI	ISRF stability, ACT non-uniform scenes	Optical quality (smile distortion)

Table 5.3 (cont.)

generated. In contrast to the standard Level-1 product described above, these data are not binned spatially, but spectrally over specified spectral intervals. They represent spectrally-averaged reflectance measurements at sub-sample spatial resolution. The high sampling in the ACT direction (200–300 m) allows for identification and correction of non-uniform scene effects in the Level-1b data.

The instrument operates in three main observation modes: The nadir mode described above, the sunglint mode in which the FOV is directed near the area of specular reflection over oceans, and the Sun-calibration mode, in which observations of extra-terrestrial Sun-spectral irradiance are performed. The number of electrons detected in the focal plane of the instrument is transformed via the radiometric calibration key data into spectral radiance for observations in nadir and sunglint mode, or into solar irradiance for Sun measurements. From these measurements the corresponding Earth reflectance in the spatial sample is derived (eq. 4.1).

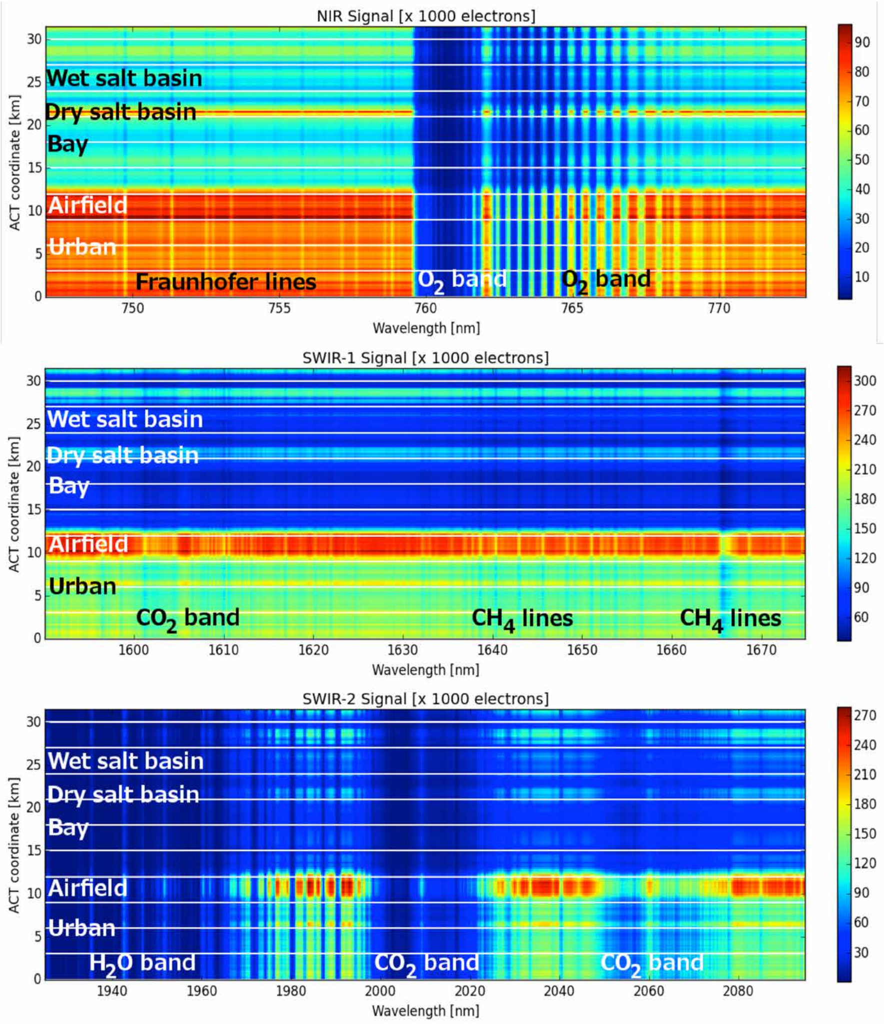

Figure 5.14. Signal acquired by the GHGIS instrument, as simulated from the AVIRIS reflectance measurements shown in Fig. 5.13. The three plots show the number of electrons detected in the observed spectral bands for a part of the swath covering 10 spatial samples (30 km ACT by 2 km ALT). The spectral structure of the signal (horizontal axis) is characterised by the absorption features of the atmospheric molecular species, as well as solar Fraunhofer lines. In the spatial direction (vertical axis), the albedo contrast from the various terrain types is clearly visible. The horizontal white lines indicate the binning windows for spatial co-adding. (ESA)

5.3.3.3 Observational requirements

The key Level-1b observational requirements driving the design of the GHGIS instrument are summarised in Table 5.3. The table also indicates for each specification the scientific requirement from which it is derived, as well as the system components or performance figures it drives.

5.3.3.3.1 Geometric requirements

Spatial coverage and sampling

A key feature of the CarbonSat mission is a relatively large swath width in combination with high spatial sampling and resolution. The coverage performance is reported in Subsection 5.2.1. The images will be constituted of rectangular spatial samples, each with an area of 6 km^2 and an aspect ratio of 3×2 km.

System integrated energy

Within these rectangular samples, the enclosed energy (fraction of energy coming from within the rectangle), referred to as the System Integrated Energy (SIE), is required to be larger than 70%. This requirement imposes a high imaging quality on the telescope and the spectrometer optics, a relatively narrow slit width and low detector crosstalk. Together with the sampling, the SIE determines the spatial resolution of the instrument.

Spatial coregistration

For an adequate retrieval of the data products it is essential that the photons detected in different spectral channels (sampled wavelengths) originate from the same location on Earth, within the limits defined by the spatial coregistration requirements. Table 5.4 summarises the coregistration requirements between spatial samples from different spectral bands (inter-band) and within one band (intra-band). The maximum tolerable displacement between the spatial samples corresponding to two spectral channels in the NIR and the SWIR bands is specified to be 15% of the ACT SSD. This value, which corresponds to just 450 m on the ground, includes the intra-band coregistration of the NIR and each of the two SWIR bands. The inter-band coregistration between the two SWIR bands is relaxed to 30% SSD (or 900 m). The requirement allows for partitioning the budget between intra-band effects (like keystone distortion) and inter-band errors (like detector misalignment).

The stringent coregistration requirements favour concepts with a common entrance slit for the three spectrometers and drive the instrument design to high mechanical stability and low image distortion (keystone). Alternatively, special binning strategies can be implemented, which co-align the spatial samples by adapting the ACT binning window along the spectral direction. This approach, which takes advantage of high ACT oversampling, is facilitated by large detector arrays.

Table 5.4. Spatial inter-channel coregistration expressed as fraction of the across-track SSD (along-diagonal: intra-band; across-diagonal: inter-band).

	NIR	SWIR-1	SWIR-2
NIR	0.15	0.15	0.15
SWIR-1		0.15	0.30
SWIR-2			0.15

5.3.3.3.2 Spectral requirements

Spectral coverage and resolution

The GHGIS requirements regarding spectral resolution (SR), spectral sampling interval (SSI) and SNR are shown in Table 5.3. The NIR band requires the highest spectral resolution (0.1 nm) because of the necessity to resolve solar Fraunhofer lines in the continuum region (for SIF correction) and the structure of the O_2-A-band for determining cirrus-cloud heights and optical depth. The required spectral resolution is lower (0.3 nm) in the SWIR-1 band, which contains the sharp, distinct absorption lines of CH_4 from which the methane products are derived, as well as a weak CO_2 band. The SWIR-2 band covers the two strongest CO_2 bands as well as a saturated H_2O band. Because of the strong absorption, this band requires the lowest resolution of 0.55 nm, but features a challenging bandwidth of 170 nm.

The requirements in Table 5.3 drive important design parameters of the spectrometer concepts. Spectral coverage and sampling impose the required number of detector pixels in spectral direction, and the spectral resolution drives the dispersion power of the gratings and focal lengths of spectrometer components.

Instrument spectral response function

The Instrument Spectral Response Function (ISRF) is determined by the entrance slit width, the spectrometer optical quality and the detector pixel size. For uniform illumination of the entrance slit, it can be calculated as a convolution of the entrance slit image (in ALT direction) with the spectrometer PSF (imaging quality) and the detector Point-Spread-Function (PSF) (detector pixel size and cross talk):

$$ISRF(\lambda_0, \lambda) = Slit(\lambda_0, \lambda) \otimes PSF_{spec}(\lambda_0, \lambda) \otimes PSF_{\mathrm{det}}(\lambda_0, \lambda) \tag{5.1}$$

Because of its fundamental importance, the ISRF will be characterised on the ground for each ACT FOV at various wavelengths, which is a time-consuming process. However, the ISRFs will change in flight owing to launch effects, gravity release and thermoelastic deformations caused by temperature variations in the instrument. Also, the natural spatial non-uniformity of the observed scene results in non-homogeneous illumination of the entrance slit, which alters the spectral shape of the ISRF in a pseudo-random manner. In order to constrain such variations, the spectral requirements are applicable over specified non-uniform scenes. Taking into account all error contributors described above, the inflight knowledge of the ISRF has to be better than 2% of its peak value over its full width (down to 1% of the peak), and the stability over non-uniform scenes better than 1%. These requirements demand a highly stable opto-mechanical structure, accurate on-ground and inflight calibrations as well as strategies to mitigate the sensitivity to scene non-uniformity.

The inflight calibration concepts are described in Subsection 5.3.3.4. A hardware solution mitigating the impact of scene non-uniformity consists in the implementation of a slit-homogeniser instead of a conventional entrance slit, which is the baseline of both concepts and will be elaborated in the description of the related subsystem.

Spectral knowledge, stability and coregistration

A slit-homogeniser device also mitigates variation in the spectral scale induced by non-uniform scenes, which makes it easier to comply with the spectral knowledge requirement, specified to be 5% of an SSI, equivalent to the spectral range covered by a single spectral pixel). In previous missions (e.g. OMI, GOME-2) similar accuracies were achieved by applying spectral shift correction of the measured spectra performed on the ground as part of the Level-1b processing. In order to ensure the performance of such correction schemes, it is necessary to impose requirements on inflight spectral stability. This specification allows for total amplitude of the spectral error, up to 25% of the SSI and 10% after removal of the mean spectral error (additive shift) over the band. The requirement translates into stringent instrument specifications, calling for a thermally and mechanically stable design.

In addition, spectral coregistration requirements have been derived in the course of the instrument studies. These specifications aim to constrain error contributions of ACT spatial scene non-uniformity (along the swath), which are not mitigated by the slit homogeniser (SH). When analysing realistic scenes (based on AVIRIS scenes as depicted in Fig. 5.14), it was found that the spectral coregistration generated by the curvature of a monochromatic line in the detector plane needs to be lower than 10% of a detector pixel (SSI) across each ACT spatial sample. This represents a demanding design specification for the image quality of the spectrometers, necessitating correction by optical elements (e.g. prisms).

5.3.3.3.3 Radiometric requirements

Signal-to-noise ratio

A fundamental specification for sizing the instrument is the required SNR, which is determined by retrieval simulation for various geophysical scenarios. Therefore, the SNR needs to be specified over the wide dynamic range of the instrument. The specification is formulated by equations yielding the required SNR as a function of input signal. The values reported in Table 5.3 represent the required SNR for given reference radiance levels (L_{ref}), which correspond to the maximum radiance (continuum level without molecular absorption) of a high-latitude scenario over low albedo (dark vegetation).

Various noise sources contribute to the total noise of GHGIS measurements. Shot noise originating from the discrete nature of light and charge is generated by the useful signal, as well as by straylight, thermal background radiation and dark current. Cooling the optics and detectors, respectively, controls the latter two noise contributors. The required temperature depends on the detector technology. Mercury-Cadmium-Telluride (MCT) devices, which are the baseline in the SWIR bands, typically need to be cooled down to temperatures around 150K. They also exhibit significant read-out noise, which tends to dominate their noise characteristic in the SWIR spectral range. Charge Coupled Device (CCD) arrays have lower dark current and can be operated at higher temperatures (~250K), but generate a smear signal during frame transfer, which adds to the total noise. Radiometric performance models, which establish a noise budget taking into account all relevant sources, were used to derive important instrument parameters such as entrance pupil size and operating temperatures.

Zero-level-offset

Another performance parameter driving the thermal concept of the GHGIS instrument is the zero-level-offset (ZLO) in darkness. Because of the impact of additive offsets in the measured radiance spectra on the Level-2 retrieval, temporal variations of detector dark current and thermal background radiation of the optics need to be constrained. The stringent specification for the residual offset after correction of 0.15–0.5% of the dynamic range minimum (see Table 5.3) enforces low and stable detector temperatures and cooled optics in the SWIR bands. It also requires correction schemes making use of dedicated dark-current measurements acquired over complete orbits, with the instrument shutter closed and continuous monitoring of the detector temperatures.

Absolute radiometric accuracy

The absolute radiometric accuracy (ARA) required for CarbonSat is mainly driven by the necessity to determine the surface albedo of the measured spatial sample. In order to retrieve this important parameter, ARA of the measured reflectance has to be better than 3% in all the spectral bands. This level of absolute accuracy calls for an extensive on-ground calibration as well as regular inflight calibration measurements. The instrument must be accurately characterised on the ground in terms of the Bidirectional Reflectance Distribution Function (BRDF) of the Sun diffuser, which establishes the onboard calibration standard for reflectance. In addition, pixel-to-pixel variations of the detector gain (Pixel Response Non-Uniformity, PRNU) will be monitored in flight by means of a white light source, e.g. a tungsten filament lamp.

Relative radiometric accuracies

The relative radiometric accuracy requirements, both in the spectral and spatial domains, are potentially more demanding than ARA. The signal changes between reflectance spectra measured over areas with elevated CO_2 concentration versus those over average background concentrations rarely exceed the 1–2% level, even in the strong absorption bands. Such considerations underscore the very high relative radiometric accuracy required to resolve the subtle spectral signal changes associated with variations of greenhouse-gas concentrations. The relative spectral and spatial radiometric errors, over an entire spectral band and the ACT field-of view respectively, are therefore constrained to below 0.5%.

The requirement for ESRA was introduced in Chapter 4. The two ESRA values for CO_2 and CH_4 are directly linked to a corresponding error in column-averaged dry mixing ratio. The requirement is formulated in terms of a maximum limit to these values: The maximum tolerable value for $ESRA_{XCO2}$ is 0.10%, corresponding to a systematic Level-2 error of 0.4 ppm XCO_2, and the required $ESRA_{XCH4}$ of 0.24% corresponds to a maximum XCH_4 error of 4.0 ppb.

While the requirements quoted in the previous paragraph only constrain the amplitude of relative radiometric errors, the ESRA requirement also accounts for the spectral correlation of the reflectance errors with the atmospheric absorption features. For the error analysis this means that the spectral dependence of the error sources, such as straylight, polarisation scrambler spectral features, diffuser speckles and detector non-linearity, need to be accurately modelled. The instrument design needs to carefully consider these error sources, minimising the generation of spectral features. In particular, this necessitates significant efforts for straylight reduction (cleanliness and super-polished surfaces), low-polarisation sensitivity (grating and scrambler design), and low-speckle design of Sun diffusers.

Straylight sensitivity

Another source of radiometric error is detection of light that does not originate from the location and wavelength that a detector pixel is associated with. Straylight is caused by unwanted imaging and scattering at various instrument elements (optical surfaces, contaminants, mounts, internal baffles, higher-order diffraction, etc.). Ghost images are generated by multiple reflections from optical and detector surfaces. The magnitude of scattered straylight depends on the roughness and particle contamination of the lens and mirror surfaces. The distribution of ghost and diffuse straylight in the focal plane also depends on the intensity of the incident radiation, as natural variability limits the accuracy of straylight correction schemes.

The requirement for the maximum tolerable straylight level (1% of the minimum spectral radiance) aims to limit its contribution to absolute and relative radiometric errors through the hardware design. It enforces careful design, avoiding ghosts by baffling and reducing scatter by use of very smooth optical surfaces. It also imposes very high levels of cleanliness, with the levels proposed for Concept A to be extremely high, during assembly, integration and testing (AIT) to avoid contamination.

The straylight performance of the two optical designs was simulated for a ground scene characterised by a sudden transition from a dark and a bright reference spectrum. Numerical analysis was performed to estimate the spurious signals from misdirected light in the instrument. From these analyses, specifications for surface roughness and cleanliness were derived, and the required reduction factors to be achieved by straylight correction algorithms in ground processing were established. The straylight performance and the impact on absolute and relative radiometric errors (in particular ESRA) are reported in Section 7.2.

Polarisation sensitivity

Grating spectrometers generally exhibit a dependence of their radiometric response to the polarisation state of the incident radiation. The processes determining the polarisation of the spectral radiance and the necessity to mitigate its impact were outlined in Subsection 4.5.3.

In principle there are several strategies to deal with radiometric errors over polarised scenes: Simultaneous measurement of the polarisation state and correction of the detected signal were attempted for SCIAMACHY. The OCO-2 mission avoids changes in polarisation by keeping the instrument FOV perpendicular to the Sun scatter direction by a continuous yaw manoeuvre along the orbit. In order to maximise the spatial coverage and make use of the instrument's full swath at any orbital position, the CarbonSat instrument demands low-polarisation sensitivity by design. The requirement establishes an upper limit to the instrument polarisation sensitivity, as defined by eq. 4.3 in Subsection 4.5.3, of 0.5% in each spectral band assuming a spectrally constant polarisation angle. Such a low value requires a hardware solution by means of a pseudo-depolariser, also called a polarisation scrambler. Details about the polarisation scrambler devices developed for the instrument concepts are presented in Subsection 5.3.3.4.

5.3.3.4 Instrument subsystem descriptions

5.3.3.4.1 Optical concepts

Concept A

A functional block diagram of Concept A is depicted in Fig. 5.15 and a sketch of the optical layout is shown in Fig. 5.16. The first optical element is a Dual-Babinet scrambler for reduction of polarisation sensitivity. Through this scrambler, the ground scene is observed using a four-mirror telescope made of Silicon Carbide (SiC). It features a focal length of 95 mm and an equivalent circular pupil diameter of 28 mm, which is fully exploited by the two SWIR spectrometers and partly (21 mm) by the NIR spectrometer. The telescope folds the beam by 90° into the plane of the main optical bench and images the scene onto the entrance of the SH. This device constitutes the common entrance slit (length: 28.8 mm, width: 108 mm) for the three spectrometers, which is beneficial for spatial coregistration between the spectral bands. The SH requires that the telescope introduces an astigmatism, focusing the light at the SH entrance in ALT direction and at the SH exit in ACT direction. This way, the radiometric non-uniformity in ALT direction, is scrambled by multiple reflections, while the intensity pattern in ACT direction is maintained. The first spectral split is performed in the divergent beam leaving the SH by a dichroic mirror. It reflects the NIR band perpendicularly out of the plane, passing the beam through the main optical bench. The SWIR beam transmitted by the dichroic mirror passes through a refractive collimator made of silicon and ZnSe elements which is common for the two SWIR spectrometers. The collimated beam is then further split between the SWIR-1 and SWIR-2 bands by the second dichroic filter. The two SWIR spectrometers have a quasi-identical optical setup and are symmetrically arranged in one SWIR assembly. After passing the SWIR collimator (136 mm focal length) the light is dispersed by silicon-immersed gratings working in reflection. The two gratings operating on third and fourth diffraction order for the SWIR-1 and SWIR-2, respectively, provide high angular dispersion owing to the large refractive index of silicon. A wedged prism is placed behind each SWIR grating to correct for smile distortion (curvature of the slit image on the spectrometer focal). The two SWIR cameras with f-number of 1.4 and 1.6 in ALT and ACT direction, respectively, image the slit with a demagnification of about 0.5. They incorporate silicon, ZnSe and fused-silica lenses, as well as dedicated band pass filters, which reduce the sensitivity

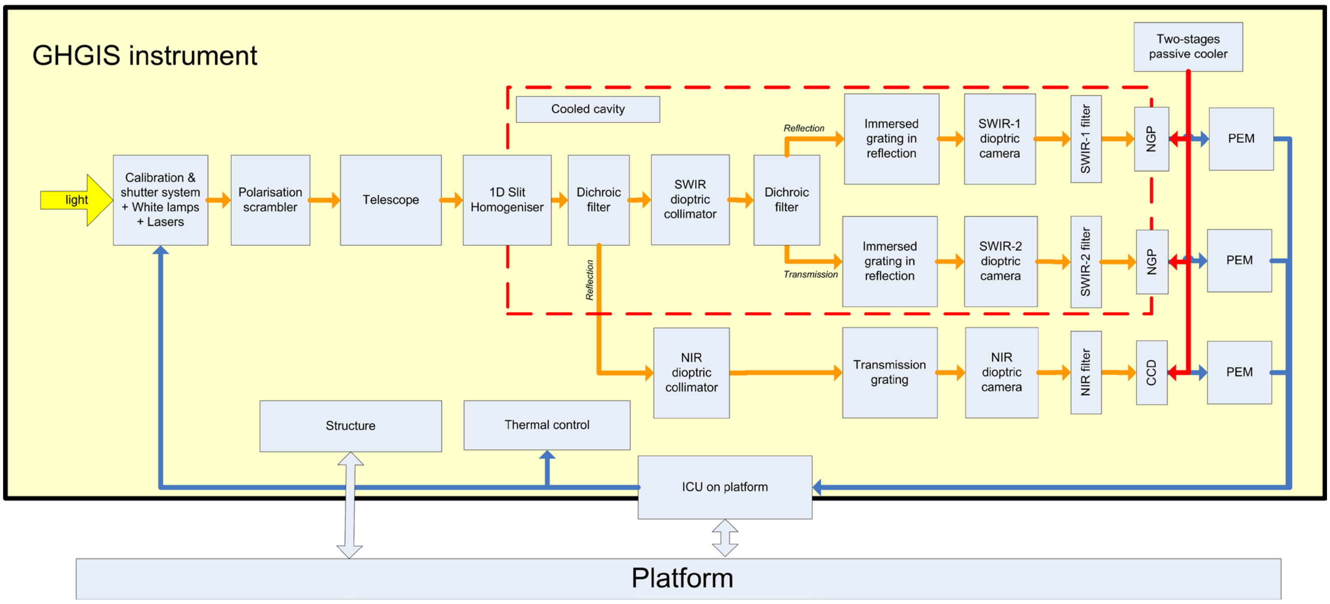

Figure 5.15. Concept A instrument block diagram. (Airbus Defence and Space)

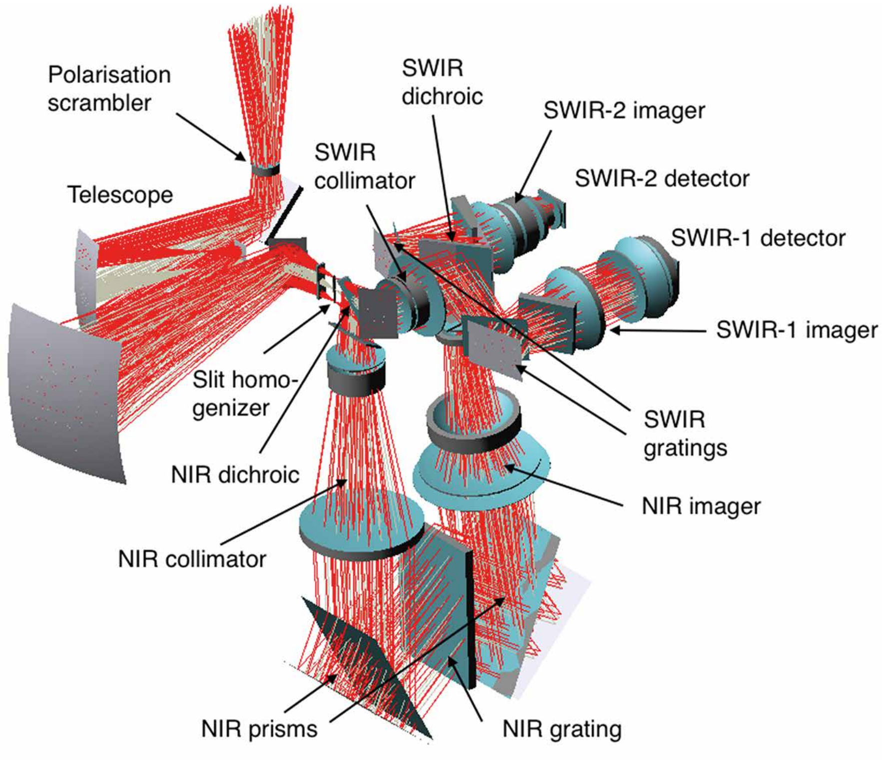

Figure 5.16. Concept A optical design. The nadir view direction is upward in this drawing. The front telescope features a polarisation scrambler near the entrance pupil and projects the ground scene via two out-of-plane reflections onto the slit homogeniser. The emerging divergent beam is then spectrally split by a dichroic mirror, reflecting wavelengths <800 nm out of the plane into the NIR spectrometer (lower part) and transmitting the longer wavelengths into the SWIR assembly. The latter features a common collimator for both SWIR bands, which are separated by another dichroic. (Airbus Defence and Space)

to out-of-band straylight. The dispersed slit image is finally detected in each SWIR band by a MCT array detector with format 1024×1024 pixels.

In the NIR spectrometer a collimator with a focal length of 340 mm is used. The parallel beam is then folded by 90° via a prism, which directs it to the transmission grating. After passing the grating the dispersed light is folded back by an identical prism before entering the imager (focal length 230 mm and de-magnification 0.66), which incorporates a spectral filter for straylight reduction. In addition to the beam folding, the prisms correct for smile distortion to comply with the spectral coregistration requirement. The NIR detection chain is based on a CCD detector, which is described in more detail in the section on the focal plane architecture.

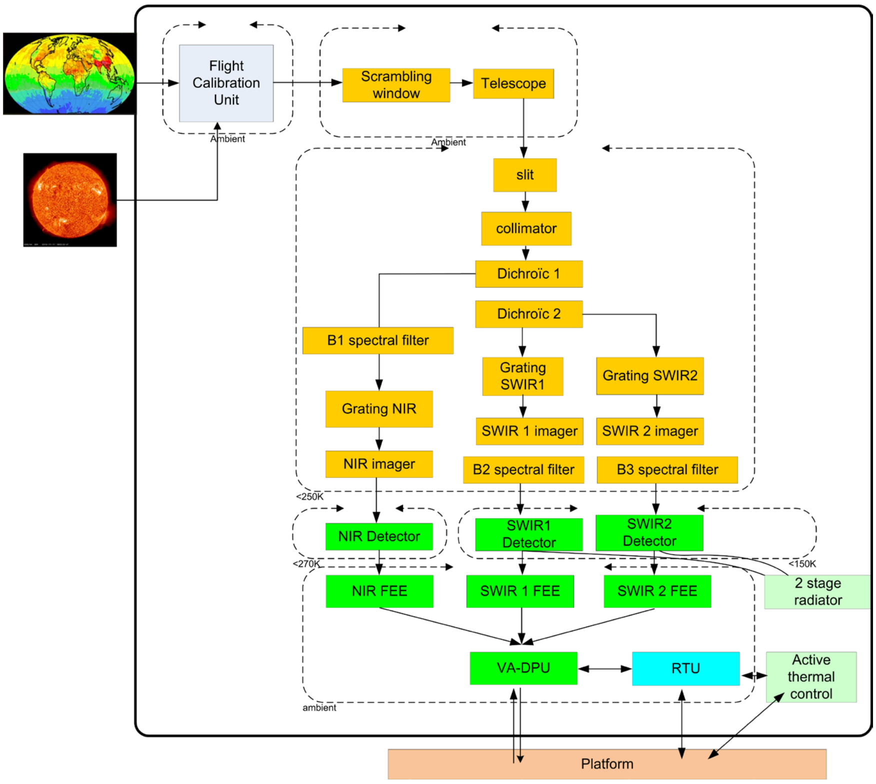

Figure 5.17. Concept B instrument block diagram. (OHB/TAS-F)

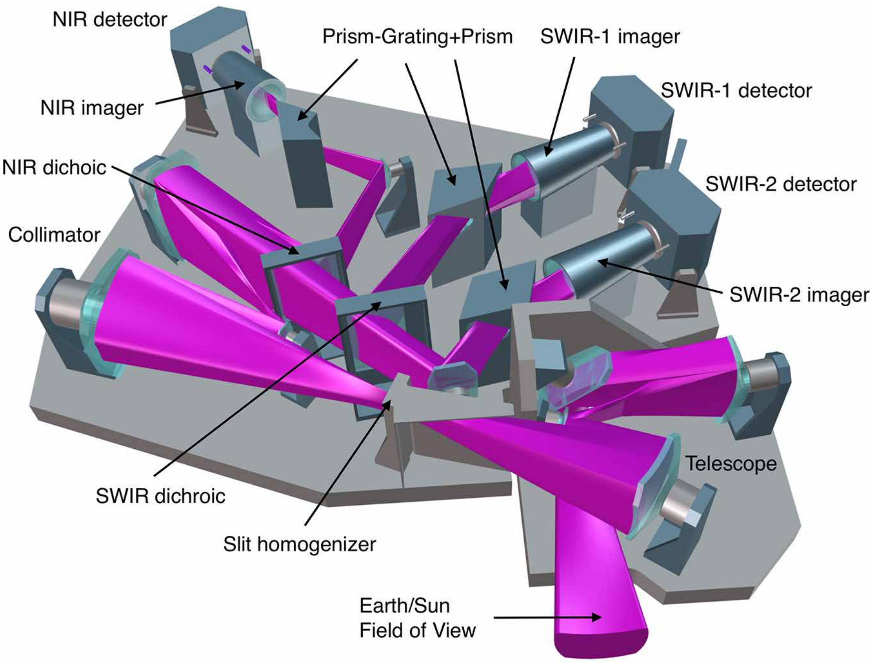

Figure 5.18. Optical layout of Concept B. The TMA telescope images the scene onto the slit homogeniser. A common reflective collimator generates a parallel beam, from which two dichroic beam splitters separate the NIR and SWIR-2 bands. Three assemblies composed of a PG+P combination disperse the light before the imager focuses it onto the detectors. (OHB/TAS-F)

The SWIR optics module is operated at a temperature of 210 K, while the SWIR detectors are cooled down to 150K and stabilised to within 50 mK. The NIR optical module is maintained at ambient temperature (293 K) with the exception of the NIR CCD detector, which is integrated into the SWIR assembly to make use of its cooling system and operates at 220 K. The system features an inflight calibration unit.

Concept B

A functional block diagram of Concept B is depicted in Fig. 5.17 and a sketch of the optical layout is shown in Fig. 5.18. As in Concept A, the calibration unit is placed before the polarisation scrambler at the entrance of the telescope.

The instrument features a three-mirror anastigmat (TMA) telescope with two additional folding mirrors as the common telescope (117 mm focal length) for all three bands. The first optical element at its elliptical entrance pupil of 29 mm equivalent circular diameter is a polarisation scrambler. The telescope images the ground scene onto the entrance of an SH device (length: 38 mm, width: 118 µm) with the required astigmatism. After several reflections within the SH, reducing scene non-uniformities across the slit, the exiting divergent beam is collimated by another TMA with a focal length of 232 mm. This reflective collimator is telecentric at the slit interface and shared between the three subsequent spectrometers. Further along the optical path, two dichroic filters successively reflect the NIR and the SWIR-1 bands from the collimated beam, while transmitting the SWIR-2 band. The general layout of the dispersers is identical between the three bands and implements a prism-grating+prism (PG+P) combination with a transmission grating bonded on the exit surface of the first prism. The second prism following the grating after an air-gap is tilted and sized to minimise the smile distortion, in order to comply with spectral coregistration requirement. The PG+P devices are all operated in first diffraction order but feature different grating parameters and prism geometries for each band, adapted to the spectral bandwidth and resolution requirements. The two SWIR imagers with f-number 1.5 (each with 88.4 mm focal length) focus the dispersed slit image onto the detector arrays with demagnification of 0.36 and 0.38 in spectral and spatial direction, respectively. They are quasi-identical for the two SWIR bands and consist of five silicon lenses, polished to very low surface roughness for straylight reduction. The four-lens NIR imager with 76.6 mm focal length is based on low index glass to intrinsically reduce straylight. In the two SWIR bands, a spectral filter is placed between the imagers and the detectors to reduce out-of-band straylight and reject thermal background radiation from the spectrometer optics emitted at its operational temperature of 250 K. These multilayer-coated filters are cooled down to 200 K, so that their own thermal emission is negligible.

The NIR spectrometer implements a reduced entrance pupil of 11 mm and the spectra will be recorded by a CCD at <240K and in the SWIR bands by MCT array detectors operated <150 K. The three Front-End-Electronics (FEE) units for each detector transmit the data to the video acquisition and data processing unit (VA-DPU), which performs the spatial binning and transmits the data to the platform data handling system. The detectors and VA-DPU are described in further detail in the corresponding subsystem sections below.

5.3.3.4.2 Optical subsystems

Polarisation scrambler

In both concepts the first element in the optical chain of the GHGIS instrument is a pseudo-depolariser, more commonly referred to as a polarisation scrambler. The purpose of this is to reduce the degree of polarisation (DOP) of the incoming radiation from nadir and sunglint observations, thus minimising radiometric errors owing to polarisation sensitivity of the optical components. Polarisation scramblers are composed of wedges of a birefringent crystal, e.g. quartz, arranged in pairs in such a way that the resulting component is chromatically corrected. As the light passes through the device, it introduces polarisation dependent phase delays that vary over the pupil, effectively reducing the DOP of the light entering the telescope. A standard Dual-Babinet polarisation scrambler is schematically depicted in Fig. 5.19.

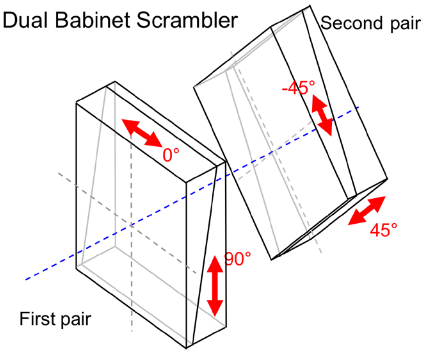

Figure 5.19. A typical Dual-Babinet scrambler. (Airbus Defence and Space)

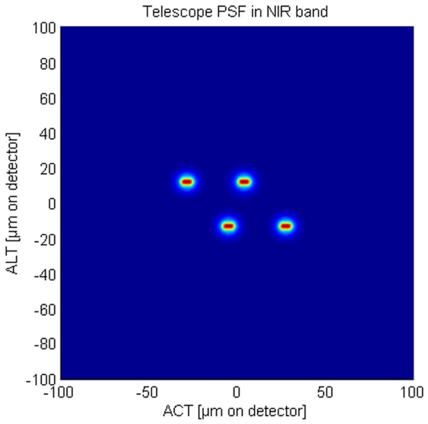

Figure 5.20. The PSF of the combined telescope and polarisation scrambler assembly of Concept B for the NIR band. (OHB/TAS-F)

An inevitable side effect of the depolarisation is an angular split and separation of the passing light into several beams. This gives rise to a spot pattern at the focal plane for any point on the ground that is detrimental to the geometric performances of the instrument. As an example, the telescope PSF resulting from the scrambler spot patterns of Concept B is shown in Fig. 5.20. The de-polarisation power of a scrambler can be adjusted by the wedge angles, so the larger the wedge angles the greater the de-polarisation. However, the wider the separation of the spot pattern (stronger polarisation scrambling) the greater the detrimental effect on geometric performances. Therefore the scrambler design and, in particular, the sizing of the wedge angles is a result of a trade-off between the conflicting requirements of polarisation sensitivity and ESRA on one hand, and spatial-coregistration and SIE on the other.

Both instrument concepts have optimised their scrambler design taking into account the polarisation sensitivity of the subassemblies (e.g. the diffraction gratings) and the optical quality (e.g. keystone distortion). The wedge angles have been determined so as to provide sufficient de-polarisation to meet the corresponding sensitivity requirements, while limiting the variation of the spot pattern barycentre to meet the coregistration requirement.

Slit-homogeniser

Owing to natural albedo variations of the ground scenes observed by the GHGIS instrument, the entrance slit is never homogeneously illuminated. The non-uniform illumination across the slit (in ALT direction) gives rise to a distortion of the ISRF, which varies quasi-randomly over the scene. In order to meet the stringent requirement on inflight knowledge of the ISRF shape, both concepts implement a hardware solution based on an SH device. It is schematically depicted in Fig. 5.21 and can be described as a 3D entrance slit, whose edges are formed by two parallel mirror surfaces facing each other. The slit width is defined by the distance between the mirrors, and the swath width by the length of the SH assembly. The difference in a conventional slit is that the SH functions as a waveguide along the optical axis. On its passage through the SH, the light experiences multiple reflections in across-slit direction. These reflections and coherent interference of the wavefronts result in a re-distribution of energy across the slit, which effectively scrambles the radiometric non-uniformity. In order to preserve the spatial radiometric information in ACT direction, the telescope images the ground scene onto the SH with a dedicated astigmatism, placing the ALT focus at the entrance and the ACT focus at the exit plane of the device. The SH is a relatively new component for use in space missions, and is currently being developed as the baseline solution for the Sentinel-5 mission.

Both concepts initiated pre-development activities for an SH device with the aim of optimising design parameters (e.g. the SH depth along the optical axis), as well as verifying experimentally the performance in terms of ISRF stability over spatially non-uniform scenes. In parallel, performance models were developed, which fully account for wave propagation and interference

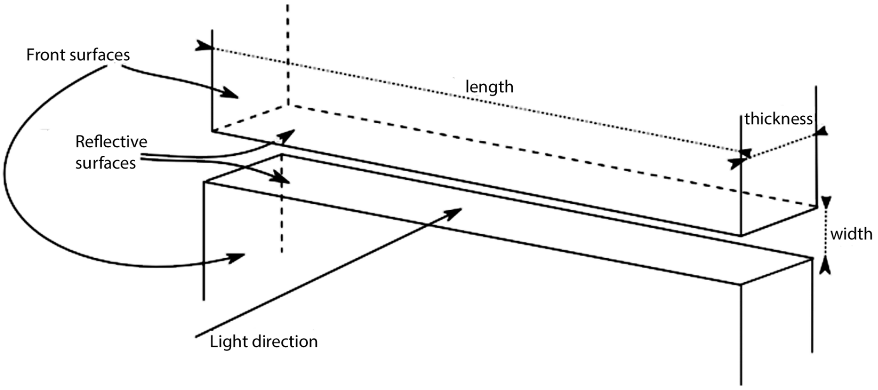

Figure 5.21. Example of 3D slit. (OHB/TAS-F)

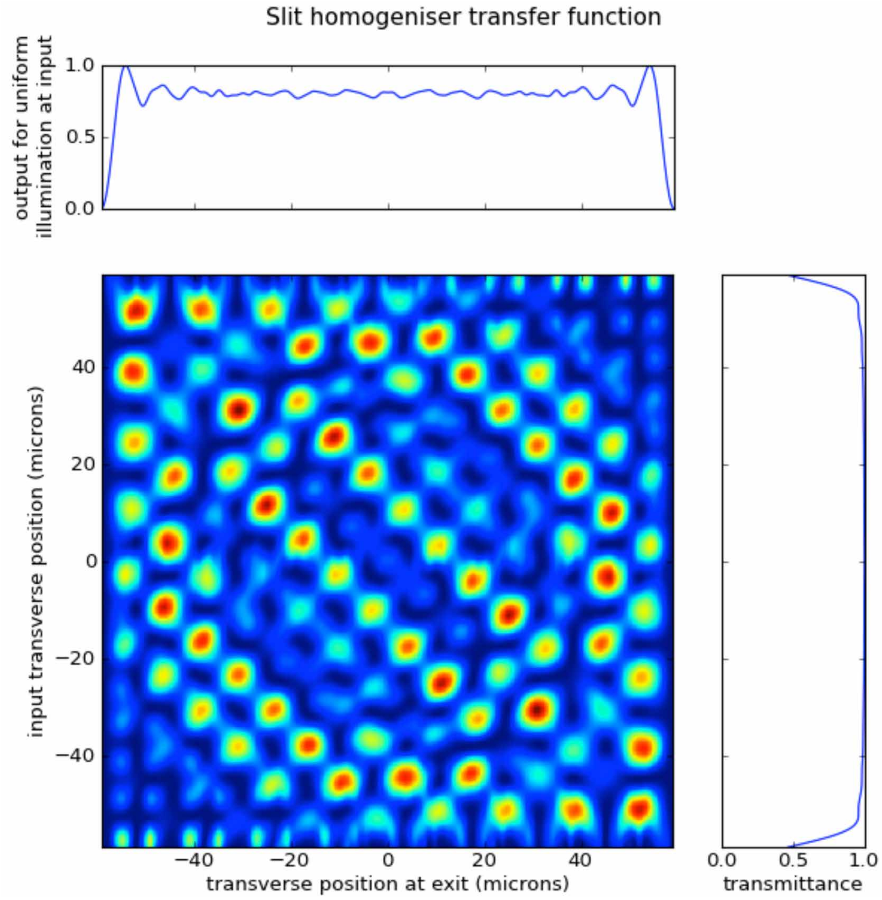

Figure 5.22 Transfer function of the SH of Concept A (SWIR-2 centre wavelength). The function describes the response of the SH device to elementary stimuli at any position across the slit opening. (Airbus Defence and Space)

effects within the device. An important intermediate result of these models are the 'transfer matrices', which describe the distribution of light across the SH exit as a function of the position of the input source at the entrance plane. As an example, Fig. 5.22 shows the transfer matrix of Concept A for the centre wavelength of the SWIR-2 band. Once this matrix is derived for a given wavelength, the stabilised ISRF can be computed for uniform and non-uniform scenes and the performance of the SH device be assessed. The results of the numerical simulations, reported in Section 7.2, indicate that the SH ensures compliance to the ISRF stability requirement.

Diffraction gratings

The selection of the diffraction grating technology is a major design driver for the GHGIS instrument spectrometers. Thorough trade-off analyses have been performed for both concepts, resulting in similar solutions for the NIR, and fundamentally different approaches for the SWIR bands.

For the NIR spectrometer, Concept A implements a transmission grating based on photonic sub-micron structures. An effective-medium grating is created by etching a binary step structure of sub-wavelength dimensions into the surface of a fused-silica substrate. Fig. 5.23 shows such structures, which are generated by an electron-beam lithography process in combination with reactive-ion etching. The trenches and bars of the binary structure are covered by a conformal titanium dioxide over-coating applied by Atomic Layer Deposition (ALD). These binary transmission gratings are operated in Littrow configuration and characterised by very high diffraction efficiency and low polarisation sensitivity. The high spectral resolution required for CarbonSat's NIR spectrometer (0.1 nm) translates into a high grating frequency in the order of 2000 lines per millimetre and deep grating profiles with high aspect ratio (trench depth-to-width ratio) of about 7:1. While these are challenging values,

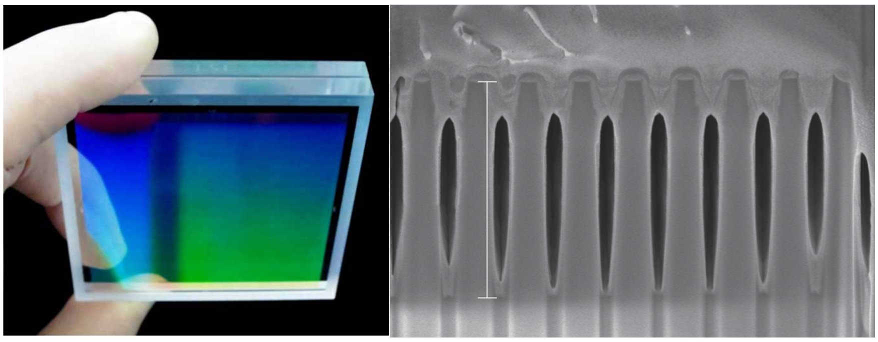

Figure 5.23. Transmission grating pre-development for the NIR spectrometer for Concept B. The photo on the left shows the grating substrate after a manual bonding test. The sub-micron binary surface structure generated by e-beam lithography and reactive-ion etching is visible in the Scanning Electron Microscope (SEM) image on the right. (OHB/TAS-F/IOF)

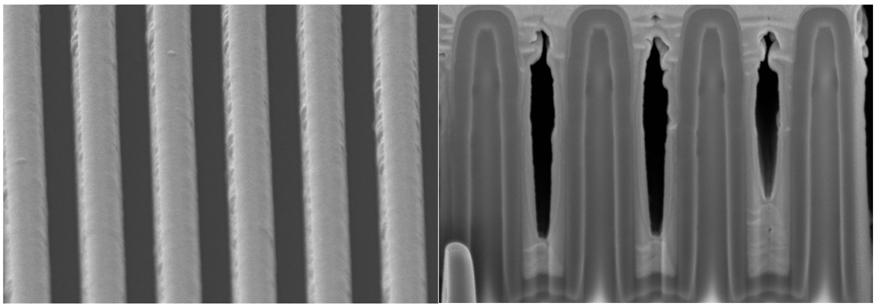

Figure 5.24. SEM images of a SWIR-1 test grating for Concept B. The left image shows the grating surface with an intact coating after thermal cycling. The right image is a cross-section through the grating profile. The multiple layers of the ALD-nano-laminate coating are visible. (OHB/TAS-F/IOF)

they are regarded as achievable, as was demonstrated by a breadboard for the FLEX mission featuring similar grating parameters.

The manufacturability of such gratings is also confirmed by the grating pre-development activities for Concept B, which deploys binary structure transmission gratings in all three spectrometers. The disperser configuration differs from Concept A, as the flat surface of the grating substrate is optically bonded to a fused-silica prism. A second prism, separated from the grating surface by an air gap, complements the disperser assembly. This PG+P assembly effectively acts as an immersed grating enhancing the angular dispersion. The prism angles are optimised for correcting keystone and smile distortions. Although PG+P assemblies are used in all three spectrometers of Concept B, the different spectral requirements give rise to very different grating parameters and coatings.

While Concept B uses photonic sub-micron structures for all three spectral bands, Concept A employs a different grating technology in the SWIR: silicon-immersed gratings disperse the light inside a silicon prism as shown in Fig. 5.25, left panel. When operated in near-Littrow configuration, the light enters this assembly through the prism surface opposite to the bonded substrate and is diffracted by total internal reflection at the silicon-air transition of the grating structure (Fig. 5.26, left). When exiting the prism, the light passes through the same surface again and is further dispersed by refraction. Such silicon-immersed gratings generate very high angular dispersion due to the diffraction inside the high-refractive index material combined with refraction at the exit surface. As a consequence, the size of the SWIR spectrometer is significantly reduced compared to concepts using conventional grating technology.

Such gratings have been developed for the Sentinel-5 Precursor mission. The manufacturing process is based on anisotropic etching in silicon, which generates facetted triangular structures on the surface of a substrate with low roughness and highly stable period (Fig. 5.25, right panel). The flat, polished side of the substrate is subsequently bonded to the surface of a monolithic, triangular silicon prism. Figure 5.25 shows the monolithic, triangular silicon prism used for the immersed gratings of the Sentinel-5 Precursor mission (left) and the grating substrate (right) being manufactured for the Sentinel-5 mission.

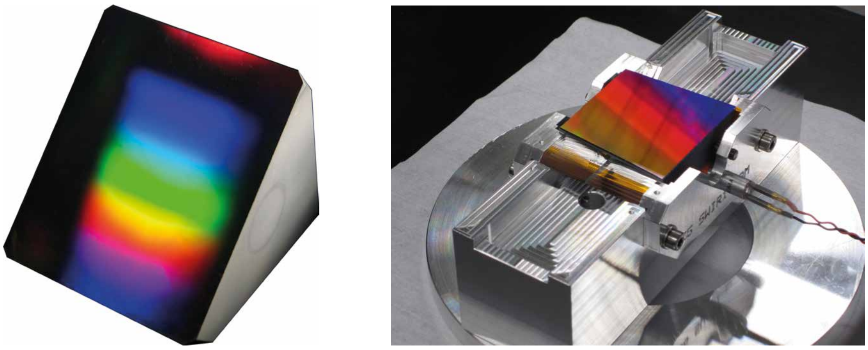

Figure 5.25. Left: monolithic, triangular silicon prism used for the immersed gratings of the Sentinel-5 Precursor mission. Right: silicon wafer of the grating substrate manufactured for the Sentinel-5 mission. The wafer will be bonded onto the large surface of a prism similar to that shown on the left. (Airbus Defence and Space/SRON)

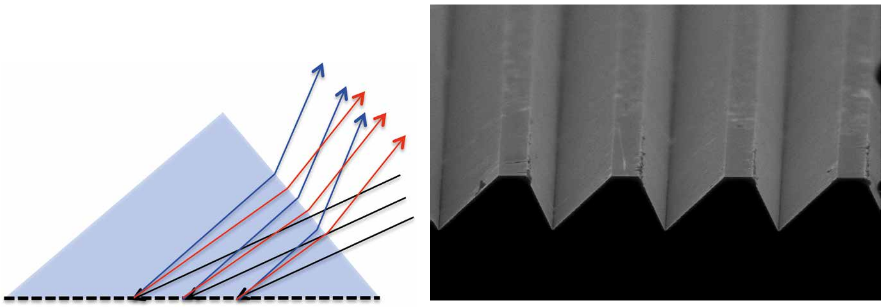

Figure 5.26. Left: principle of a silicon-immersed grating. Incident light (black) enters a silicon prism and is dispersed at the triangular grating profile etched into its large surface. The exiting light is further dispersed by refraction at the silicon-air transition. Right: SEM image of a typical grating profile. The periodic facetted structures are generated by anisotropic silicon-etching. (Airbus Defence and Space/SRON)

A pre-development activity to manufacture and characterise the immersed gratings for the SWIR-1 spectrometer of Concept A is ongoing.

Diffusers

The current knowledge concerning the impact of the Sun diffuser on the radiometric accuracy (diffusor speckles) has been judged to be unsatisfactory. Pre-development activities have been initiated to better quantify the effects and to optimise the approach of solar calibration. Parallel pre-development activities have been initiated that include the development of numerical models and measurements using various diffuser materials. The envisaged wavelength range of the measurements does not cover all CarbonSat bands, but in conjunction with the modelling activities will allow the estimation of the radiometric impact. The experimental characterisation and the numerical modelling are both challenging tasks, but results will potentially not only serve CarbonSat, but will also be useful in a wider context.

5.3.3.4.3 Mechanical and thermal architecture

The two instrument concepts significantly differ in the mounting geometry, which is largely driven by the choice of the satellite platform. In Concept A, which employs a recurrent platform (see Subsection 5.3.4), the instrument is accommodated on the nadir-pointing panel, being dedicated to the payload. The instrument baseplate is mounted at a cant angle of 25° to optimise the orientation to the Sun (Fig. 5.9). Concept B, in contrast, uses a custom platform, which allows the payload to be accommodated on the rear panel. One commonality for both concepts is that the thermal analysis and trade-offs resulted in passive-thermal concepts for cooling of the detector and optics. The mechanical and thermal architectures of the two concepts are described in more detail in the following.

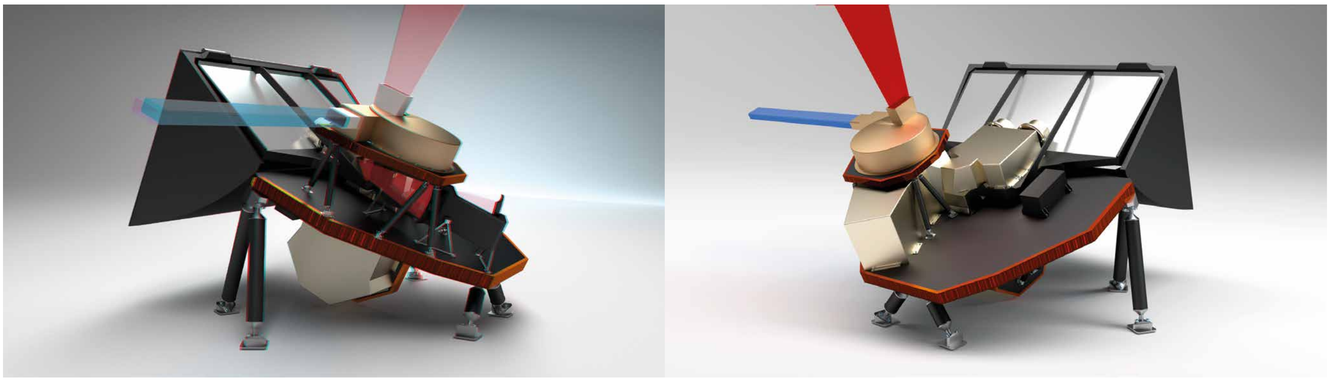

Figure 5.27. Mechanical layout and accommodation of Concept A (Earth FOV in red and solar FOV in blue). (Airbus Defence and Space)

Concept A

The instrument mechanical configuration of Concept A is built around the Main Instrument Baseplate (MIB), a sandwich panel made of carbon-fibre reinforced plastic (CFRP) isotropic skin and aluminium honeycomb as core material. On the nadir-pointing side, the MIB supports the telescope, the SWIR optics, focal planes, the FEE and the calibration mechanism. The NIR spectrometer is mounted on the opposite side between the baseplate and the platform, in the space opened by the tilt of the MIB with respect to the platform panel. It is fixed onto the platform with a cant angle of 25° via isostatic mounts.

The NIR and SWIR subassemblies are mounted on their individual optical benches made of CFRP honeycomb and SiC, respectively. Both are thermally and mechanically decoupled from the MIB by a set of bipods (CFRP with titanium end fittings). In order to limit thermoelastic stress on the dioptric subassemblies, the lenses of the collimators and cameras are accommodated in individual titanium barrel housings. These barrels are mounted onto the optical bench via isostatic bipods to minimise thermo-mechanical coupling. To provide a stable thermal environment for the optics, the instrument is completely protected with multilayer insulation (MLI) blankets.

The instrument is split into three main thermal cavities:

- the front cavity that includes the telescope, the calibration mechanism and the NIR optics, thermally controlled at about 293K

- the SWIR optics cavity, thermally controlled in the 210K temperature range with a stability of 100 mK over one orbit. The NIR CCD detector is also mounted inside the SWIR thermal cavity (through a hole in the optical bench) to take advantage of the operational temperature, which corresponds to the CCD detector temperature

- the SWIR detector-packages are thermally controlled in a narrow temperature range around 150 K

The passive cooling solution of Concept A employs a two-stage radiator accommodated inside the protecting baffle. The radiator is oriented away from the Sun and tilted to be tangential to Earth in order to avoid any direct coupling with Earth's albedo. During the pitch manoeuvre performed in sunglint mode, however, Earth may come into the FOV of the radiator, temporarily degrading the cooling performance, but staying within the required performance. The baffle architecture of the thermal system is similar to that of the Sentinel-5 Precursor instrument. A shutter is foreseen to protect the radiator during the Launch and Early Orbit Phase (LEOP).

The overall dimensions of the complete instrument are 1265 mm, 1240 mm, and 900 mm in length, width and height, respectively.

Concept B

The mechanical architecture of Concept B is based on the following elements:

- an instrument base structure to accommodate the whole instrument on the platform
- two separate optical benches for the telescope and spectrometers, fixed on the instrument structure by isostatic mounts
- a secondary structure to support the sunshield baffle

The instrument main panel is a sandwiched aluminium honeycomb structure with CFRP skin, which is mounted on the platform via CFRP bipods with titanium end fittings. The closure panels stiffen the structure and serve as radiators for dissipating components (e.g. proximity electronics). Via three bipods the instrument panel supports the spectrometer optical bench, which is manufactured from ceramic material (Si_3N_4). It provides the high stiffness and stability needed to comply with spectral and geometric stability requirements. The electronic units are mounted on the instrument main panel (flight calibration unit (FCU) and VA-DPU) or their radiative closure panels (Remote Terminal Unit (RTU), FEE).

The internal mechanical and thermal layout of Concept B is presented in Fig. 5.28. The thermal architecture comprises a two-stage (0.07 m^2 and 0.23 m^2) radiator for the SWIR detectors and their cold boxes. The connection between them is established via assemblies of two thermal braids on each side of a copper bar, which is connected to the ceramic bench via glass-fibre reinforced plastic (GFRP) blades. This ensures mechanical flexibility between the radiator and the detector cold boxes, while providing an efficient thermal link between them. Thermal analysis established sufficient margin (15K) for operation of the detectors at 150K, which is actively controlled within ±25 mK. The spectrometer cavity is cooled below 240K via two redundant heat pipes connected to a separate single-stage radiator. The temperature of the spectrometer sub-

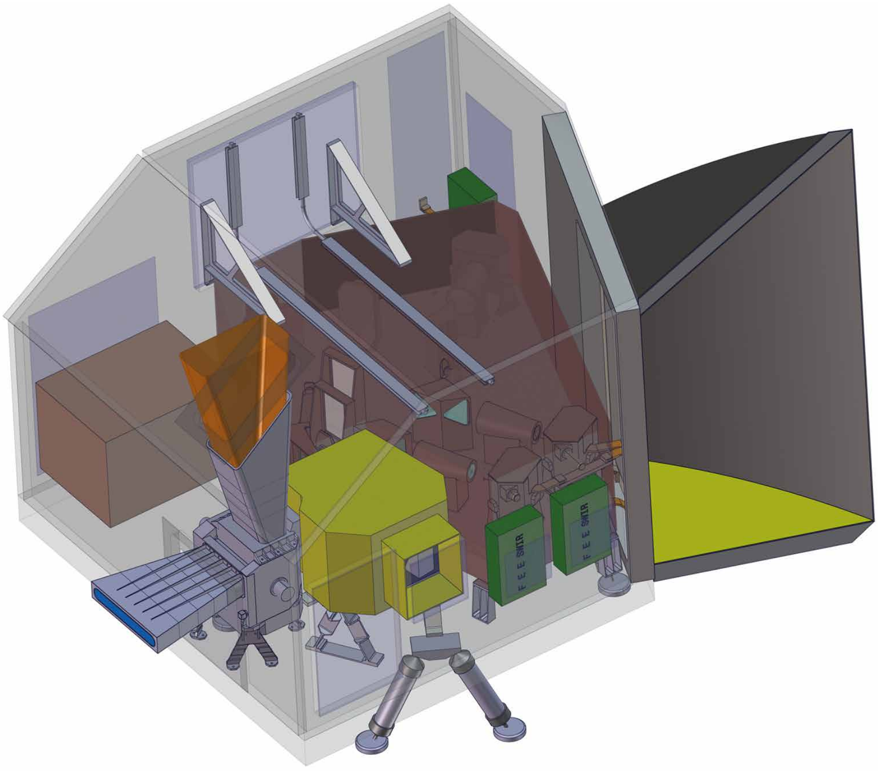

Figure 5.28. Mechanical and thermal layout of Concept B. The instrument main panel (grey) supports the spectrometer optical bench and assembly (brown), the telescope assembly (yellow), the FCU and baffles (silver), and detector proximity electronics (green). The two-stage radiator with sunshield baffle (dark grey) is close to the detector cold boxes, while the spectrometer cavity is connected via heat pipes to a separate radiator. Telescope and FCU are cooled via SLI radiative tunnels. Earth FOV in blue and Sun FOV in red. (OHB/TAS-F)

assembly is regulated under an aluminium thermal guard. The telescope unit is surrounded by an MLI cavity. Like the FCU and FEE, it is cooled to 293K via SLI radiative tunnels located on a side panel secondary structure. The accommodation of the instrument on the platform and the geometry of the radiator baffle exclude fluxes from Earth and the Sun. The overall dimensions of the complete instrument are 1969 mm, 1243 mm, and 1450 mm in length, width and height, respectively.

5.3.3.4.4 Detectors and focal plane architecture

Thorough trade-offs and analyses regarding the detector choice have been performed in the early stages of the studies. For the SWIR bands, this included the Teledyne H2RG, which was subject to tests under operational conditions at ESA facilities. These tests indicated that the off-the-shelf detector, which is optimised for low-temperature operation, would require active cooling technology with serious drawbacks in terms of cost and complexity. Therefore the SWIR detector currently prototyped and tested in the frame of the Sentinel-5 mission is the reference detector for both concepts (Fig. 5.29). The so-called Next-Generation Panchromatic (NGP) detector features a large (1024×1024) array with small square pixel size (15 μm^2) and is optimised for Earth observation applications, with operating temperatures above 130K. First test results confirm that the performance of the NGP detector is suitable for the CarbonSat mission.

By applying MCT substrate removal, the NGP is also sensitive in the VIS and NIR spectral regions. Despite this, both concepts give preference to the use of silicon CCD detectors for the NIR band spectrometers. This choice is

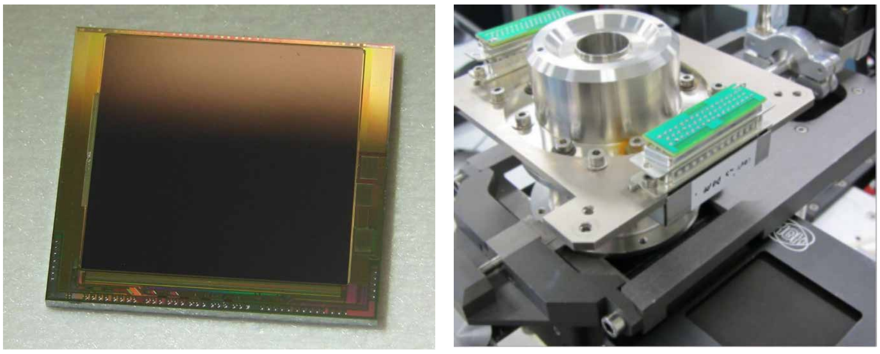

Figure 5.29. Prototype NGP detector. Left: MCT array and Read-Out Integrated Circuit. Right: detector mounted in a cryostat for performance testing. (Sofradir)

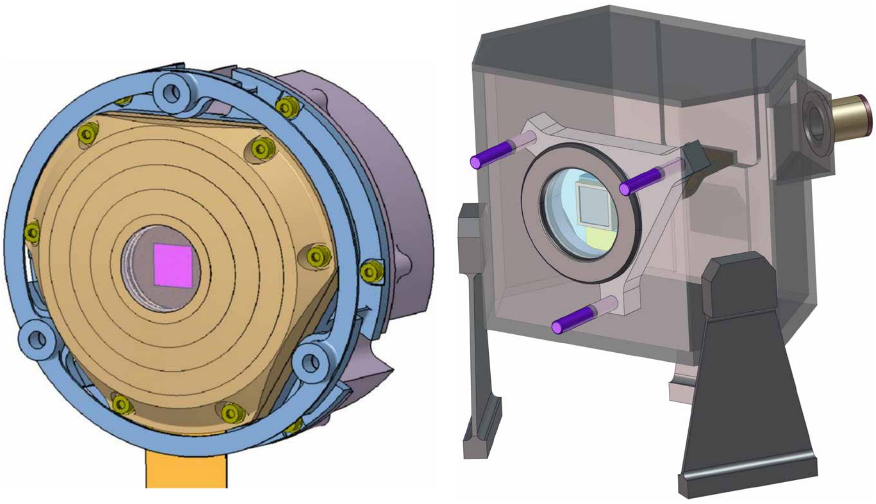

Figure 5.30. Focal plane architectures Left: Concept A (Airbus Defence and Space). Right: Concept B. (OHB/TAS-F)

mainly driven by the stringent requirement on zero-level-offset in this band, which demands a very low dark current. A CCD can also be operated at higher temperatures, relaxing the requirements on the thermal design. The selected CCDs apply a frame transfer of the acquired spectrum into a storage zone. As the recorded spectrum is smeared along the clock-out direction (either spatial or spectral), illumination during this frame transfer gives rise to radiometric artefacts. This ‘smear effect’ can be measured and corrected for by implementing dedicated small regions of the detector matrix over which the signal is clocked-out. The implementation of these smear-bands is enforced by a design requirement.

Concept A selected the Sentinel-5 NIR CCD as a reference detector. The pixel pitch is rectangular (20×30 µm) with the longer side oriented in the spatial direction to maximise spatial coverage and comply with spectral sampling requirements. For the detector read-out, the concept implements a split-frame transfer in the spatial direction. The full-well capacity (FWC) of 2.1 million electrons greatly exceeds the maximum expected signal for the exposure time of ~300 ms, dictated by the ALT SSD. The radiometric models predict detector-filling rates from less than 1% to a maximum of 20% for spectral radiances within the dynamic range. As a consequence, the non-linearity of the detector needs to be accurately characterised down to very low detector fillings. The SWIR detectors are located inside individual dewars, shown in Fig. 5.30 (left). The focal plane array is mechanically mounted onto the camera and thermally linked with the cold radiator via thermal braids.

Concept B employs an off-the-shelf CCD from E2V, with much lower FWC than Concept A (~100 000 electrons) and consequently higher detector-filling rates (3–60%) within the dynamic range. The back-illuminated CCD features square pixels (13 µm^2), arranged in a large matrix of 1024×1024 pixels. The frame transfer will be performed in the spectral direction. The two SWIR detectors are accommodated in titanium cold boxes as depicted in Fig. 5.30 (right). The cryostat is connected with the radiators via copper braids providing high thermal conductivity while avoiding mechanical stress from the main structure.

5.3.3.4.5 Instrument electrical architecture

A functional block diagram of the electrical architecture of Concept A is depicted in Fig. 5.31. It is organised around an Instrument Control Unit (ICU)

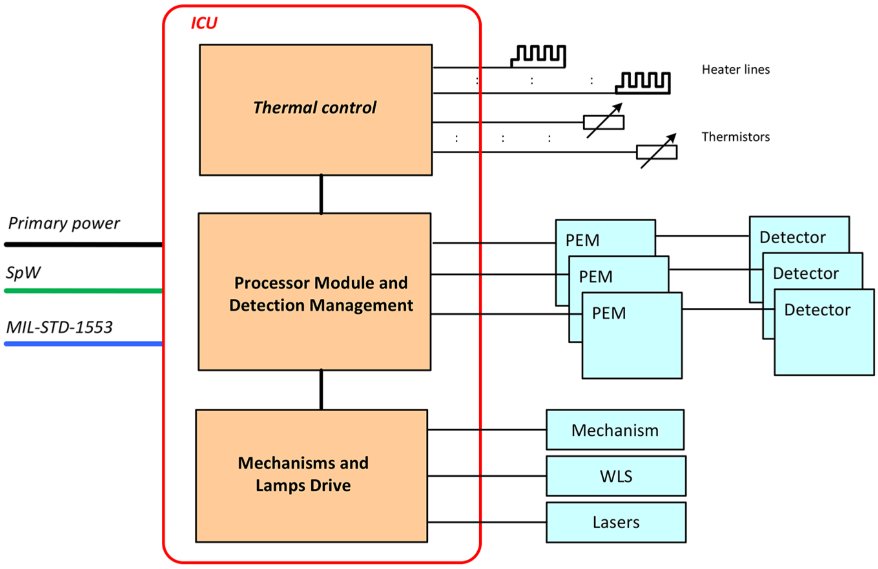

Figure 5.31. Electrical architecture of Concept A. The instrument ICU consists of three main blocks dedicated to thermal control, detection management and calibration (lamp and mechanism). (Airbus Defence and Space)

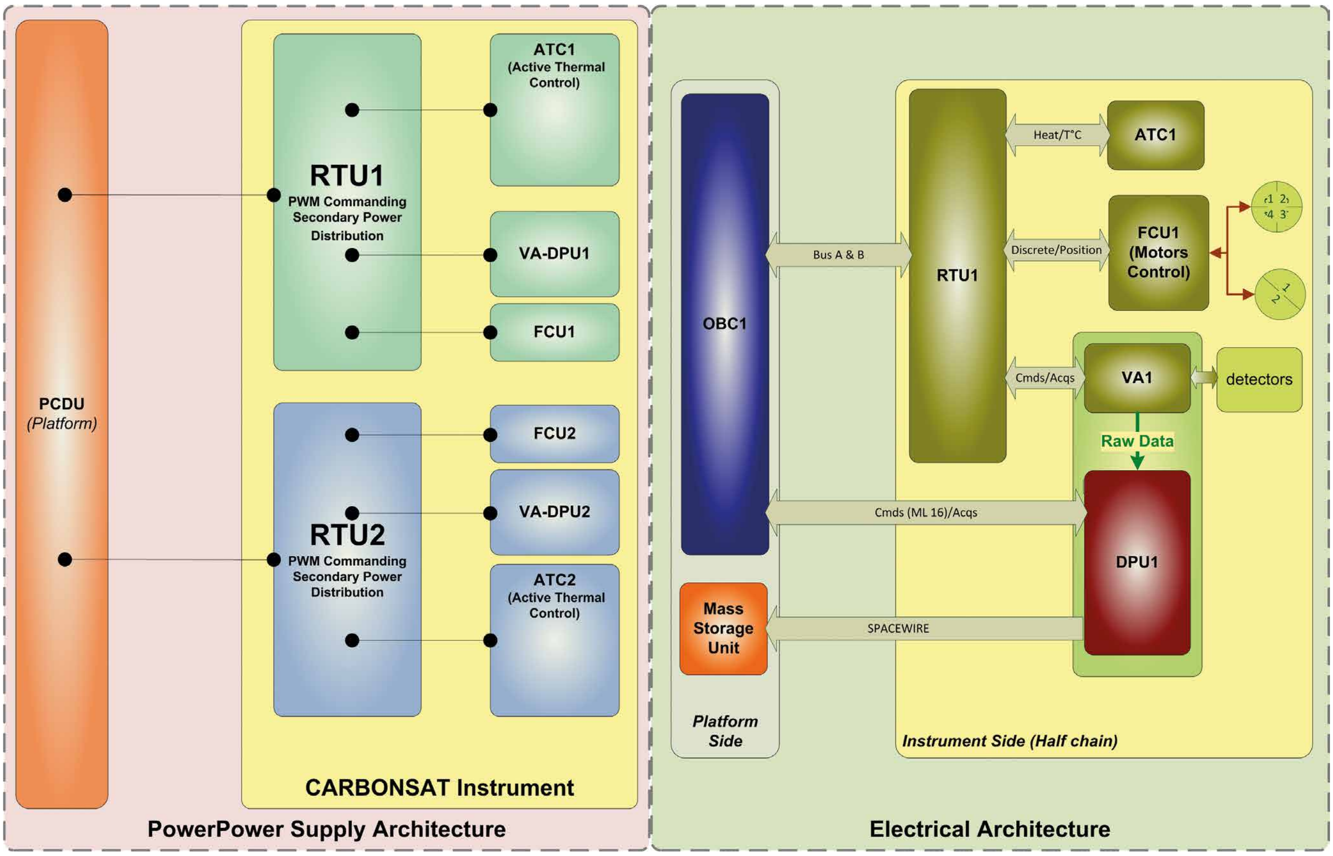

Figure 5.32. Power supply (left) and control (right) architecture of Concept B. Two redundant RTUs (RTU1 and RTU2) are supplied by the platform and configured by the onboard computer (OBC1). The two RTUs manage the thermal control (ATC1 and ATC2) and video acquisition units (VA1 and VA2). (OHB/TAS-F)

comprised of three sub-units. The thermal control unit processes the signals from the temperature sensors in a Field-Programmable Gate Array (FPGA), which controls the solid-state switches providing the power to the operational heater lines. The Processor Module and Detection Management (PMDM) unit controls the Proximity Electronics Modules (PEMs) of the three detectors, providing them with power and synchronising the acquisition with its clock module. It also performs the onboard signal processing and transfers the data to the telemetry units. Finally, the Mechanics and Lamps Drive (MLD) manages the calibration unit by controlling the filter wheel position and the light sources (detailed in the next section). All three sub-units of the ICU are powered by dedicated primary supply-lines. The standardised electrical interfaces with the platform are centralised at ICU level, except for the non-operational thermal control discrete lines (heaters, temperature sensors), which are managed by the platform central computer. Two distinct cold-redundant ICU blocks are implemented with cross-strapping between the ICU and the three detection chains.

The instrument in Concept B is controlled by the RTU, which centralises the interfaces with the platform and controls the instrument units. Apart from supplying electrical power to all GHGIS sub-units, the RTU fulfils multiple functions for instrument control. It acquires and processes the signals from the instrument thermistors and commands the instrument operational heaters. It also drives the motors of the filter wheel mechanism in the calibration unit and acquires the signals of its position sensors. It also interfaces with the VA-DPU for basic configuration and housekeeping. The VA-DPU is in charge of all functions for management of the video electronics (VE), such as power supply, acquisition and A/D conversion of video outputs from the detector, as well as generation of clocking and synchronisation signals for the detector. The VA-DPU also performs the co-addition (binning) of temporally and spatially over-sampled data to form the spatial samples of Earth spectral radiance and the solar irradiance spectra. Finally, it formats the science data before transmission to the Payload Data Handling and Transmission subsystem via the SpaceWire (SpW) cable. The functional scheme of the two redundant RTUs and the two VA-DPUs are depicted in the left panel of Fig. 5.32.

5.3.3.4.6 Mechanisms

Both instrument concepts employ a mechanism driven by a step-motor to operate the calibration wheel. In Concept A, the instrument radiator is protected by a shutter during the LEOP phase. This is for protection against contamination and to prevent immediate cooling of the instrument, which could create cold traps before available power allows for heating in decontamination mode. To ensure that no problems with Sun-impingement occur during safe-mode episodes, the radiator has a specific design and coating. In Concept B no dedicated radiator shutter is foreseen.

5.3.3.4.7 Instrument on-ground characterisation and inflight calibration

Inflight calibration

Compliance to the demanding radiometric and spectral requirements can only be achieved and maintained over the mission lifetime by means of regular calibration measurements. Thus, both concepts feature an onboard calibration mechanism capable of exposing the instrument to various light sources. As most radiometric requirements are applicable to the derived reflectance (eq. 4.1), an onboard calibration standard for this quantity is established by means of Sun diffusers, which are absolutely calibrated on the ground in terms of their BRDF. The diffuser BRDF relates the detected signal with the incident radiation intensity in terms of irradiance and spectral radiance. Sun diffusers are prone to degradation in space because of the effects of radiation altering the BRDF over the mission's lifetime, thus two redundant Sun diffusers are employed by both concepts. One diffuser will be used less frequently than the other and serves as a reference for degradation monitoring.

During the instrument definition studies various types of Sun diffusers were traded off. The most important criterion was the minimisation of spectral features by speckle patterns in the reflected sunlight. Such variations in the measured solar signal are caused by mutual interference of multiple wavefronts, e.g. scattered from a rough surface. Different candidate diffuser types have been identified, which will be operated in reflection and are commensurate with the design geometry of the calibration assemblies: a quasi volume diffuser, a volume scattering material based on synthetic quartz and spectralon are planned to be assessed in dedicated pre-development activities.

Figure 5.33 depicts the calibration assemblies. Both concepts rely on a wheel mechanism, which is positioned by a rotating mechanism, driven by step motors. The solar calibration will be performed in the anti-flight direction (back-view) close to the South Pole, before the satellite enters the eclipse part of the orbit, being representative of the thermal conditions of Earth observation modes. In Sun-calibration mode the wheel is rotated to expose the diffuser to the open Sun port while simultaneously closing the Earth port of the instrument.

Apart from radiometric and spectral calibration via Sun diffusers, the calibration assemblies of both concepts fulfil several additional functions. Signal is acquired in the eclipse part of every orbit during normal operations, when the instrument FOV is exposed to the night side of Earth. From these

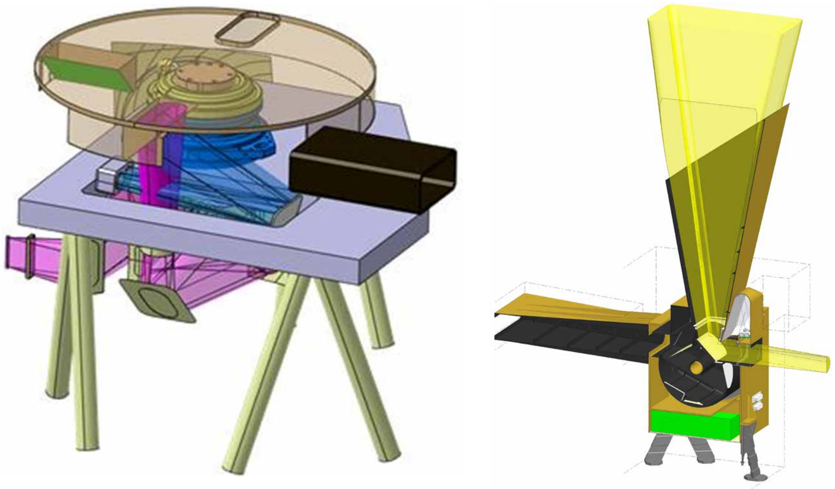

Figure 5.33. Design sketches of the inflight calibration unit for Concept A on the left (Airbus Defence and Space) and Concept B on the right (OHB/TAS-F). The calibration wheels feature two Sun diffusers operated in reflection. The drawings show a deployed diffuser in Concept A, while the White Light Source is operated in Concept B.

measurements, dead and bad detector pixels can be identified. In addition, dark current calibration is regularly performed during complete orbits (including the sunlit part, shutter closed). The temperatures of the focal plane and spectrometer optics are recorded during acquisition of dark spectra to establish the dark current dependence from thermal conditions. These measurements are indispensable for accurate dark current correction in Level-1b processing, which is necessary to comply with the zero-level offset requirement.

The PRNU is monitored throughout the mission's life by regularly performing flat-field measurements using a white light source. This is usually realised by illuminating the Sun diffuser with a tungsten halogen lamp, resulting in a spectrally and spatially uniform distribution of intensity at the focal plane. The acquired flat-field spectra are used to monitor the gain variation of individual detector pixels, which is corrected for in Level-1b processing.

Both calibration assemblies also implement strategies to characterise the spectral response of the instrument in flight. The ISRF may be altered by a defocus of the imagers owing to launch effects as well as thermo-mechanical deformations. Therefore, it will be monitored in flight utilising quasi-monochromatic light sources. Concept A implements two laser diodes for each of the three spectral bands, which can be frequency-tuned over a spectral interval corresponding to about five detector pixels. This allows for regular measurements of the ISRF in the vicinity of the laser diode central wavelength. Provided that the spectral dependence of the ISRF shape has been accurately characterised on the ground, any changes detected at the diode wavelengths can be interpolated to recover the spectral response over the complete bandwidth. Concept B implements a similar setup, but with one distributed feedback laser diode per band plus a redundant backup diode. The active approach is complemented by the retrieval of the spectral response utilising the regular irradiance measurements via the Sun diffuser to ensure compliance to the demanding inflight knowledge requirement for the ISRF.

On-ground instrument and system characterisation

The requirements for radiometric, spectral and geometric accuracy demand that the GHGIS instrument will be subject to an extensive on-ground calibration and characterisation campaign. Because of the need to suppress the thermal background radiation in the SWIR bands, especially in SWIR-2, most calibration measurements must be performed in a thermal vacuum chamber.

The calibration campaign will establish the radiometric absolute calibration in terms of derived reflectance. The BRDF of the two onboard diffusers will be characterised using standardised lamps, which can be traced to international calibration standards. Their light will be coupled into the instrument via calibrated diffusers or integration spheres. The Earth and Sun ports of the instrument will be calibrated separately to absolute accuracies commensurate with the ARA requirement the Level-1 products.

An extensive straylight characterisation of the instrument will be performed to correct for this error source at Level-1b. Straylight correction algorithms require key data, which describe the distribution of the detected radiation across the focal plane in both spectral and spatial directions. Diffuse straylight from scattering owing to surface roughness and contamination can be described by straylight kernels. They can be determined from the instrument's response to spectral and spatial point sources, usually realised by lasers. These measurements are also used to map ghost images from unsuppressed reflections within the instrument, which also need accurate correction.

The on-ground calibration will also establish the initial spectral scale of the instrument, associating the detector pixels to the wavelengths sampled by them. This can be achieved by the use of dedicated spectral line sources, (e.g. gas discharge lamps), which produce light in narrow spectral intervals. The positions of the measured emission lines on the detector array can be determined with accuracies of a few percent of a pixel width. From the detector positions of a multitude of emission lines spanning the bandwidth of the spectrometer, the dispersion law of the spectral band is derived. This mathematical function associates all detector pixels to their centre wavelengths, including those between the measured emission lines.

The most time-consuming characterisation procedure is potentially the measurement of the ISRF and its variation across the spectral bands of the instrument. The challenging knowledge requirement (Table 5.3) translates into the necessity to measure the ISRF shape far out into its wings, where it is smaller than 1% of its peak and barely distinguishable from straylight. The need to reach sufficient SNR in the far wings of the ISRF drives the required integration times and, therefore, calibration duration. ISRF shape measurements have to be performed for many wavelengths across the bandwidth, and the sampling will depend on the variability across the spectrum. However, since it is expected that it varies smoothly with wavelength, interpolation between measured shapes is potentially sufficient to reach the required accuracy for every spectral channel. On-ground ISRF characterisation to the required accuracy is considered as demanding.

The instrument will also be characterised in terms of its spatial coregistration performance. The most important parameter to be determined will be the keystone distortion as a function of wavelength. The curvature of a line on the detector array corresponding to white light from a spatial point source needs to be characterised across the entire swath width. This can be performed by means of point source or knife-edge stimuli, which are scanned across the swath width while recording the radiometric response of the instrument. This characterisation verifies the predicted keystone distortion as well as the accuracy of the rotational alignment of the detectors. It also determines the binning windows for onboard co-addition of detector pixels in ACT direction, which form the spatial samples transmitted to the ground.

5.3.4 Platform

5.3.4.1 Overview

The two platform concepts proposed by industry are quite different in that one concept is based on a flight-proven platform with extensive use of off-the-shelf components, whereas the other concept is a custom platform design. Both consortia propose a platform concept with tank capacities in excess of the goal of five years mission duration.

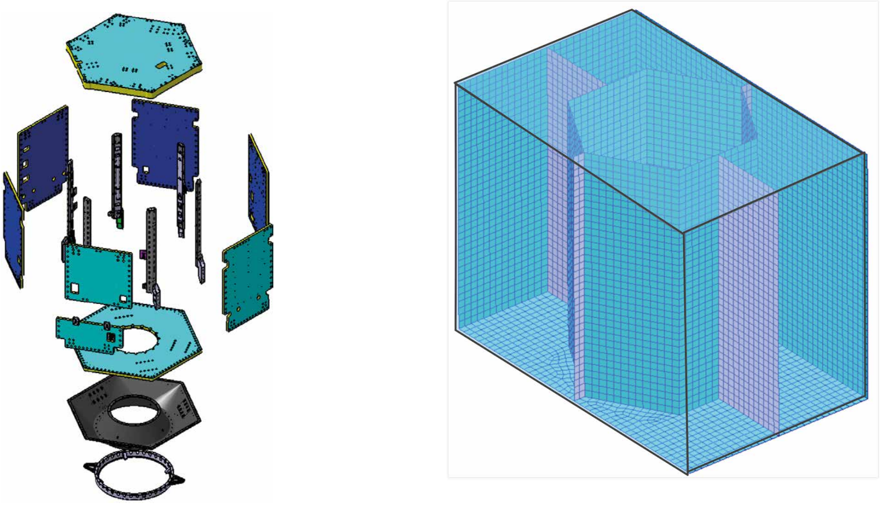

Figure 5.34. Concept A platform structure on the left (Airbus Defence and Space) and Concept B platform structure on the right (OHB).

This subsection describes in detail each platform subsystem and provides the rationale for the architecture of the subsystems and the selection of the components.

5.3.4.2 Structure

Besides the compatibility with the launch environment, the CarbonSat mechanical design is driven by the instrument accommodation, which requires an unobstructed view of nadir and sunglint directions and room for the passive radiator pointing to cold space, in combination with the volume available within the Vega fairing. Figure 5.34 shows the two structural concepts, which are designed to sustain the launch loads by means of a direct load path to the launcher. Concept A (left) is based on the reuse of the AS250 structure implemented for Sentinel-5 Precursor. Similarly to that, the instrument of CarbonSat is mounted on the top floor, which is based on a solid aluminium/aluminium honeycomb panel. The stiffness of this panel is tuned to fit the tight axial eigenfrequency requirements from the launcher. In case of unavailability of the baseline launcher, Vega, a change of the top panel would be required to make use of the backup launcher PSLV.

The position of the instrument allows a good optical co-alignment with the startrackers, placed on the platform. The folding side panels ensure good accessibility to all the equipment. Modular equipment packing and installation as well as assembly ensure flexible mating, test and integration. The structure mechanical behaviour is compatible with the launch environment. The launcher interface is a standard 937-mm diameter ring.

Concept B is based on a bespoke platform, with a structural design optimised for the payload and any constraints from the launcher (Fig. 5.34, right, Finite Elements structural model). The central hexagon is made of aluminium sandwich panels. The other elements of the primary structure are the internal shear webs, which transfer the loads from the exterior panels to the central hexagon and down to the Launch Vehicle Adapter (LVA). The shear webs are made of aluminium sandwich panels. Since the central hexagon uses the same material, the thermoelastic stress at the interfaces is minimised. Using a central hexagon instead of a central tube requires an interface with the launch adapter and the dispersion of the launch loads throughout the latter. For the Vega launcher, an aluminium circular adapter attached to the satellite via a clamp band is used. The central hexagon uses an interface bracket milled from a hexagon to a circle.

5.3.4.3 Mechanisms

Both concepts make use of hold-down and release mechanisms to keep the solar arrays in the stowed position during launch and release them for deployment. Concept B implements a solar array with a Solar Array Driving Mechanism (SADM) attached to the main structure side panel facing the +y-axis, whereas Concept A uses three fixed solar panels attached to three of the main side panels. For Concept A, the solar panels are stowed against the satellite sidewalls during launch, each supported by two hinges and four hold-down points. The choice of actuation device to unlock the solar arrays (pyrotechnic devices or thermal knives) depends upon the final solar array hold-down and release mechanism design.

In Concept B, the solar array is similarly contained in stowed position by hold-down and release mechanisms. Off-the-shelf flight-proven mechanisms are implemented. The Concept B solar array is inclined with a cant angle of 7.5° to optimise power generation. The SADM operates in open-loop mode with respect to satellite attitude and rotates at a fixed rate.

5.3.4.4 Thermal Control

The main function of the thermal control subsystem is to guarantee operating and non-operating temperature ranges for all the satellite components. Thermal requirements are not critical for the CarbonSat platform, in contrast to the GHGIS instrument, and can be fulfilled with well-proven passive thermal control design (MLI, radiators, specific paints to optimise radiative surface properties, etc.), assisted by an actively controlled heater system (heater lines and thermistors).

For Concept A, the thermal architecture of the CarbonSat satellite follows that of the standard AS250 platform, since the GHGIS payload is well within the capabilities of the existing design. The modular design of the satellite allows for separation of the payload and the platform thermal environments, with the subsystems managing their own thermal control. Over the whole orbit the satellite remains in nadir mode (for observations and during eclipse), but performs a pitch manoeuvre for glint observations. Thus, the variation in solar loads drives the variations in temperature throughout the orbit. The high dissipation payload and platform equipment is located on the internal surfaces of radiator panels, providing a simple coupling to the latter.

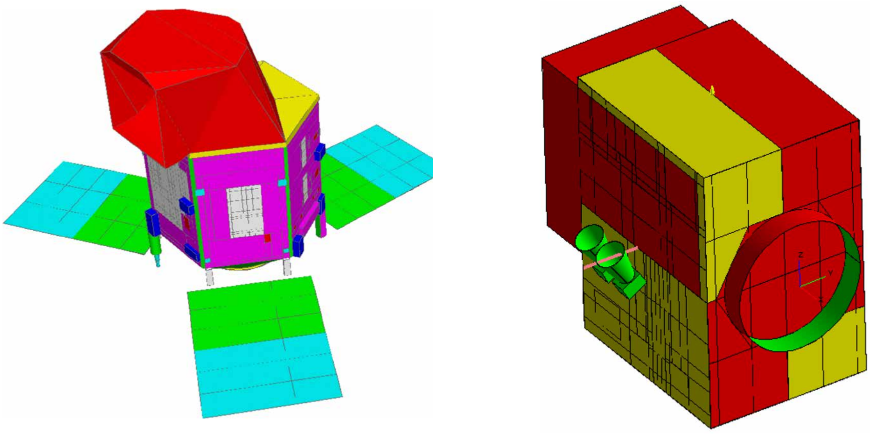

Figure 5.35. Different thermal surface properties of Concept A (Airbus Defence and Space) and B (OHB).

5.3.4.5 Electrical architecture

The overall system electrical architecture is similar to most LEO satellites and composed of the following subsystems and equipment:

- Command and Data Handling Subsystem (CDHS), including the OBC, for primary spacecraft command and control, and dedicated platform and payload command-and-control MIL-1553B data busses and either a Remote Interface Unit (RIU), or a centralised architecture with an OBC including the I/O interface modules for non-MIL-1553B platform equipment interfaces

- Power Subsystem, including the Power Conditioning and Distribution Unit (PCDU), solar array, battery and heaters

- Telemetry , Tracking and Command (TT&C) subsystem for realtime command, telemetry and ranging, including the S-band transponders and antennas

- Attitude and Orbit Control System (AOCS), described in detail below.

- Payload Data Handling and Transmission (PDHT) subsystem, including the Solid-State Mass Memory (SSMM) for storage of payload data, auxiliary data and platform telemetry and the X-band data downlink system for high data rates

- GHGIS payload ICU or RTU, to control payload and interfaces to OBC and SSMM

The primary power, generated by the solar array(s) and stored in the batteries, is distributed to the main bus users by the PCDU via individually switchable Latching Current Limiters (LCLs). The electrical architecture of Concept A provides a single unregulated 28-VDC primary power bus, directly connected to the batteries. All satellite units, except those needing regulated secondary supplies (such as minor units powered through the RIU), are powered by the primary power bus through on/off switchable LCLs, for essential and non-essential loads such as ICU, PDHU, or S-band transmitters. Fold-back current limiters (FCLs) are implemented for vital loads, namely OBC and S-band TC receivers. Figure 5.36 shows the electrical platform architecture for Concept A.

A similar power bus is implemented for Concept B. The baseline PCDU unit has a modular design where each main function is allocated to a specific module/board. The proposed architecture is based on a similar unit developed for the AGILE satellite, an Italian astrophysics mission.

5.3.4.6 Command and data handling

The CDHS provides the following functionality:

- overall satellite command and control and execution of AOCS algorithms
- supporting of the onboard autonomy and Failure Detection Isolation and Recovery (FDIR)
- provision and distribution of ground commands and software updates to the satellite
- collection and storage of satellite housekeeping telemetry
- onboard time generation, synchronisation, maintenance and distribution

The CDHS consists in general of two units, the OBC and the RIU. The modular approach of separating the OBC from the mission-specific interfaces has the advantage of allowing the reuse of existing hardware with minimal

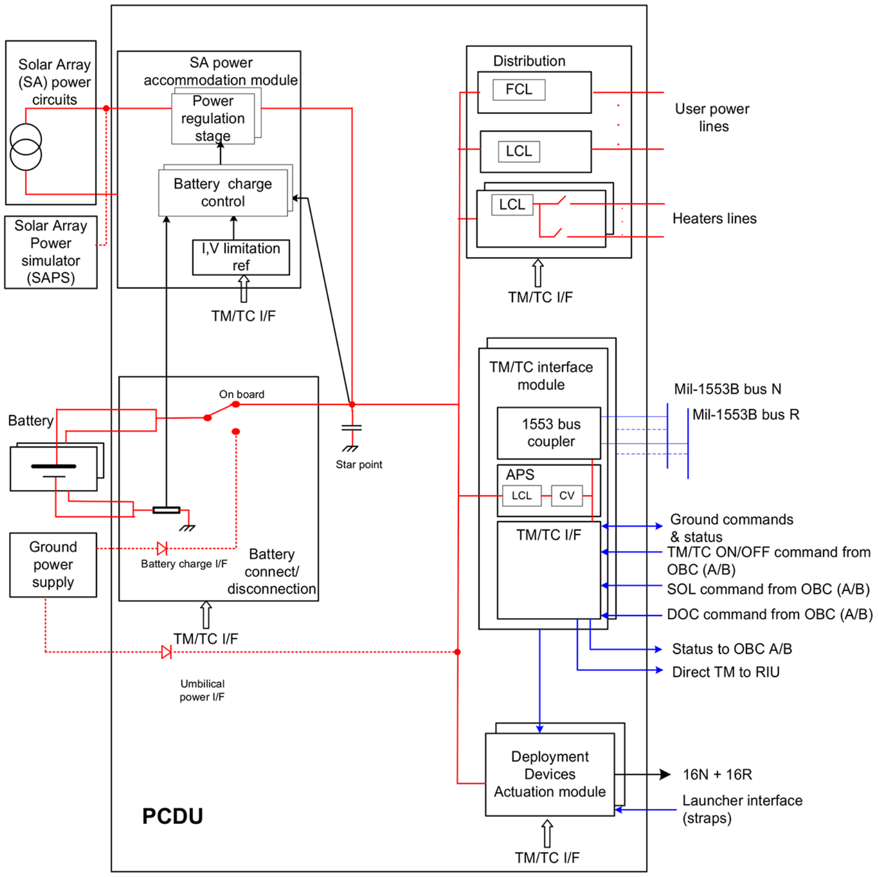

Figure 5.36. Concept A electrical platform architecture. (Airbus Defence and Space)

modifications and enables early testing. Two MIL-1553B data busses are used, one to connect to platform units and one dedicated to command and control of the payload units. The second concept is based on a centralised architecture with a single main OBC, which also includes the I/O interface modules (no separate RIU). The OBC is the core part of the subsystem, providing the following functionality:

- processing functions
- data memory and safeguard memory management
- onboard time generation, synchronisation, distribution and servicing
- bus controllers for the MIL-1553B busses
- TT&C interface functions
- reconfiguration functions

The processing requirements of the OBC are within the typical range of a standard LEO mission. The CarbonSat mission does not require any specific onboard processing, binning of the GHGIS data being carried out in the payload electronics. Realtime HKTM is acquired by the OBC and transmitted to ground using the S-band downlink. A dedicated interface between the OBC and the SSMM enables stored HKTM to be downlinked via the X-band system. The onboard time is synchronised to the GPS time reference provided by the GNSS receiver. The RIU is a mission-specific unit that includes all discrete interfaces from the OBC to the platform and payload equipment for the units that do not use the MIL-1553B data bus. The same applies for the I/O interface modules integrated in the OBC in the second concept. In general, the RIU and the I/O interface modules will contain interfaces to the following equipment:

- reaction wheels
- magnetorquers

- magnetometers
- propulsion subsystem units
- thermistors
- X-band modulators and amplifiers
- solar array deployment mechanism

The payload data handling architecture is based on flight-proven equipment. The data downlink system passes the data, which has been generated by the payload, to the ground processing system. In the space segment this chain starts with the ICU or the Terminal Unit, which passes the data to the onboard mass memory unit. This stores the data until a scheduled ground station pass occurs, when it passes the data to the X-band system for transmission to ground. Finally, the ground station receives the data and forwards it to the ground processing system. The onboard PDHT subsystem consists of three main elements:

- SSMM
- X-band payload data downlink system
- interfaces between the payload and SSMM

The SSMM unit is used to store the payload data, the auxiliary data required for payload data processing (e.g. GNSS data, attitude data) and payload and platform telemetry. The unit formats the data for transmission to the ground in standard CCSDS transfer frames.

The choice for Concept A to implement the AS250 avionics suite leads to existing options for the PDHT. The mission needs can be fulfilled with the mass memory units used on other AS250 satellites (CORECI unit) and a downlink capability in X-band with one channel at 310 Mb s^{-1} (no onboard compression). The PDHT consists of one internally redundant PDHU from Sentinel-5 Precursor, providing 480 Gb of capacity in flash memory at EOL, to be compared to the mission need of ~400 Gb. Two X-band transmitters in cold redundancy are being cross-strapped to both halves of the PDHU. The OBC proposed is a recurring unit based on the SEOSAT OBC (Fig. 5.37). Both OBCs are connected to both MIL-1553B busses with cross-strapping between OBC and MIL-1553B managed exclusively by ground command. The RIU consists of two

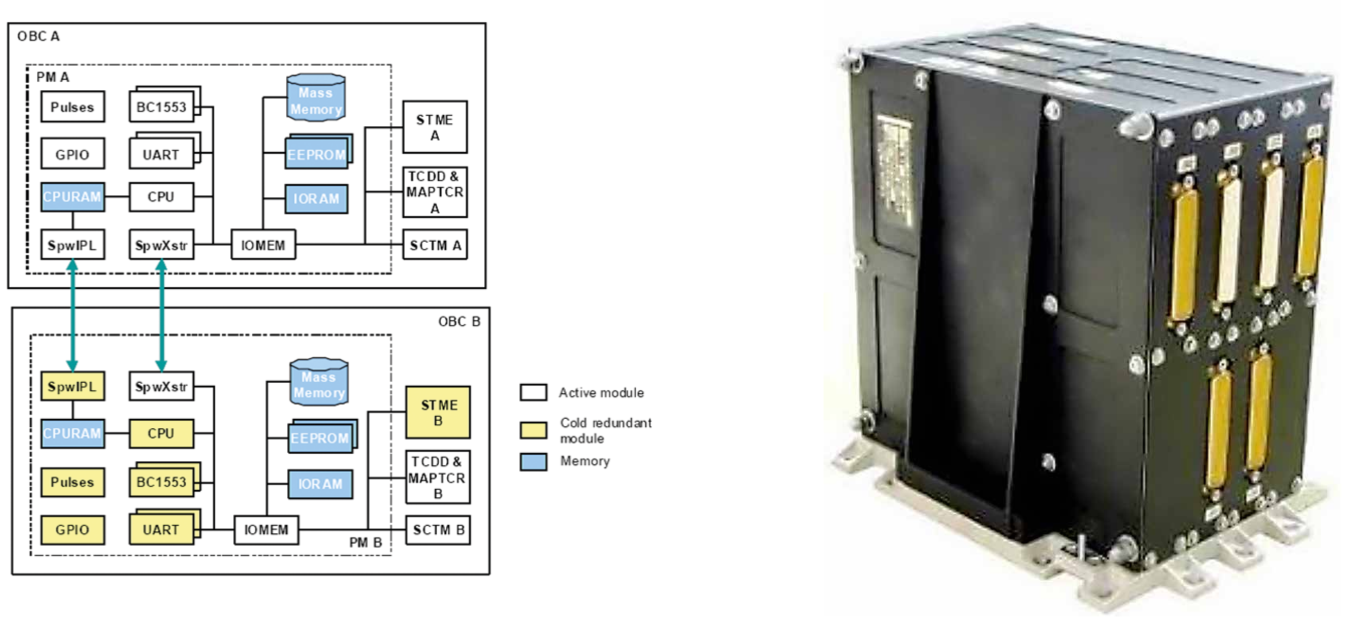

Figure 5.37. Concept A OBC processor module architecture (left) and OBC unit (right). (Airbus Defence and Space)

cold-redundant modules. For each module, the internal configuration can be adjusted to minimise power consumption or to provide the relevant electrical inhibits by powering on only the relevant circuits for a given satellite mode.

The Concept B concept is based on a centralised architecture with a single main OBC, which also includes the I/O interface modules instead of a separate RIU. The PDHU implements a redundant SpaceWire interface with the instrument for reception of the scientific data. A 640-Gb EOL mass memory board based on NAND flash memory modules stores the scientific data. The maximum data volume onboard is calculated to be ~550 Gb (including 25% margin). Simultaneous acquisition and downlink is supported. The OBC is based on two cold-redundant LEON2 processor modules supplemented by support I/O modules. Two MIL-1553B busses, nominal and redundant, are used to command platform and payload, and additionally a discrete RS-422 interface is implemented. For transmission of ancillary data a SpaceWire interface is foreseen.

Payload command

Concept A implements a redundant dedicated 'intelligent' ICU, giving flexibility of independent S/W development and maintenance through parallel platform and payload SW life cycles. A similar advantage is apparent in the area of AIT where the ICU solution allows an independent instrument verification campaign with validation of instrument operations and databases prior to mating the instrument with the platform.

In Concept B, an internally cold-redundant RTU is the main instrument I/O manager under the control of the OBC and powered by the satellite's PCDU. The RTU only acts as an extension of the OBC in sending commands to the instrument's units, collecting the acquisitions from instrument units and extending the number of synchronisation signals to the instrument units. It also extends the PCDU by supplying power and heater lines to the units.

Data transmission

Concept A includes a standard X-band isoflux antenna as baseline, mounted in the +Z direction (nadir). It supports communications during eclipse and observations. The PDHU command and monitoring is via the MIL-1553B. The data interface between the PDHU and the instrument is assumed to be a single redundant high-speed serial G-link between the instrument, computer and the PDHU; the downlink is managed through Orbit Position (OPS) tagged commands.

Concept B provides similar functionality using a single channel in X-band with a data rate of ≥273 Mb s^{-1}. The proposed PDHU subsystem is shown in Fig. 5.38 and features an Instrument Interface Unit, a Memory Module Unit, a Telemetry Manager Unit, and a Supervisor Unit.

5.3.4.7 Electrical power and energy storage

The baseline concept for the power subsystem of Concept A uses units from SEOSAT and SPOT-6/-7 or Sentinel-5 Precursor missions, including three fixed solar arrays of ~2.1 m^2 each, based on GaAs triple junction cells, two 78 Ah Li-ion batteries and a PDHU with internal redundancy for power regulation, battery charge management and bus power distribution. The selected battery comprises two units, each providing 78 Ah capacity. The concept meets the energy requirement margin for up to five sunglint orbits per day (SZA limit 60° in the southern hemisphere); with fewer sunglint orbits, as baselined, observations up to the SZA limit of 80° in the northern and southern hemispheres are possible.

The Concept B design is based on the use of a single articulated solar array for power generation and two Li-ion batteries of 66 Ah. The solar generator is

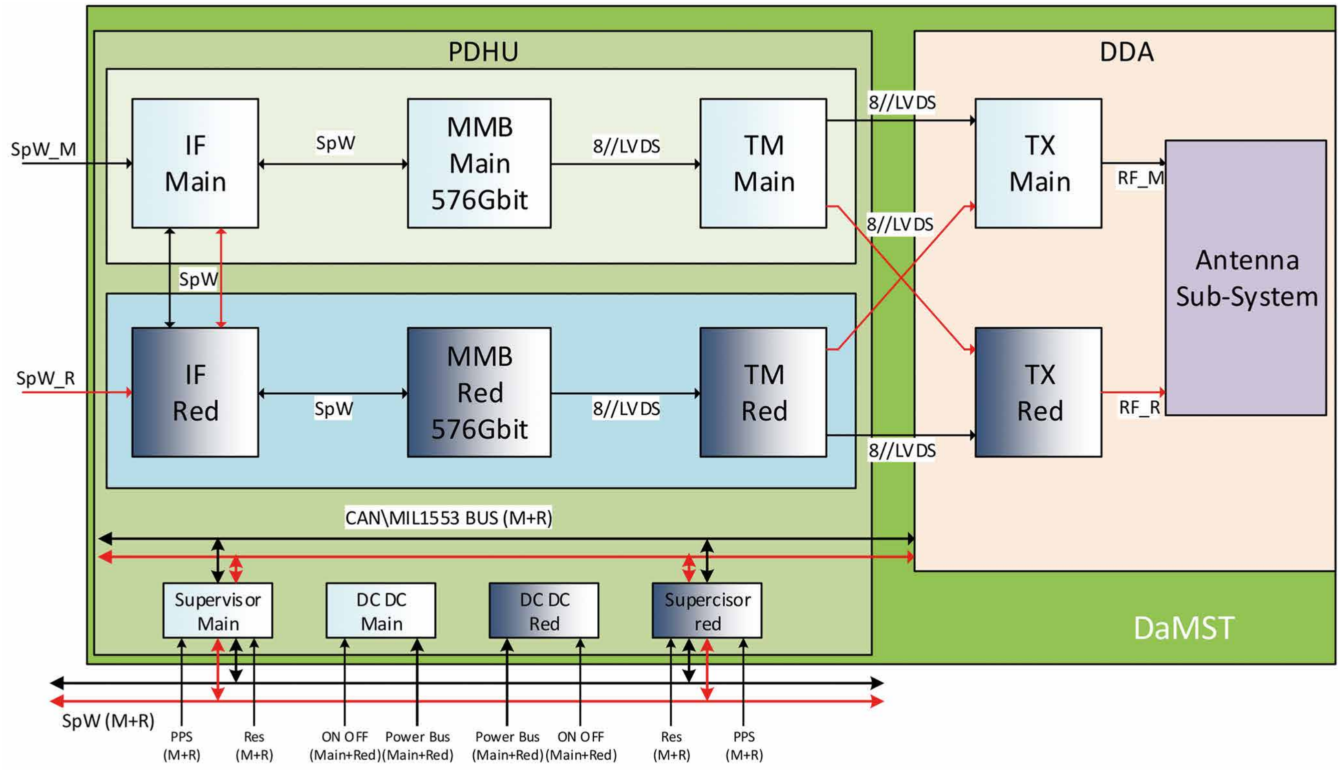

Figure 5.38. Concept B PDHU and DDA subsystems overview. (OHB)

based on a solar array wing driven by a SADM such that the Sun-incidence angle on the array is always kept optimal. During sunglint pointing, the SADM will continue the same rotation, therefore some losses will be incurred owing to sub-optimal geometrical conditions. The solar array is inclined with a cant angle of 7.5° to counteract the effect of the orbit Right Ascension of the Ascending Node (RAAN). This is realised by connecting the solar array to the SADM by means of a custom-made yoke. The solar array wing of 7.2 m^2 is made of three identical panels.

The concept meets the energy requirement margin with no limit to the number of sunglint orbits per day, with observations up to the SZA limit of 80° in northern and southern hemispheres.

5.3.4.8 Telemetry, tracking and command

The TT&C subsystem provides the S-band communication capabilities between the satellite and ground station. Two active omni-directional antennas ensure a communication link for all satellite attitudes (nominal as well as non-nominal). The following functionality is provided:

- command function for reception and demodulation of commands send from ground
- telemetry function for modulation and transmission of realtime housekeeping data to ground
- ranging and range rate functionality for satellite orbit determination in addition to the onboard GNSS system for emergency operations

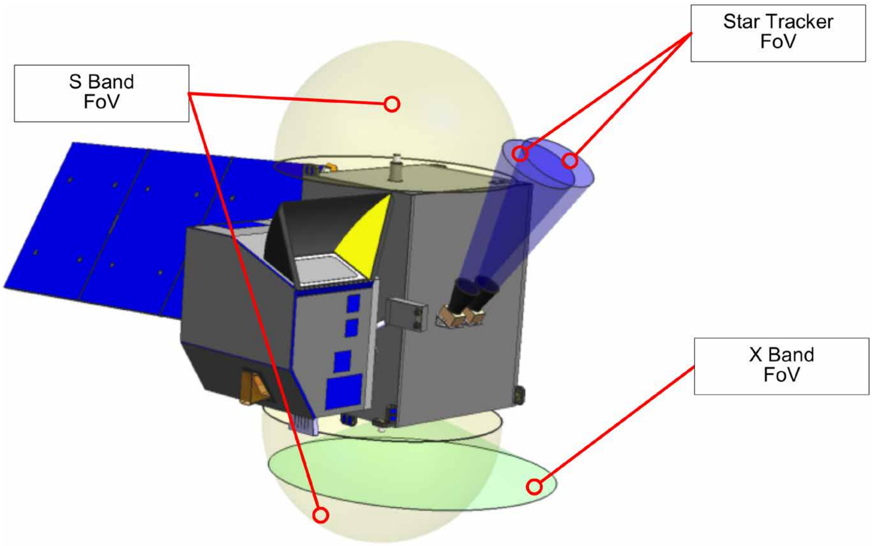

Figure 5.39. An example of Concept B startracker, S- and X-band FOVs. (OHB)

In the proposed operative concepts, it is foreseen to use the S-band downlink during nominal operations only for realtime telemetry; the recorded HKTM is transmitted together with the science data in X-band. If the X-band downlink is not available, e.g. during LEOP or in Safe Mode, the S-band link is used to downlink the recorded HKTM.

For Concept A the S-band subsystem is based on the AS250, but, in order to downlink the recorded housekeeping telemetry in X-band, some modifications have to be implemented. HKTM data will be interleaved with GHGIS data and downlinked in a separate virtual channel. This approach requires a modification of the PDHU: the Payload Data Ground Segment (PDGS) will unpack the HKTM data and forward it to the Flight Operations Segment (FOS).

The TT&C system supports an uplink rate of 64 kb s^{-1}, a low telemetry data rate of 128 kb s^{-1} with simultaneous ranging, and a high telemetry data rate of 2048 kb s^{-1}. Both receivers operate in hot redundancy and each transmitter works in cold redundancy. Opposite circular polarisations are used in order to distinguish between the reception paths via zenith or nadir antenna. The ground station performs a polarisation selection dependent on the maximum received power.

5.3.4.9 Attitude and orbit control system

The AOCS is based on a gyro-less architecture, comprising a number of distinct modes of operations, which are intrinsically similar for both concepts. All modes are implemented in software, with each mode using a specific set of sensors and actuators; the main modes mostly comprise several sub-modes.

Concept A

Concept A employs an existing AOCS suite customised for the mission. The actuators consist of four reaction wheels, three magnetorquers (used for reaction wheel offloading and rate damping) and a monopropellant propulsion system. The sensors comprise three startrackers, an internally redundant GPS unit, two magnetometers and a Coarse Sun Sensor (CSS).

The proposed architecture uses the startrackers to meet the pointing requirements, providing tolerance against blinding or failure, guaranteeing full single failure tolerance. The startrackers are mounted on the top floor of the platform. Two GNSS receivers in cold redundancy supply accurate

Figure 5.40. Overview of the AOCS architecture of Concept A. (Airbus Defence and Space)

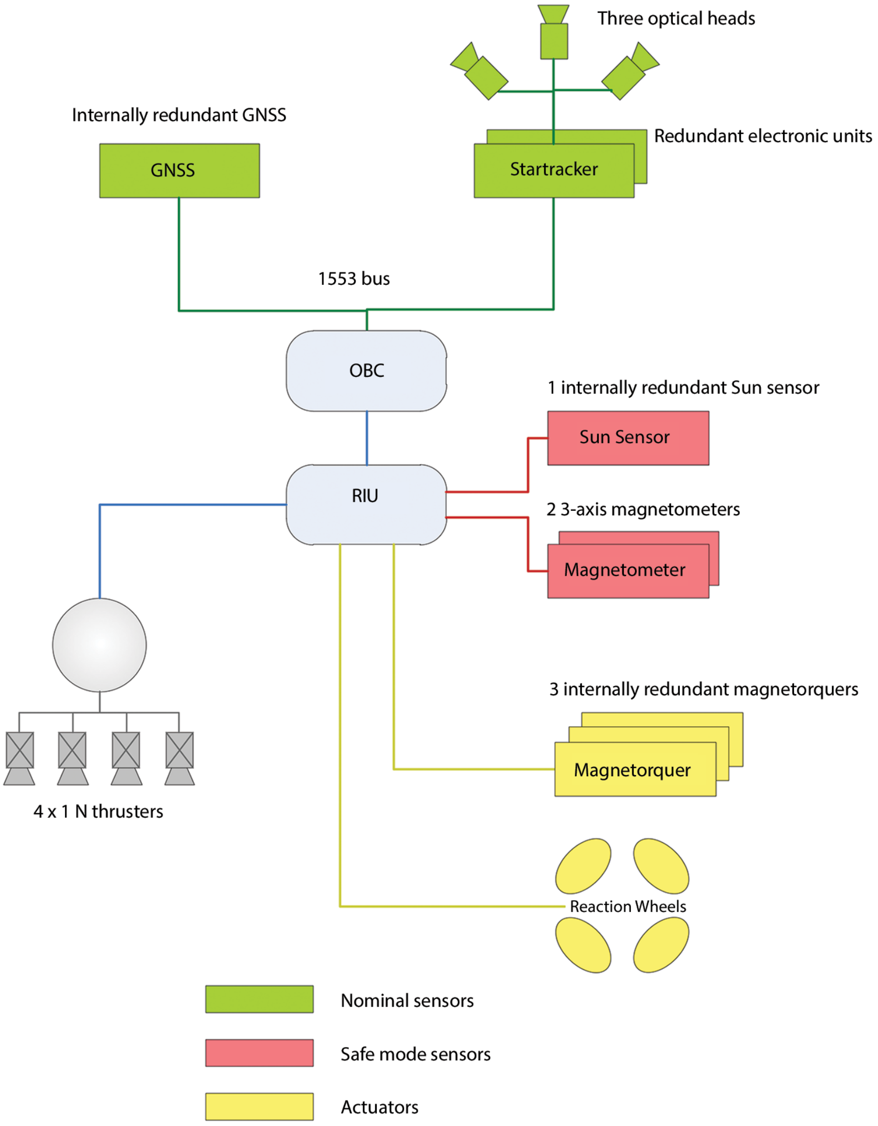

position, velocity and timing to the satellite. Coupled with the onboard orbit propagation function providing robustness against outages, the combination of startrackers, GNSS and guidance laws delivers a highly autonomous AOCS.

Four reaction wheels in a tetrahedral configuration provide the fine actuation and slewing capability required during nominal operations while providing failure tolerance. Used in combination with internally redundant magnetorquers, this actuator suite also guarantees control during Safe Mode. During nominal operations, the magnetorquers plus a magnetic field model are used to manage the wheel momentum. By design, the Safe Mode is robust to a wheel failure; the FDIR hierarchy allows the swapping of units to isolate failures. The cluster of four reaction wheels (torque capability of ~0.2 Nm and angular momentum capacity of 20 Nms) allows, thanks to a preferential torque capability, the satellite to perform slews or 'sunbathing' over the poles with substantial agility: ~35° slew in 60 s around the pitch axis. The propulsion system is only used for orbit manoeuvres, not for attitude control.

The following three AOCS modes have been defined in previous programmes (e.g. SEOSAT, SPOT-6 and -7) and are in accordance with CarbonSat functional requirements:

Acquisition and Safe Hold Mode is used to perform the initial attitude acquisition after launch and to align the solar arrays to the Sun. It is also used as Safe Mode, with an automatic transition from any other mode after a critical failure is detected.

Normal Mode (NM) is used the majority of the time to perform the nominal mission providing the accurate pointing required for scientific observations. Normal Mode is fully autonomous: once in NM and without any action from the ground, the AOCS automatically maintains attitude and manages wheel angular momentum. Based on the star sensors for three-axis absolute attitude measurement and GNSS for autonomous navigation, the cluster of reactionwheels provides full three-axis control torque while the magnetorquers, aided by a magnetic field model, perform continuous momentum management.

Orbit Control Mode (OCM) is dedicated to the orbital correction manoeuvres. The orbit correction attitude is acquired in NM so that the thrust can be applied in the direction specified by ground, which is a bias with respect to geocentric pointing.

The failure management function (FDIR strategy) for the generic AS250 avionics is defined to fulfil three main objectives:

- guarantee the satellite integrity in case of failure leading to the irreversible loss of the nominal mission
- optimise the mission operational availability
- implement simple and generic actions for anomaly recovery

Concept B

For Concept B the sensor set consists of two startrackers (one active, one redundant) mounted on a lateral panel close to the instrument to minimise the impact of thermoelastic deformations. In nominal mode the startrackers provide the main input to attitude determination; the internally redundant GNSS receiver provides input for determining the satellite position. The seven redundant small Sun sensors are the main sensors used for coarse attitude determination in safe and acquisition mode. The fully redundant magnetometer measures the magnetic field vector and is used in a feedback loop with the redundant magnetorquers for momentum dumping in nominal

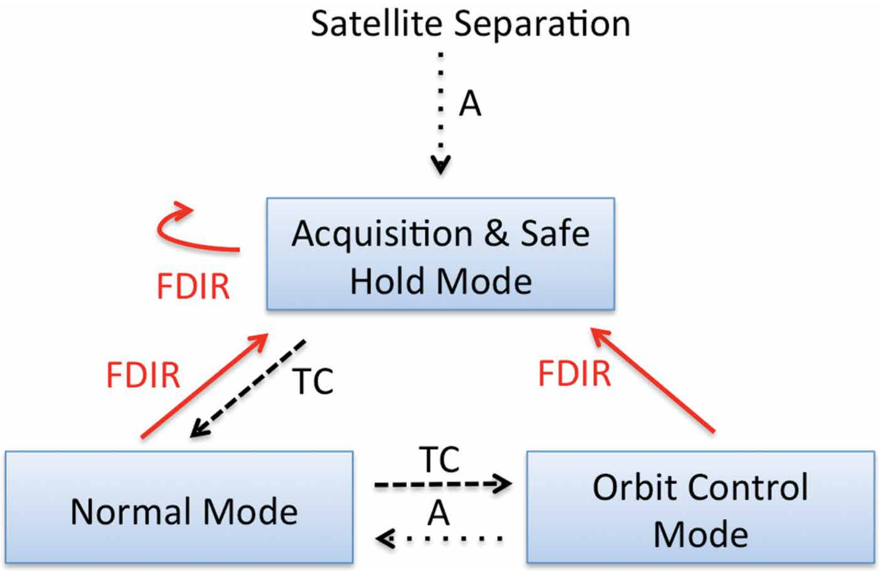

Figure 5.41. Concept A FDIR baseline. (Airbus Defence and Space)

Figure 5.42. Concept B FDIR baseline. (OHB)

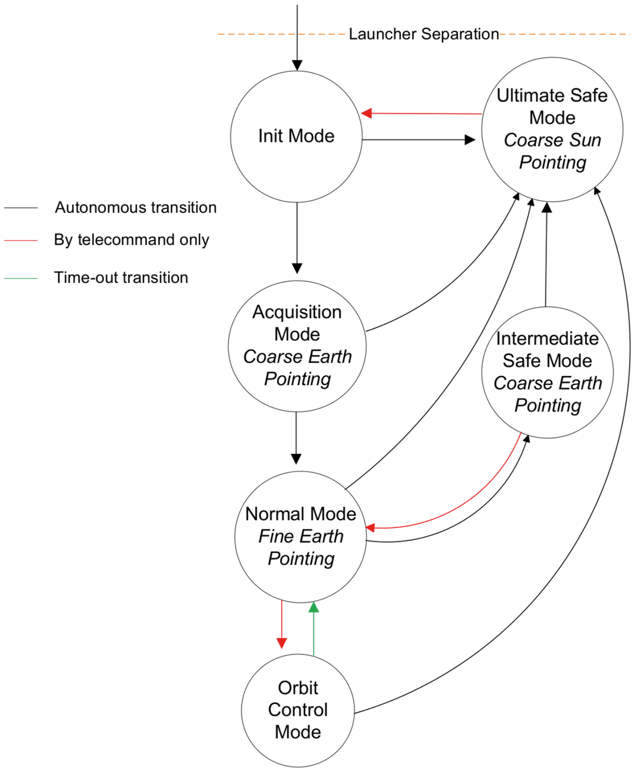

mode. The latter are used as main actuators in safe and acquisition mode, providing a coarse level attitude control.

Besides the magnetorquers, the actuator set consists of four reaction wheels, in tetrahedral configuration (one hot redundant), used as main actuators in nominal mode for attitude keeping and fast slewing manoeuvres in 3-axis control.

The monopropellant propulsion system is only used for orbit acquisition and orbit control. Several AOCS modes are defined:

Init Mode (IM) starts after satellite activation, OBC reset or as consequence of a detected critical failure. Its functions mainly include performing FDIR operations and AOCS initialisation.

Acquisition Mode (AM) is used after separation from the launch vehicle. Its main functions are to dump all angular rates and to bring the satellite into a stable Sun-pointing attitude.

Normal Mode (NM) for fine Earth pointing is the nominal AOCS mode and is used in all day-to-day satellite operations, as well as instrument observations/calibrations and downlink activities.

Intermediate Safe Mode (ISM) coarse nadir pointing is initiated after entering satellite Safe Mode. Its main function is to maintain a stable attitude, while optimising the power generation performance.

Ultimate Safe Mode (USM) Sun pointing is entered after detection of a failure in the AOCS (or general loss of attitude). Similar to Safe Mode, its main functions are to maintain a stable attitude, while optimising the power generation performance.

The FDIR Strategy is defined to fulfil the following main objectives (with heritage from Galileo):

- guarantee satellite integrity in case of safety critical anomalies
- optimise mission availability
- implement simple and generic anomaly recovery

5.3.4.10 Propulsion

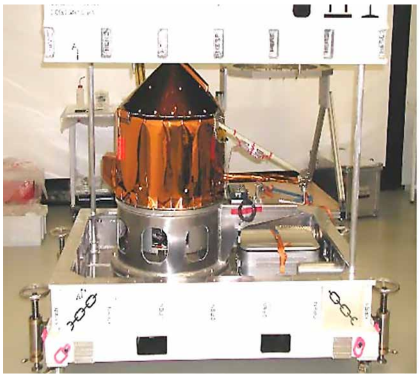

Figure 5.43. Concept A PM22 integrated propulsion module. (Airbus Defence and Space)

The propulsion system is needed for initial orbit acquisition and orbit maintenance throughout the mission as well as for collision avoidance manoeuvres. If necessary a final burn at end of mission will be performed to bring the satellite into an orbit that leads to an uncontrolled reentry within 25 years. The manoeuvre frequency is different for both concepts owing to the different orbit altitude and thus drag environments. According to regulations on space debris mitigation, the propulsion subsystems will be passivated at satellite EOL.

The baseline system of Concept A is the PM22 flight-proven propulsion system. This system is used to provide single-axis thrust in the satellite Z-axis during orbit control manoeuvres with pointing provided by the reaction wheels on the platform. The propulsion system is not required to generate torques since the reaction wheels are off-loaded by the magnetorquers. The PM22 has a minimum propellant mass of 62 kg and maximum of about 81 kg, using four 1-N flight-proven thrusters, with a predicted degradation during the mission from approximately 1.2 N to 0.5 N.

If thrusters fail, all orbital correction manoeuvres can still be performed with two out of four thrusters. A second latch valve has been added to the SEOSAT propulsion subsystem to remove the risk of single-point failure of the PM22.

The total ΔV worst-case estimate for CarbonSat is currently 102 ms^{-1}, which corresponds to approximately 48.5 kg of hydrazine for a monopropellant system. This is well within the PM-22 capability of 81 kg of hydrazine, including residuals, and thus there is a margin in excess of 39.5% on the total propellant mass.

In case of a single thruster failure, both the faulty thruster and its counterpart (symmetrically accommodated in the propulsion module) are deactivated. This way, a non-symmetric configuration during boost is avoided, which otherwise would cause a significant torque around either the roll or pitch axis. The reaction wheel cluster controls the attitude around those axes in that case.

Concept B also follows an off-the-shelf approach for the propulsion subsystem based on a hydrazine monopropellant solution.

The system uses a standard topology for hydrazine monopropellant systems. It accommodates two thruster branches of two pairs of 1-N thrusters

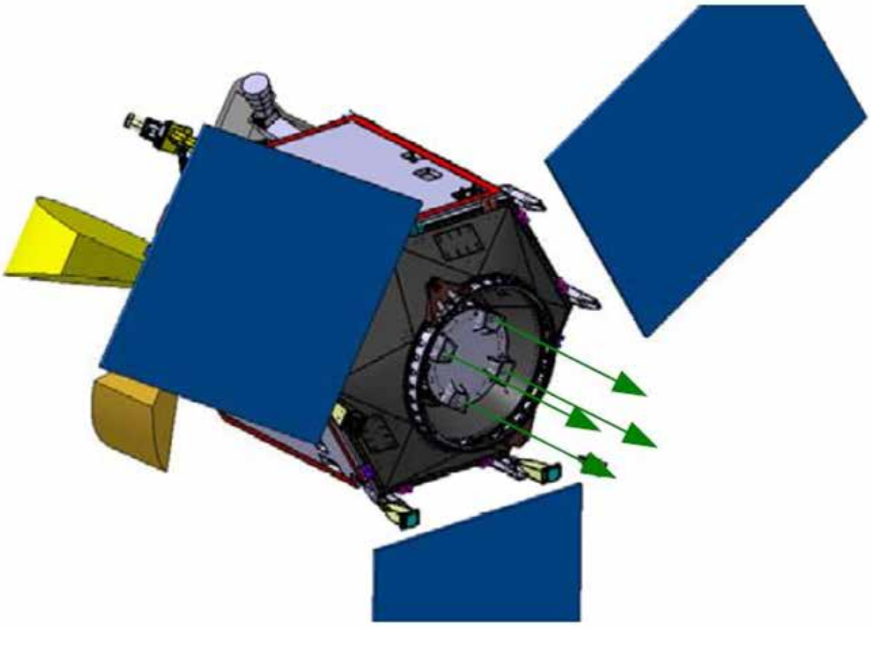

Figure 5.44. Concept A thruster configuration with direction of thrust indicated as on Sentinel-5 Precursor. (Airbus Defence and Space)

Figure 5.45. Concept B block diagram of the propulsion subsystem, an example of a monopropellant propulsion subsystem. (OHB)

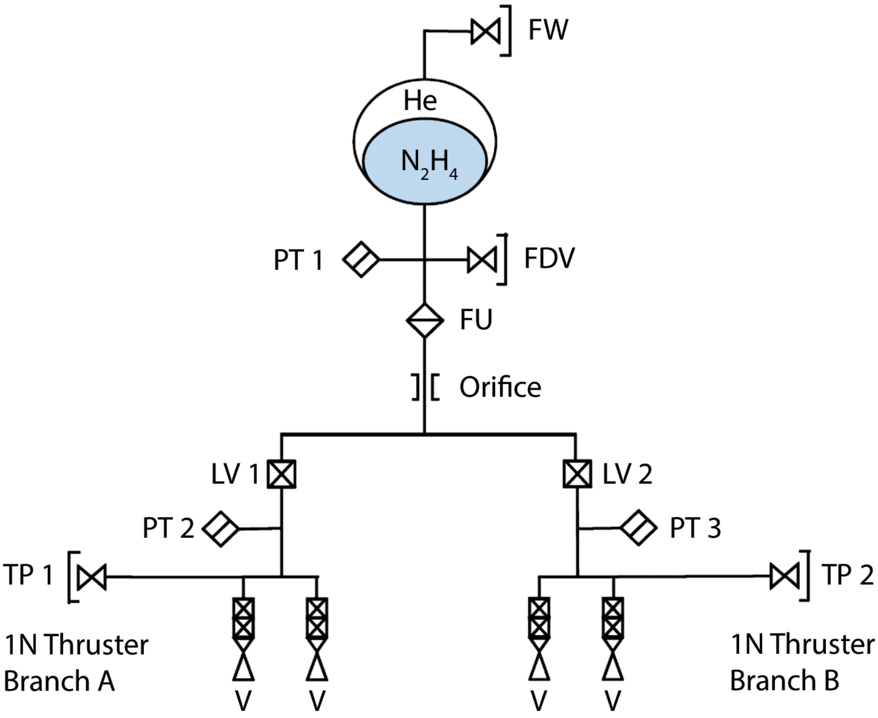

each, granting full redundancy. The thrusters will be accommodated via brackets on the panel the instrument is mounted on, such that the thrust vector will act through the satellite Centre of Mass (CoM). The thrusters will be accommodated with an intended off-axis angle of 15–20° on the brackets to exclude the risk of contamination by plumes. Thus the desired thrust can be applied without slewing the satellite. A plume impingement analysis was performed to quantify the risks associated with this configuration.

The torques generated are balanced by the companion thrusters on the opposite side of the platform. In case of the failure of a thruster, e.g. malfunction or open thruster failure, the system switches over to the redundant branch to minimise torque.

A non-pressure regulated diaphragm tank accommodates the hydrazine propellant and the helium pressurant gas. The size of the propellant tank is based on the estimated ΔV, which is 89.9 ms^{-1} for a five-year mission assuming the EOL specific impulse (I_{sp}) of 210 s for the hydrazine propellant and no additional margins. In summary, a five-year mission will require 50.8 kg of propellant. The MT-A tank PTD-96 offers a propellant mass storage of up to 68 kg, which would accommodate this requirement with margin for additional operations.

5.3.5 Budgets

5.3.5.1 Mass Budget

Table 5.5 reports the mass budgets for the two baselines and includes the following margins:

- harness: 30%
- completely new developments: 20%
- new developments derived from existing hardware: 15%
- existing units requiring minor/medium modification: 10%
- existing units: 5%

Table 5.5. Mass budgets for Concepts A and B. Total values are indicated in grey rows.

	Concept A [kg]	Concept B [kg]
Data Handling	25.8	30.46
Electrical Power S/S	95.8	95.3
Harness	74.9	52.6
X-band comm S/S	11.3	24.74
S-band comm S/S	7.0	7.8
AOCS	60.4	64.7
Structure	221.3	178.6
Thermal S/S	31.5	30.8
Propulsion	27.8	19.6
Balance Mass	60.0	0.0
Platform total	615.8	504.6
Payload total	160.0	213.0
Dry mass total	776.0	717.6
System mass margin	119.4	107.6
Dry mass incl. margin	895.4	825.2
Propellant + Residual	82.2	68.0
Pressurant	0.1	1.5
Wet mass	977.7	894.7
LVA	76.5	78.0
Total mass	1054.2	972.7
Launcher performance	1270	1392
Launcher performance contingency	–100	–100
Launch margin	115.8	319.3

Table 5.6. Delta-V and propellant budgets for Concepts A and B assuming a five-plus-two-year mission life, no gauging error included. Total values are in grey rows.

	Concept A		Concept B	
	Delta-V [ms^{-1}]	Propellant Mass [kg]	Delta-V [ms^{-1}]	Propellant Mass [kg]
Orbit injection correction	18.20	8.52	28.61	15.30
Orbit maintenance	9.36	4.48	64.07	33,30
Collision avoidance	4.36	2.09	3.02	1.5
Deorbit manoeuvre	70.41	33.44	0.00	0.00
Total	102.33	48.53	89.90	50.10
Propellant residuals	-	1.20	-	1.40
Propellant margin	-	32.47	-	15.50

An additional 15% margin at system level has been applied against unpredictable mass evolutions and/or balancing needs. An uncertainty margin of 100 kg is applied as Vega uncertainty margin; satellite propellant tanks are assumed to be fully loaded. The launch margins give good confidence on the robustness of the concepts with respect to the mass aspect.

Table 5.7. Power budgets for Concepts A and B.

Operating Mode	Concept A [W]	Concept B [W]
Initial acquisition	383	376
Decontamination mode	685	389
Safe mode	397	453
Orbit correction mode	467	489
Nominal mode, payload on nadir	451	466
Nominal mode, payload on sunglint	451	509
Payload on downlink X-band	584	561
White light source calibration	474	469

Table 5.8. Data rate and mass memory estimates.

		Concept A	Concept B
Instrument data rate [Mb s^{-1}]	Observation	14.85	18.37
	HSS	0.77	1.17
	Internal calibration	14.85	18.37
	External calibration	14.85	18.37
	Dark signal in eclipse	1.50	5.83
Downlink rate [Mb s^{-1}]		310	280
Mass memory requirements [Gb]		320	588
Mass memory size EOL [Gb]		480	640
Level-0 data $year^{-1}$ [Tb]		37	50
Level-1b data $year^{-1}$ [Tb]		179	200

Table 5.9. Geolocation performance for Concept A and Concept B.

	Concept A		Concept B	
	Performance [m]	Requirement [m]	Performance [m]	Requirement [m]
Nadir	341	400	287	400
Sunglint	569	793	434	780

5.3.5.2 Delta-V and propellant budget

The ΔV increments required for the two concepts and the respective propellant budgets are presented in Table 5.6. The different allocations of Concept A with respect to Concept B are due to the fact that they have different orbits. The propellant budgets presented include a 15% margin on all ΔV components.

5.3.5.3 Power budget

The summary of power budgets (including margins) for both concepts is presented in Table 5.7. Concept A's budget for the decontamination mode exceeds that of Concept B significantly since it has a margin of a factor of two regarding the thermal power needed. Furthermore, the power consumption for nadir and sunglint observation modes represents the average of both. The higher power consumption of Concept B in Safe Mode stems mainly from platform demand of thermal power.

For Concept A the power budget has been established using data available from the ongoing programmes from which the baseline platform is derived; for

Concept B, from analysis. The budgets include all applicable margins including 15% system margin. A margin of 20%, for new developments derived from existing hardware, has been applied to the GHGIS instrument power budget.

5.3.5.4 Data rate and volume budget

The data rate and volume budgets are presented in Table 5.8. The different data volumes are due to the different swath widths adopted by the two concepts, max. SZA in Southern Hemisphere (60° Concept A) and thus different coverage.

5.3.5.5 Pointing and geolocation budget

There are no specific pointing requirements defined at Level-1 for the mission. The pointing stability is constrained by the required integrated energy of a sample acquisition and the required coverage.

The achieved geolocation performance is reported in Table 5.9, both concepts meet the requirement of 400 m in nadir. For sunglint observations, the requirement is derived from the nadir one via a scaling law, which depends on the orbit. Concept B foresees an in-orbit bias calibration, whereas Concept A meets the requirements without it.

5.4 Launcher

For the satellite dimensions, the baseline launcher, namely Vega, is the smallest usable in terms of fairing diameter, which limits the satellite allowable envelope. In terms of payload mass, there is a good margin in view of the satellite mass, which is around 1000 kg. The transition to Vega-C (first launch envisaged in 2018 and which can be assumed to be completed by the time of the CarbonSat launch), provides additional margin. PSLV is selected as alternative for Concept A, which would require an adaptation of the top panel to meet the launcher requirements. Concept B assumes Vega as the baseline launcher and PSLV-XL as a suitable backup.

Figure 5.47 shows the accommodation of Concept A in the Vega and PSLV fairings, and Fig. 5.48 shows accommodation in the Vega and PSLV fairings for Concept B. No geometrical interferences occur between the satellite and launcher envelope. Simulations show compatibility with the launch environment for

Figure 5.46. Vega launcher. (ESA)

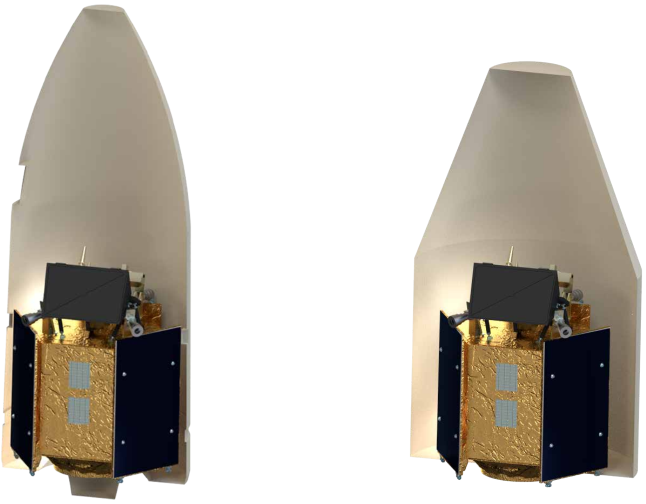

Figure 5.47. Concept A accommodation in the launcher Vega fairing (left) and PSLV fairing (right). (Airbus Defence and Space)

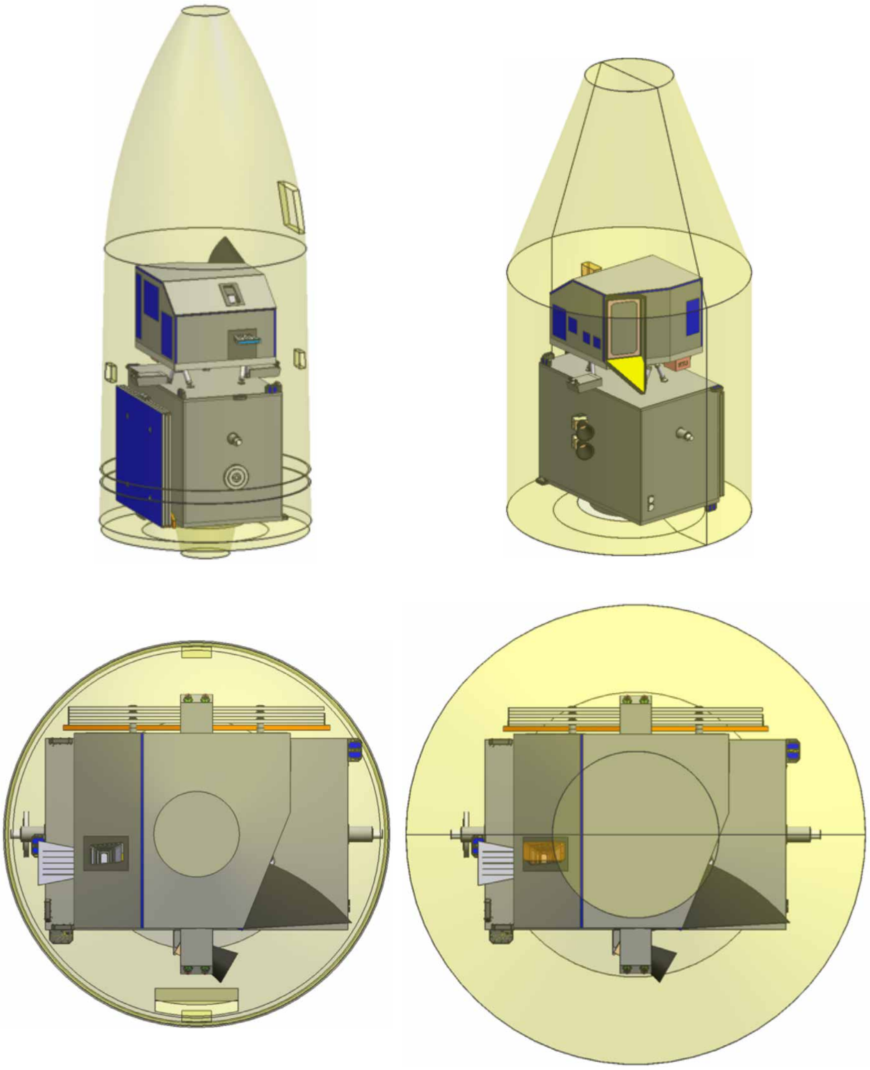

Figure 5.48. The Concept B accommodation in the launcher Vega fairing (left) and the PSLV fairing (right). (OHB)

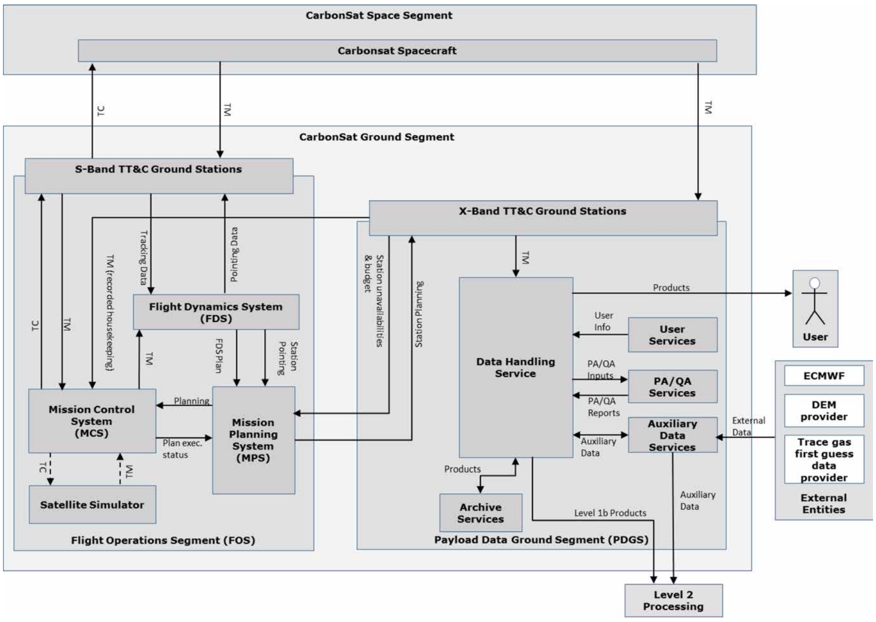

Figure 5.49. General CarbonSat ground segment architecture. (OHB/GMV)

baseline and backup launchers for both concepts, although for Concept A compatibility with PSLV can only be achieved with a modified top panel.

5.5 Ground Segment and Data Processing

5.5.1 Ground Segment Elements

The CarbonSat GS consist of two main elements, namely the FOS and the PDGS. The FOS includes the TT&C ground station and the Flight Operations Control Centre. The TT&C ground station provides the following main functions:

- housekeeping telemetry acquisition
- telecommand uplink
- satellite tracking
- data connection to the Flight Operations Control Centre

During LEOP, a dedicated ground station network, using Estrack core and enhanced stations where possible, supports operations. The Flight Operations Control Centre, based at ESA's European Space Operations Centre, ESOC, will provide the following main functions:

- satellite monitoring and control
- flight dynamics and manoeuvre planning
- TT&C ground station network and control
- overall satellite operations planning
- onboard software maintenance
- mission simulation
- FOS supervision
- spacecraft system data distribution
- interface with the launch site for LEOP

The PDGS is primarily responsible for receiving the science data from the satellite, applying the appropriate processing algorithms and delivering the resulting products to the users. It consists of the following functions:

- payload data acquisition and ingestion function for downlink of science data telemetry
- processing function
- archiving function
- dissemination function
- mission planning function
- quality control and Calibration/Validation (Cal/Val) function
- monitoring and control function
- user services

5.5.2 Flight Operations Segment

The FOS is based on existing ESA hardware and software infrastructures, adapted where necessary for CarbonSat.

5.5.2.1 FOS operational approach

The mission operations are automated, as far as possible, to minimise risk and to limit the size of the operations team. Operations support is restricted to normal working hours, i.e. five days per week. Out of hours, on-call engineers can be alerted automatically should a serious anomaly be detected. A serious anomaly is one that threatens system availability, such as significant data loss or danger to the health of the satellite. The latter should, in principle, be excluded thanks to the spacecraft autonomy. Other anomalies are only investigated during working hours.

Contacts with the FOS ground station via the TT&C are limited to those necessary for the uplink of the mission plan for nominal operations. This is foreseen in the order of every five to seven days, taking full advantage of the spacecraft autonomy. During commissioning, a number of contacts per day during the first three days are expected. In view of the low frequency of TT&C passes, regular spacecraft health monitoring is assured via recorded HKTM data, downlinked in X-band and forwarded to the FOS from the PDGS. Frequency and latency are not critical, but nominally the TM would be acquired at each pass and forwarded as a single file after reception. Near-realtime planning is not required.

5.5.2.2 FOS–PDGS interface

The FOS and PDGS are kept as independent as possible. In particular, payload data are not processed by or transmitted through the FOS. Data exchanged between FOS and PDGS includes mission-planning requests and results (no user requests are foreseen), orbit data, recorded HKTM data from PDGS to FOS, and processed HKTM data from FOS to PDGS. Existing interface formats and specifications supported by the ESA infrastructure software are used wherever possible.

5.5.2.3 Telemetry, tracking and command

The baseline S-band TT&C ground station is located in Kiruna, Sweden. Both realtime telemetry and telecommand functions are transmitted in S-band. No modification to the Kiruna ground station equipment is needed to support the CarbonSat mission. The primary source for orbit determination in the routine operation phase is the onboard GNSS receiver. The principal task for TT&C passes in routine operations is the uplink of telecommands. Realtime housekeeping telemetry will also be acquired during these passes, but is not the driver for the minimum number of required passes. The TT&C ground station is not dedicated to CarbonSat, but shared with other missions. The Estrack Management and Scheduling System (EMS) performs allocation planning for both TT&C and PDGS, in cooperation with the Mission-Planning System (MPS). EMS also generates the detailed operation schedules executed by the Estrack ground station monitoring and control systems.

5.5.2.4 Mission control system

The Mission Control System (MCS) is based on the Earth Explorer MCS (EEMCS), which is an extension of SCOS-2000. The EEMCS is continuously upgraded with the functionality needed for specific missions. A degree of customisation of the system is likely to be necessary for CarbonSat, including some functional modifications depending on the satellite design, ground interface specifications, the final operations concept, and the existing capabilities of the EEMCS at the start of implementation.

5.5.2.5 Flight dynamics

No mission-specific modifications to the ESA flight dynamics infrastructure will be needed. Flight dynamics is a service provided to missions, which delivers orbit information and event files to the various planning entities as well as the orbital predictions used by the Estrack ground stations. It also generates command sequences that are transferred to the MCS directly or via the MPS. Flight dynamics receive radiometric measurements from ground stations as well as satellite data, including GNSS tracking data from the MCS.

5.5.2.6 Mission-planning system

The FOS MPS is based on the EEMCS mission-planning kernel. It generates schedules for execution by the EMS as well as command sequences for uplink to the spacecraft. The MPS will require configuration for mission-specific rules and constraints. As for the MCS, some functional modifications may be needed, but no specific functional adaptation has been identified as necessary at this stage. The Estrack Management and Scheduling is responsible for planning the ground station allocation to missions supported by Estrack, and generation of detailed ground station schedules.

5.5.2.7 Simulator

The spacecraft simulator is built using the SIMSAT infrastructure, existing ground models and the generic dynamics and space environment models. Spacecraft subsystem models will in general need to be developed specifically for CarbonSat, though reuse will be possible for heritage subsystems already modelled in predecessor simulations. The onboard flight software is executed on an emulator.

5.5.2.8 FOS implementation

A single S-band TT&C ground station (Kiruna) with an average of one contact in five to seven days is assumed. As current baseline the TT&C ground station is collocated with the science-data downlink station. A dedicated ground station network supports operations during LEOP.

In general, the ground segment architecture is fixed and based heavily on existing ESA hardware and software. The goal is to limit operations costs by reducing TT&C access to the spacecraft while increasing the level of onboard autonomy.

Regardless of the operations model selected for the nominal phase, the FOS development will still have to prepare for all reasonable eventualities. The move towards office-hours-only support and automated monitoring and alarming during nights and weekends is a natural evolution of the operations concept. Apart from this, the design of the FOS is familiar in terms of the functional blocks to be used: the MCS will be based on the MCS Earth Explorer Kernel, the Mission Automated System will execute control procedures and schedules, and in general the ESA Ground Operations System infrastructure will be employed.

5.5.3 Payload Data Ground Segment

This section details the main functions and features of the CarbonSat mission PDGS.

5.5.3.1 Acquisition and ingestion

Science data, along with recorded HKTM, will be transmitted via X-band to the ground station, nominally placed in Kiruna. Since CarbonSat has no near-realtime requirement and the data latency requirement for Level-1b products is set to 48 hours, the selection of the X-band station is mainly driven by the need to avoid completely filling the onboard memory. A single station located at the latitude of Kiruna or higher is sufficient to support the mission.

5.5.3.2 Processing

The scientific data downlinked to the ground station are systematically processed up to Level-1b, generating the radiance, irradiance and reflectance products, along with intermediate Level-0 and Level-1a products. The user segment will generate the higher-level products.

5.5.3.3 Archiving

The Level-0, Level-1a and Level-1b products will be systematically generated and archived by the PDGS archiving function. The approximate total amount of data resulting from the Level-0 and Level-1b products generated will amount to 212 Tb for Concept A and 250 Tb for Concept B per year, which includes capacity to store products from two previous reprocessing campaigns. The archiving function also interfaces with the user services to provide access to products and auxiliary data to users.

5.5.3.4 Reprocessing

Besides the reprocessing of limited reference datasets, usually handled by the main processing facility, systematic bulk reprocessing following e.g. upgrades of the processors on the ground is supported by a separate infrastructure. In view of the important computing resources required over a limited time by bulk reprocessing campaigns, the current trend is to procure reprocessing as a service relying on shared resources.

5.5.3.5 Mission planning

This function is in charge of defining the plan of activities for the GHGIS instrument. This function is also in charge of planning X-band downlink activities over acquisition stations. For the generation of the payload plan the mission planning will implement a set of CarbonSat specific rules and constraints, covering instrument swath model and operations constraints, definition of areas to be observed in a specific mode, ground station visibilities, ground station and payload availability, recording and downlink rates, calibration requests etc. In principle, the CarbonSat mission acquires data systematically within the general observation constraints (mainly max. SZA in the northern and southern hemispheres and glint or no glint orbits). No implementation of specific user observation requests is foreseen.

5.5.3.6 Calibration facility

The main functions of the calibration facility are:

- processing of inflight calibration measurements and update of onboard instrument settings or calibration parameters used by the ground processors, as required
- identification and characterisation of deviations based on the processing of inflight calibrations or vicarious measurements that may trigger payload planning requests (e.g. additional inflight calibrations) or possibly processor evolution
- support to calibration/validation users (provision of special calibration products)
- configuration control of the instrument calibration databases. Further details about instrument calibration can be found in Subsection 5.3.3.4

The calibration relies on the key data recorded during a complex on-ground calibration campaign, which characterises the instrument in terms of radiometric and spectral response. This database needs to be constantly updated/complemented by calibration data measured inflight plus instrument health monitoring.

Concept B needs to perform an inflight bias calibration to achieve the required absolute geolocation accuracy.

5.5.3.7 Instrument performance and monitoring

The quality control function is responsible for the continuous assessment of the quality of the products as well as to ensure that the products meet a minimum level of quality prior to distribution. The function is generally split into several sub-functions:

- a service in charge of systematic control of all generated products prior to their distribution to users
- offline tools allowing specific analyses on products, triggered by feedback from users
- the quality control function is supported by a long-term sensor performance function, which allows key parameters of the payload to be monitored

5.5.3.8 Monitoring and control

The main objective of the Monitoring and Control function is to ensure that the PDGS fulfils its objectives, particularly in terms of performance and availability.

5.5.3.9 User services

ESA pursues a policy of developing a multimission infrastructure for the distribution of data products to end users. The user services will support data product browsing, access and visualisation, and provide general information on the mission status and a help desk.

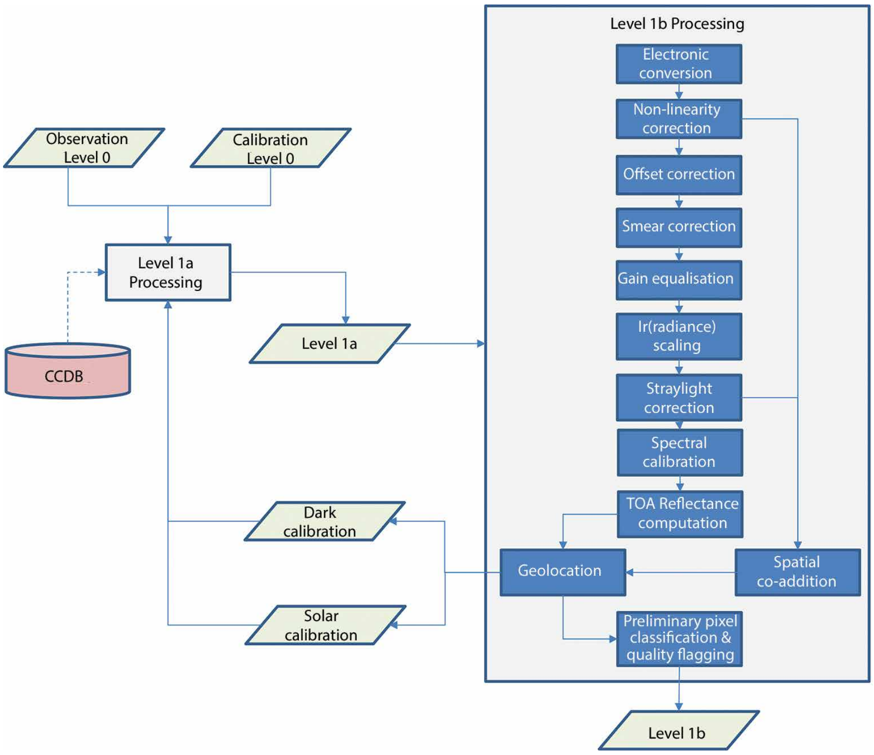

Figure 5.50. CarbonSat Level-1b ground processor flow diagram. (OHB/GMV)

5.5.4 Mission Data Processing

A mission-specific ground processor is required to provide the end users with Level-1b data for higher-level processing up to Level-2 and above. Processing of the data from Level-0 to Level-1b does not necessitate access to additional information other than the calibration parameters.

In summary, the ground segment for the CarbonSat mission does not present any new technology or infrastructure. The principal mission-specific development activities are the ground processor and the access to meteorological fields (e.g. European Centre for Medium-range Weather Forecast (ECMWF)) and Digital Elevation Model (DEM), depending on the algorithms used and first guess CO_2 and CH_4 data for Level-2 processing. In this section the baseline for the data processing chain is proposed, as shown in Fig. 5.50.

The example Level-1b processing shown in Fig. 5.50 applies to both observation and calibration modes. The calibration modes follow part of the processing of the observation mode, taking as input the calibration Level-0 products (Sun and dark). The Characterisation and Calibration Database (CCDB) stores the parameters that characterise the instrument, although this database will not normally be directly accessible by the processing. Additional auxiliary data such as processing parameters and data from external sources (e.g. land/sea map) will be required in addition.

The main Level-1b products will be Earth's radiance, Sun irradiance, Earth's reflectance and HSS data. The observed data is spatially binned onboard, while HSS data is spectrally binned onboard. The Level-0 to Level-1b processing applies all the conversions from measured electrons in the detectors to radiance and irradiance. A number of corrections are applied using key data from on-ground and inflight calibration (e.g. smear correction for CCDs, non-linearity, gain, dark current, straylight etc.) to yield radiometric calibrated data.

In a next step the observed radiance and irradiance data are spectrally calibrated using the key data from on-ground and inflight calibration.

Operational Phase	Duration
LEOP	<1 week
Commissioning	~4 months
Nominal Operations Phase	3 years
Extended Operations Phase	2 years
Additional Operations Phase	2 years
EOL	3 months, reentry <25 years

Table 5.10. Mission phases and durations, the range is given for both concepts.

To derive reflectance, the radiance and irradiance have to be interpolated to the same spectral grid. The geolocation is assigned to the samples and they are flagged as sunglint or nadir.

5.6 Operations and Utilisation Concept

CarbonSat observations are based on a systematic recording of Earth's reflectance in two observation modes, allowing for a high level of autonomy for both space segment and ground segment. Table 5.10 gives the mission phases and durations, which have similar values for both concepts.

Each of the mission phases is described below from the standpoint of operations.

5.6.1 LEOP and Commissioning

The LEOP covers the period from switch-over to internal power on the launch pad until the satellite is in its deployed configuration in orbit and the AOCS is operating in Normal Mode. The duration of the CarbonSat LEOP is estimated to be a maximum of seven days. The first part of the LEOP sequence is performed autonomously and only requires ground intervention if deployment fails. Upon completion of the sequence, S-band communications will be initiated and an initial satellite checkout will be performed to confirm success of the sequence. The next steps will take the satellite from the Initial Acquisition Mode to the Normal Mode. After completion of a further checkout to confirm that the nominal attitude is being maintained, the launcher dispersion corrections will be completed. This concludes the LEOP activities and triggers the start of the commissioning activities. An outline of the LEOP phase, based on Concept A, is given below:

- launch
- ascent
- separation of satellite from the launch vehicle
- switch-on of S-band transmitter
- solar array deployment
- rate damping using magnetic torquers
- Sun pointing during Sun phase and B-dot law during eclipse with a rotation around the pitch axis

Figure 5.51. Example for a sequence of routine operations, Concept A. (Airbus Defence and Space)

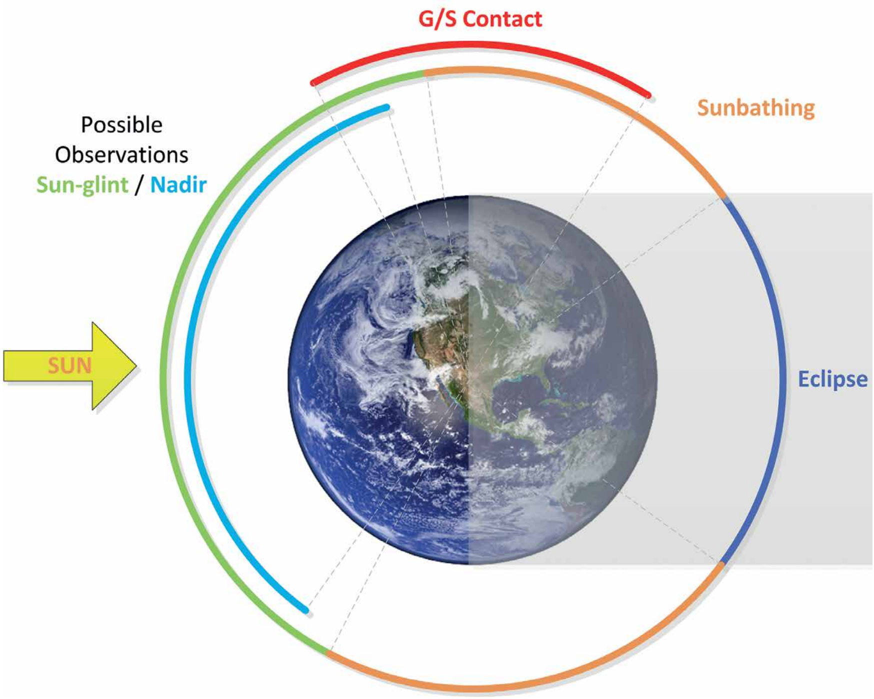

- AOCS equipment activation by Flight Control Procedure: activation and checkout of AOCS equipment required for Normal Mode operation
- switch to AOCS Normal Mode: acquisition of precise 3-axis attitude control based on the available precision position and attitude knowledge
- orbit correction as needed: execution of orbit control manoeuvres to correct for launcher injection errors

The commissioning phase concerns both platform and payload and will last nominally for four months. This phase consists of the complete characterisation of the performance of the platform, payload and ground segment to verify that the system is ready for the transition into the routine operational phase and to ensure that the GHGIS payload is calibrated.

The first part of the commissioning phase will be used to perform in-orbit functional and performance tests of all platform subsystems, including the payload data handling subsystem. Upon completion of the platform commissioning activities, the spacecraft will be in the operational attitude and orbit with the AOCS in Normal Mode. At this point, commissioning of the payload can begin. During the payload commissioning phase, the instrument functionality will be exercised over its full operational range with respect to all modes. For each state, HKTM and product annotations will be monitored to verify that the instrument responds correctly to commands. Level-0 products obtained in all the operational states of the instrument will be verified by monitoring a range of parameters and comparing them with expected values. To secure the instrument performance the instrument will be kept in a ‘hot’ state until decontamination is over. This prevents the formation of cold traps for particles resulting from outgassing caused by the transition from ambient pressure and temperature to a vacuum.

For Concept A, a shutter protects the instrument radiator from Sun-impingement during LEOP until solar arrays are deployed, nominal power supply is established and the AOCS is in Normal Mode. This also ensures that the instrument does not cool down during the initial phase until the power for decontamination is available.

5.6.2 Routine Operations

In the operational phase, the GHGIS instrument will take imagery according to the acquisition plan. Nadir and sunglint observations will be recorded in a repeating pattern, as well as the calibration sequences. The mission concept allows a high level of autonomy; operations will be executed according to a sequence of commands uploaded from ground. This schedule will be uploaded typically once every five to seven days. The Nominal Operations Sequence repeats with the orbit repeat cycle except the nadir/glint orbit allocation. Routine mission operations around the orbit are illustrated in Fig. 5.51. In-Plane manoeuvres are usually executed over the North Pole, Out-of-Plane manoeuvres at the equator. Sun calibration takes place over the South Pole, after the sunlit part of the orbit in anti-flight direction, dark calibration in eclipse and with the instrument shutter closed, also in the sunlit part of the orbit.

5.6.3 Contingency Operations

The CarbonSat satellite is designed to survive for up to 72 hours in the case of a single failure. A hierarchical FDIR concept is employed, which will fall back to safe mode only for serious failures. The mission will not continue operations in case of a major failure.

The FDIR design follows the common concept tailored in five failure levels, based on the degree of intervention:

Level-0 failures are those associated to an internal single failure in one equipment unit, which can be automatically recovered by the unit itself without any impact on the rest of the system hardware devices or software applications. This level of functionality is fully autonomous and may be transparent to the FDIR system.

Level-1 failures happen when the unit cannot autonomously recover. The surveillance is performed by the onboard software (OBSW) through a simple health check on acquired parameters and recovery actions are ordered. The failures might also require ground intervention.

Level-2 failures are identical to those in Level-1 as they are recovered completely by the OBSW. However, they are not confined to a single subsystem and may require recovery actions across several subsystems. The detection of these failures is based on the monitoring of subsystem health and status information and cross-correlated checks of acquired parameters.

Level-3 failures are OBC internal and cannot be neutralised autonomously by the OBSW, and, as such, are distinctly more severe than Level-0 failures. The recovery is done by hardware via the OBDH reconfiguration module.

Level-4 failures are those that have not been detected and recovered at lower levels and managed completely by hardware through proper independent system alarms hardwired to the relevant reconfiguration module. These failures are considered as global satellite malfunctions. A fundamental aspect of an FDIR approach is that survival of the satellite has priority over availability during all phases of the life of the satellite. To ensure satellite safety, the transponder is completely managed in hot redundancy, i.e. fail operational without outages. All FDIR functions implemented in the OBSW are triggered by parameter values stored in the satellite. These functions can be enabled or disabled via TC from the ground and may be adapted and set according to the operational needs. A history log stores any FDIR data for investigation on the ground. The ground station has the final overall control over all failure recovery activities, even if the satellite performs them autonomously.

5.6.4 EOL and Space Debris Mitigation

Both concepts include the passivation of the satellite at EOL, as required. An orbit decay and subsequent reentry within 25 years has to be guaranteed to ensure compliance with space debris mitigation requirements. A maximum casualty risk of 10^{-4} is required and, as the initial design exceeds this value, measures to lower the risk below the threshold need to be implemented based on design-to-demise concepts. Both consortia assumed an overall extended mission duration of 7.5 years, with a launch in 2022–23. Concept A implements a perigee lowering approach that actually guarantees reentry within ~2.5 years, with an estimated ΔV for the EOL disposal manoeuvre of ~138 ms^{-1}, so impacting the fuel budget heavily. The lower baseline orbit of Concept B actually results in reentry after ~15.5 years without any intervention after ceasing orbit maintenance manoeuvres. To minimise the casualty risk, which increases over time with population density, an EOL disposal manoeuvre as for Concept A is planned, to achieve an uncontrolled reentry in ~5 years.

To assess the casualty risk, the Debris Risk Assessment and Mitigation Analysis (DRAMA) tool was used by both consortia, requiring a number of assumptions to be made e.g. the altitude at which the satellite will break up. For Concept A, existing SCARAB simulations were used for consistency checks and to scale the DRAMA results (SCARAB simulations exist for the platform and a similar kind of instrument). 100% of the mass is accounted for in the simulations. The resulting casualty risk is calculated to be on average $2{\times}10^{-4}$ for an uncontrolled reentry in the year 2036. For Concept B, the SESAM/SERAM module of DRAMA v2 was used, calculating the casualty risk with the SARA module. The survivability of the components was calculated in the tool for varying atmospheric densities (11 cases within nominal density ±20%). The simulations account for ~90% of the total mass, taking into account 515 objects described as plates, boxes, spheres or cylinders, each composed of a single material out of 13 materials characterised by density, melting point, specific heat capacity, heat of fusion and emissivity. Assuming an uncontrolled reentry in the year 2040. An additional de-orbit manouvre would reduce the risk further in line with the proposed schedule, results in a casualty risk of $7.0{\times}10^{-5}$.

DRAMA is in general a conservative tool, based on a number of worst-case assumptions. At this stage the inherent uncertainty is still significant, and a more in-depth analysis using more advanced tools and descriptions for platform and instrument is necessary in future. Of course, a source of inherent uncertainty, independent of the tool, is the assumption on the population growth until the calculated reentry year.

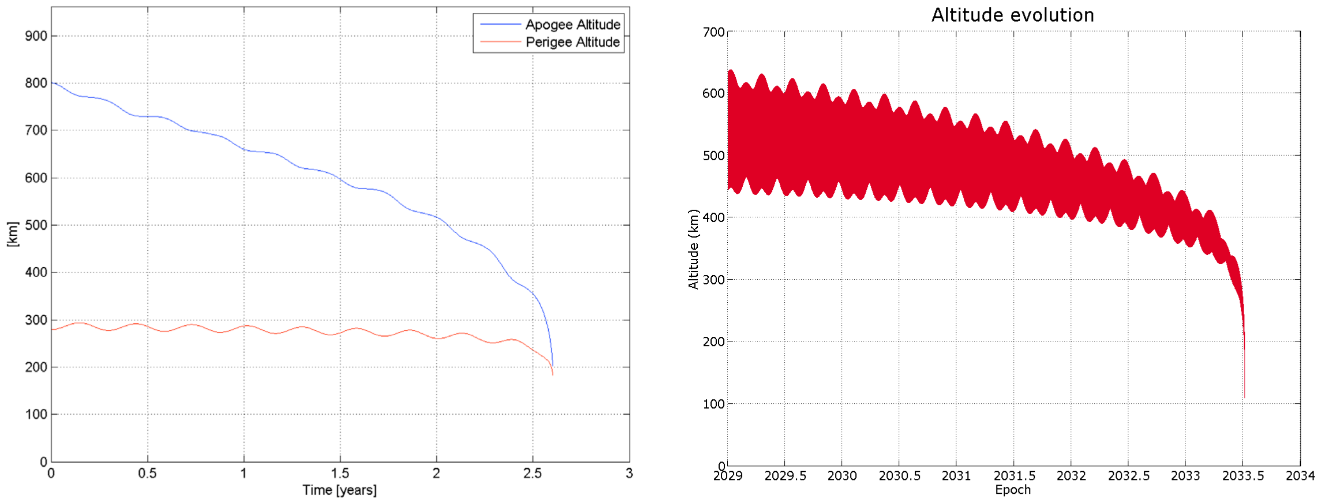

Figure 5.52. Deorbit timeline for uncontrolled reentry for Concept A (left) (Airbus Defence and Space) and Concept B (right). (OHB/GMV)

→ SCIENTIFIC DATA PROCESSING AND VALIDATION CONCEPT

6. Scientific Data Processing and Validation Concept

6.1 Introduction

The atmospheric data products (Level-2) are the column-averaged dry-air mole fractions of CO_2 and CH_4, denoted as XCO_2 and XCH_4 (explained in Fig. 1.1). These products are derived from calibrated, spectral reflectances or radiances as measured in nadir or sunglint mode (Level-1 products) using Level-1 to Level-2 retrieval algorithms. An overview of the processing chain is presented in Fig. 6.1. The Level-1 data are obtained from the uncalibrated, raw measurements (Level-0 products) by applying radiometric and spectral calibration. The Level-4 products, which are CO_2 and CH_4 surface fluxes, i.e. the source/sink products, are generated from the Level-2 dataset using data assimilation and inverse-modelling methods.

This chapter outlines the basic methods (Section 6.2) and state-of-the-art processing schemes (Section 6.3) needed to retrieve XCO_2 and XCH_4 from the spectral observations in the near-infrared/shortwave-infrared (NIR/SWIR) spectral region and it presents the concepts for validating these retrievals (Section 6.4). Furthermore, an overview of the methods required to generate higher level data products is given (Section 6.5).

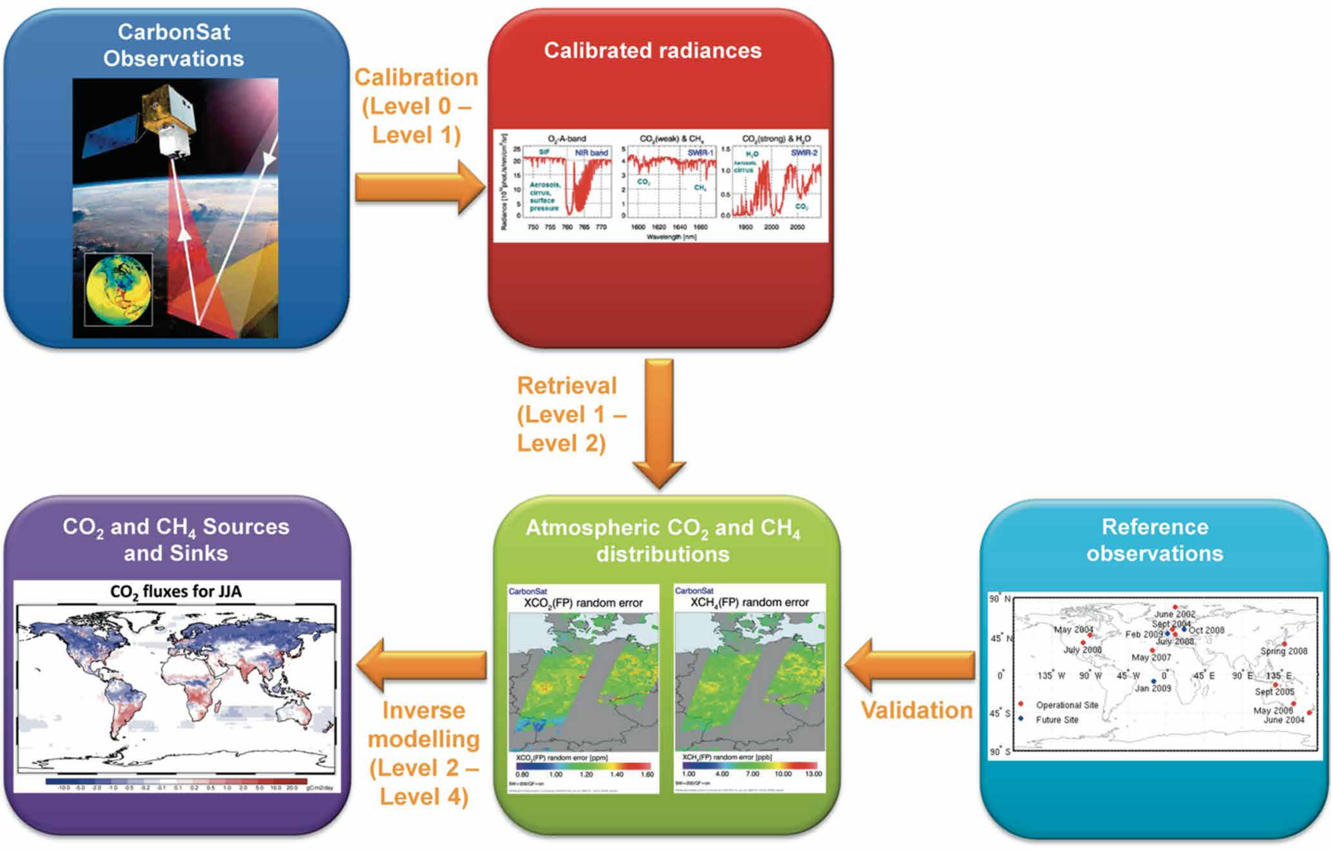

Figure 6.1. Overview of the processing chain from uncalibrated, raw measurements (Level-0) to calibrated radiances (Level-1), atmospheric products (Level-2) and, finally, to sources and sinks (Level-4). (H. Boesch–University of Leicester)

6.2 CarbonSat Radiances and Retrieval Concept

A typical radiance spectrum is shown in Fig. 6.2. It shows the radiances in the three spectral bands of CarbonSat, denoted as NIR, SWIR-1 and SWIR-2. The essential information provided in different parts of the spectral bands is highlighted in different colours. The spectral region to obtain information on Solar Induced Fluorescence (SIF), which is used for correction in the retrieval, is indicated in purple. The spectral range dominated by H_2O absorption, which provides additional information on the presence of cirrus clouds, is indicated in grey. Other interfering parameters, such as aerosols and clouds, are indicated in the similar Fig. 4.8.

Gas molecules such as CO_2 and CH_4 can absorb electromagnetic radiation, which excites different vibrational and rotational states of the molecules. The characteristic wavelength-dependence of this absorption is described by the 'absorption cross section', which is a unique spectral fingerprint of a molecule and can be measured with high accuracy in the laboratory. Of particular interest for CarbonSat is the absorption of solar radiation by CO_2 and CH_4 in the SWIR range of the spectrum. Assuming that the path of solar radiation in the atmosphere can be modelled well enough using an appropriate radiative transfer model, the spectral modulation of the measured radiance together with the spectral fingerprint information can be used to identify which gas is present in the atmosphere and how much is present.

The absorption of light is described by the well-known Lambert-Beer Law, which is the simple form of the radiative transfer equation:

$$I(\lambda) = I_0(\lambda) \times e^{-\tau(\lambda)} \tag{6.1}$$

This equation allows the computation of spectral radiance, $I(\lambda)$, after the light has passed through a well-defined path characterised by optical depth $\tau(\lambda)$. Here, $I_o(\lambda)$ is the incoming radiation, e.g. solar radiation before entering the atmosphere. For a well-defined single light path L, the optical depth is given by:

$$\tau(\lambda) = \int_L c(l) \times \sigma(\lambda, l)\, dl \tag{6.2}$$

with c being the concentration of the gas of interest and σ its absorption cross section.

For CarbonSat, however, a more complex form of the radiative transfer equation has to be used, as both single and multiple scattering must be considered, i.e. the light will typically not travel along a single, undisturbed

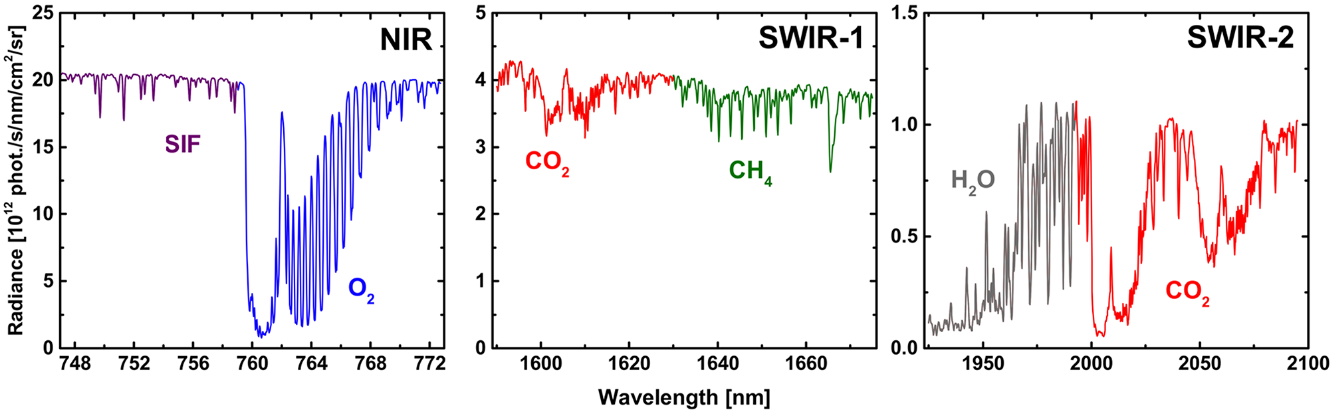

Figure 6.2. Simulated CarbonSat radiance spectrum assuming typical conditions. The spectral line absorption signatures of CO_2 (red), CH_4 (green) and O_2 (purple) are clearly visible. (H. Boesch–University of Leicester)

path through the atmosphere, but along multiple paths. Furthermore, the radiative transfer equation needs to be inverted to extract information on the atmospheric composition from the measured radiances. This inversion (or retrieval) of XCO_2 and XCH_4 data products is based on a well-established method that compares measured radiance spectra to spectra simulated with a radiative transfer model. The main ideas of the retrieval method are described in the following paragraphs.

As shown in Fig. 6.2, CarbonSat will measure reflected and scattered sunlight in the spectral region covered by the CO_2 and CH_4 absorption bands centred around 1.6 microns (SWIR-1 band, Fig. 6.2, middle). This relatively transparent SWIR-1 band is the main band needed to obtain information on columns of CO_2 and CH_4 with high sensitivity down to Earth's surface. However, this band alone is not sufficient to meet the demanding accuracy requirements for XCO_2 and XCH_4 products. Clouds and aerosols cause (multiple) scattering of light in and out of the observed volume of air, changing the path of light through the atmosphere and, thereby, changing the radiance measured by the instrument. To still meet the accuracy requirements, two additional bands are needed, covering a strong absorption band of O_2 at shorter wavelengths (NIR band, Fig. 6.2, left) and strong absorption bands of CO_2 and H_2O at longer wavelengths (SWIR-2 band, Fig. 6.2, right). Since the O_2 mole fraction of dry air is well known, changes of the retrieved O_2 column can be used to quantify light path variations owing to clouds and aerosols and to convert the measured O_2 column into the dry-air column or surface pressure. The CO_2 and H_2O bands in SWIR-2 provide additional information on aerosols and clouds (e.g. thin cirrus clouds). Only the combination of all three bands observed by CarbonSat allows the measurement of atmospheric columns of CO_2 and CH_4, corrected for variations in light-path length. This approach is also used for other greenhouse-gas missions such as GOSAT and OCO-2.

The mathematical approach for the retrieval of CO_2 and CH_4 concentrations from the observations applies the well-established optimal estimation method (Rodgers, 2000) where the three spectral ranges measured by CarbonSat are simultaneously fitted to infer information on CO_2 and CH_4 abundances together with meteorological parameters (temperature, humidity, surface pressure), aerosols, cirrus clouds and surface reflectance. These retrieved parameters form the state vector $\mathbf{x}$. An optimal value for $\mathbf{x}$ is inferred by minimising a cost function χ^2 with a non-linear, iterative scheme that combines *a priori* information with the information provided by the measurement in an optimal way, weighted by their respective uncertainties. The scheme makes use of the Jacobian matrix $\mathbf{K}$, where elements are the change of the (simulated) observation $\mathbf{y}$ with respect to a perturbation of the elements of the state vector $\mathbf{x}$. The columns of this matrix are spectra showing the sensitivity to a change (perturbation) of a certain state vector element. For example, if the CO_2 concentration at a certain altitude is changed in the model atmosphere, the corresponding column of $\mathbf{K}$ shows a spectral profile in which the locations of all the CO_2 absorption lines are clearly visible (see Fig. 6.3). The figure also shows a zoom (with values multiplied by a factor of 13) for SIF in the spectral region around 755 nm and for CO_2 in the SWIR-1 band.

A key advantage of the employed retrieval scheme is that it not only provides the main variables XCO_2 and XCH_4, but also other quantities essential for users of Level-2 products. The error covariance matrix $\mathbf{S}_x$ provides an estimate of the random errors of the retrieved parameters and of the correlations between them. The averaging kernel matrix $\mathbf{A}$ characterises the altitude sensitivity of the retrieval and the dependence of the result on the *a priori* information. For CarbonSat, the values for the averaging kernels in the troposphere show sensitivity to atmospheric layers near the surface. The values are close to unity, which means that changes in the atmospheric mixing ratios throughout the troposphere are fully mapped into the retrieved total columns.

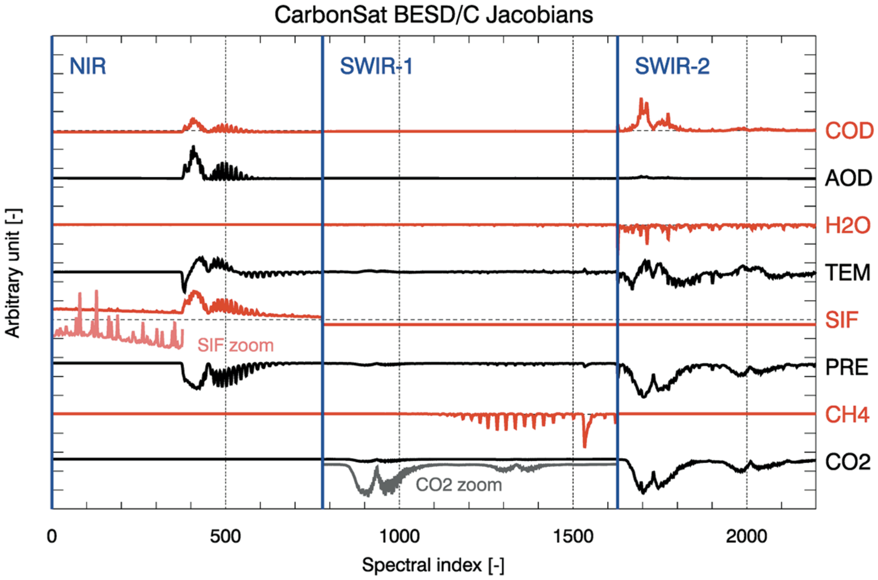

Figure 6.3. Typical example of a CarbonSat Jacobian matrix K, which represents the sensitivity (i.e. spectral response) to cirrus optical depth (COD), aerosol optical depth (AOD), water vapour (H_2O), atmospheric temperature (TEM), solar induced fluorescence (SIF), surface pressure (PRE), CH_4 and CO_2. (M. Buchwitz–IUP)

6.3 State-of-the-art Retrievals

By virtue of the vast experience obtained with previous greenhouse-gas missions (SCIAMACHY, GOSAT and recently OCO-2), the retrieval methods for CO_2 and CH_4 from shortwave infrared observations have improved significantly and have reached a high level of maturity. This is reflected in the very low biases of less than 1 ppm against ground-based data from the Total Carbon Column Observing Network (TCCON) (Buchwitz et al., 2015a). The progress in retrieval methods is also reflected by the inclusion in the ESA Climate Change Initiative for the development of essential climate variables. The CarbonSat mission will benefit directly from past and current missions.

Several processing schemes have been developed (BESD (Reuter et al., 2011), WFM-DOAS (Buchwitz et al., 2000), RemoTeC (Butz et al., 2011), UoL-FP (Boesch et al., 2011), ACOS (O’Dell et al., 2012), NIES (Yoshida et al., 2011)) and have been used extensively to analyse SCIAMACHY and GOSAT measurements over land. GOSAT also acquires soundings in sunglint geometry over the ocean, providing useful measurements within a 20° latitude band around the sub-solar point. This implies that the sunglint retrieval algorithms can be tested for CarbonSat using existing space-based data.

All retrieval algorithms fit the measured shortwave-infrared spectra to simulated spectra obtained from a multiple-scattering radiative transfer model (‘forward model’). An iterative scheme is used to fit the spectra optimally to infer atmospheric and surface parameters (state vector) simultaneously. The main differences between these algorithms are the choice of regularisation method, the choice of co-retrieved parameters, in addition to CO_2 and CH_4, the choice of the *a priori* data, the choice of auxiliary data, the adopted radiative transfer solvers, the treatment of aerosols and thin cirrus clouds and the (pre-)screening e.g. for clouds and quality flagging.

For performance assessments and optimisation for nadir observations over land, a dedicated optimal estimation retrieval method, BESD/C algorithm, has been implemented, which is similar to the SCIAMACHY BESD algorithm but optimised for CarbonSat (Buchwitz et al., 2013a). An overview of the different processing steps is shown in Fig. 6.4.

All algorithms rely on accurate tables of the O_2, CO_2, CH_4 and H_2O absorption cross-sections. Recent work on spectroscopy for the OCO-2 mission has led to important advancements in our understanding of the spectroscopy so that more accurate spectroscopic tables are now available. These tables take into account effects from line-mixing, advanced non-Gaussian line-shape

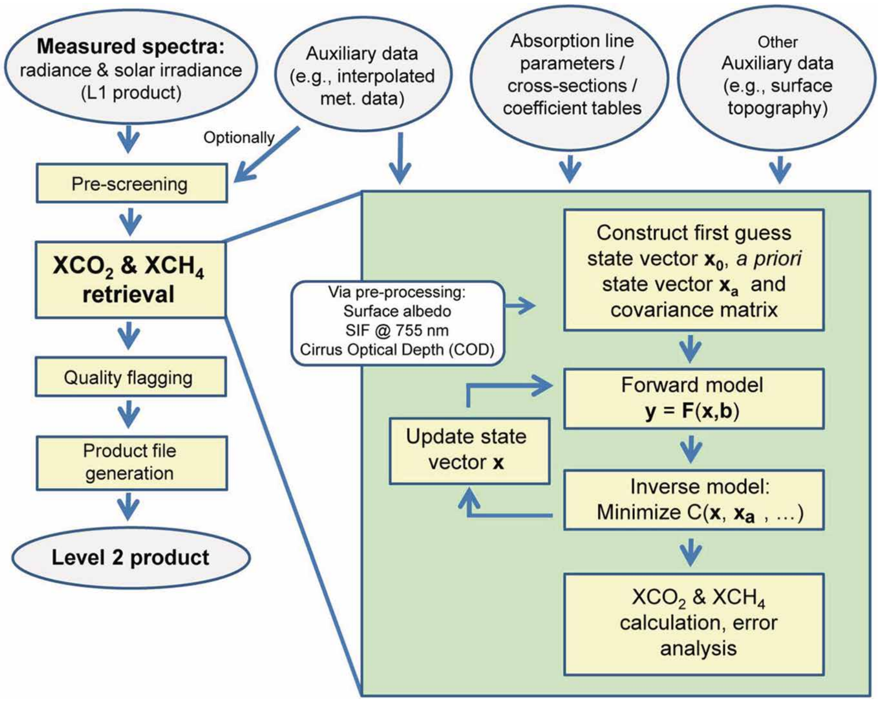

Figure 6.4. Overview of the retrieval algorithm used for CarbonSat. (M. Buchwitz–IUP)

models and collision-induced absorption (Long et al., 2012; Thompson et al., 2012). However, to meet the very stringent requirements on accuracy of XCO_2 and XCH_4, further improvements in spectroscopy including improved laboratory results and a better understanding of molecular line-shapes will be needed.

Furthermore, one may distinguish between 'full physics' (FP) retrieval schemes, such as BESD, RemoTeC and UoL-FP, and 'proxy' (PR) retrieval schemes. With the PR scheme one retrieves, e.g. the XCH_4/XCO_2 ratio to generate a XCH_4 dataset, which is then effectively using CO_2 columns instead of O_2 columns to compute XCH_4. A major advantage of the PR retrieval is its very low sensitivity to aerosol and cloud scattering, resulting in a much better coverage over areas prone to cloud and aerosols. However, the disadvantage is that retrieved XCH_4 will have a dependence on the assumed constant CO_2 distribution (Schepers et al., 2012). The PR retrieval method is especially powerful for observations of CO_2 or CH_4 plumes at fine spatial scales where enhancements in the retrieved XCH_4/XCO_2 ratio can be directly interpreted and potential biases are effectively eliminated, as has been demonstrated with the MAMAP instrument (Krings et al., 2011, 2013).

CarbonSat will push towards innovative processing schemes to process the large data volume rapidly enough with sufficient accuracy. Until now, the focus has primarily been on accuracy, but, in the future, processing speed will also need significant attention. Radiative transfer simulation methods such as Low-Stream Interpolator (O'Dell, 2010) and linear-k (Hasekamp and Butz, 2008) have already led to an efficiency gain of two orders of magnitude without a significant loss in accuracy. Examples for fast retrieval algorithms are WFM-DOAS (Schneising et al., 2014a), which is based on a look-up-table scheme to avoid online radiative transfer simulations, and IMAP-DOAS (Frankenberg et al., 2006), which is used for proxy XCH_4 retrieval using a fast radiative transfer model based on a parameterisation of the radiative transfer neglecting scattering (Oshchepkov et al., 2008).

Figure 6.5. Overview of the TCCON ground-based XCO_2 and XCH_4 observation sites. (NASA's Earth Observatory/D. Wunch–California Institute of Technology)

6.4 Validation Concept

Validation is an important component of the CarbonSat mission to ensure the accuracy of the XCO_2 and XCH_4 retrievals. It also provides a bridge between space-based observations and the World Meteorological Organization (WMO) standard for *in situ* greenhouse-gas measurements, which is used for intercalibration of ground-based and airborne *in situ* observations. The connection to the WMO standard is critical for the acceptance of space-based data by the carbon-cycle community, as they rely on its high quality.

The validation concept at the global to regional scale includes using the Total Carbon Column Observation Network (TCCON), which is a well-established ground-based network of direct-solar-viewing Fourier Transform Spectrometers (FTS). This network was created in 2004 with the setup of the first site at Park Falls, US, and has gradually expanded to 22 stations around the world (Fig. 6.5), with further stations expected to become available in the coming years. TCCON provides very accurate and precise column observations of CO_2 and CH_4 from the ground with a 2-σ uncertainty of 0.2% for XCO_2 and 0.4% for XCH_4 (Wunch et al., 2011b). TCCON is calibrated against the WMO reference gas standards by aircraft carrying calibrated *in situ* instruments. The limited coverage of the stratospheric column by the *in situ* observations is currently the largest contributor to uncertainties in this calibration process.

The more recently developed ‘aircore’ *in situ* measurement technique (Karion et al., 2010) is based on passive sampling of air by a long tube attached to a balloon, which can reach altitudes of up to 30 km. It has the potential to further improve the accuracy of the TCCON observations towards 0.1% for XCO_2 and 0.25% for XCH_4.

The validation methods for space-based column observations of CO_2 and CH_4 using the TCCON observations are well established and routinely applied to observations from GOSAT, SCIAMACHY and OCO-2 (e.g. Nguyen et al., 2014; Wunch et al., 2011a). Figure 6.6 shows an example for the validation of CO_2

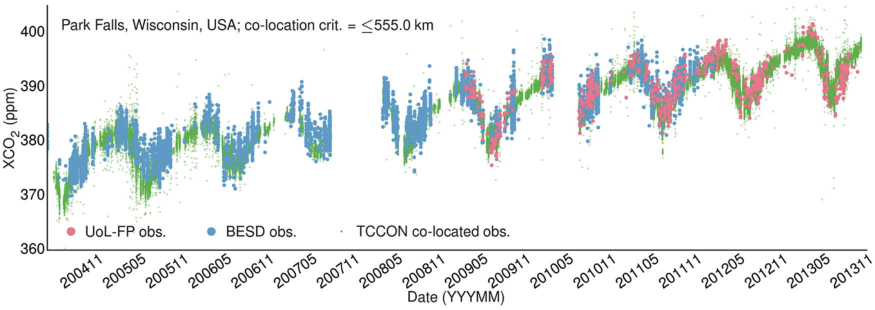

Figure 6.6. Validation example for SCIAMACHY (BESD retrieval, blue) and GOSAT (UoL-FP retrieval, orange) compared to measurements taken at the TCCON site at Park Falls in the US (green). Satellite data are from overpasses within 555 km of the site. (W. Hewson–University of Leicester)

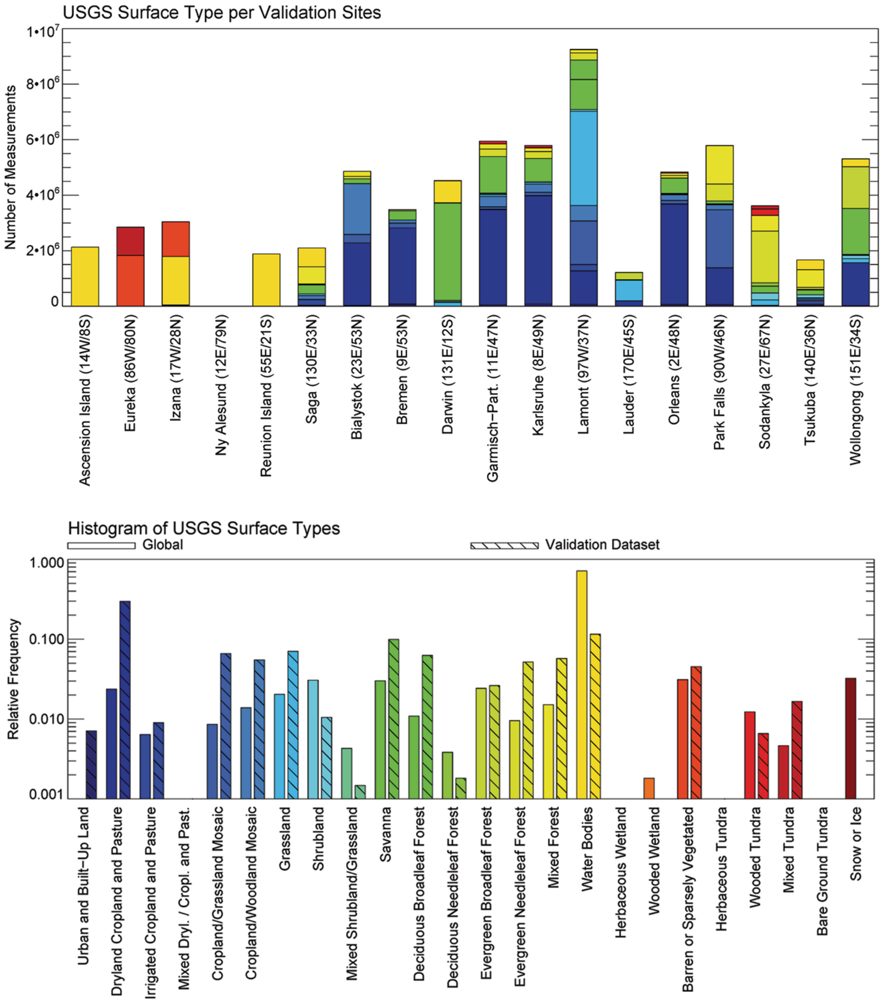

Figure 6.7. Top: number of cloud-free CarbonSat soundings per TCCON site from a one-year simulated dataset within a colocation distance of 500 km. Different biome types are indicated with different colours. Bottom: the relative frequency of soundings for the whole dataset and those that have been colocated with TCCON sites. (M. Reuter–IUP)

retrievals from SCIAMACHY and GOSAT against TCCON data from Park Falls. While GOSAT and OCO-2 require a special target mode to collect sufficient observations for the validation, CarbonSat will nominally collect several million observations per TCCON site within a colocation radius of 500 km using its main (nadir) mode (Fig. 6.7 top). This is because its wide swath and high spatial resolution should lead to more robust validation compared to previous missions. A major strength of TCCON is the fact that it is distributed globally, covering a wide range of surface types and climatic regimes. The large validation dataset obtained by CarbonSat around TCCON sites could also allow more sophisticated validation methods targeting the effect of specific biomes on the retrieval. The various Earth biomes are sufficiently represented in the validation dataset as compared to the global dataset (Fig. 6.7).

Existing uncertainties in spectroscopy and instrument calibration, and potential, subtle errors in the implementation of retrieval algorithms, can lead to spurious XCO_2 and XCH_4 retrievals. For retrievals from current satellite missions, a bias correction is applied that removes small biases on large-to-global-scales based on observed differences between satellite and TCCON data (Wunch et al., 2011a). Therefore, if a bias correction is necessary for CarbonSat, well-established methods can be applied with the additional benefit of a larger number of validation soundings acquired by CarbonSat (Fig. 6.7). To efficiently apply bias-correction schemes, the combination of high single-measurement precision with the high spatial resolution and along/across-track imaging capabilities of CarbonSat is very beneficial, as it allows application of bias correction schemes on a finer temporal and/or spatial grid compared to existing missions. Alternatively, a bias correction term can be directly included in the surface-flux inversion (Alexe et al., 2015).

At country to local scales, the validation of CarbonSat Level-2 data will be complemented by airborne remote-sensing, such as from the Methane Airborne Mapper MAMAP (Krings et al., 2011, 2013) and GHOST (Humpage et al., 2014), and *in situ* aircraft instruments. Dedicated aircraft campaigns will be needed to facilitate validation at fine spatial scales for the objective of characterising localised and urban plumes. Aircraft with different flight ranges and speeds will be needed to cover the large range of spatial scales CarbonSat addresses. There is the clear need to have a 2D imaging spectrometer covering the same spectral bands as CarbonSat to image CO_2 and CH_4 gradients at local scales to help validate Level-2 and Level-4 data. Based on the heritage and lessons learned from the MAMAP instrument, concepts like the Airborne Imaging Greenhouse Gas Spectrometer (AIGGS) are under development. This can be combined with observations offered by new, portable FTS instruments for column observations (Gisi et al., 2012) that would be more suited for continuous deployment around emission plumes of cities and point sources.

Additional validation opportunities may be provided by routine *in situ* profile observations, (e.g. from the HIPPO follow-on project ATOM (Wofsy, 2011), Aircore and Contrail) and from non-TCCON ground-based column measurements (e.g. from those performed in the Network for Detection of Atmospheric Composition Change (Ostler et al., 2014).

6.5 Estimation of Sources and Sinks

The geophysical data products of CarbonSat are XCO_2 and $XCH_{4,}$ as derived from the measured spectral radiances using the retrieval techniques described in Sections 6.2 and 6.3. However, since the objective of the mission is to improve the quantification of CO_2 and CH_4 sources and sinks, this requires translation of the retrieved total column mixing ratios (Level-2) into sources and sinks (Level-4). This processing step involves the use of inverse modelling.

Atmospheric chemistry and transport models (ACTMs) are essential to the inverse modelling technique, which calculates the relationship between surface fluxes and atmospheric mixing ratios by simulating dispersion and chemical transformation in the atmosphere. These models calculate the impact of trace-gas fluxes on their dry-air mixing ratios (from Level-4 to Level-2), which is in the opposite direction, hence the term ‘inverse problem’. To solve this problem, inverse modelling techniques use an ACTM in combination with an optimisation algorithm to infer the most likely set of surface fluxes given the available atmospheric measurements.

Atmospheric measurements alone do not provide sufficient resolution and coverage to constrain the spatial and temporal variability of greenhouse-gas sources and sinks. Instead, optimal solutions are derived by combining *a priori* information, e.g. from a carbon-cycle process model with the constraints on spatio-temporally integrated budgets from atmospheric measurements. This different information is usually combined in a Bayesian probabilistic framework, deriving solutions that maximise probability and minimise subsequent uncertainty.

Inverse modelling is an innovative field of scientific research with heritage in applications using measurements from global and regional surface-monitoring networks. Initial steps towards the operational use of inverse-modelling methods are progressing, for example within the Copernicus Atmosphere Monitoring Service. With the availability of more satellite measurements, these methods are becoming computationally more efficient at dealing with volumes of data. They can now account for slight inconsistencies between constraints imposed by surface and satellite data within the atmospheric-modelling framework.

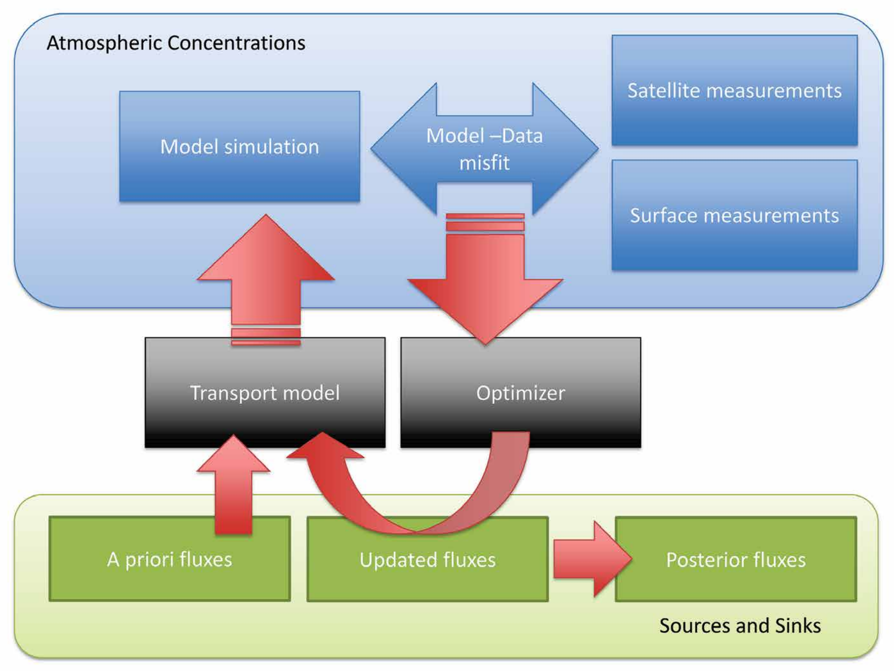

Figure 6.8. Schematic representation of the variational inverse-modelling technique. (S. Houweling–SRON)

Other methods for solving the inverse problem are currently under development, such as the variational technique, the Ensemble Kalman Filter, and the geostatistical approach. Figure 6.8 shows a schematic representation of the variational technique, which originates from the use of 4D-VAR in numerical weather prediction (Chevallier et al., 2005). As the figure illustrates, the inverse-modelling procedure starts with a model simulation of atmospheric concentrations of CO_2 and CH_4, using *a priori* surface fluxes, the result of which is compared to measurements. The mismatch between them is fed into an optimiser, which computes the sensitivity of the surface fluxes to the mismatches, from which an updated set of surface fluxes is derived. The updated fluxes enter a new cycle, and the process continues until convergence is achieved. The method is numerically efficient because the iteration process avoids the need to keep large matrices in memory, and because the sensitivities can be computed highly efficiently using the adjoint of the transport model. For the application of this method to existing satellite data see, for example, Chevallier et al. (2014a) and Bergamaschi et al. (2013).

Methods using the Ensemble Kalman Filter (Peters et al., 2005) are gaining ground. They are designed to make efficient use of the computational power of multi-parallel super computers by representing the probabilistic state by an ensemble. This indicates how model developers are preparing for large volumes of data from a new generation satellites.

Another emerging inverse-modelling approach is the application of satellite-retrieved total columns of CO_2 and CH_4 to a Carbon Cycle Data Assimilation System (CCDAS). Here the land-surface process model becomes an integral component of the optimisation system, and the measurements are used to constrain uncertain process model parameters rather than surface fluxes (Rayner et al., 2005). The advantage of this approach, and an exciting prospect for the use of CarbonSat data, is that it allows the combination of different types of measurements, such as CarbonSat-derived XCO_2 and SIF to constrain the gross fluxes of carbon (GPP and heterotrophic respiration). This can further be improved by ingesting other ecosystem parameters into a CCDAS system (Schimel et al., 2015).

The use of SCIAMACHY and GOSAT retrievals has pointed to the importance of systematic errors in satellite measurements as well as atmospheric transport models. Bias correction techniques have been developed to mitigate the impact of such errors, either within the inversion or by using measurements from the TCCON ground-based FTS instruments before the data enter the inversion (Houweling et al., 2014). In parallel, new statistical techniques are being investigated to estimate uncertainties from the data themselves, such as in the geostatistical approach (Michalak et al., 2005). The research community is putting a big effort into mitigating the impact of systematic errors and into improving atmospheric transport and radiative transport models accordingly. CarbonSat will be able to benefit from these efforts (Reuter et al., 2012; Houweling et al., 2015). In turn, the excellent coverage of CarbonSat will help to identify remaining sources of error.

The inverse modelling technique has been used to estimate the performance of CarbonSat at Level-4, through observing system simulation experiments (OSSEs). This method and results are presented in Chapter 7.4.

6.5.1 Flux Estimation at Country Scales

CarbonSat will provide data with sufficient resolution and coverage to investigate CO_2 and CH_4 sources and sinks, not only at regional to global scales, but also at country scales. This will open new possibilities for the investigation of biospheric and anthropogenic fluxes, enabling a better separation of their contributions. Owing to the highly fragmented landscapes and sharp contrast between urbanised and natural environments in many regions of the globe, high spatial resolution is essential to identify the signatures in XCO_2 and XCH_4 from different ecosystems and anthropogenic activities (Broquet et al., 2011, 2013).

Regional-scale inverse-modelling of greenhouse-gas sources and sinks is a young but rapidly evolving discipline, which, so far, has been dominated by studies using ground-based observations. Important applications are the independent verification of national bottom-up inventories of anthropogenic greenhouse gases (Nisbet and Weiss, 2010) and the estimation of CO_2 fluxes from different ecosystems on a sub-country (Göckede et al., 2010) and country-scales (Schuh et al., 2010). Ground-based networks with sufficient density, however, only exist in a few regions, such as the tall tower networks established in the US through the North American Carbon Program (NACP) and in Europe through the Integrated Carbon Observation System (ICOS). The inversion methods applied on those data are essentially the same as outlined above, but here mesoscale instead of global transport models are required to resolve trace-gas variations at the scales of interest. Many regional scale studies adopted Lagrangian rather than Eulerian transport models because Lagrangian models are 'self-adjoint' and source-receptor-relationships can, therefore, be computed easily (Seibert and Frank, 2004). Since mesoscale models only cover a limited domain, background concentrations entering the domain at the boundaries must be properly accounted for. A novel approach to tackle this problem is to combine Lagrangian simulations in the limited domain with simulations from a global Eulerian model and to perform an inversion on both domains either sequentially (Rödenbeck et al. 2009) or simultaneously in a single step (Rigby et al. 2011).

Regional-scale inversions rely on measurements taken sufficiently close to the sources so that the source signatures are discernible above the large-scale background. Accurately simulating these signatures, however, requires an accurate representation of the dynamics of the atmospheric planetary boundary layer, which is currently one of the largest uncertainties in regional-scale modelling (Gerbig et al., 2008).

So far, satellite data have only played a marginal role in regional-scale inversions owing to the relatively limited data constraints provided at such scales by instruments like GOSAT, whose surface footprints are separated by ~250 km. OCO-2 provides high-resolution (2.25 km) data along a narrow

(< 10 km) ground track and is expected to improve this situation, but there are still huge gaps between adjacent ground tracks. The launch of CarbonSat would change this dramatically, providing ten times as much data from a much broader swath. Remote-sensing data could become an important component of country-scale carbon observing systems. Satellite remote sensing at these scales is attractive because total-column measurements make the fluxes derived by inverse modelling less dependent on the representation of boundary layer dynamics in models. In addition, the measurement coverage provided by CarbonSat would be highly complementary to that of the surface network.

6.5.2 Flux Estimation of Point Sources and Cities

The application of inversion modelling to point sources has been limited to dedicated campaigns studying specific sources, such as industrial complexes, landfills and, more recently, emissions from entire cities (Cambaliza et al., 2015). Measurements have been taken from ground-based sites and mobile platforms, from aircrafts and by ground-based remote sensing (Kort et al., 2014). Accurate quantification of point sources is very challenging because plume structures are often complex, with concentrations varying greatly at small spatial and temporal scales. These variations, which are driven by fluctuations in the wind and by the chaotic nature of atmospheric turbulence, are difficult to capture precisely in atmospheric transport models (Bréon et al., 2015). Therefore, many studies rely on budget approaches quantifying the fluxes into and out of a control volume directly from observations rather than using transport-model simulations in combination with inverse estimation. However, this requires a dense sampling of the heterogeneous and fluctuating concentration field, which is difficult to obtain from *in situ* observations alone.

CarbonSat will be the first mission to explore the potential of deriving emissions of strong point sources and cities. Unlike current approaches, CarbonSat will allow images of individual source plumes to be collected multiple times a year, rather than taking measurements at single locations during limited campaigns. The imaging of total columns has the great advantage of measuring the integral signal of the source over a large volume of air, which makes it much less sensitive to small-scale fluctuations. CarbonSat measurements will provide invaluable input for budget studies. This has been demonstrated for CH_4 emissions from the gas and oil production regions in North America (Schneising et al., 2014b) and for NO_2 emissions from cities (Beirle et al., 2011). They will also be useful in combination with idealised Gaussian plume models as demonstrated for airborne measurements of XCO_2 and XCH_4 over power plants and coal-mine ventilation shafts (Krings et al., 2011, 2013) as well as in combination with more sophisticated atmospheric simulations such as Large-Eddy-Simulations (LES) of point source plumes or mesoscale transport simulations of urban plumes.

When methods are established for well-known local sources, such as for power plants and large cities in the US or Europe with known emission inventories, then these methods can be used to gauge unknown sources such as rapidly growing large cities around the world.

→ PERFORMANCE ESTIMATION

7. Performance Estimation

7.1 Introduction

The system and instrument performances achieved for the mission concepts described in Chapter 5 are presented in this chapter. The performance at Level-1b is compared with the requirements in Section 7.2 and, where relevant, justification or further explanation regarding the key performance parameters is given. The performances addressing coverage are reported in Section 5.2.1, and geolocation performance is reported in Section 5.3.5.5. Simulated Level-2 performance results are presented in Section 7.3 giving an overview of the CarbonSat End-to-End Simulator (E2ES) in Section 7.3.1, and Level-2 performance estimates are provided in Section 7.3.2.

A stand-alone framework for assessing Level-2 performance is presented in Section 7.3.3. This framework is used to simulate a one-year dataset representative for CarbonSat, and its Level-2 characteristics are presented in Section 7.3.4. This dataset is used in Observing System Simulation Experiments (OSSEs), where the data are used to drive inverse models to assess CarbonSat's potential to constrain fluxes of CO_2 and CH_4 from global to regional (Section 7.4.1) and local scales (Section 7.4.2). The overall expected performance of CarbonSat is summarised in Section 7.5.

7.2 Level-1b Performance

7.2.1 Overview

This section summarises the performance achieved by the instrument at Level-1b. The main figures of merit were estimated by means of dedicated instrument models and by simulating the geometrical, radiometric and spectral performances of the payload concepts presented in Chapter 5. The performances are compared to the relevant requirements, and the most important results are discussed in terms of compliance, margins and criticality. Table 7.1 summarises the performance of both instrument concepts with respect to the key system requirements at Level-1b. It corresponds to Table 5.3, highlighting the instrumental aspects driven by each requirement. A high level of compliance with the requirements is achieved by both instrument concepts. The geometric, radiometric and spectral performances are summarised in the following section.

7.2.2 Geometric Performance

Both concepts implement rectangular spatial samples, which are extended in the ACT direction (Concept A: 3.0 km; Concept B: 2.8 km). They provide the same sampling in ALT direction of 2 km, resulting in an integration time of 300 ms. The two concepts are based on different orbit altitudes and swath widths to comply with the spatial coverage requirements. Concept B measures 69 ACT samples within a swath width of 185 km, while Concept A implements a swath width of 240 km with 80 ACT samples. Concept A assumes a considerably higher orbit altitude (795 km) than Concept B (594 km). Despite its larger swath, Concept A has a narrower instantaneous field-of-view in ACT: 17.3° compared to 18.6° for Concept B. The resulting coverage performances are reported in Section 5.2.1.

Apart from the SSD, the second figure of merit for spatial resolution is the System Energy Distribution Function (SEDF), which describes the spatial origin of the detected photons on the ground. It is determined by the imaging quality

Table 7.1. Level-1b performance of Concepts A and B.

	Requirement	Concept A	Concept B
Geometric			
Swath width	Derived from coverage requirement	240 km (80 ACT samples)	185 km (69 ACT samples)
Spatial sampling [km^2, ALT×ACT]	6 km^2	2.0×3.0 km^2	2.0×2.8 km^2
Integrated energy	> 70% over 1.0×1.0 SSD > 90% over 1.5×1.5 SSD	82% (1.0×1.0 SSD) 99% (1.5×1.5 SSD)	81% (1.0×1.0 SSD) 98% (1.5×1.5 SSD)
Spatial coregistration [% of SSD]	NIR–SWIR: 15% SWIR-1–SWIR-2: 30%	NIR–SWIR: 15% SWIR-1–SWIR-2: 17%	NIR–SWIR: 10% SWIR-1–SWIR-2: 9%
Radiometric			
SNR@ reference radiance L_{ref}	NIR: 150 SWIR-1: 160 SWIR-2: 130	NIR: 242 SWIR-1: 344 SWIR-2: 180	NIR: 188 SWIR-1: 292 SWIR-2: 170
Absolute radiometric accuracy	< 3% (all bands)	NIR: 2.7% SWIR-1: 2.7% SWIR-2: 3.0%	NIR: 2.0% SWIR-1: 1.4% SWIR-2: 2.7%
Relative spatial radiometric accuracy (RxRA)	< 0.5% (all bands)	NIR: 0.50% SWIR-1: 0.35% SWIR-2: 0.50%	NIR: 0.30% SWIR-1: 0.10% SWIR-2: 0.45%
Relative spectral radiometric accuracy (RλRA)	0.5% (all bands)	NIR: 0.45% SWIR-1: 0.40% SWIR-2: 0.45%	NIR: 0.20% SWIR-1: 0.20% SWIR-2: 0.20%
Effective spectral radiometric accuracy	<0.10% (CO_2) <0.24% (CH_4)	<0.08% (CO_2) <0.23% (CH_4)	<0.07% (CO_2) <0.20% (CH_4)
Zero-level offset [% of L_{min}]	NIR: 0.15% SWIR-1: 0.50% SWIR-2: 0.30%	NIR: 0.10% SWIR-1: 0.25% SWIR-2: 0.15%	NIR: 0.15% SWIR-1: 0.35% SWIR-2: 0.20%
Polarisation sensitivity	<0.5% (all bands)	NIR: <0.15% SWIR-1: <0.15% SWIR-2: <0.20%	NIR: <0.15% SWIR-1: <0.15% SWIR-2: <0.25%
Straylight sensitivity at 5 SSD from contrast transition after correction (factor five ghosts, factor seven diffused SL)	<1% over cloud contrast scene	NIR: 1.5 % SWIR-1: 0.5 % SWIR-2: 0.8 %	NIR: 1.0% SWIR-1: 0.1% SWIR-2: 1.2%
Spectral			
Spectral range	NIR: 747–773 nm SWIR-1: 1590–1675 nm SWIR-2: 1925–2095 nm	NIR: 747–775 nm SWIR-1: 1590–1675 nm SWIR-2: 1925–2095 nm	NIR: 747–775 nm SWIR-1: 1590–1675 nm SWIR-2: 1925–2095 nm
Spectral resolution	NIR: <0.1 nm SWIR-1: <0.3 nm SWIR-2: <0.55 nm	NIR: <0.1 nm SWIR-1: <0.3 nm SWIR-2: <0.55 nm	NIR: <0.1 nm SWIR-1: <0.3 nm SWIR-2: <0.55 nm
Spectral sampling	>3 in all bands	>3 in all bands	>3 in all bands
Instrument Spectral Response Function (ISRF) shape knowledge	2% in flight	NIR: 1.9% SWIR-1: 2.0% SWIR-2: 1.9%	NIR: 1.55% SWIR-1: 1.54% SWIR-2: 1.69%

	Requirement	Concept A	Concept B
Spectral (continued)			
Spectral channel knowledge	NIR: <0.002 nm SWIR-1: <0.005 nm SWIR-2: <0.009 nm	NIR: <0.002 nm SWIR-1: <0.003 nm SWIR-2: <0.008 nm	NIR: <0.002 nm SWIR-1: <0.004 nm SWIR-2: <0.008 nm
Spectral channel stability	NIR: <0.010 nm SWIR-1: <0.025 nm SWIR-2: <0.045 nm	NIR: <0.003 nm SWIR-1: <0.006 nm SWIR-2: <0.010 nm	NIR: <0.002nm SWIR-1: <0.004 nm SWIR-2: <0.005 nm

SSD=Spatial Sampling Distance; ALT=Along-Track; ACT=Across-Track; Lmin and Lref are the minimum and reference value, respectively, of the dynamic range for spectral radiance; SL=straylight; SNR=signal-to-noise ratio.

Table 7.1 (cont.)

of the telescope, the slit width and the spot pattern induced by the polarisation scrambler. The integral of the SEDF over a spatial sample defines the System Integrated Energy (SIE). Figure 7.1 depicts the SEDF of one nadir sample for both concepts. Both instruments feature telescopes with high imaging quality, which results in SEDFs with sharp edges at the spatial sample boundaries. They also employ narrow entrance slits, which, when projected on Earth, are smaller than the SSD. For this reason, the achieved SEDF integrals reach values larger than 80%, even considering tolerances for optical quality, therefore exceeding the requirement with margin. This is favourable for the spatial resolution of the mission concepts and enhances the potential merit of spatially un-binned data (cf. Section 5.3.3.2), providing sub-sample information at a resolution of a few hundred metres, albeit without spectral information (i.e. spectrally binned).

Both instrument concepts also comply with the important requirement for spatial coregistration, following different strategies for achieving the performances stated in Table 7.1. Concept A relies on high imaging quality in terms of keystone distortion, which is achieved by optimising the optical design. The spectral image corresponding to a spatial point deviates from a straight line by less than one detector pixel. This can be seen in Fig. 7.2 left, which shows the maximum keystone error of Concept A across the swath for all three focal planes. Other contributors to the coregistration budget include alignment errors (e.g. detector displacement and rotation), which are typically in the order of 10 µm (<1% of the ACT SSD). The total budget, including thermo-mechanical tolerance analysis, is compliant, albeit marginal in the SWIR-2 band at the edge of the swath.

Concept B implements a different approach to coregistration, taking advantage of high spatial oversampling. Each spatial sample of 2.8 km in the ACT direction is formed by adding 14 detector pixels corresponding to the same wavelength. This binning-window is shifted along the spatial direction

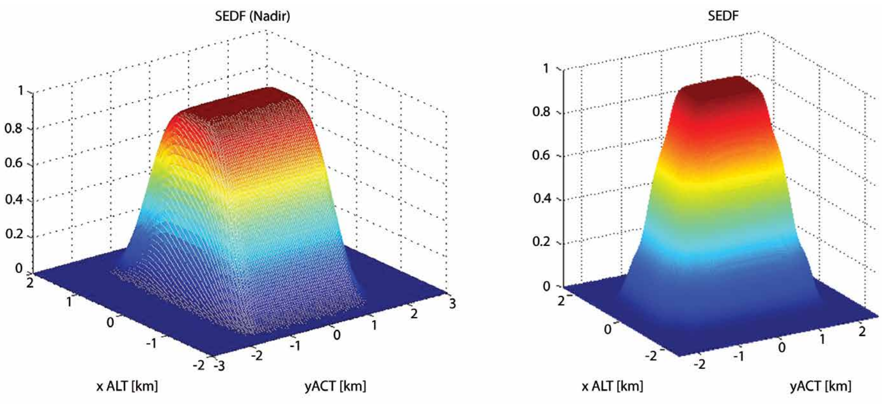

Figure 7.1. SEDF of Concept A (left, Airbus Defence and Space) and Concept B (right, OHB/TAS-F), showing the spatial distribution of detected energy (photons) of one spatial sample. Both concepts achieve a high integrated energy.

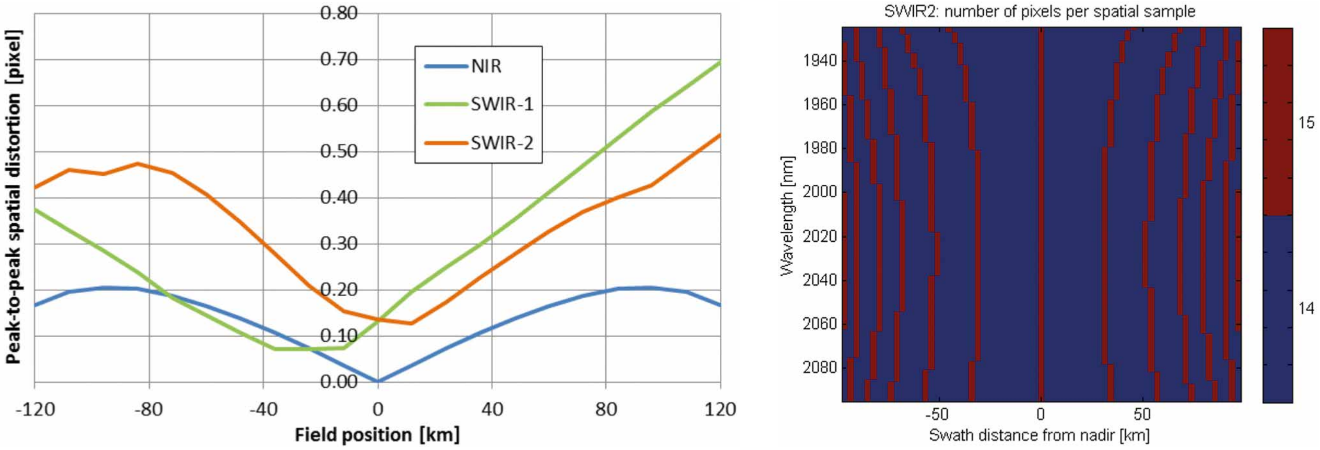

Figure 7.2. Left: keystone performance across the swath width of Concept A (Airbus Defence and Space). The maximum deviation of a point-source spectrum from a straight line is less than a pixel width. Right: map of the implemented spatial sampling across the focal plane of the SWIR-2 spectrometer of Concept B (OHB/TAS-F). The red lines indicate spatial samples formed by adding 15 pixels, and the blue area is formed by adding (nominal) 14 pixels. Alternating between the two factors allows for compensation of spectral variation in magnification.

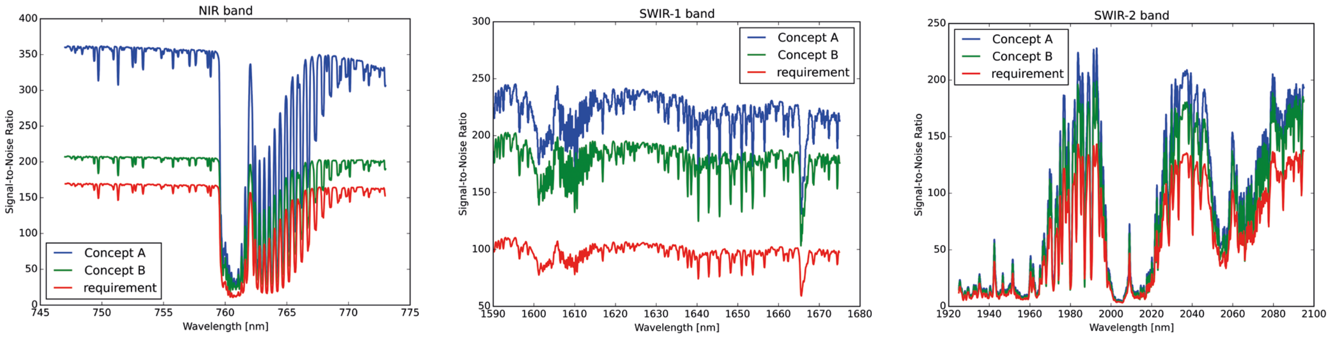

Figure 7.3. SNR performance of Concept A (blue) and B (green) for the high-latitude dark reference scenario. The required SNR as a function of input radiance is indicated by the red curve. (ESA)

of the focal plane to follow the curvature of the spectral image on the detector. The keystone distortion is compensated by successive shifts of the binning-window by one pixel. In this way, the maximum keystone contribution to the coregistration error is limited to the width of one detector pixel. In a similar way, adapting the size of the binning-window (number of pixels per spatial sample) can compensate for spectral variations of ACT magnification. In Concept B, the ACT oversampling factor is switched between 14 and 15 to correct for this effect. As an example, Fig. 7.2 (right) shows a map of the implemented spatial sampling across the focal plane of the SWIR-2 spectrometer. With the techniques described above, the coregistration performance for Concept B is better than 10% of an SSD and compliant with significant margin.

7.2.3 Radiometric Performance

The SNR is closely related to the precision of the XCO_2 and XCH_4 measurements. The current instrument concepts provide significant margins in SNR. Figure 7.3 presents an example of the estimated SNR performance for the high-latitude dark scenario (solar zenith angle 75°, albedo 0.05). The plots indicate that the requirements are exceeded in all three bands, albeit with different magnitudes in spectral regions of strong absorption and the continuum. The particularly high SNR achieved by Concept A in the NIR is because of the larger entrance pupil implemented in the spectrometer measuring this band (21 mm versus 11 mm for Concept B). In the two SWIR bands, the entrance pupil of both concepts is similar (28 mm and 29 mm, respectively).

The budgets for the absolute and relative radiometric accuracies have been established by analysis of different error sources, including:

— detector non-linearity
— straylight
— polarisation sensitivity
— dark current variation
— diffuser effects (speckle and ageing)

Since the radiometric requirements are applicable to Level-1b data, the reported performances take into account correction procedures applied during Level-1b processing, and include uncertainties from calibration measurements. The latter are typically the largest contributors to the absolute radiometric accuracy and the requirement of 3% calls for extensive on-ground calibration. The error budgets of both concepts indicate compliance with little margin. They are considered achievable, provided extensive state-of-the-art calibration methods will be employed for CarbonSat.

The relative spatial and spectral radiometric accuracies (RxRA and RlRA) are dominated by variations of the above listed error sources along the spectral and spatial dimensions of the focal plane. The radiometric performance analysis for both instrument concepts revealed significant contributions from spectral and spatial straylight. Therefore, detailed straylight analyses were carried out, performing simulations of diffuse scatter owing to surface roughness and contamination, as well as of reflections from optical elements and detectors giving rise to ghost images. Figure 7.4 (left) shows an example of a ghost map on the focal plane of Concept A. The dashed line marks the position of the input stimulus on the detector. Such simulations were performed for various wavelengths and field positions of the light source, allowing for simulation of the complete ghost image for the straylight reference scene. The impact of diffuse (scattered) straylight can be described in terms of the Bidirectional Scatter Distribution Function (BSDF). The right panel of Fig. 7.4 depicts an example of a simulated BSDF from analysis of Concept B. For ghosts and diffused straylight, such model calculations were used to simulate the impact on the derived reflectance. From the simulated error spectra

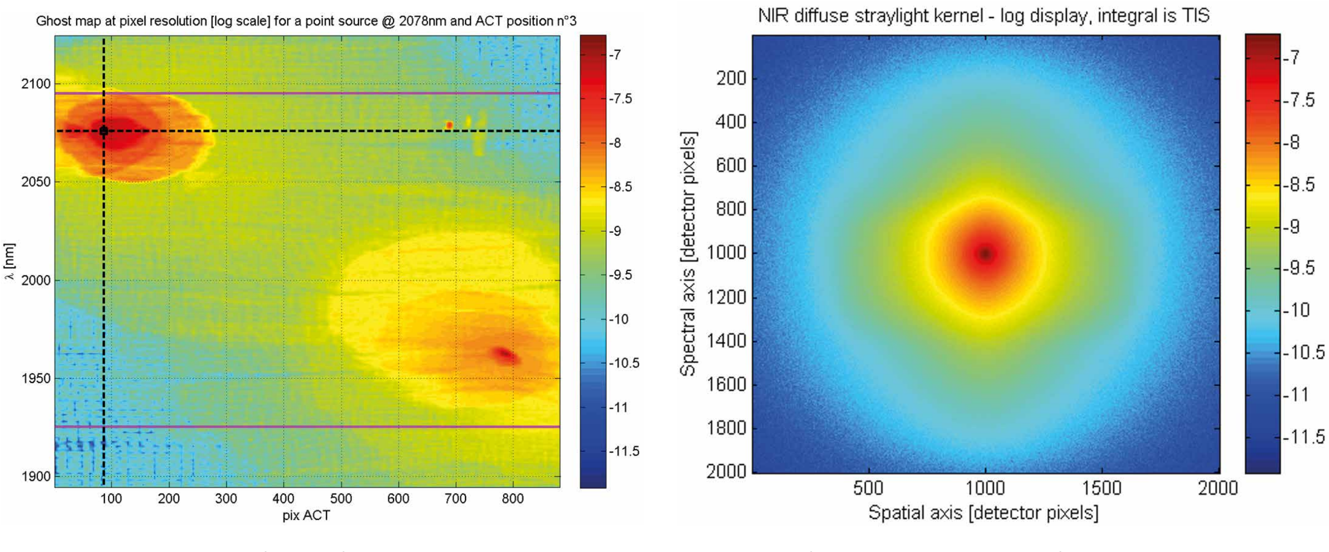

Figure 7.4. Left: ghost map (SWIR-2) from reflection at optical surfaces in Concept A (Airbus Defence and Space). Right: simulated BSDF from diffuse straylight analysis of Concept B (OHB/TAS-F).

Table 7.2. Straylight analysis results.

	Spectrometer Concept A			Spectrometer Concept B		
Straylight	NIR	SWIR-1	SWIR-2	NIR	SWIR-1	SWIR-2
Diffuse	6.38%	1.28%	1.75%	5.20%	1.10%	4.00%
Ghosts	2.86%	1.08%	2.05%	0.60%	0.50%	1.40%

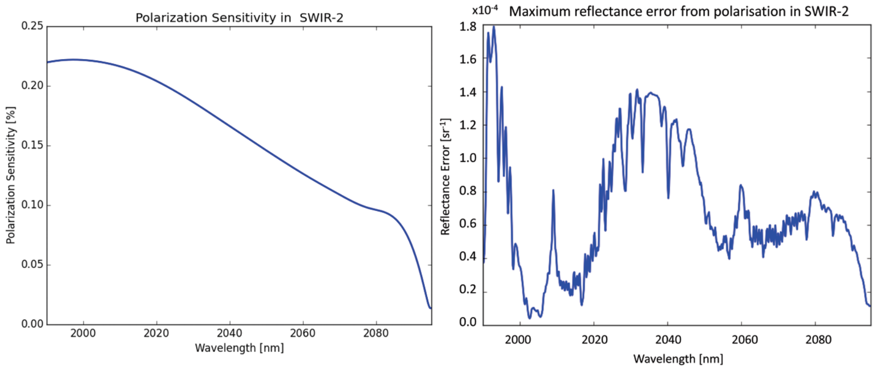

Figure 7.5. Polarisation performance derived from computed Mueller matrices of Concept B. Left: the polarisation sensitivity across the SWIR-2 band. Right: the reflectance error from the two most significant Mueller matrix elements. These error spectra are scalar multiplied with the gain vectors to yield the ESRA performance, which is directly linked to the resulting Level-2 error. (ESA)

the resulting performance in terms of RlRA, RxRA, and Effective Spectral Radiometric Accuracy (ESRA) were estimated.

Assumptions for the straylight analysis range from 30–40 ppm (inside barrels and detector) to 100–250 ppm (other surfaces inside the instrument) and a surface roughness range of 0.5 nm root mean square (flat surfaces) to 2 nm root mean square (curved surfaces). The worst-case straylight errors for each band relative to the minimum of the dynamic range are reported in Table 7.2. They are relevant to estimate the correction levels to be achieved at Level-1b processing for compliance with the absolute radiometric accuracy requirement.

The straylight analyses established that both instrument concepts meet the requirements (Table 7.1) after radiometric correction performed during Level-1b processing. The correction algorithms, making use of key data acquired by pre-flight calibration, are assumed to achieve a straylight reduction factor of five for ghost images and seven for diffuse straylight.

These factors are considered achievable, but impose stringent requirements on surface roughness of optical elements and extremely high cleanliness standards during assembly, integration and testing. The results also underscore the necessity of straylight characterisation during on-ground calibration.

Another contributor to radiometric errors is the polarisation sensitivity defined in Section 4.5.3. It has been analysed by determining the Mueller matrix of the instruments and its variation over the complete spectral bandwidth. The Mueller matrix relates the Stokes vectors of the incoming radiation to that incident on the detector and fully describes the polarisation response of the instrument. Both consortia have performed ray-tracing calculations for their concepts yielding Mueller matrices, which allow for accurate computation of the radiometric errors owing to polarisation effects. As an example, Figure 7.5 shows the polarisation sensitivity of Concept B (left) and the corresponding reflectance measurement error (right) in the SWIR-2 band due to polarisation of the high-latitude dark ground scene. It shows that the reflectance error from polarisation exhibits a spectral structure similar to the absorption spectrum. In the evaluation of ESRA, the error spectra of all three bands are mapped into the resulting Level-2 error for XCO_2 and XCH_4 by forming the scalar product with the gain vector plotted in Fig. 4.11. The analysis proves that the polarisation scramblers efficiently mitigate the impact of polarisation (Section 5.3.3.4) and ensure compliance to ESRA and the polarisation sensitivity requirements.

7.2.4 Spectral Performance

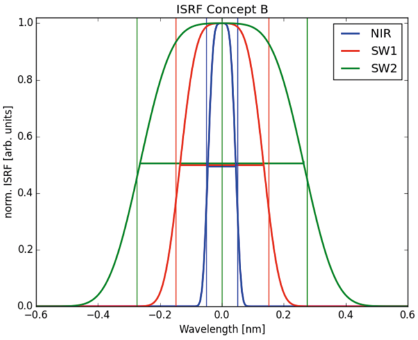

Figure 7.6. Simulated, normalised ISRF shapes of all spectral bands for Concept B. Note that the spectral resolution requirements are met. (ESA)

As pointed out in Section 4.5.3, the spectral response of the instrument is fully described by the Instrument Spectral Response Function (ISRF). Most spectral performance requirements therefore constrain the functional parameters of the ISRF or the knowledge thereof. Figure 7.6 depicts the three simulated ISRFs for Concept B, corresponding to the nadir field-of-view at the centre wavelength of each spectral band. The vertical lines correspond to the spectral resolution requirements, while the horizontal bars indicate the achieved Full Width at Half Maximum (FWHM) of the ISRF. As can be seen, the spectral resolution is compliant in all three bands. The ISRF of Concept A shows similar performance.

Without any additional measures, a non-uniform illumination of the slit leads to a wavelength-dependent distortion of the ISRF. However, for accurate retrieval it is important that the shape of the ISRF is stable over the observed scene. As described in Section 5.3.3.4, both concepts implement a slit homogeniser, which mitigates the effect of ISRF distortion from non-uniform illumination of the entrance slit. The ISRF deformation for measurement over non-uniform scenes was simulated for both concepts. To this end, a reference scene was defined which is characterised by steep intensity contrast in ALT and depicted in the left panel of Fig. 7.7. It features a sudden transition from a tropical dark to bright radiance scenario corresponding to an albedo change from 0.1 to 0.5 in the middle of the spatial sample. The impact of this scene on the ISRF shape is shown in the right panel of Fig. 7.7.

The plot shows the resulting ISRF shapes with and without a slit homogeniser device for the most affected spectral channel in the NIR band. It is evident that a ground scene with large radiometric contrast would give rise to a strong ISRF distortion of up to 20% of the peak if a conventional entrance slit were deployed. In presence of a slit homogeniser, however, the ISRF over the contrast scene is effectively stabilised, ensuring that the inflight requirements of ISRF shape knowledge and stability are met. This can be seen in Fig. 7.7, where the simulated ISRF shape with a slit homogeniser is very similar to the undistorted one measured over a uniform scene.

The slit homogeniser not only stabilises the ISRF shape, but it also reduces changes in the ISRF barycentre induced by non-uniform scenes. The device largely eliminates the contribution of scene non-uniformity to the knowledge error on spectral channel positions, leaving other effects like thermo-mechanical deformations as the main contributors. The latter are minimised by the mechanical design and thermal stability of the instrument, leading to a significant margin regarding the required spectral channel stability (Table 7.1). However, further correction is needed to meet the spectral channel knowledge requirement, which has been demonstrated to be achievable with correction techniques in Level-1b processing. Such spectral calibration algorithms have been implemented in Level-1b processors of various heritage missions (e.g. the

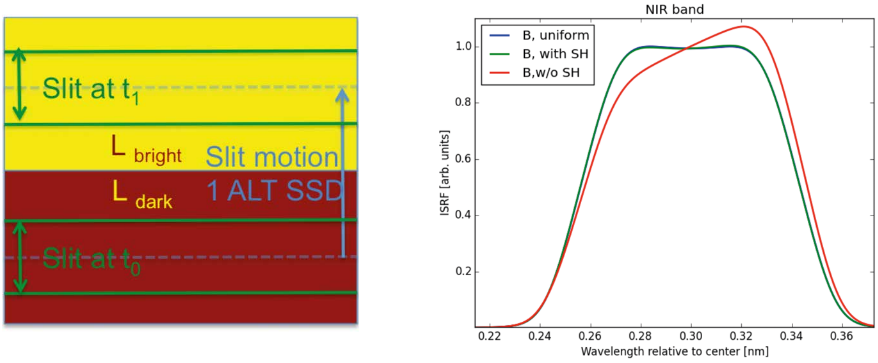

Figure 7.7. The image on the left shows the non-uniform reference scene featuring a sharp radiometric contrast in the ALT direction. The transition occurs halfway along the ALT SSD, as the slit projection moves over the scene during integration time. The right plot shows the resulting ISRF as measured over this scene without (red) and with (green) a slit homogeniser. (ESA)

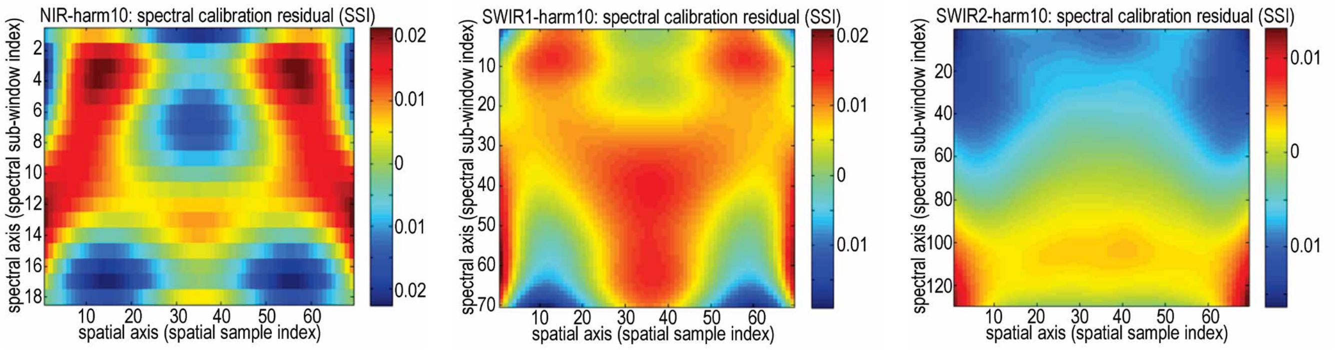

Figure 7.8. Residual spectral errors after 2D polynomial fit of an irradiance measurement (NIR, SWIR-1 and SWIR-2 from left to right). The simulation demonstrates the effectiveness of Level-1b spectral calibration, compliant to the specification of 5% of a spectral pixel. (OHB/TAS-F)

Ozone Monitoring Instrument, OMI) and analyses performed during the instrument studies have demonstrated their effectiveness for the CarbonSat spectral bands.

An example of such results is shown in Fig. 7.8, where the fit residuals of a spectral correction procedure are plotted for the entire focal plane of Concept B. The algorithm utilises a 2D polynomial fit (spectral and spatial coordinates) to match a simulated Sun-irradiance measurement to which spectral errors and noise have been applied, with a solar reference spectrum. The maximum residual spectral errors do not exceed 2% of a spectral sampling interval (corresponding to one detector pixel), which is in-line with the requirement of 5%.

In summary, the major error sources and mechanisms have been analysed by the industry consortia, and the results indicate that both instrument concepts can meet the key system requirements at Level-1b. The level of correction required for straylight during Level-1b processing (under the current cleanliness and surface roughness assumptions) is in the order of five for ghosts and seven for diffused straylight. Some performance aspects were identified as difficult to quantify with sufficient accuracy (e.g. diffuser spectral features). Dedicated performance measurements for these effects are planned in the frame of pre-development activities.

7.3 Level-2 Performance Simulations

7.3.1 Overview

The primary Level-2 data products of CarbonSat are the atmospheric quantities XCO_2 and XCH_4. To estimate their expected data quality in terms of random and systematic errors, simulation frameworks have been developed.

Retrieval algorithms (Level-1 to Level-2 data processing, see Chapter 6) are applied to simulated spectra, i.e. to the CarbonSat Level-1 data (spectral radiances and irradiances). The spectra are generated for a range of representative scenarios covering various atmospheric conditions (e.g. aerosols, cirrus clouds), Earth surface types (e.g. different spectral albedos) and instrument errors (e.g. additive and multiplicative radiometric errors, spectral calibration errors) in order to quantify their impact on the precision and accuracy of the XCO_2 and XCH_4 data products.

The spectral radiances are computed using a radiative transfer model and an instrument model. The instrument model transforms the high spectral resolution radiance and solar irradiance spectra to CarbonSat spectral resolution and sampling, applying quasi-realistic noise and errors.

The outputs of the retrieval module are the retrieved values of XCO_2 and XCH_4 and their estimated uncertainty. The estimated uncertainties are the XCO_2 and XCH_4 random errors (single measurement precision). They are primarily determined by the instrument's SNR. Systematic errors are obtained by computing the difference between the retrieved and the true XCO_2 and XCH_4 values, where the true values have been computed using the model atmosphere.

7.3.2 CarbonSat End-to-End Simulator

The CarbonSat E2ES generates Level-1b spectra and Level-2 data products based on detailed instrument models, from the system studies and retrieval algorithms, and from the science support studies along with realistic input data. This simulation activity represents a useful tool to assess the end-to-end mission performance, to support the consolidation of the technical requirements and conceptual design, as well as to allow users to assess the compliance to mission requirements. Figure 7.9 shows the simulator high-level modular architecture which includes the following modules:

- a Geometry Module (GM), calculating orbits and viewing angles
- an atmospheric Scene Generator Module (SGM) providing the geophysical parameters
- two Observation System Simulators, namely L1M comprising the instrument simulator and Level-0 to Level-1 processing simulator, and L2M comprising the Level-1b to Level-2 processing dedicated to retrieval for land and look-up table for sunglint observations, and the performance evaluation module (PEM), which is used as a tool to compare and plot different outputs.

The Open Simulation Framework (OpenSF) is used as a generic simulation framework where models and product retrieval tools can be plugged in using a well-defined and documented integration process.

Results reported are based on the validated alpha version of the E2ES, with functionality as reported below.

From a functional point of view, the E2ES consists of the following:

- GM#1 and GM#2 simulate the orbit of the platform together with the pointing of the instrument, which includes calculating the observing geometry for Concepts A and B, respectively
- The SGM calculates the radiance of the scene and the respective irradiance, for a given observing geometry and the selected geophysical state using the radiative transfer model SCIATRAN
  - the top of atmosphere radiance spectra in each of the instrument's spectral bands at a spectral resolution higher than the instrument resolution
  - the Sun irradiance spectra in each of the instrument's spectral bands, at spectral resolution higher than the instrument resolution
  - realistic heterogeneous scenes, with geophysical parameters derived from databases according to the geolocation of the scene
  - information for single ground pixels, selected ground pixels across-track and full swath. All across-track sets can be extended along-track

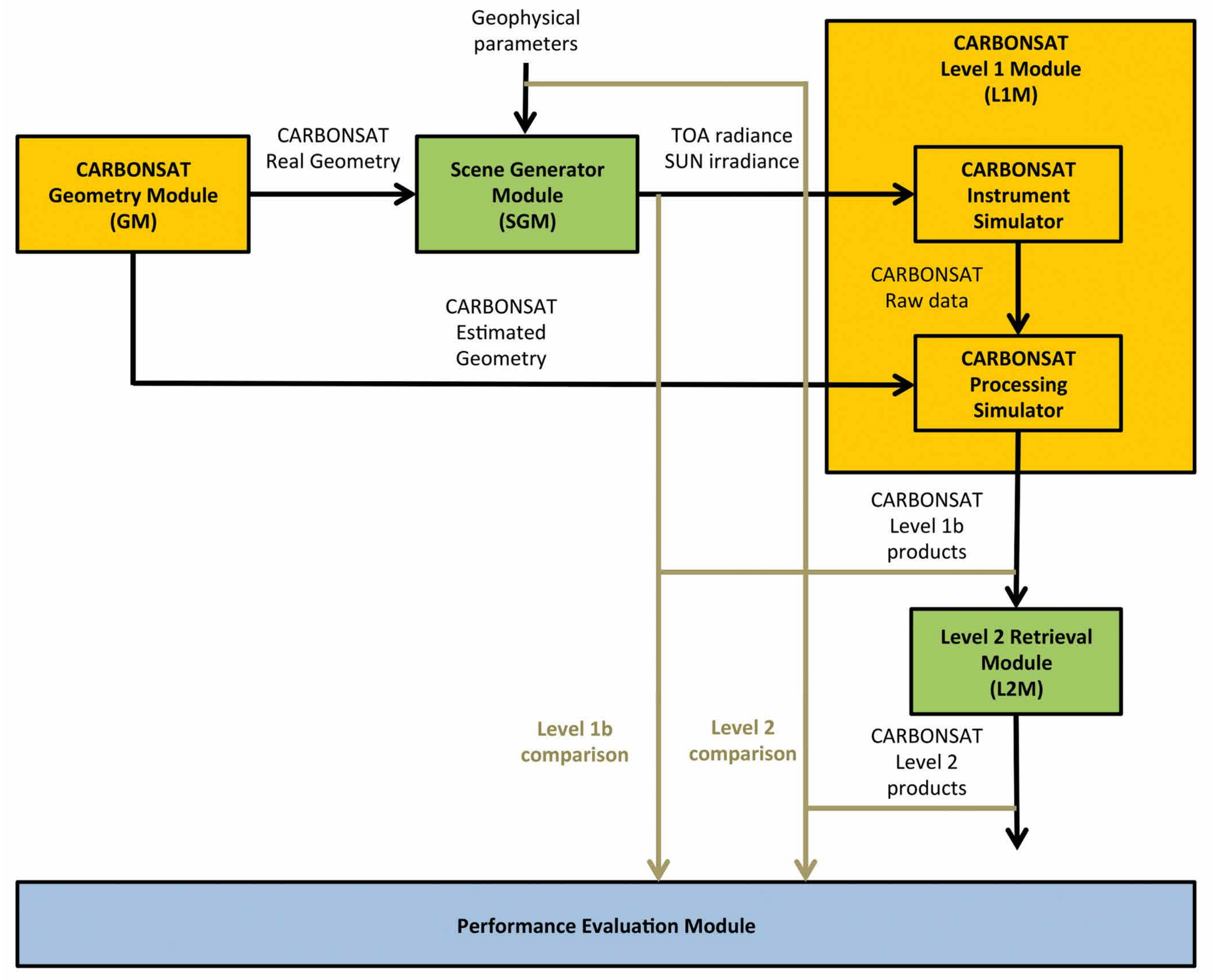

Figure 7.9. CarbonSat End-to-End Simulator. (ESA)

Databases used in the scene generator:

- land cover: USGS Biosphere Atmosphere Transfer Scheme, *http://edc2.usgs.gov/glcc/tabgoode_globe.php*
- MODIS/Terra Snow Cover Monthly L3 Global 0.05 Deg CMG (MOD10CM), *http://nsidc.org/data/mod10cm*
- albedo at 858 nm, 1640 nm, and 2130 nm based on NASA's filled surface albedo, which is based on a climatology (2000–2004) of MODIS, MOD43B3, *http://modisatmos.gsfc.nasa.gov/ALBEDO/index.html*
- surface elevation based on GTOPO30 digital elevation model
- aerosol optical depth (AOD) at 750nm: based on MACC
- cirrus cloud optical depth (COD), cirrus cloud top height (CTH): based on effective COD (eCOD) of CALIPSO
- altitude, pressure, temperature, water vapour profiles: European Centre for Medium-Range Weather Forecasts (ECMWF) ERA Interim
- CO_2: NOAA CarbonTracker 2011
- CH_4: NOAA CarbonTracker 2010

— The Level-1 Module (L1M#1 and L1M#2 for concept A and B, respectively) comprises two parts:

The instrument simulator calculates the instrument response from the incoming radiance and irradiance by simulating all relevant parts of the optics and the electronics. The alpha version includes simulation of:

- the polarisation instrument behaviour through the Mueller matrix (if polarised input spectra are used)
- the instrument point spread function for the spatial convolution of the high-resolution input scene
- the ISRF for the spectral convolution of the high-resolution homogeneous input scene
- the instrument smile
- instrument transmittance in the bands and out of band
- the detector quantum efficiency
- the instrument radiometric noises: shot noise, dark current, smear, detector read-out noise, video chain noise and quantisation noise

The final version includes simulation of:

- the ISRF for the spectral convolution of the high-resolution input scene considering scene heterogeneity and the slit homogeniser optical model
- straylight (diffuse and ghost)
- diffusor speckles

From the instrument's measured response, the Level-1b processor derives the radiance and irradiance in physical units. The alpha version includes:

- reconstruction of photon counts through radiometric calibration
- smile correction
- spectral calibration

The final version includes:

- straylight correction

— The L2M performs the retrieval to determine the XCO_2 and XCH_4 columns for the scene, based on the calibrated radiance and irradiance. The L2M comprises two retrievals corresponding to the two measurement modes of the instrument: nadir for the default measurement mode for land scenes and glint for ocean scenes with suitable glint geometry. Currently, for nadir data a dedicated retrieval is performed by default (Chapter 6), whereas for glint data a linear parameterised retrieval (using a look-up table) is performed by default, which is less accurate.

— The performance evaluation module investigates the performance of the full simulation chain. The comparison can be performed at two levels. Firstly, the PEM compares the measured and calibrated radiance and irradiance from the L1M with the simulated radiance and irradiance from the SGM. Secondly it compares the retrieved XCO_2 and XCH_4 columns from the L2M with those assumed in the radiative transfer calculations of the SGM. Almost all intermediate results are dumped and can be used in the performance evaluation module.

7.3.2.1 E2ES estimated performance at Level-2

Sensitivity analysis

The sensitivity of the Level-2 retrieval depends on the geophysical conditions. Small systematic errors from varying atmospheric conditions affecting the

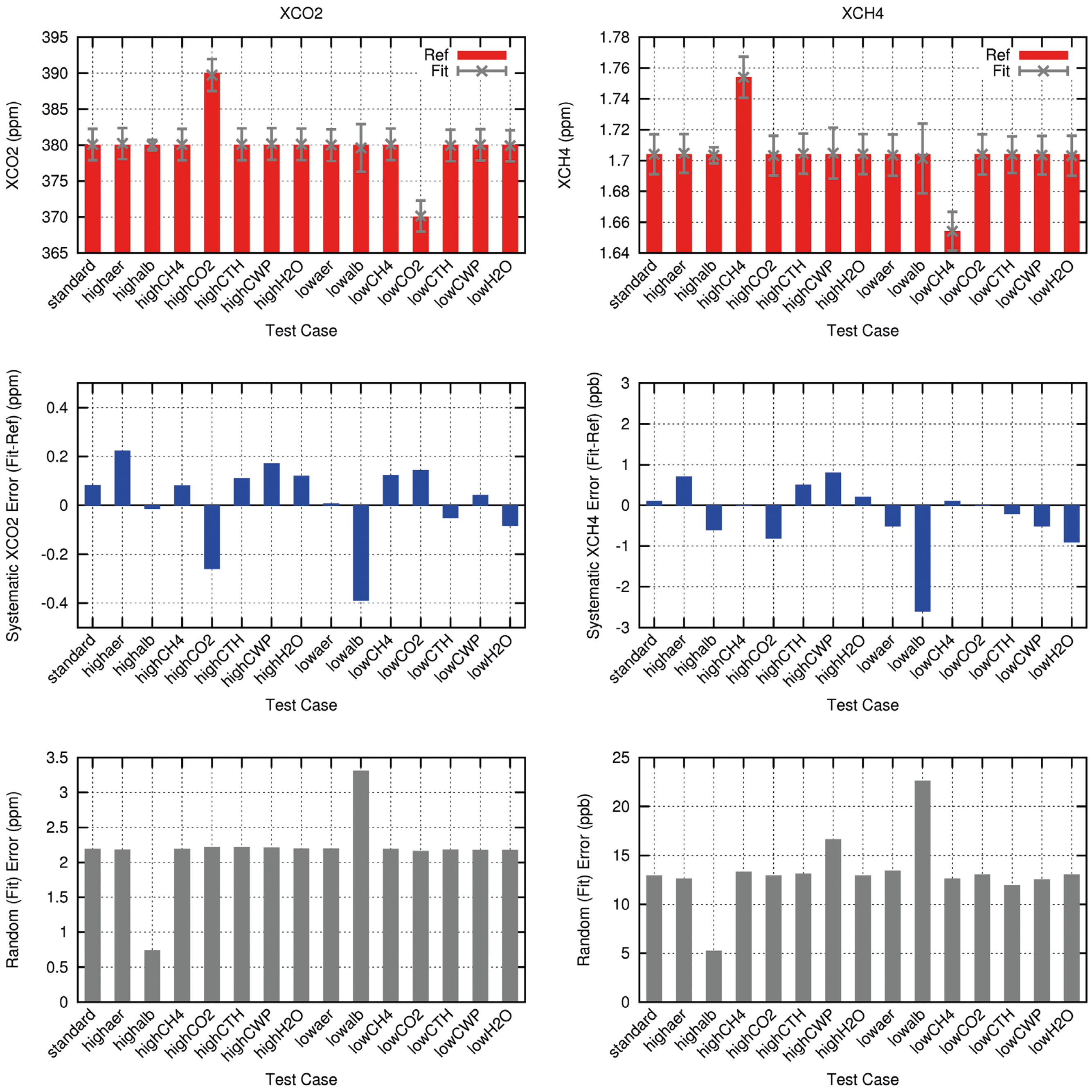

Figure 7.10. Results of varying geophysical conditions on simulated and retrieved columns, systematic errors and random errors. (S. Noel–IUP)

atmospheric scattering are known to be critical for the use of XCO_2 and XCH_4 in inverse modelling frameworks to derive greenhouse-gas fluxes. The E2ES was used to establish the dependence of systematic errors in Level-2 products on varying geophysical conditions using realistic instrument concepts. Fig. 7.10 shows the sensitivity of the retrieval to different geophysical conditions.

The simulations generate calibrated spectra and calculate their estimated errors, which are dominated by the instrument's noise. In most simulations, the noise is not added to the Level-1b spectra. The spectra are noise free, although the error (SNR) calculated for the spectra includes the noise component. This approach allows a straightforward way of separating random and systematic errors. The retrieval algorithm (optimal estimation) maps the spectra's covariance to the random error (single measurement precision) of the retrieved

XCO_2 and XCH_4. Since the retrieved values from noise-free spectra have no random error component, the remaining differences between simulated and retrieved XCO_2/XCH_4 are systematic errors only.

A standard scenario is considered with a solar zenith angle (SZA) of 52° and a column composition: CO_2: 380 ppm, CH_4: 1704 ppb, H_2O: 1.43 g m^{-2}, albedo: 0.2/0.1/0.05 (NIR/SWIR-1/SWIR-2), AOD@750 nm: 0.136, CTH: 10 km, cloud water path (CWP): 3 g m^{-2} (COD ~0.1). Sensitivity analysis is performed by changing one parameter at a time between the following maximum and minimum values:

- high /low aerosol: standard ± 50%
- high/low albedo: 0.35/0.05, same for all bands
- high/low CH_4: standard ± 50 ppb
- high/low CO_2: standard ± 10 ppm
- high/low CTH: standard ± 4 km
- high/low CWP: 10 g m^{-2}/1 g m^{-2}

Simulated performance over part of an orbit

To estimate performance at Level-2 in realistic atmospheric conditions, one orbit of nadir data were simulated accounting for varying SZA, surface albedo and atmospheric composition along the orbit. Cirrus clouds have been taken into account retrieved from the SGM database, as were the other parameters, but otherwise cloudfree conditions are assumed (cloud covered pixels would be filtered). The approach to use noise-free observations to separate random from systematic errors, as described above, was also applied here. Figure 7.11 shows the performance of the instrument in respect to the requirements for systematic errors to be <0.5 ppm for XCO_2 and <5 ppb for XCH_4. A section from Russia to South Africa is shown.

To reduce computational time, one nadir measurement is simulated every hundred seconds. The geophysical parameters in this simulation are taken either from climatologies or selected measurements of existing satellite instruments as described in Section 7.3.2. The results of the simulation in terms of XCO_2 and XCH_4 along the orbit include the simulated and retrieved columns, the difference between these two and the random error. The simulated measurements are able to accurately identify the latitudinal variation of XCO_2 and XCH_4, the retrieved columns follow the north to south gradient. Random errors are small in regions of high albedo and increase with lower surface albedo as well as with large SZAs.

A similar approach is taken to simulate sunglint observations over the Atlantic Ocean (Fig. 7.12). Here, a standard scenario for the geophysical conditions was assumed using only CO_2 and CH_4 retrieved from the database (windspeed: 5 m s^{-1}, AOD: 0.1, aerosol height: 1 km, COD: 0.02, CTH: 10 km).

Both random and systematic errors meet the Level-2 requirements for XCO_2 and XCH_4. In contrast with the simulated nadir orbit, no dedicated retrieval is performed but a pre-calculated look-up table is used. The look-up table currently used is too coarse for large glint angles. A dedicated retrieval will be used in the future to better exploit the complete range of sunglint observations. These end-to-end simulations demonstrate that under variable SZA the systematic error for XCO_2 is below 0.5 ppm and the random error is between 0.7 and 1.7 ppm (single measurement). For XCH_4 the systematic error is below 3 ppb and the random error between 5 and 10 ppb. These results are obtained with an approach described above, estimating the random error component as part of the optimal estimation retrieval, based on the SNR of the measurement.

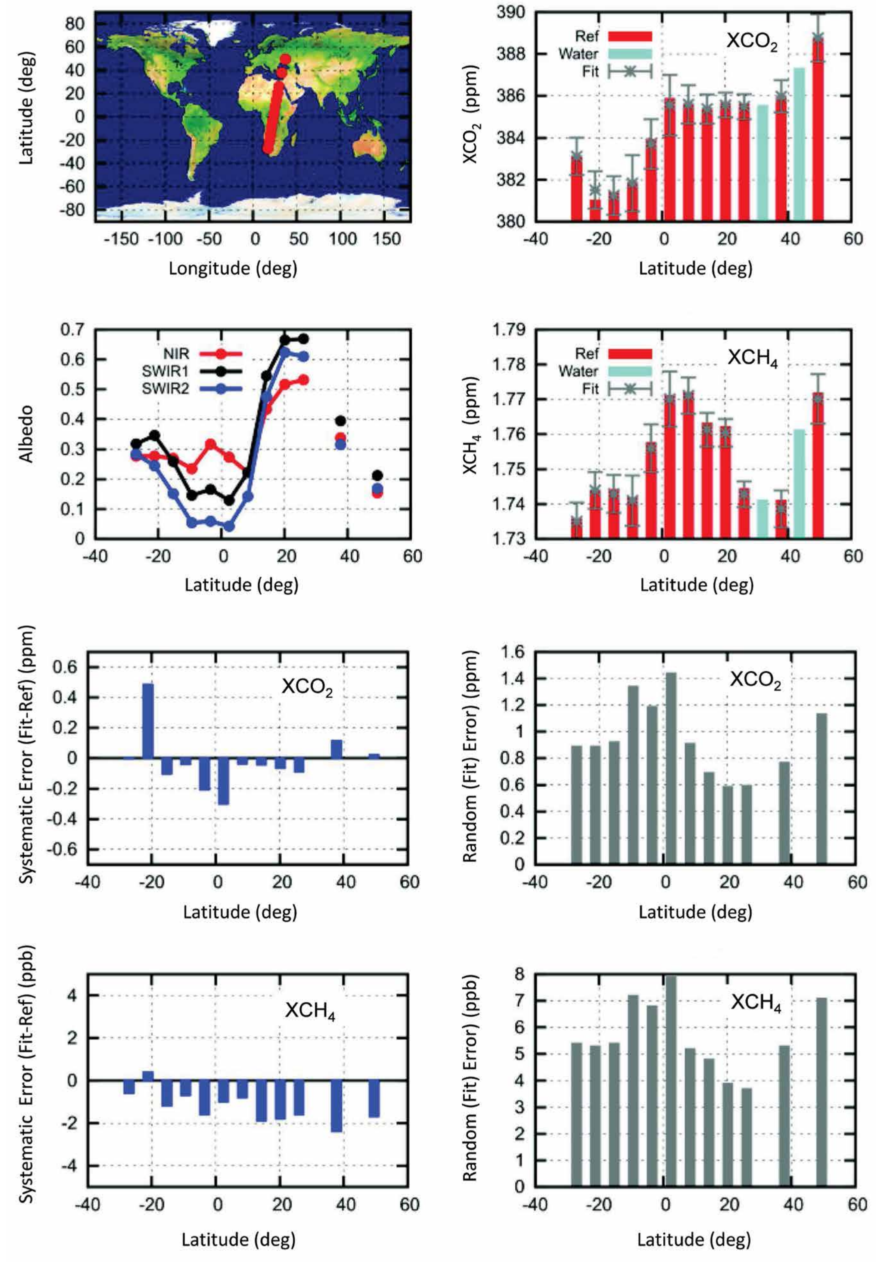

Figure 7.11. Measurement performance for XCO_2 and XCH_4 along one orbit, simulating one nadir measurement every 100 seconds (no continuous coverage) for spring equinox. The upper left plot illustrates the simulated orbit with measurements from Moscow in Russia to Cape Town in South Africa. The plot underneath shows the corresponding ground albedo. The lower four plots show XCO_2 and XCH_4 simulated (Ref) and retrieved (Fit) columns together with their differences (systematic error) and the random error from the Level-2 retrieval fit. (S. Noel–IUP)

Imaging potential

The CarbonSat design potentially allows to image major point sources of greenhouse gases. Figure 7.13 shows a case study for a 30×30 km^2 area around the Jänschwalde power plant in Germany.

A plume model, using the emission rate of the power plant and assuming a moderate wind speed, calculates the distribution of the XCO_2 emission as shown in Fig 7.13 (left):

— Jänschwalde power plant (51.84N, 14.46E)
— emission rate 25 Mt CO_2 yr^{-1}
— source width: 500 m
— Pasquill stability class (A, B, C,...): A
— wind speed: 4.5 m s^{-1}, wind direction: 228°

The plume is added to the CO_2 background, and the other geophysical quantities are taken from databases depending on geolocation.

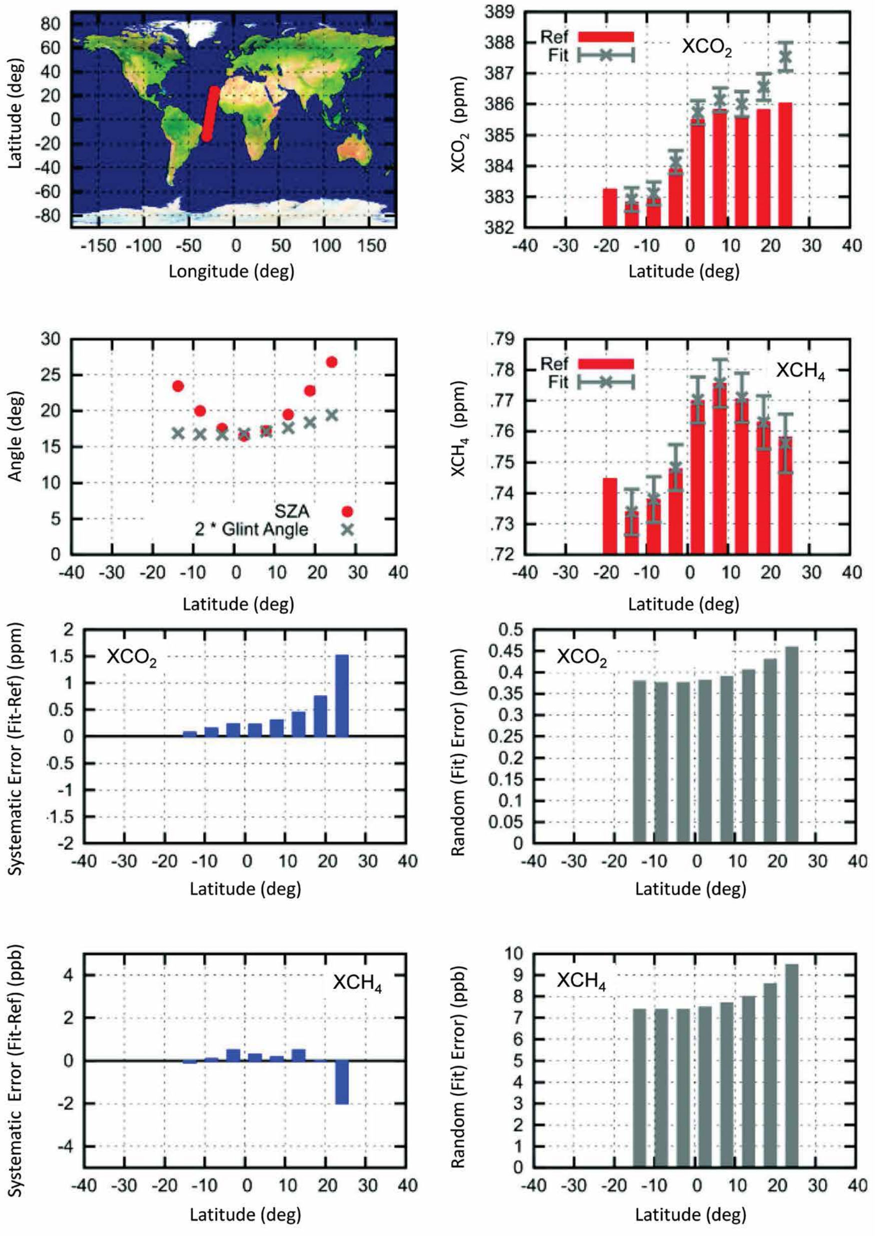

Figure 7.12. This is the same as Fig. 7.11 but indicates measurement performance along one orbit, simulating one sunglint measurement every 100 seconds over the Atlantic Ocean. (S. Noel–IUP)

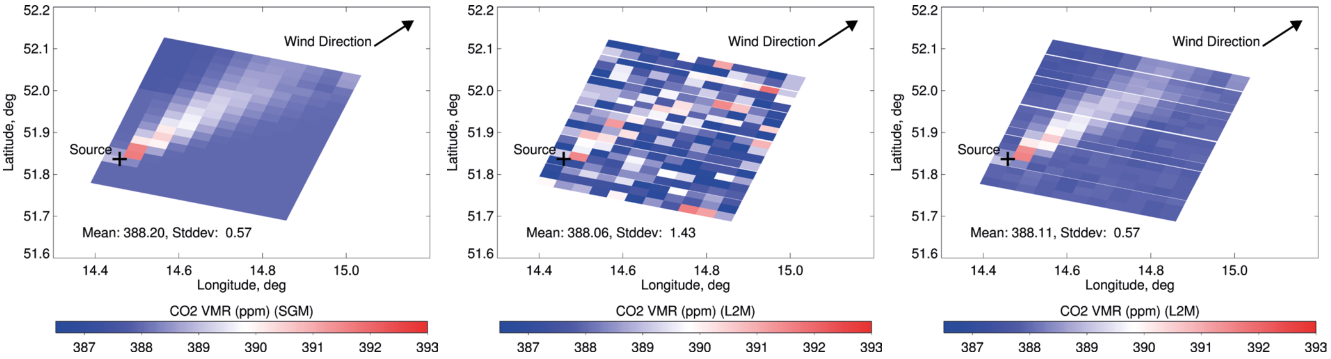

Figure 7.13. Plume simulation. Left: the CO$_2$ emission from the Jänschwalde power plant simulated by a plume model and gridded to the CarbonSat spatial resolution. Middle: the end-to-end retrieved XCO$_2$ including noise on the spectrum (single measurement performance). Right: the end-to-end retrieved XCO$_2$ columns for the noise-free simulation. The 'mean' given in the plots is the XCO$_2$ column in ppm averaged over the scene. The 'Stddev' is the standard deviation of this mean, indicating the variability over the scene. (S. Noel–IUP)

The retrieved XCO_2 including noise on the spectra of single measurement is shown in Fig. 7.13 (middle). The retrieved XCO_2 in the noise-free case (Fig. 7.13, right) shows a mean difference to the simulated scenario of 0.1 ppm, indicating the expected systematic error (bias) of the retrieved column. The mean random error on the retrieved XCO_2 columns is 1.3 ppm. To achieve a random error below 0.5 ppm, five to six views of the same scene need to be averaged assuming the same local conditions (mainly emission rate, wind speed and direction). Alternatively, for larger local-scale sources, such as cities, spatial averaging (Fig. 4.5) will allow their source strength to be quantified.

7.3.3 Stand-alone Sensitivity Analysis

The main purpose of the stand-alone Level-2 sensitivity analysis was to provide key inputs for the OSSEs applied in Section 7.4 for the quantification of greenhouse-gas fluxes from CarbonSat observations. These inputs are realistic estimates of the random (uncorrelated) and systematic (correlated) errors of the CarbonSat Level-2 products XCO_2 and XCH_4. To be useful for the different OSSE applications, a full one-year dataset of Level-2 errors was generated based on assumptions about orbit, swath width and pixel size, using the Level-1b requirements and considering realistic scenarios in terms of geophysical parameters such as SZA, surface albedo, aerosols, and cirrus clouds affecting the retrievals.

The stand-alone framework is conceptually similar to the CarbonSat E2ES, with the following main differences:

- Level-1 performance is assumed independent of the specific sensor implementation and uses the specified Level-1 requirements in Chapter 4, and in special cases uses expected Level-1 performance

- the Level-2 retrieval enables detailed investigations of the impact of atmospheric scattering on XCO_2 and XCH_4 systematic errors including optimisations of the Level-2 retrieval model

- the system is not implemented in Open SF and performance evaluations are performed individually

More details of the framework for the stand-alone simulations have been published in Buchwitz et al. (2013a).

Particular attention was paid to the influence of aerosols and cirrus clouds, since from knowledge of the physics of atmospheric radiative transfer and experience gained with data from SCIAMACHY and GOSAT it is known that errors resulting from scattering by clouds and aerosols are the dominant systematic errors in XCO_2 and XCH_4 (e.g. Reuter et al., 2010, and references given therein). In addition to AOD, the type of aerosol was also considered as a potentially important source of error (Buchwitz et al., 2013a). Another purpose of the stand-alone retrieval framework was, therefore, not only to quantify these error sources, but also to mitigate them by optimising sensor requirements and Level-2 retrieval methods. In addition, these simulations were used to establish a Level-2 error budget for XCO_2 and XCH_4.

Key characteristics of the one-year simulated Level-2 data set are summarised in Section 7.3.4 and OSSE results using the dataset are presented in Section 7.4.

Because it is important to control and mitigate systematic errors in XCO_2 and XCH_4 caused by atmospheric scattering, systematic retrieval simulations were carried out in addition to the sensitivity studies with the CarbonSat E2ES presented in Section 7.3.2.1, in particular, to estimate the impact of variations of aerosols and cirrus clouds on the retrieved XCO_2 and XCH_4. Figure 7.14 shows

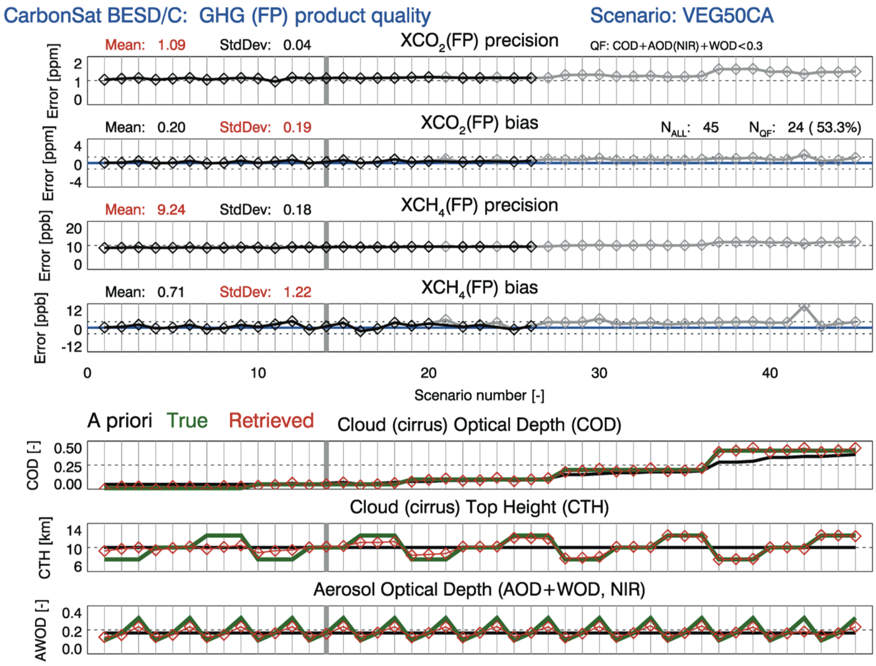

Figure 7.14. Detailed assessment results for XCO_2 and XCH_4 errors owing to atmospheric scattering (optically thin clouds and aerosols). The three panels at the bottom show the 45 selected scenarios in terms of COD, CTH and AOD. Green lines show the true values, black lines the *a priori* values used for the BESD/C retrieval, and red symbols are the values as retrieved from the simulated CarbonSat observations. The four panels at the top show the XCO_2 random and systematic error and XCH_4 random and systematic error for each of the 45 scenarios. Symbols for scenarios that fall outside the criterion for 'good observations' (retrieved COD+AOD <0.3) are shown in grey. (M. Buchwitz–IUP)

results from 45 scenarios, defined by different combinations of COD, CTH and AOD. For COD the *a priori* value is obtained via pre-processing of the CarbonSat spectra exploiting the saturated water band spectral region around 1939 nm.

Before analysing the data, a quality flagging has been applied. The total retrieved scattering optical depth (COD+AOD) is a good indicator for the retrieval quality. A threshold value for COD+AOD of 0.3 has been chosen based on experience with SCIAMACHY and GOSAT data (Buchwitz et al., 2015a). For scattering optical depths smaller than 0.3, XCO_2 and XCH_4 can be derived with good precision and accuracy (Fig. 7.14). Even for scattering optical depths larger than 0.3, the retrieved XCO_2 and XCH_4 values are still within requirement limits for almost all of the scenarios. However, it can be seen that this is not always the case, e.g. for large SZAs. As can be seen in Fig. 7.14, the random errors are typically around 1.1 ppm for XCO_2 and 9 ppb for XCH_4. These values are primarily determined by SNR.

For the results shown in Fig. 7.14, the threshold SNR requirement has been used. The aerosol- and cirrus-related systematic errors of the quality-filtered observations are, in this case, stated in terms of mean value plus or minus standard deviation: 0.20 ±0.19 ppm for XCO_2 and 0.72 ±1.2 ppb for XCH_4. The scattering-related parameters COD and CTH can be retrieved well, while the retrieval of AOD is less reliable.

As shown in Chapter 4, systematic simulations have been carried out to estimate the impact of all other known error sources on Level-2, in particular instrument-related error sources that impact the quality of the Level-1 products such as various types of radiometric (additive, multiplicative, spectral dependence) and spectral calibration errors.

The results from all these simulations have been used to establish the XCO_2 and XCH_4 error budget. Table 7.3 summarises the error budget for nadir-mode observations over land. A similar table was generated for the glint mode observations over water. An error characteristic has been specified for each error source by determining a random and systematic component. Some error sources are purely random, but most of the error sources also have a systematic part (at monthly–regional scale).

In summary, it can be stated that even in unfavourable atmospheric conditions of scattering optical depth of up to 0.3, the corresponding errors

Table 7.3: CarbonSat error budget for the XCO_2 and XCH_4 data products for nadir observations over land.

Error source	Error contributors			
	Random error per sounding 'Precision'		Systematic error (monthly–regional scale, non-constant part only) 'Relative Accuracy'	
	XCO_2 [ppm]	XCH_4 [ppb]	XCO_2 [ppm]	XCH_4 [ppb]
Algorithm				
Clouds & aerosols	0.40	3.00	0.30	3.00
Meteorology	0.10	0.80	0.10	0.80
Spectroscopy	0.10	0.80	0.10	0.80
Other	0.10	0.80	0.10	0.80
Instrument				
SNR	1.20	9.00	0.00	0.00
Radiometric:				
Multiplicative/absolute	0.17	1.80	0.10	0.80
Multiplicative/relative	0.40	4.00	0.20	2.00
Additive (zero-level offset)	0.17	1.80	0.10	0.80
ISRF	0.17	1.80	0.10	0.80
Spectral calibration	0.20	1.97	0.17	1.80
Spatio-temporal coregistration	0.48	3.00	0.48	3.00
Heterogeneous Scenes/Pseudo Noise	0.32	2.62	0.30	2.50
Other	0.14	1.13	0.10	0.80
Total Error (root-sum-square)	1.50	11.70	0.47	4.33
Threshold Requirement	3.00	12.00	0.50	5.00

in the Level-2 product remain below the threshold requirement (Chapter 4). In addition, when analysing the impact of contributors to the error budget (Table 7.3, including sensor- and retrieval-related error sources) this set of sensitivity simulations demonstrates Level-2 retrieval performance is compliant with the requirements (Table 4.2).

7.3.4 One Year of Simulated Level-2 Data Characteristics

A one-year dataset of simulated CarbonSat Level-2 errors has been generated and analysed to characterise the expected performance of CarbonSat over seasons and regions. The dataset has been generated by considering typical distributions of surface albedo, aerosols and clouds. Surface albedo (including snow/ice), aerosol (AOD, Angström exponent from the Copernicus Atmosphere Monitoring Service) and cloud information (cloud faction) were obtained from MODIS, and cirrus information (optical depth, cirrus altitude) from CALIPSO satellite observations. Meteorological parameters from ECMWF have also been used. The number of quality-filtered observations from nadir mode over land for July at 5°×5° spatial resolution is shown in Fig. 7.15.

As can be seen, CarbonSat will deliver a vast amount of data even after quality filtering. Compared to real 2010 data from GOSAT and SCIAMACHY (Table 7.4), CarbonSat will provide several orders of magnitude more data points per grid cell. Based on scaling the CarbonSat simulated results, OCO-2 has one order of magnitude less data. This amount of anticipated CarbonSat data should enable research on climate-induced disturbances (temperature

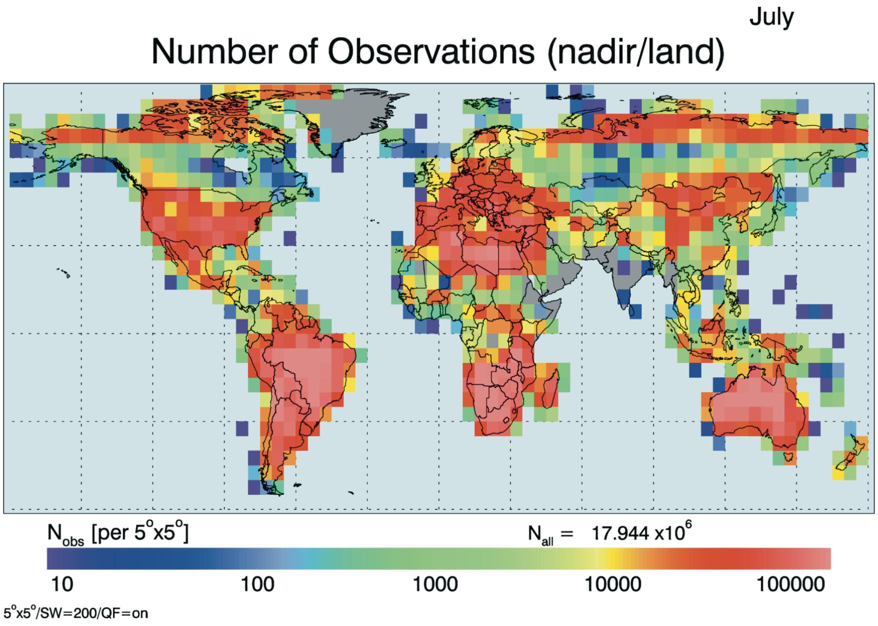

Figure 7.15. Number of quality-filtered CarbonSat observations over land for July at 5°×5° spatial resolution and assuming a swath width of 200 km. (M. Buchwitz–IUP)

Table 7.4. Estimated number of CarbonSat quality-filtered XCO_2 observations per month at 5°×5° spatial resolution over Europe and Amazonia compared with real data from other missions. Statistics for XCH_4 are similar.

	Europe (40° N–70° N, 15° W–30° E)		Amazonia (20° S–10° N, 80° W–40° W)	
	January	July	January	July
SCIAMACHY	2	22	15	102
GOSAT	1	9	4	15
OCO-2	3000	5500	3500	12 000
CarbonSat	26 000	47 000	31 000	105 000

H_2O, etc.) of the natural carbon cycle on monthly temporal and sub-regional spatial scales.

After typical cloud distributions are taken into account (as provided by MODIS), the spatio-temporal distribution of the XCO_2 and XCH_4 mean random errors are derived and shown in Fig. 7.16. Both nadir/land and glint/ocean observations have been considered. The mean random errors vary mainly with surface albedo and SZA. Detailed statistical results for two land regions are presented in Fig. 7.17. As can be seen, the errors are typically well below the threshold requirement.

In addition, the simulated Level-2 dataset has been used to generate maps of the random and systematic XCO_2 and XCH_4 errors as shown in Fig. 7.18 for two orbit sections over Germany. The database yields a systematic analysis of the origin of spatial structures in the random and systematic errors. As expected, the random errors correlate with surface albedo (not shown). For systematic errors, other parameters such as the amount and type of aerosols, COD, CTH and SZA are also important.

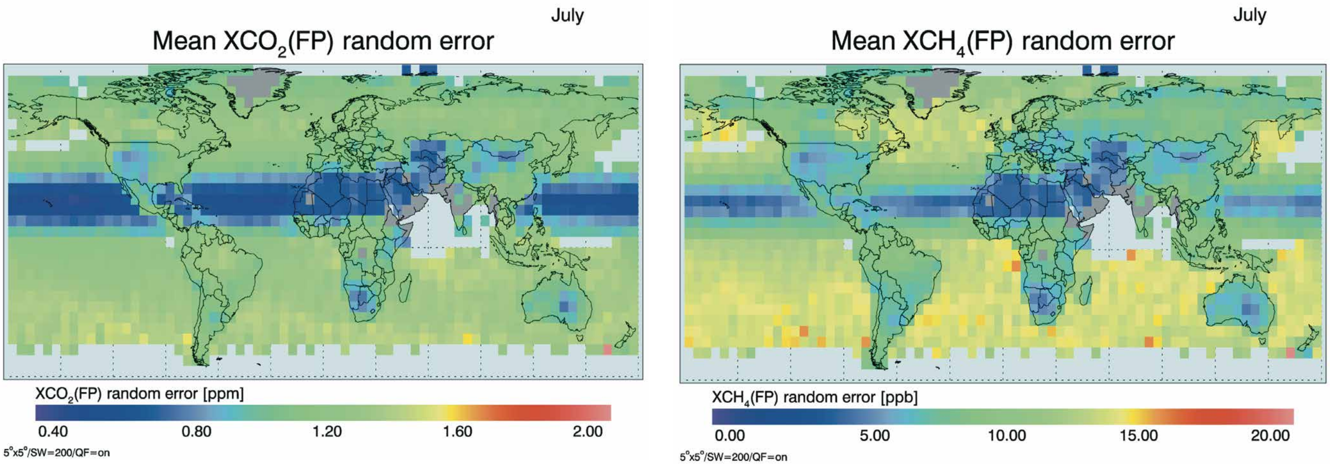

Figure 7.16. Mean of single pixel random errors of XCO_2 (left) and XCH_4 (right) for July over 5°×5° grid cells. The assumed swath width is 200 km. The values can be compared with the requirements of 1 (G) to 3 (T) ppm for XCO_2 and 6 (G) to 12 (T) ppb for XCH_4. (M. Buchwitz–IUP)

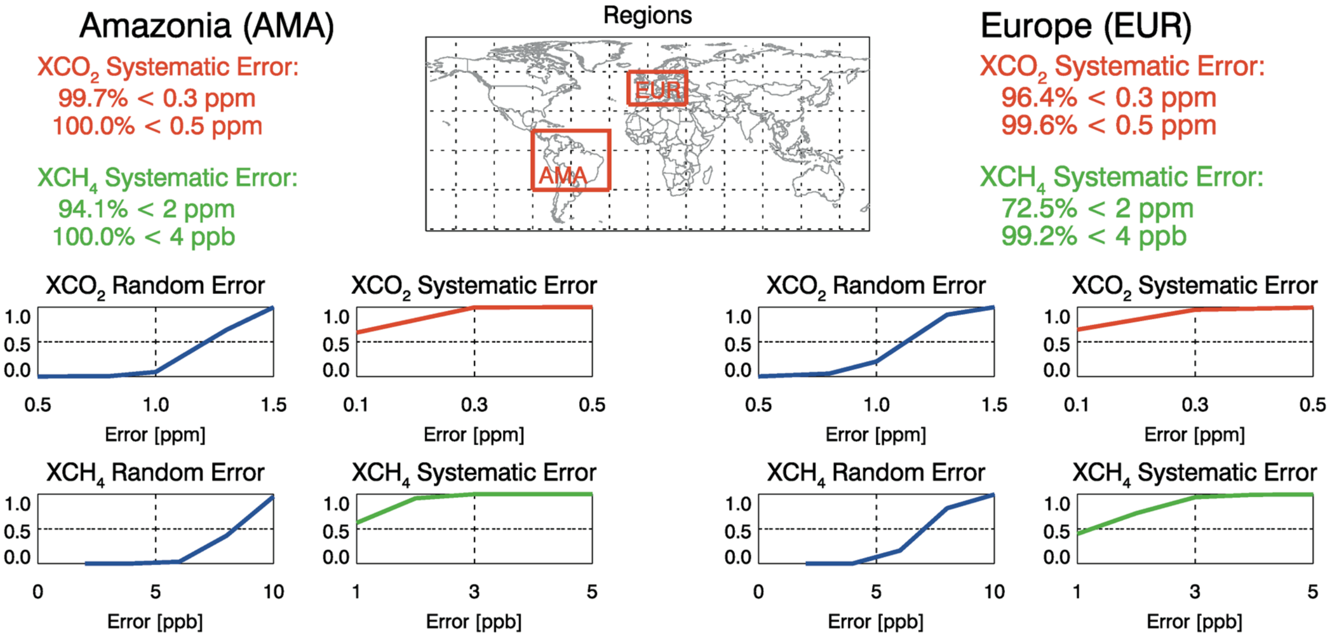

Figure 7.17. Regional cumulative error distributions (1.0=100%) for XCO_2 (red) and XCH_4 (green) over Europe and tropical South America for July 2008. The x-axis shows the errors for XCO_2 and XCH_4 in ppm and ppb. Figures for other regions can be found in Buchwitz et al. (2013a). (M. Buchwitz–IUP)

7.4 Estimated Scientific Impact

7.4.1 Global, Regional and Country Scale

To assess the expected benefits of the CarbonSat mission for regional to global scale greenhouse-gas emission estimation, performance beyond Level-2 has been quantified using OSSEs using the one-year global dataset of simulated CarbonSat retrievals presented in the previous section. The aim of these experiments is to estimate how well sources and sinks of CO_2 and CH_4 can be estimated using CarbonSat, and how the performance compares with other missions. The experiments make use of the TM5-4DVAR inverse modelling system (Basu et al., 2014, Houweling et al., 2014) applied to the CarbonSat dataset. Figure 7.19 shows a schematic representation of the setup of the OSSE

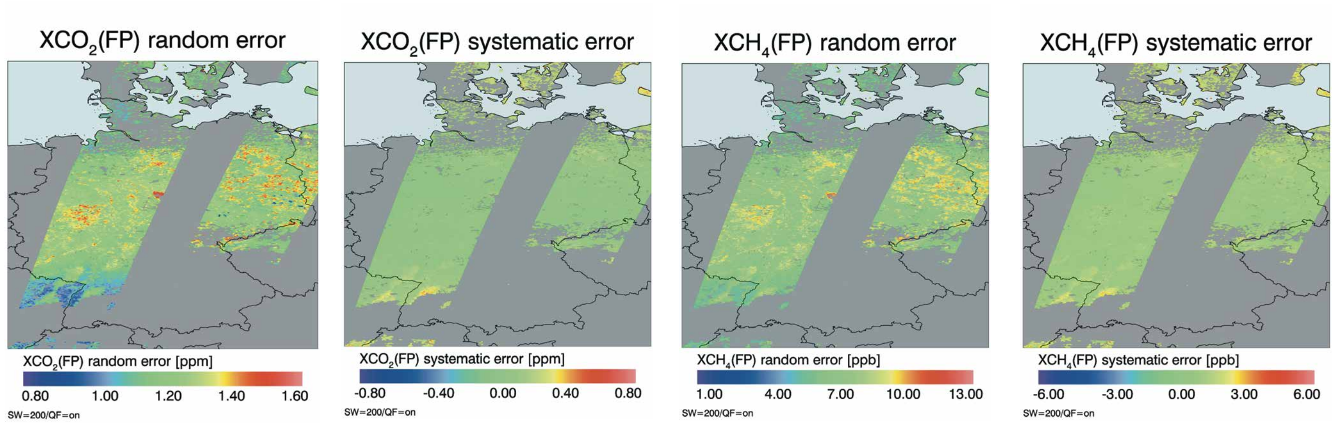

Figure 7.18. Estimated CarbonSat XCO$_2$ and XCH$_4$ single ground pixel retrieved precision and systematic error for quality-filtered ground pixels over land for two orbits over Germany (for June 2008 meteorological conditions). Data gaps are primarily due to the presence of clouds and extent of the swath. (M. Buchwitz–IUP)

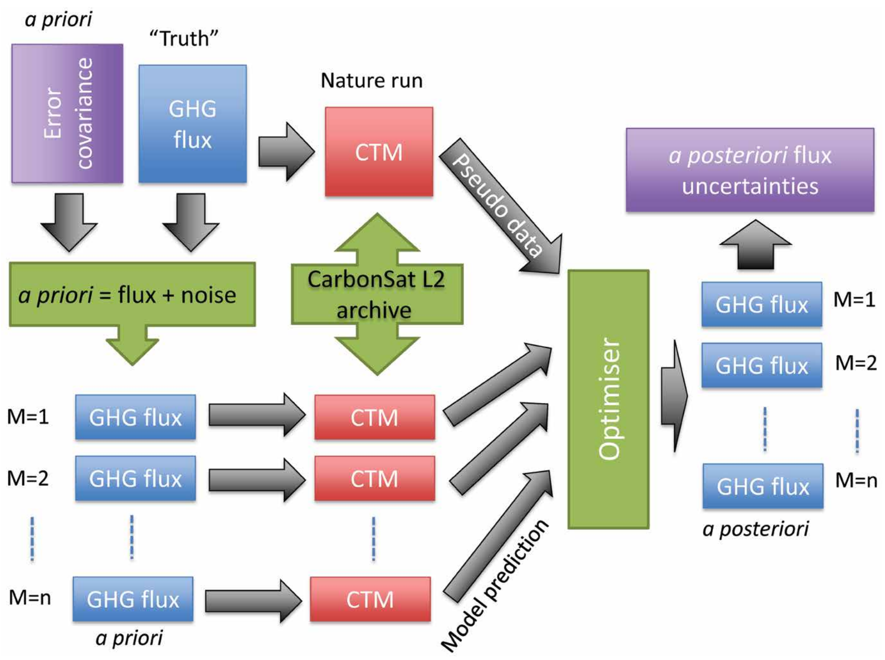

Figure 7.19. Schematic representation of the experimental setup of OSSE experiments to test the expected quality of global to regional-scale CO$_2$ and CH$_4$ fluxes obtained using CarbonSat. A Monte Carlo method is applied using M=n ensemble members. Subsequent flux uncertainties are derived from the statistics of the inversion-optimised ensemble. (S. Houweling–SRON)

experiments. The calculation of *a posteriori* flux uncertainties are essential to this method so they are accurately estimated by applying the variational inversion technique described in Section 6.5 with a Monte Carlo approach (see e.g. Chevallier et al., 2007). The benefit of CarbonSat is estimated by its capability to reproduce predefined 'true' surface fluxes of CO$_2$ and CH$_4$. To stay as close as possible to reality, the 'truth' represents what is currently known about the global CO$_2$ and CH$_4$ sources and sinks. These fluxes correspond to the prior fluxes that were used in previous applications of the TM5-4DVAR to GOSAT data (see Basu et al., 2014, Houweling et al., 2014).

In an OSSE experiment, the *a priori* fluxes are the true fluxes perturbed by errors, which reflect the uncertainty in state-of-the-art CO$_2$ and CH$_4$ flux estimates derived from emission inventories and land-surface process models. These errors are random realisations of the *a priori* error covariance matrices that have been used in previous GOSAT inversions, and that are also used here in the OSSEs. A set of CarbonSat measurements is generated by sampling a nature run of the atmospheric transport model TM5, using the true fluxes, at the times and locations where CarbonSat measurements are made. These samples are perturbed using the corresponding Level-2 random and systematic

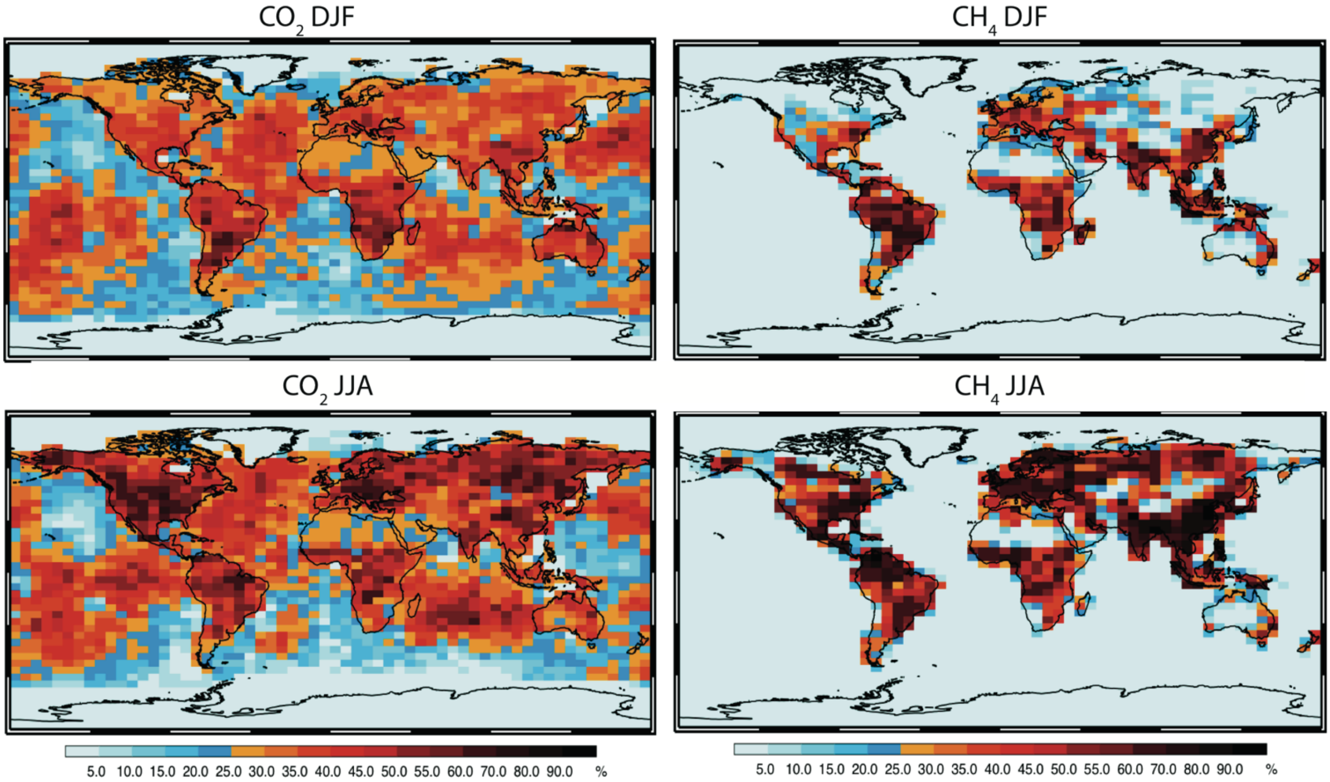

Figure 7.20. Uncertainty reduction of monthly CO_2 (left panels) and CH_4 (right panels) fluxes at 500×500 km^2 for January (top panels) and July (bottom panels). (S. Houweling–SRON)

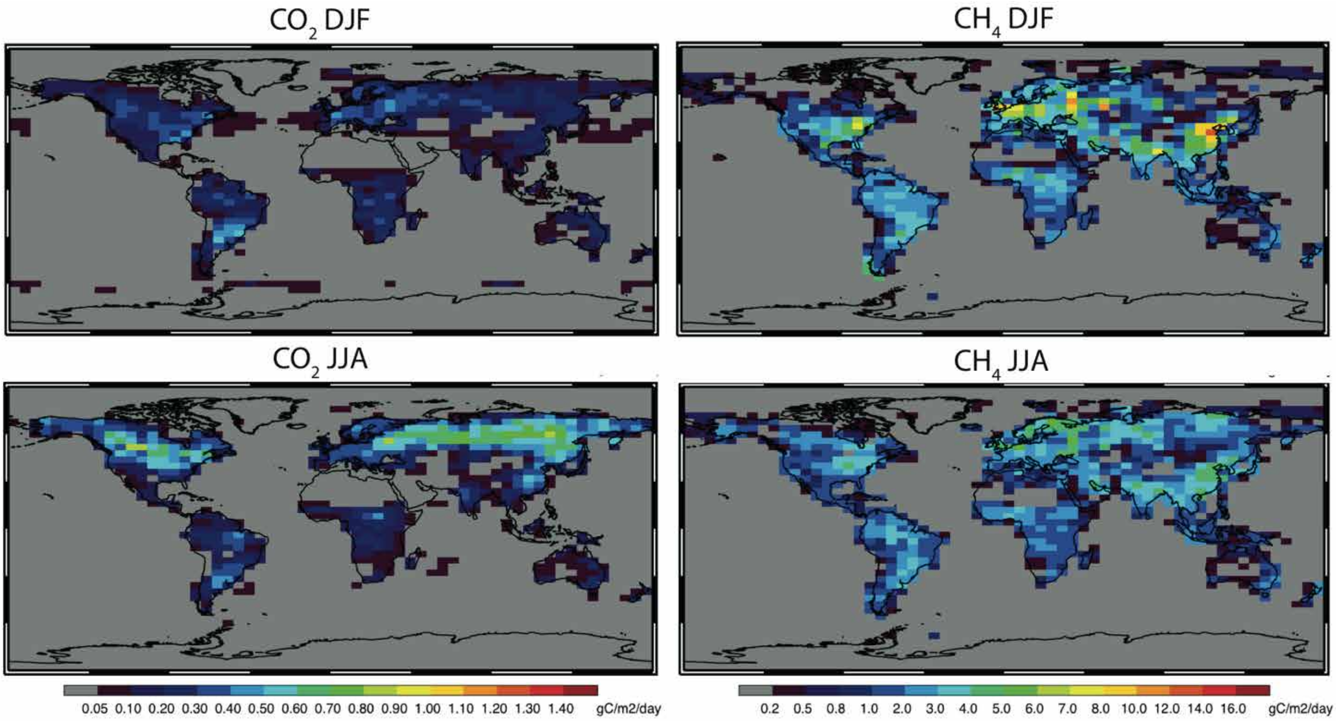

Figure 7.21. *A posteriori* uncertainties of monthly CO_2 (left panels) and CH_4 (right panels) fluxes at 500×500 km^2 for the (Northern Hemisphere) winter (top panels) and summer (bottom panels). (S. Houweling–SRON)

errors from the CarbonSat dataset presented in Section 7.3. The CarbonSat orbits are filtered for retrievals that do not pass predefined filtering criteria, related to cloudiness, aerosol loading, and other factors that compromise the quality of the retrieval (Section 7.4). This procedure is again similar to what is used in real-world applications of satellite data. The performance of CarbonSat is evaluated by its ability to retrieve the true fluxes, as quantified by the uncertainty of the *a posteriori* fluxes. Since the *a priori* fluxes in the OSSEs are random perturbations of the truth and the optimisation problem is linear, these uncertainties correspond to the root mean square difference between the inversion-estimated fluxes and the truth.

One way of assessing the performance of CarbonSat is to compare the *a priori* and *a posteriori* flux uncertainties, expressed as the reduction in flux uncertainty (UR) that is gained using the satellite instrument (Eq 7.1).

$$UR = \left(\sigma_{a\ priori} - \sigma_{a\ posteriori}\right) / \sigma_{a\ priori} \tag{7.1}$$

Figure 7.20 shows these reductions, defined such that 0% and 100% represent the theoretical limits of no uncertainty reduction and exact reproduction of the truth, respectively. The global patterns of uncertainty reduction reflect the flux-resolving power of CarbonSat, but also variations in *a priori* flux uncertainties. For globally homogeneous measurement constraints, the largest uncertainty reductions are achieved where the *a priori* uncertainties are largest. Large uncertainty reductions (>50%) in Fig. 7.20 indicate that *a posteriori* flux uncertainties reflect the performance of the instrument rather than the quality of the *a priori* fluxes. Low uncertainty reductions are found over the Sahara despite excellent measurement coverage in the absence of clouds, because the *a priori* uncertainties are low. The largest uncertainty reductions are found in regions with a combination of uncertain greenhouse-gas fluxes and good measurement coverage. The first differs between CH_4 and CO_2, which explains differences in the patterns that are found.

The OSSE results in Fig. 7.20 demonstrate that CarbonSat will be a major improvement on current global greenhouse-gas monitoring systems. While inversions based on the global surface network and GOSAT are only able to resolve continental-size regions or broad zonal bands, with the help of CarbonSat it is expected that significant uncertainty reductions on much smaller scales of individual 500×500 km^2 grid cells will be achieved. The OSSE results also indicate that potentially important uncertainty reductions can be achieved over oceans.

The *a posteriori* uncertainties in the surface fluxes (i.e. after optimisation using CarbonSat data), are presented in Fig. 7.21. The uncertainty ranges, as reflected in the colour legends, confirm that CarbonSat meets the needed Level-4 performance at the 500×500 km^2 monthly scale (Table 4.1). For CO_2, *a posteriori* uncertainties are around 0.5 gC m^{-2} day^{-1} in most parts of the world, which is a major improvement compared to the current state of the art, given the relatively small size of the regions that are solved in the inversion (500×500 km^2). This is true even more for CH_4, with uncertainties below 5 mg CH_4 m^{-2} day^{-1} in most parts of the world where important sources of methane are located.

To compare the performance of CarbonSat with current operational satellites, additional OSSEs were performed using the LMDz transport model in combination with an analytical inversion technique (Hungershoefer et al., 2010). The advantage of using this method is that it allows a direct comparison with published results. Figure 7.22 presents uncertainty reductions of monthly CO_2 fluxes derived from these inversions. The spatial resolution of the analytical inversions is somewhat lower compared to TM5-4DVAR to keep the computational burden of the analytical inversion method within acceptable limits. The advantage of this approach is that the *a posteriori* uncertainties are very accurate, because they can be calculated analytically rather than

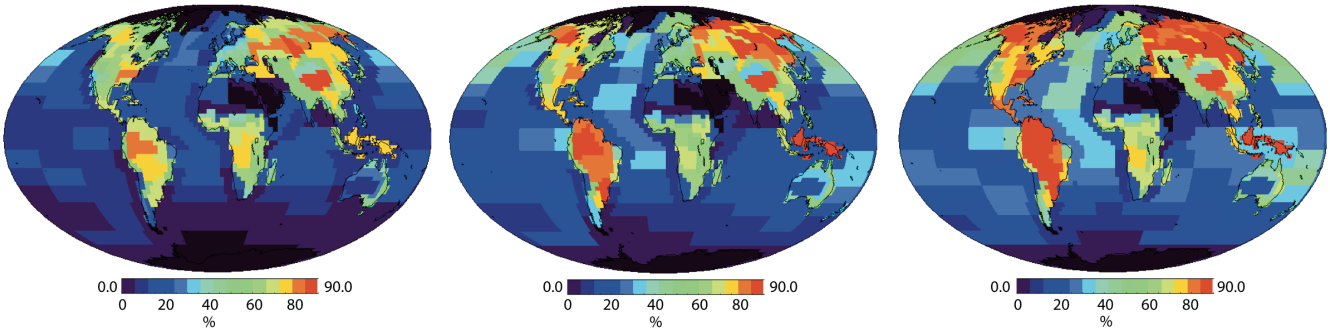

Figure 7.22. Inverse modelling-derived *a posteriori* flux uncertainties for CO_2 comparing CarbonSat to current operational satellites. The values represent monthly uncertainty reduction (for July) for GOSAT (left), OCO-2 (middle), and CarbonSat (right). (C. Bacour–NOVELTIS/LSCE)

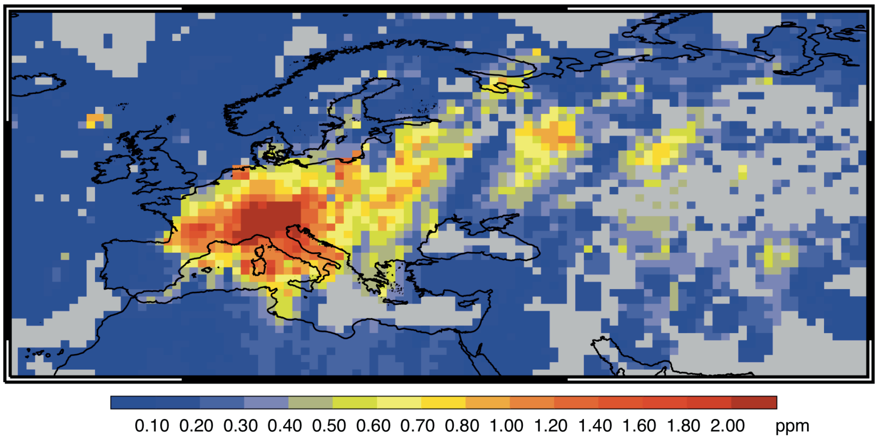

Figure 7.23. Model simulated impact on total column CO_2 of a European heatwave, similar to the heatwave that struck Western Europe in 2003, as it would be observed by CarbonSat. (S. Houweling–SRON)

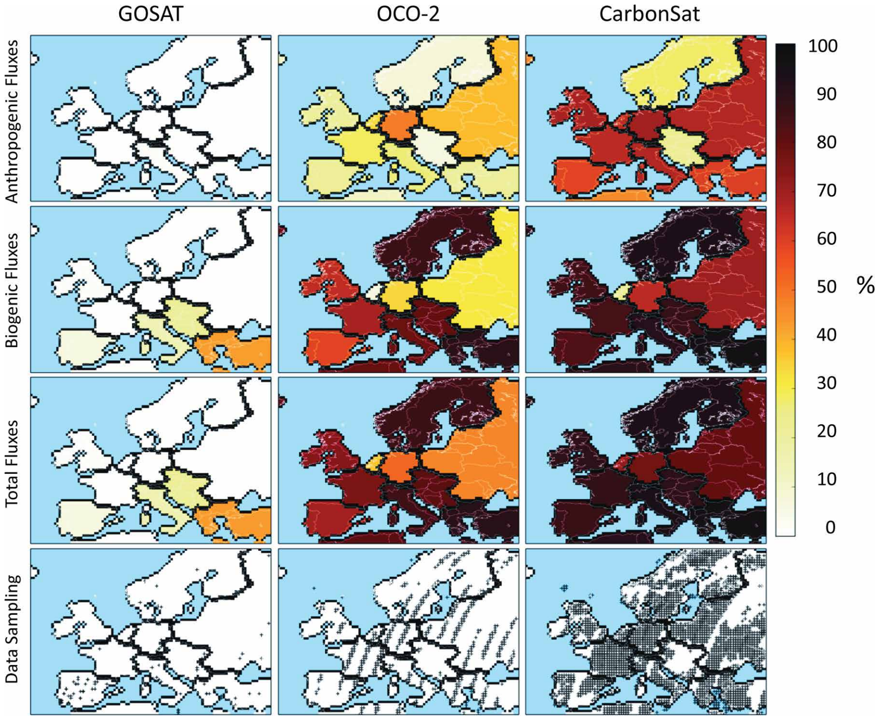

Figure 7.24. Uncertainty reduction (as a fraction of the uncertainty prior to the inversion) achieved by a meso-scale inversion system for 1-week mean fluxes in the regions indicated by the thick borders when using GOSAT (left), OCO-2 (centre) and CarbonSat (right). Results are shown for anthropogenic (1st row), biogenic (2nd row) and total (3rd row) surface fluxes (typical values derived for a week in June 2010). The location of valid satellite observations that are assimilated during the week are plotted in the 4th row. (G. Broquet–LSCE)

approximated numerically as in 4D-VAR. Note that because of differences in the inversion setup between the LMDz and TM5, the results of the methods cannot be compared directly. As can be seen in Fig. 7.22, CarbonSat performs better than any of the other measurement configurations that were tested over land, both at low and high latitudes. Over critical areas like tropical rainforests and northern boreal forests, uncertainty reductions of 70–90% are reached. Corresponding uncertainty reductions for the existing surface network (Hungerhoefer et al., 2010) do not exceed 50% over land, except for Europe, US and Japan, which are monitored by tall tower networks. The results demonstrate that CarbonSat is capable of pushing the state-of the-art to a level that is beyond what can be achieved by GOSAT and OCO-2.

With CarbonSat, annual sources and sinks of CO_2 on sub-continental scale regions are estimated with *a posteriori* uncertainty of close to 0.1 PgC yr^{-1} and of CH_4 with *a posteriori* uncertainty of close to ~1 Tg yr^{-1}.

The monthly resolution of CO_2 and CH_4 fluxes achievable with CarbonSat will allow anomalous fluxes in response to extreme events to be detected. To estimate the typical size of such events that CarbonSat could detect, the anomalous biological CO_2 outgassing caused by the European heatwave of 2003 was simulated using the global transport model TM5 at 1°×1° spatial resolution. The CO_2 loss from European ecosystems during this event has been estimated at 0.5 PgC (Ciais et al., 2005). Figure 7.23 shows how such an extreme event would be detected by CarbonSat after collecting one month of data. As can be seen, the signals of the event exceed 1.5 ppm at a scale of 1°×1°. Given the number of measurements that are collected in cloud-free boxes of this size, it is expected that CarbonSat will be able to resolve anomalies that are even about a factor of five smaller.

When studying fluxes at smaller scales, global OSSEs cannot take full advantage of the measurements provided by CarbonSat owing to the limited horizontal resolution of the models used. To estimate the uncertainty reduction that could potentially be achieved by CarbonSat for country-scale CO_2 fluxes, additional OSSEs were performed using the meso-scale atmospheric transport model Chimere (Broquet et al., 2013). The results (Fig. 7.24) confirm that CarbonSat significantly outperforms GOSAT and OCO-2 with respect to the determination of CO_2 surface fluxes at these scales. The difference is caused by the much larger number of data and better coverage provided by CarbonSat, as indicated by black dots in the bottom row of Fig. 7.24. These results confirm that CarbonSat has the potential to become the first mission to resolve emissions from large countries in the European Union, such as Germany and France. This of course not only holds for whole countries, but also for other areas of similar scale.

According to the OSSEs aiming at the country scale (shown in Fig. 7.24), the largest uncertainty reductions are obtained for the biogenic fluxes, which are the most uncertain, but also for the better known anthropogenic fluxes.

CarbonSat has the potential to separate biogenic from anthropogenic fluxes with a more direct approach by going down to even finer scales so that anthropogenic emissions, such from cities, can be resolved. Assessing the constraints of CarbonSat measurements on fluxes at even smaller scales requires different analysis tools, which will be described in further detail in the remainder of this section.

7.4.2 Local Scale

As already highlighted, none of the current satellite missions was designed to detect and quantify the emissions of localised CO_2 or CH_4 source areas at the local scale. CarbonSat, in contrast, is optimised for this important application as a result of its imaging capability. It is therefore expected that a wealth of

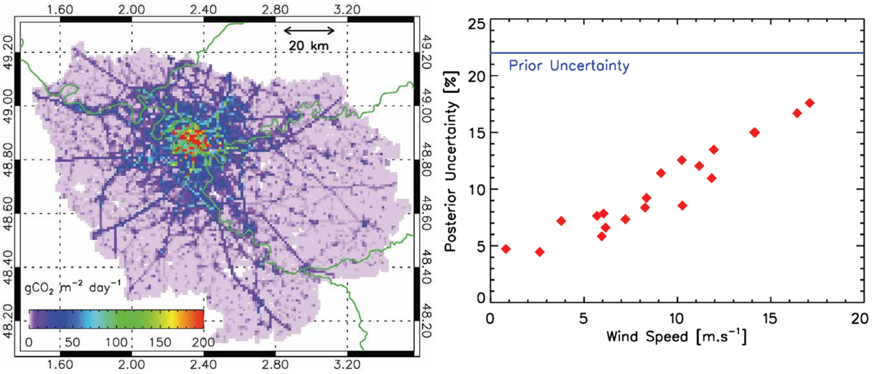

Figure 7.25. Left: map of the estimated fossil fuel CO_2 emissions in the Ile de France region surrounding Paris. Right: uncertainty in the 06:00–11:00 fossil fuel emissions for the Paris area as a function of wind speed. The blue line shows the estimated current uncertainty. The red dots are uncertainty when CarbonSat data is applied and account for CarbonSat sampling (clouds) and atmospheric transport conditions. (F-M. Bréon–LSCE)

new information on various CO_2 and CH_4 emission hot spots will be available from CarbonSat, significantly advancing our knowledge at this scale.

To quantify the potential of CarbonSat to constrain the CO_2 emission of individual cities, OSSEs have been conducted for Berlin and Paris. A complicating factor in the case of Berlin is that there are large power plants close to the city that produce CO_2 plumes of a magnitude comparable to the city plume. OSSE results have been obtained for all CarbonSat Berlin overpasses in one year using the simulated Level-2 XCO_2 dataset presented in Section 7.3. CarbonSat is able to quantify the emissions of Berlin (approx. 43 Mt CO_2 yr^{-1}) with a random error (1-sigma) per overpass of typically 10–15% and systematic errors of typically below 10% (see Buchwitz et al., 2013b). For a swath of 200 km approximately 10–12 overpasses per year with good observation conditions are expected.

The analysis of Paris used the same set of simulated CarbonSat observations together with a high-resolution emission map (Fig. 7.25 left) and a high-resolution (2 km) atmospheric transport model to fully exploit the information content of the observations. For these OSSEs, a number of uncertainty factors were accounted for, such as the uncertain temporal profile of the emissions, the contribution of distant sources and sinks to the CO_2 spatial pattern, and the poorly constrained spatial distribution of the emissions. Results shown in Fig. 7.25 (right) indicate the *a posteriori* uncertainty obtained through the analysis of CarbonSat observations over the Paris area for the aggregated emissions from 06:00–11:00. The current uncertainty is estimated at 22%. This is reduced to 10% and even better when introducing the observations, depending on the wind speed. Low wind speeds are more favourable as the CO_2 signal is less diluted and easier to observe. With a 200 km swath, CarbonSat will provide about 10 favourable observations of the Paris area per year, accounting for the cloud cover and variability in the wind speed. Innovative data analysis methods may be needed to properly account for all relevant factors, including the contribution of biogenic fluxes, distant emission patterns and systematic errors in CarbonSat measurements.

The examples of Berlin and Paris indicate that CarbonSat has the potential to significantly contribute to reducing uncertainty in local-scale CO_2 emissions from cities.

Examples for CH_4 on a comparable local scale are emissions from oil, gas and coal production. For an area of natural gas production in North America, an approximately 482 kt CH_4 yr^{-1} emission was estimated from airborne *in situ* data (Karion et al,. 2013). Based on this information, a CH_4 emission plume was simulated using a Gaussian model assuming a wind speed of 5 m s^{-1} and unstable atmospheric conditions. Figure 7.26 shows simulations of XCH_4 for CarbonSat (2×2 km^2, single measurement precision 9 ppb) and Sentinel-5 (7×7 km^2, single measurement precision 18 ppb). CarbonSat will observe a clear signature from this type of source within one overpass. Several overpasses are needed for Sentinel-5 to derive meaningful information. Quantifying such a

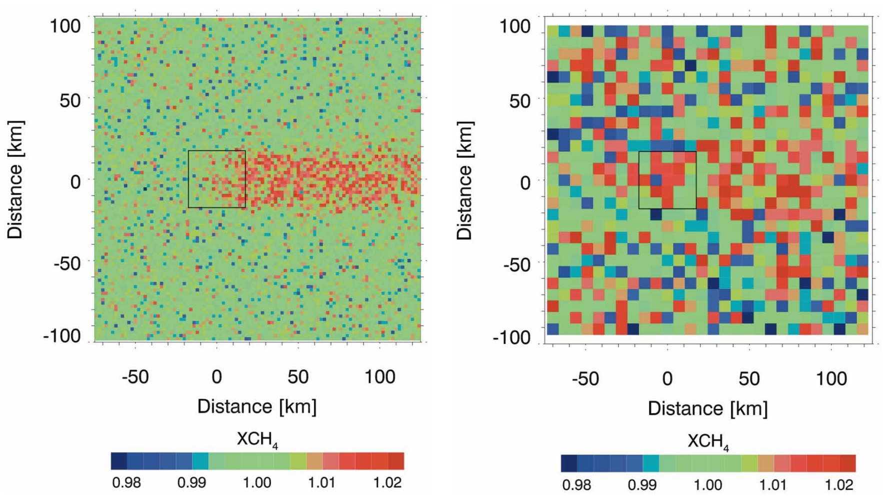

Figure 7.26. Simulation of a strong CH_4 source (482 kt CH_4 yr $^{-1}$, Karion et al., 2013) from an area of 35×35 km^2 for CarbonSat (left) and Sentinel-5 (right). (T. Krings–IUP)

source with SCIAMACHY data required several years of data to be averaged, as demonstrated for the example of emissions from the Four Corners oil and gas production region in the US (Fig. 2.18).

At the point-source scale there are a number of important, strong emitting point-source targets. Detection and quantification of such strong targets of CO_2 and CH_4 via remote sensing has been demonstrated using aircraft observations of XCH_4 and XCO_2 from the Methane Airborne Mapper (MAMAP) instrument as shown in Krings et al., 2011, 2013 (see Chapter 4).

For CarbonSat, two specific campaigns (C-MAPExp in 2012 and COMEX in 2014) were executed to consolidate and validate the new methodology of using XCO_2 and XCH_4 imagery to derive strong point-source emissions from the XCO_2 and XCH_4 fields. The airborne spectrometer MAMAP (Gerilowski et al., 2011) was used to determine spatial gradients in XCO_2 and XCH_4 introduced by strong local sources of either CO_2 or CH_4 (Fig. 4.3). A proxy retrieval approach (Chapter 6) was applied to the MAMAP observations in the SWIR-1 bands, which covers the weak absorptions of CO_2 and CH_4. Measurement data from around a power plant (for which emissions are known) are shown in Fig. 4.3. Using mass-balance inversions it was shown that even at CarbonSat's spatial resolution, the signal allows for the estimation of the point-source emission strength (Bovensmann et al., 2014a). Consequently, under favourable conditions these signals will be detected by CarbonSat even within a single overpass; under less favourable conditions, multiple overpasses need to be averaged.

In Bovensmann et al. (2010), it was shown that power plant CO_2 emissions can be detected and quantified with CarbonSat data. The estimated statistical uncertainty of the inferred power plant CO_2 emission owing to instrument noise is in the range 2–6 Mt CO_2 yr^{-1} per single overpass for typical near-surface fair weather wind speeds in the range 2–6 m s^{-1}. This corresponds to 6–18% of the emission of large power plants (26 Mt CO_2 yr^{-1}). For strong localised CH_4 point sources the estimated precision of the inferred CH_4 emission is 4–12 kt CH_4 yr^{-1} per single overpass for typical near-surface fair weather wind speeds in the range 2–6 m s^{-1}. As opposed to the assumptions in Bovensmann et al. (2010), the current CarbonSat spatial sampling is slightly degraded. As a consequence of the threshold spatial resolution chosen in combination with a threshold SNR, quantification will be possible for a single overpass under favourable conditions (high SNR, strong source, relatively low wind) or under less favourable conditions using temporally averaged data. Such performance may enable the demonstration of space-based quantification of point-source emissions.

7.5 Summary

This chapter has shown the performance estimates of the CarbonSat concepts, as developed during Phase-A/B1. The analysis shows that the performances at Level-1 and Level-2 are compliant with the mission requirements. The Level-1b performance has been established by design and performance simulations as summarised in Chapter 5 and Section 7.2, respectively.

For system requirements at Level-1b, the major error sources have been analysed by the industry consortia, and the results indicate that both instrument concepts can meet the system requirements at Level-1b. For requirements that have been identified as difficult to quantify the performance with sufficient accuracy, dedicated measurements are planned in the frame of pre-development activities.

Performance at Level-2 has been established by two different simulation approaches. One approach used the CarbonSat E2ES to simulate performance sensitivity, which confirmed that Level-2 requirements will be met. The second approach used a stand-alone framework for sensitivity simulations and analysed a one-year simulated dataset assuming the required Level-1b performance will be met.

Using OSSEs, it has been shown that on all scales, from local to country to regional and global scales, the data delivered by CarbonSat will be able to reduce uncertainties and add important new information.

OSSEs have been carried out to establish the link between CarbonSat's performance at Level-2 and Level-4, verifying whether the mission fulfils its scientific objectives (Chapter 3). For fluxes at global to regional scales, the OSSE results confirm that CarbonSat would outperform other existing satellite missions, mostly because of its superior measurement coverage, which includes both land and ocean.

Although CarbonSat is not primarily designed to improve the estimation of CO_2 fluxes over the ocean, the OSSE results indicate that potentially important uncertainty reductions could nevertheless be achieved over oceans.

The performance of CarbonSat at Level-4 increases as compared to GOSAT and OCO-2 towards smaller scales, which has been demonstrated showing large uncertainty reductions for European countries. At the regional scale (500×500 km^2) the estimated performance meets the Level-4 requirement for most parts of the world.

On the local scale, OSSEs for Paris and Berlin confirm that CarbonSat will be able to determine CO_2 emissions from large cities with an uncertainty of 10–20%. Similar performance is expected for intensive CH_4 emissions (several 100 kt CH_4 yr^{-1}) from large areas (several 10 km) like oil/gas fields.

For point sources at the local scale CarbonSat will be able to detect strong sources of CO_2 and CH_4. Quantification of their emissions with data from a single overpass will be possible under favourable observing conditions (high SNR, low wind speed). Under less favourable observing conditions temporal averaging will be needed to allow the quantification of the emissions.

→ MISSION CONTEXT

8. Mission Context

This chapter describes the global context for the CarbonSat mission (Section 8.1), in terms of planned operational satellites and research missions (Section 8.2), potential spin-off products (Section 8.3), user communities (Section 8.4), and applications and operational potential (Section 8.5).

8.1 Global Context

As described in Chapter 2, the warming of Earth's climate system is clear, and since the 1950s, many of the observed changes have been unprecedented over decades to millennia. These are unequivocally attributed to increased anthropogenic emissions of greenhouse gases (IPCC, 2013). The CarbonSat mission will be of direct relevance not only to national and international programmes concerned with climate change, climate-change impacts and the carbon cycle, but also relevant for monitoring greenhouse gases and verifying emission reporting.

The Intergovernmental Panel on Climate Change (IPCC) needs reliable information on the global carbon cycle because the biogeochemical processes involved and their modification through human activity determine the amount and distribution of carbon dioxide (CO_2) and methane (CH_4) in the atmosphere, thereby increasing Earth’s greenhouse effect (Chapter 2). The carbon cycle also responds to climate change, and understanding the ability of the various carbon-cycle processes to continue their roles as partial sinks of fossil-fuel emissions into the future will be a vital factor in determining ‘permitted’ fossil-fuel carbon emissions. The science-based Global Carbon Project[1] coordinates the regular update of the global carbon budget, including both its biophysical and human dimensions. Earth-system modelling groups participating in the IPCC develop and apply carbon-cycle models coupled with climate, and are engaged in a series of international model intercomparison and benchmarking exercises (e.g. International Land Model Benchmarking project; Land-use and Climate, Identification of robust impacts; the Ocean Carbon-Cycle Model Intercomparison Project).

It is well recognised that all major economies will need to make substantial reductions of greenhouse-gas emissions if global warming is to be limited to an increase of 2°C above pre-industrial times. Negotiations are in progress through the UN Framework Convention on Climate Change (UNFCCC) to conclude a new international agreement on greenhouse-gas emission reductions for the post-Kyoto era with the aim of achieving a binding and universal agreement between all the nations. It is intended to adopt the agreement as a protocol to the UNFCCC at the Paris climate conference in late 2015, with implementation from 2020 onwards. In late 2014 and early 2015, the US and China jointly announced proposals to cap (China) or to make further reductions in (US) emissions. Separately, the European Union (EU) has already put in place legislation to reduce greenhouse-gas emissions to 20% below 1990 levels by 2020. As part of a roadmap for moving to a competitive low-carbon economy, the European Commission (EC) has proposed that the EU should cut emissions to 80% below 1990 levels by 2050. The current mechanisms for assessing actual emission data are based on self-reporting by the individual nations and expert reviews of the reports, but so far there is limited or no check for consistency with actual atmospheric concentrations. The scientific community has, therefore, emphasised the argument that regulation of greenhouse-gas emissions can

---

[1] *http://www.globalcarbonproject.org/index.htm*

only have integrity if verified by direct atmospheric measurements (Nisbet and Weiss, 2010).

The Global Atmosphere Watch programme of the World Meteorological Organization (WMO) promotes systematic and reliable observations of the global atmospheric environment. CO_2 and CH_4 (together with other greenhouse gases) are ‘essential climate variables’ (GCOS, 2010). This report explicitly states that “accurate knowledge about essential climate variables is required to support the work of the UNFCCC and the IPCC”.

Recognising the growing need for improved Earth observations, over 130 governments and leading international organisations collaborate through the Group on Earth Observations (GEO) to establish a Global Earth Observation System of Systems (GEOSS). In its Carbon Strategy Report (Ciais et al., 2010), the GEO Carbon Community of Practice (COP) acknowledged the significant advances in the science and observational capabilities of space-based (and *in situ*) measurements and recognised their future role in enhancing our knowledge of the global carbon cycle and in supporting the international monitoring and verification of CO_2 and CH_4 emissions. In response to this and the urgent need to build a coordinated global carbon observing system, the Committee on Earth Observation Satellites (CEOS) formed a special task force on carbon observations from space, which established a clear and bold long-term vision of the satellite missions needed to observe CO_2 and CH_4 concentrations and to document fluxes: the CEOS Strategy for Carbon Observations from Space (CEOS, 2014). ESA, a member of CEOS, has made atmospheric CO_2 and CH_4 measurements from space a high priority in its revised science strategy (ESA, 2015a).

The WMO-led Global Framework for Climate Services provides climate information to assist decision making. Such services involve high-quality observation data from national and international databases on the state of the atmosphere, land surface and oceans, as well as maps, risk and vulnerability analyses, and long-term projections and scenarios. Similarly, the EU Copernicus Programme provides reliable and sustained information for the global environment and security. It supports environmental legislation and policies, with a particular focus on climate change, and enables their implementation to be monitored and their effectiveness to be assessed. CarbonSat will add the missing capability of the Copernicus space system to deliver high spatial resolution information on CO_2 and CH_4.

8.2 Past, Current and Planned Missions

CarbonSat builds on the heritage of the short-wave infrared (SWIR) measurements made by the SCIAMACHY (Envisat), TANSO-FTS (GOSAT) and OCO-2 instruments. As shown in Fig. 8.1, there will be a succession of missions over the next decade with a range of CO_2 and/or CH_4 measurement capabilities. The figure does not include missions which are candidates under consideration within various space agencies but not necessarily selected for launch, such as NASA’s Active Sensing of CO_2 Emissions over Nights, Days, and Seasons (ASCENDS, CO_2) or the French MicroCarb (CO_2). Each of the missions shown has specific capabilities, for example, to improve the precision and accuracy of the measurements, the spatial and temporal resolution, and the spatial coverage. CarbonSat is the only mission with imaging capability to quantify greenhouse-gas fluxes and emissions. Given the finite lifetime of each mission shown in Fig. 8.1, there is very little or no overlap between the operational phases of these missions. As anthropogenic-driven climate change increases, the need for accurate information on the dry mole fractions, the surface fluxes of CO_2 and CH_4 and feedback, will increase. The CarbonSat mission is a critical link in the measurement chain beyond 2022 to ensure there are no measurement gaps and thereby sustain a continuous CO_2 and CH_4 flux record over the next 10–15 years.

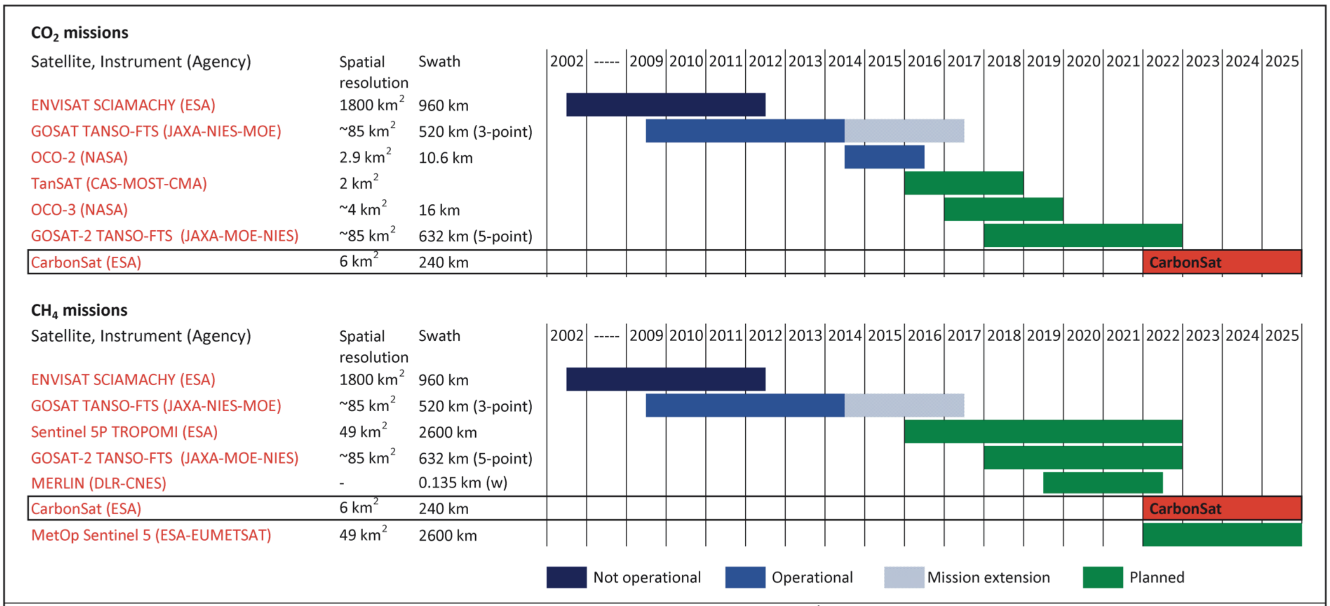

Agencies: CAS: Chinese Academy of Sciences, CMA: Chinese National Satellite Meteorological Center; CNES: Centre National d'Études Spatiales, France; DLR: Deutsches Zentrum für Luft- und Raumfahrt e.V; ESA: European Space Agency; JAXA: Japanese Space Exploration Agency; MOE: Ministry of the Environment, Japan; MOST: Ministry of Science and Technology of China; NASA: National Aeronautics and Space Administration, USA; NIES: National Institute for Environmental Studies, Japan.

Figure 8.1. Timeline of past, current and planned SWIR CO_2 and CH_4 satellite missions with sensitivity to the atmospheric planetary boundary layer. (G. Hayman–CEH)

While the datasets produced by CarbonSat will be unique and not dependent on other satellite missions, they will complete and enhance the time series acquired by the preceding greenhouse-gas missions. Other satellite missions observing the atmosphere, land and ocean domains will also add to the value of the CarbonSat measurements.

8.2.1 Space-based Measurements of Atmospheric Composition

Atmospheric columns of CO_2 and CH_4 are also derived from the thermal-infrared (TIR) channels in the Tropospheric Emission Spectrometer (TES) on NASA's AURA satellite, Atmospheric Infrared Sounder (AIRS) on AQUA, the Improved Atmospheric Sounding Interferometer (IASI) on MetOp-A and TANSO-FTS on GOSAT. The TIR measurements are not directly usable per se to improve knowledge of surface fluxes because they mainly reflect CO_2 and CH_4 concentrations in the middle atmosphere (see Fig. 4.1). The combination of TIR and SWIR measurements can, however, provide a dual constraint on the vertical distribution of CO_2 and CH_4 and thus atmospheric vertical transport and mixing processes. Another promising prospect is to combine CarbonSat's XCO_2 with carbon monoxide column (XCO) measurements from a contemporaneous mission to discriminate between XCO_2 signals from different carbon emission sources (the slope of XCO/XCO_2 varies between fossil-fuel combustion and biomass burning) and from CO_2 exchange fluxes with the biosphere (uncorrelated with XCO). The separation of anthropogenic and biological fluxes can be further improved by using information about other gases such as NO_2 and CO, which are emitted with anthropogenic CO_2 in fossil-fuel combustion. Similar concepts have been applied before by combining satellite measurements of formaldehyde, HCHO and glyoxal (CHOCHO), which are produced by the oxidation of volatile organic compounds, with measurements of NO_2 to distinguish between regions dominated by different sources such as anthropogenic fossil-fuel combustion, biomass burning and biogenic emissions. In the time frame of the CarbonSat mission, NO_2, CO, HCHO and CHOCHO data products will be available operationally from the Copernicus Sentinel-5 mission.

8.2.2 Space-based Measurements of Land Surface and Ocean Properties

An extensive global sample of atmospheric concentrations of CO_2 and CH_4 provides an important independent check on terrestrial and oceanic carbon-cycle models and observations (Chapter 2). Estimates of above-ground biomass change, such as from instruments like ESA's Biomass mission, and of air–sea CO_2 fluxes using ocean-colour phytoplankton measurements, physical parameter measurements and biogeochemistry models, are highly complementary and synergistic. By using Biomass measurements of yearly above-ground biomass carbon change (as a baseline) and combining these with CarbonSat cumulative CO_2 fluxes, it would be possible, for the first time, to infer the distribution of forest soil carbon change, which is one of the biggest sources of uncertainty in current carbon-cycle models and future projections. Earth observation data on fires (radiative power, burned area and fire counts) and biomass burning are relevant for both CO_2 and CH_4. For CH_4, rice paddy and wetland ecosystems are significant sources that are measured inadequately or poorly known. Arctic permafrost soils thaw in the spring and summer, creating the potential for significant CH_4 and CO_2 release, but the regional-scale flux is poorly determined. Earth observation products such as inundation extent, soil moisture, soil thawing and distribution of wetlands, derived from the Sentinel-2 and Sentinel-3 missions, for example, together with XCH_4 observations from CarbonSat, will help to constrain methane emissions from these sources.

8.3 Spin-off Products

CarbonSat will deliver several Level-2 spin-off data products. These include SIF (solar-induced vegetation fluorescence) derived from solar Fraunhofer lines in the 749–759 nm spectral region without interfering gas absorption, using established retrieval approaches (Joiner et al., 2011; Frankenberg et al., 2014). As shown in Buchwitz et al. (2013a) and illustrated in Fig. 8.2, this product will be of high quality, as the estimated single measurement precision is approximately 0.23 mW m^{-2} nm^{-1} sr^{-1}, i.e. about 10% of the expected maximum signal of approximately 3 mW m^{-2} nm^{-1} sr^{-1} for a geophysical scenario of vegetation albedo and a Solar Zenith Angle (SZA) of 50°, assuming threshold signal-to-noise performance (Buchwitz et al., 2013a). This assessment shows

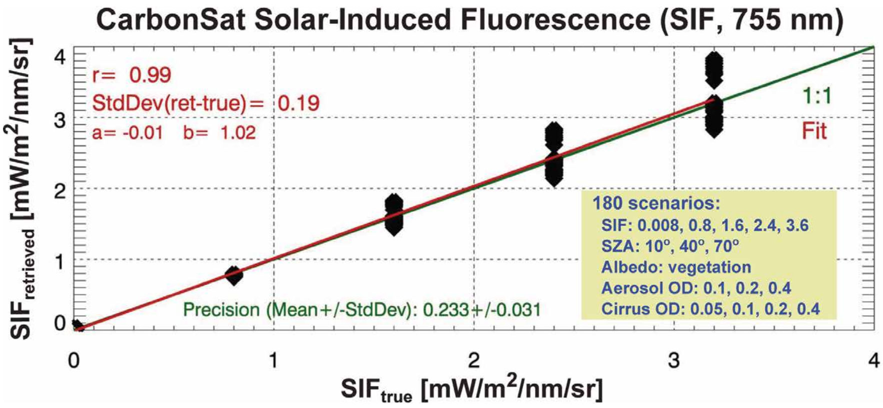

Figure 8.2. CarbonSat SIF modelled retrieval results for 180 scenarios defined by different fluorescence levels, SZAs, aerosol and cirrus amounts. The assumed signal-to-noise ratio corresponds to the threshold requirement. The mean precision is 0.23 mW m^{-2} nm^{-1} $sr^{-}1$ and the standard deviation of the systematic error is 0.19 mW m^{-2} nm^{-1} sr^{-1}. (M. Buchwitz–IUP)

that SIF retrievals from CarbonSat will be similar in precision to that expected from OCO-2, which will be in the range 0.3–0.5 mW m^{-2} nm^{-1} sr^{-1} (15–25% of typical peak values, Frankenberg et al., 2014). As a result of its larger swath, CarbonSat will, however, provide more than an order of magnitude better coverage compared to OCO-2.

The CarbonSat spectral range covers many weak, moderate and strong (i.e. saturated) water vapour lines. CarbonSat will deliver a high-quality data product of the total water vapour column, with the potential to derive vertical profile information.

As discussed in Chapter 7, the CarbonSat measurements are very sensitive to cirrus clouds and aerosols. Cloud optical depth, cloud top height and aerosol optical depth will be retrieved with good quality. CarbonSat is sensitive to very small cirrus optical depths down to a few hundredths, i.e. the optical depth of sub-visible cirrus clouds. The high spectral resolution O_2-A-band can also be used to derive aerosol layer height information.

CarbonSat O_2-A-band spectra acquired in sunglint mode over the ocean provide surface pressure observations with very small random errors. This has the potential to fill the gaps of surface-based measurement networks in remote areas such as the southern hemispheric oceans if systematic errors related to aerosol and clouds can be successfully mitigated.

8.4 User Communities

There are a number of user groups that will make use of the CarbonSat products.

8.4.1 Greenhouse-gas Monitoring and Observing System

There is a very active and fast growing research community making atmospheric concentration and flux measurements from a variety of platforms (*in situ*, towers, aircraft and satellites). The ‘carbon from space’ component of this user community has grown from a handful of experts ten years ago to a thriving international research community, which produces a number of high profile papers (8.4.2) and meets each year for the International Workshop on Greenhouse-Gas Measurements from Space (IWGGMS). This dedicated workshop (mainly on CO_2 and CH_4) now attracts around 200 participants.

The GEO Carbon COP is a major driving force (i) to build and improve the infrastructure and interoperability of the global carbon observing system and (ii) to monitor and assess the effectiveness of carbon sequestration and emission reduction measures (Section 8.1). The COP aims to integrate carbon observations from all platforms, reservoirs, and across time and spatial scales. The Earth observation community has made important steps towards the realisation of such a system through the deployment of an increasing number of satellites observing the atmosphere, land and ocean domains. CarbonSat is a key element of the evolution of the planned global observing system and meets the user requirements for the next generation greenhouse-gas satellite mission.

8.4.2 Inverse Modelling

Significant progress has been made in recent years to derive fluxes between the land surface and atmosphere from the satellite measurements of XCO_2 and XCH_4, since the initial publications using SCIAMACHY measurements (Bergamaschi et al., 2007; Meirink et al., 2008). The capability and increasing maturity of the field can be seen in recent studies:

- reporting flux estimates of CO_2 (e.g. Basu et al., 2013; Basu et al., 2014; Deng et al., 2014; Maksyutov et al., 2013) and CH_4 (Fraser et al., 2013) from the GOSAT-TANSO instrument on global and continental scales

- multiyear analyses of SCIAMACHY data (Bergamaschi et al., 2013; Houweling et al., 2014)

- investigating the consistency of flux estimates (of CH_4) derived from different spaceborne sensors: SCIAMACHY and GOSAT (Monteil et al., 2013) and SCIAMACHY, GOSAT and IASI (Cressot et al., 2014)

- multimodel intercomparisons organised by inverse modellers cooperating in the international TRANSCOM (TRANsport model COMparison) project (Houweling et al., 2015)

None of the missions has provided a seamless improvement of regional flux estimates because of sparse data (e.g. clouds over the Amazon) or insufficient accuracy. A significant step forward is expected from the recently-launched OCO-2 mission (CO_2 only) and the forthcoming GOSAT-2, OCO-3 (CO_2 only) and Sentinel-5 Precursor (CH_4 only) missions. The improving quality of satellite XCO_2 measurements is challenging the current generation of inverse modelling tools (Basu et al., 2013; Chevallier et al., 2014a; Houweling et al., 2015). These planned missions should help stimulate the inverse modelling community to develop the tools and methods to handle the large volumes of data expected from the CarbonSat instrument and to improve atmospheric models, especially atmospheric transport processes, used in their inverse modelling systems. In addition, improvements are expected to the radiative transfer models and retrieval algorithms used to convert radiances into concentrations.

8.4.3 Carbon Cycle, Climate and Earth System Modelling

The carbon cycle is central to the Earth system, being inextricably coupled with climate, the water cycle, nutrient cycles and the production of biomass through photosynthesis on land and in the oceans (Chapter 2). There is an active and extensive carbon-cycle research community using observations to improve and benchmark process-based carbon-cycle models. Much of the current knowledge has been derived from surface sites measuring atmospheric concentrations, energy and gas fluxes, carbon stocks, and plant and soil physiological and biochemical parameters. The use of satellite observations of XCO_2 has been limited because of the relatively short observational datasets, biases in the satellite retrievals and/or errors in the chemical transport models (Chevallier et al., 2014a). The potential to observe the response of the carbon cycle to climate variations has recently been illustrated by GOSAT, for instance, in the detection of significant anomalies in XCO_2 in response to major droughts in the Amazon (Parazoo et al., 2013) and heatwaves in Europe and Russia (Belikov et al., 2014). The development of long-term, consistent datasets suitable for climate studies from the reanalysis and intercomparison of satellite greenhouse-gas observations is the goal of the ESA Greenhouse Gas Climate Change Initiative project (Buchwitz et al., 2015a). Furthermore, recent advances in the remote sensing of SIF (Frankenberg et al., 2011b; Joiner et al., 2011; Joiner et al., 2013) have opened up a new possibility in carbon-cycle research to measure the rate of planetary photosynthesis and its response to the climate and other drivers. CarbonSat, with its simultaneous measurements of both XCO_2 and SIF, will provide additional insight through separation of the photosynthesis (SIF, XCO_2) and respiration (XCO_2) components (Section 2.7.3).

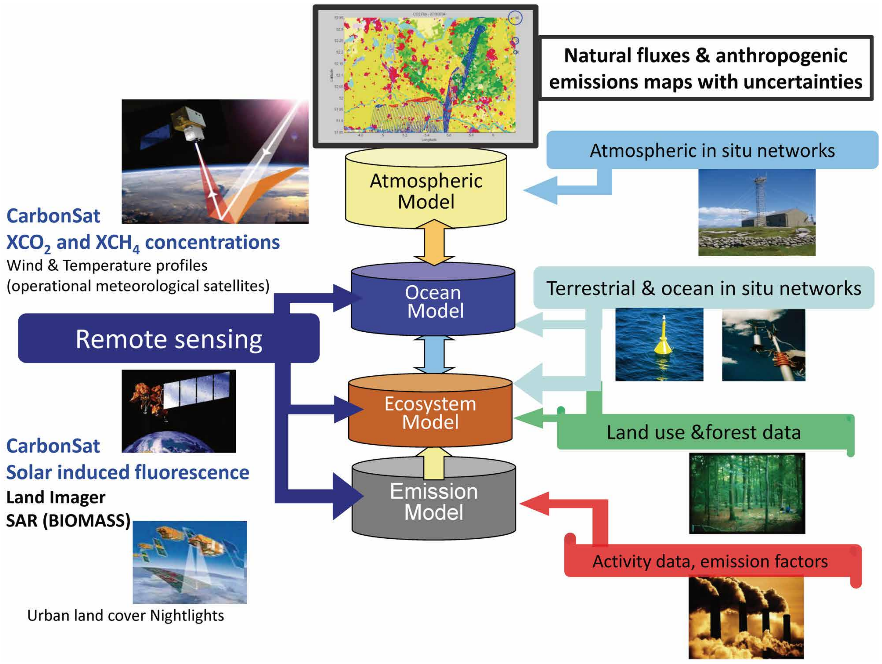

Figure 8.3. A future carbon-cycle data assimilation system using multiple data streams, including XCO_2, XCH_4 and vegetation fluorescence from CarbonSat. (P. Ciais–LSCE)

CarbonTracker[2] was one of the first systems to combine measurements and modelling to track the sources and sinks of carbon dioxide around the world. A number of carbon-cycle data assimilation systems (CCDASs) have since been developed (Section 2.5.1 and Chapter 3), which aim to constrain the key driving processes of the global carbon cycle by combining complementary data streams. Example CCDASs include what was developed as part of the EU CARBONES project[3] and the Integrated Global Carbon Observation and Analysis System in the GEOCARBON project[4], which uses 5 CCDASs. The contribution of CarbonSat to a future CCDAS (Fig. 8.3) comprises not only excellent state-of-the-art global datasets of XCO_2 (and XCH_4), but also the synergistic vegetation chlorophyll fluorescence product.

For methane, there is a significant gap between emission estimates from top-down approaches using atmospheric measurements and bottom-up process-based models, especially of biogenic sources such as wetlands (Kirschke et al., 2013). One of the three projects of the Atmosphere-Land Interactions Study (ALANIS), which was co-sponsored by ESA and the Integrated Land Ecosystem-Atmosphere Processes Study (iLEAPS), made use of SCIAMACHY XCH_4 data. This and other datasets were used in the ALANIS methane project[5] to evaluate the wetland methane emission scheme in the UK land surface model (Hayman et al., 2014). The SCIAMACHY XCH_4 data have also been applied to evaluate the methane emission and chemistry schemes in chemistry-climate/Earth system models (Shindell et al., 2013; Hayman et al., 2014). Further use of such Earth observation datasets is expected in the future, especially in combination (i.e. of multiple components such as O_3, NO_2, CO, etc.), as these models evolve. A breakthrough in the identification and quantification of the diverse and often elusive CH_4 sources is expected from the high resolution and high accuracy images of CarbonSat.

The production and use of data for Earth system modelling and evaluation is a key element of ESA's latest science strategy (ESA, 2015a) and a strategic

---

[2] *www.esrl.noaa.gov/gmd/ccgg/carbontracker/*

[3] *www.carbones.eu/wcmqs/project/ccdas/*

[4] *www.geocarbon.net/index.php*, Component 2

[5] *www.alanis-methane.info*

priority for a number of national programmes (e.g. the UK National Centre for Earth Observation and the German Ministry of Economics' Plan for Space).

8.4.4 Emission Monitoring and Verification

Greenhouse-gas emission inventories are estimates that are compiled from a range of sources using internationally-agreed guidelines (e.g. IPCC, 2006) to ensure transparency, consistency and comparability. Atmospheric observations are essential to validate and/or verify these estimates (Nisbet and Weiss, 2010).

The precision and accuracy of current space-based measurements provide only weak constraints, even for the largest emission sources such as megacities and power stations. Kort et al. (2012) reported persistent XCO_2 enhancements over two coastal megacities (Los Angeles in US and Mumbai in India) when compared with nearby 'clean' observations representative of background air. For methane, Kort et al. (2014) report that the observed XCH_4 enhancements from SCIAMACHY for the Four Corner region in the US could only be reconciled with larger methane emission fluxes (by a factor of 3.5) than those derived from available estimates. The direct quantification of emissions from such sources using satellite measurements is a more challenging target, given the current, limited number of observations available. With its increased density of soundings, OCO-2 is expected to make progress in the monitoring of CO_2 emissions from specific megacities and large point sources. CarbonSat will be able to demonstrate the potential of space-based observations to verify emission estimates in a consistent manner across the globe in support of the IPCC and as an objective evidence base to assess the effectiveness of UNFCCC protocols.

8.5 Application and Operational Potential

8.5.1 Potential Scientific Synergy

Significant synergies in data assimilation are expected with the planned Sentinel-5 Precursor and Sentinel-5 missions using, for example, CO, SO_2 and NO_2 as additional proxies for different fossil-fuel emission sources (biomass burning, anthropogenic fossil fuel burning etc.).

8.5.2 Copernicus Atmosphere Monitoring Service

The pre-operational Copernicus Atmosphere Service, called the Monitoring Atmospheric Composition and Climate-Interim Implementation (MACC-II) and its successor MACC-III[6], assimilate satellite measurements of both XCO_2 (from the GOSAT-TANSO instrument) and XCH_4 (from the TANSO, IASI, and previously SCIAMACHY instruments), within 4–5 days of the satellite acquisition (MACC-III). Satellite measurements have been used to derive surface fluxes for CH_4 (SCIAMACHY and now GOSAT). For CO_2, although the assimilation of GOSAT CO_2 column retrievals has been investigated, these data are still of insufficient quality for routine exploitation for flux inversion (MACC-II, 2014). Further experience will be gained from assimilating CO_2 using measurements from the recently-launched OCO-2 mission. The operational Copernicus Atmosphere Monitoring Service (CAMS) is expected to use CarbonSat products.

---

[6] *www.alanis-methane.info*

8.5.3 Greenhouse Gas Monitoring

The 2014 GEO Carbon Strategy Report (CEOS, 2014) clearly states the need for higher spatial and temporal resolution measurements over the entire globe to discriminate surface sources and sinks of CO_2 and CH_4 from atmospheric transport processes to the extent needed to accurately quantify the emissions associated with human activity from the much larger natural sources and sinks. Using the operational meteorological observation system as a model, CarbonSat could evolve into a future greenhouse-gas observing system either as a CarbonSat constellation or a constellation of similar systems to achieve the coverage needed for operational greenhouse-gas monitoring, or could be incorporated into a system of multiple coordinated greenhouse-gas satellites, together with aircraft, balloons, and ground-observing systems, in a true 'system of systems'. The CarbonSat mission delivers the required spatial resolution and imaging capability, and can be considered an enabling mission towards the creation of a satellite constellation. Increased international collaboration and coordination through CEOS will be essential and is already underway.

→ PROGRAMMATICS

9. Programmatics

9.1 Introduction

This chapter presents the maturity, heritage and risks as evaluated or identified after completion of the Phase-A/B1 activities. Those associated with the mission-level scientific concepts are described in Section 9.2 and the system-level technical concepts are described in Section 9.3. The corresponding development approach and schedule is presented and discussed in Section 9.4.

9.2 Scientific Readiness

9.2.1 Maturity

The scientific concept of CarbonSat builds on a wide experience and heritage obtained in atmospheric chemistry missions. As well as satellite missions observing CO_2 and CH_4 such as SCIAMACHY, GOSAT and OCO-2 (CO_2 only), this also includes future mission concepts measuring trace gases in the optical domain, such as the Copernicus Sentinel-4, Sentinel-5 Precursor and Sentinel-5 operational missions. Consequently, the observational requirements can be considered mature and consolidated, and will be fine-tuned further based on lessons learned.

The OCO-2 mission, which is currently operational, is the closest to CarbonSat in observing spectra relevant for measuring CO_2 with sensitivity to the lowest atmospheric layers. In this respect, OCO-2 can be seen as an in-orbit demonstrator albeit with significantly less spatial coverage and not observing CH_4. The main challenges with CarbonSat arise from its stringent observational requirements in combination with high spatio-temporal resolution.

Several of the science aspects have been tested in dedicated campaigns using the Methane Airborne Mapper (MAMAP). The measurement concept is similar to CarbonSat in that it exploits similar spectral bands, but it cannot be considered as a fully representative demonstrator since it lacks the SWIR-2 band and swath capability. Nevertheless, measurement campaigns with MAMAP have demonstrated that local-scale CO_2 and CH_4 sources can be detected. The data were also used for quantifying emissions at the spatial resolutions of MAMAP and CarbonSat. An advanced version of MAMAP is in preparation, which can be seen as an airborne demonstrator including mapping capabilities.

An end-to-end performance simulator up to Level-2 has been developed, tested and validated using realistic measurement scenarios. The performance model used is applicable to a predefined range of conditions. As demonstrated, it can be used to address the needs originating from the science requirements in an end-to-end manner. Retrieval algorithms applicable to a realistic range of error sources (both geophysical and technical) have been demonstrated with a predefined set of performance requirements. Consolidated geophysical retrievals have been established and implemented. These algorithms provide results that respond directly to the observation requirements. Further processing beyond these Level-2 products has been assessed in flux inversion models using simulated data. These assessments confirmed the validity of the observational requirements established for CarbonSat.

The user community has continued to grow with the availability of SCIAMACHY, GOSAT and OCO-2 observations. There are several analysis codes to use the kind of data provided by CarbonSat. It is expected that the developments will be further promoted, especially for CO_2, with the availability of OCO-2 observations, and for CH_4 with the launch of Sentinel-5 Precursor expected in 2016. The retrieval codes will have to be adapted and fine-tuned to the specifics of CarbonSat and the lessons learned will benefit respective developments.

The user community has expanded with the availability of higher quality data, including the inverse modelling community, which until recently mainly used *in situ* observations. The science readiness of this community is expected to further mature with the availability of GOSAT and OCO-2 data. The annual dedicated workshop (i.e. the International Workshop on Greenhouse-Gas Measurements from Space, IWGGMS) reflects this interest and now has around 200 participants.

The potential scientific impact of the data at the spatio-temporal scale targeted by CarbonSat is more difficult to assess. Initial attempts have been made using Observation System Simulation Experiments (OSSEs). The resulting performance assessments have, so far, confirmed the mission concept. It is noted that the observations are only one contributor to the overall performance and the uncertainty inherent to the underlying models is part of the overall performance.

9.2.2 Critical Areas and Risks

Inherent to the maturity of the scientific concept, there are no major critical areas or risks associated with the mission. Obviously with the mission at the end of Phase-B1, there are still areas that will require further attention in the implementation phase. For example, the number of observations will require an optimised processing strategy. To best exploit the data, a full physics algorithm provides the most accurate retrieval results, but at the moment requires significant processing time. Similar challenges are currently faced for processing all OCO-2 data and evolutions can be expected. The expected abundance of CarbonSat data will allow for stringent quality filtering, but care has to be taken to not exclude certain regions with persistent unfavourable observation conditions (e.g. the Amazon basin, which is prone to cloud cover).

The mission objectives include an improved scientific understanding of CO_2 and CH_4 fluxes. This encompasses a variety of processing steps beyond Level-2. The spatial resolution of CarbonSat is currently not represented in mesoscale and global models. This implies that either data thinning or averaging has to be considered. It can be expected that model resolution will increase with growing computing power, and leading numerical weather prediction centres already run at much better grid resolutions. Nevertheless, dedicated work will be needed to advance existing models to enable them to ingest the vast amount of CarbonSat data and fully exploit the information content.

Flux inversion models (more generally, all kinds of transport model) are sensitive to biased input data. Bias monitoring techniques are important, such as frequent comparison to TCCON stations and, potentially, implementation of correction algorithms. Therefore, care will be needed to develop appropriate calibration and validation plans by adapting and expanding existing schemes to suit CarbonSat, especially for its novel scientific products at finer spatial resolution. Quantification of emissions from local scale sources will require refinement of existing models and rigorous validation.

Accurate quantitative estimation of emissions from point sources such as power plants from a single overpass remains challenging. While imaging the same source several times may improve estimates, this entails the complication of viewing the source target under different meteorological conditions (e.g. wind speed and direction, and cloud cover) and/or changing emission rates. Further work is foreseen that combines airborne campaigns employing swath imaging (using the augmented MAMAP instrument) with plume models to quantify the improvement in accuracy and reduction in uncertainty that can be achieved by multiple measurements.

In assessing the performance at regional scales, the model results indicated significant improvement when data obtained over the ocean were included. Although there is experience with data from sunglint-mode observations from GOSAT and OCO-2, further attention to retrieving accurate products from these measurements is necessary to fully exploit the potential of the mission.

From the heritage of previous and existing satellite missions, awareness of potential risks is quite high so appropriate mitigation efforts have been formulated in terms of targeted observational requirements.

9.3 Technical Maturity, Critical Areas and Risks

9.3.1 Platform

The CarbonSat mission poses no specific challenges to the platform, which is in line with the requirements of a typical medium-sized Earth observation mission. The only real driver identified in the industrial studies is the passive cooling concept (accommodation of the instrument radiator) in combination with the satellite pitch manoeuvre for sunglint observations. However, solutions have been found by both consortia. The analysis of the platform subsystems shows that most of them are at Technology Readiness Level (TRL) 8–9, having flown on a number of spacecraft in the past. In general, no TRL level higher than eight is assumed to take mission-specific environmental conditions into account. The high level of maturity is specifically true for Concept A, based on a recurrent platform. For Concept B, based on a bespoke platform, the subsystems generally have heritage in other missions such as EnMap, SAR-Lupe, Galileo, European Data Relay System and Meteosat Third Generation. However, qualification activities will be required at platform level. For some platform components, TRL 6 is assumed since minor adaptations are necessary to fulfil the specific mission needs, but no specific challenges have been identified.

9.3.2 Greenhouse Gas Imaging Spectrometer

The main challenges for the CarbonSat instrument arise from the stringent observational requirements. It is recalled that an in-depth revision of the requirements was realised during Phase-A after the Preliminary Concept Review (PCR), when both consortia had shown that the initial requirements stemming from the CarbonSat proposal were unfeasible.

Effects known from similar missions, such as scene heterogeneity and radiometric errors from diffusers or straylight, have been taken into account in the overall instrument design. The level of accuracy required to meet radiometric and spectral specifications is a direct consequence of the challenge to quantify small variations in the total column of a well-mixed trace gas like CO_2.

In general, very high mechanical and thermal stability is required and driven by multiple requirements. This means that the instrument needs tight alignments, detailed characterisation and calibration.

Since straylight has to be tightly controlled, a high level of cleanliness is also required. In particular, the level inside the instrument is demanding. A higher level of contamination increases the straylight, and thus also the required straylight correction factor to be achieved in Level-1b processing. Based on the analysis, correction factors for diffused straylight, and ghosts in the range 5–7 have to be assumed to reach compliance with requirements at Level-1b. The assumptions concerning the effectiveness of correction algorithms are under discussion. To acquire the key data necessary as input to the correction algorithms, a sophisticated and time-consuming instrument ground-characterisation will be necessary. The exact quantification of achievable correction factors is difficult, since they not only depend on the instrument, its on-ground characterisation and changes of the latter in orbit, but also on the observed scene.

Both instrument concepts envisage the implementation of a slit homogeniser, which essentially represents a 3D slit. After Sentinel-5, CarbonSat is the second mission stipulating the need for this novel device. The expected performance has been estimated by mathematical models, which have also been used to find the optimal dimensions of the slit. In order to allay any remaining risk, pre-development activities have started. Breadboards are implemented to validate the model results and current dimensioning. The slit homogeniser breadboard will be integrated in the Optical Engineering Model (OEM) for end-to-end verification. Although a slit homogeniser is, in principle, a simple optical component, the required manufacturing tolerances are tight.

The dispersers of a spectrometer are critical elements that define performance. For CarbonSat, all gratings are subject to pre-development activities for risk mitigation. The shortwave-infrared (SWIR) spectrometers are based on either silicon-immersed reflective gratings or transmission binary gratings using sub-wavelength technology. For the near-infrared (NIR) spectrometer, both consortia have baselined transmission binary gratings. In Concept A, the transmission grating in the NIR is covered by a pre-development for the Fluorescence Explorer (FLEX) candidate mission, which is justified by the grating similarity. In SWIR-1 and SWIR-2, silicon-immersed gratings are baselined. A flight-representative SWIR-1 grating breadboard is being manufactured and characterised to establish the grating manufacturability for both bands (since the SWIR-1 grating is the most critical in terms of design parameters). In terms of performance, the silicon-immersed gratings present risks with respect to straylight. In this context, the breadboard serves as risk mitigation. A grating that is similar from a manufacturing point of view was produced and characterised in the frame of Sentinel-5 activities. For Concept B, test samples of the NIR and SWIR-1 transmission gratings have been manufactured and analysed to validate the process. Subsequently, fully flight-representative SWIR-1 and NIR gratings are being manufactured and characterised based on the results from the test gratings. SWIR-2 is implicitly covered by the similarity to the NIR grating. The pre-development includes the bonding of the SWIR-1 grating to a prism in order to demonstrate the flight-representative prism-grating configuration.

The envisaged detectors, especially those for the SWIR bands, are on the critical path since they are long-lead items. The designs of both consortia use as reference detector for the SWIR-1 and SWIR-2 bands the NGP (Next-Generation Panchromatic) detector, currently under development. Prototypes have been manufactured and characterised. For the NIR spectrometer, Concept A uses as reference the CCD under development for Sentinel-5 NIR spectrometer, while Concept B uses a CCD recurrent model.

The current knowledge concerning the impact of the Sun diffuser on the radiometric accuracy (diffuser speckles) has been judged to be unsatisfactory, hence pre-development activities have been initiated to better quantify the effects and to optimise the approach to solar calibration. The risk of unacceptable performance is considered low, since a number of approaches can be envisaged to reduce speckle, with potentially no impact on the calibration unit design. Pre-development activities include the development of numerical models and measurements using different diffuser materials. The envisaged wavelength range of the measurements does not cover the SWIR-2 band, but will allow, in conjunction with the modelling activities, for an estimate of the radiometric impact to be made. The experimental characterisation and the numerical simulation are both challenging tasks, and the results have the potential to be useful in a wider context than just CarbonSat.

Ground calibration will require significant effort and time in thermal vacuum. Notably, the radiometric characterisation, e.g. straylight, ISRF and non-linearity, will be time-consuming and, in the case of the non-linearity characterisation, also technically challenging. The documentation, processing of the results and generation of the calibration database should not be underestimated. Approaches to reduce this can be envisaged, but remain to be confirmed.

9.4 Development Approach and Schedule

9.4.1 Overall Design and Development Approach

CarbonSat will follow a phased development process (Phases B2/C/D/E1) with system reviews (System Requirements Review (SRR), Preliminary Design Review (PDR), Critical Design Review (CDR), etc.) to verify the status of system design, development, procurement and integration of the flight models. In order to establish a robust development schedule, the instrument and platform developments can be decoupled. As reference planning to minimise the project cost and schedule, both industrial consortia have proposed parallel development activities on the instrument, platform and satellite, with integration to be performed during the assembly, integration and testing (AIT) phase.

Since both concepts aim to maximise the reuse of existing hardware for the platform, the payload and platform integration, testing and verification can be performed as independently as is practical in order to minimise schedule impacts propagating into other areas. Hence the platform-related activities and procurements will start after the instrument-related procurements have begun.

For the platform and related avionics, the development approach is based either on a strict Proto-Flight Model (PFM) approach (as for Sentinel-5 Precursor, Concept A), or on a PFM approach complemented by a Structural Model (SM) and an Electrical Engineering Model (EEM) for the platform (bespoke platform of Concept B). Both concepts make use of additional software models.

For both concepts, a PFM is used for full qualification and acceptance testing in terms of mechanical, thermal, electromagnetic compatibility and functional/operational requirements. Specific qualification and validation tasks in critical areas are performed on dedicated models and test benches. For Concept B, an SM is used for qualification of the structure for launch loads, for verification of structural stability, strength and stiffness, for verification of the finite element model and for validation of the interface loads for platform equipment and instruments. An EEM is then used for command, control and electrical interface verification of the platform avionics, for onboard software/hardware interaction verification, for Attitude Orbit Control System (AOCS) performance verification by closed-loop testing, for development and debugging of checkout software, and for initial validation of onboard flight procedures.

For the instrument, the approach of both consortia includes:

- an OEM consisting of the SWIR-1 optics breadboard and non-representative detector planned in the frame of a pre-development activity. The objective of the OEM is to debug and optimise the test and optics alignment procedures, including the necessary Optical Ground Support Equipment, and to verify the overall optical performance. The OEM will undergo functional and performance tests, but no environmental tests

- the instrument PFM

Furthermore, for Concept A there will be:

- a refurbished and enhanced OEM including SWIR-1, SWIR-2 and NIR breadboards and flight-representative detectors (opto-thermal model)
- an electric model fully representative of the instrument flight electronics and software design (detectors, front-end electronics, instrument control unit)

And for Concept B:

- an enhanced OEM for the SWIR-1 spectrometer – optically fully representative, including a flight-like detector
- a detection breadboard model consisting of EM detectors for SWIR-1 and NIR, the front-end electronics and a breadboard model of the video acquisition electronics
- an SM of the instrument
- an EEM fully representative of the instrument flight electronics and software design (video acquisition, data-processing unit, remote terminal unit, flight calibration unit)

9.4.2 Schedule

The schedule for the satellite development, shown in Fig. 9.1, assumes a Phase-B2/C/D/E1 kick-off in mid-2017 to allow for a period of six months at the start of the next cycle of the Earth Observation Envelope Programme for issuing the Phase-B2/C/D/E1 Invitation to Tender, for proposal submission

Figure 9.1. The CarbonSat development schedule. (ESA)

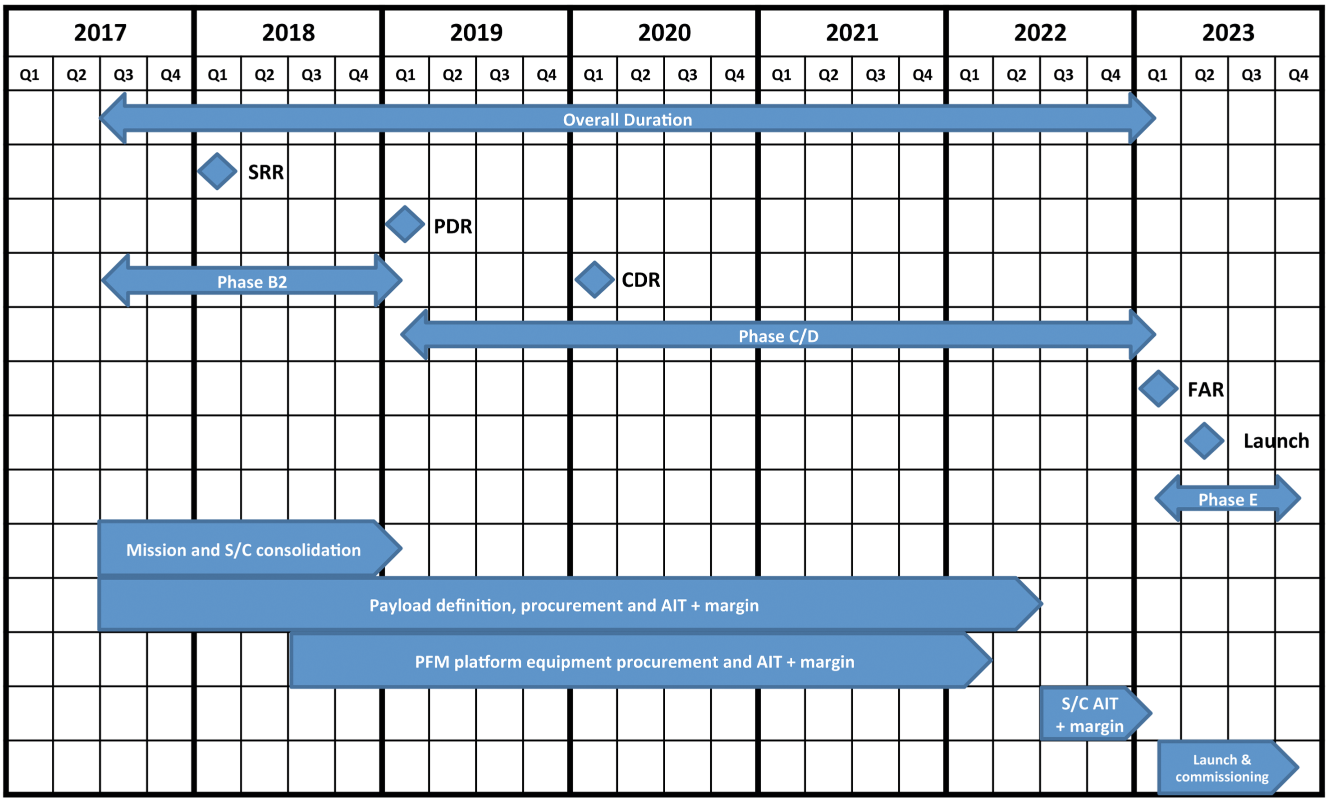

and evaluation, and for contract negotiations. The schedule also includes an instrument PFM contingency of about five and a half months, a platform contingency of about three months and a satellite contingency of about three months.

Early in Phase-B2, an SRR will be held to consolidate the satellite design and to set the baseline for the full development. The schedule includes a Phase-B2 of 19 months from kickoff to PDR, a Phase-C/D of 46 months, a Flight Acceptance Review (FAR) of the satellite after 67 months, a Phase-E1 of eight months, including the launch campaign (two months) and Launch and Early Orbit Phase (LEOP) and in-orbit commissioning (six months).

Assuming a successful outcome of the ongoing pre-development activities, the maturity of critical technologies will reach the required level prior to the start of the implementation phase. The instrument development, AIT and characterisation will require special attention during all the development phases. The development schedule is compatible with a launch by 2023.

→ REFERENCES

References

Agustí-Panareda, A., et al. (2014). Forecasting global atmospheric CO_2. *Atmos. Chem. Phys.*, **14**, 11959–11983.

Alexe, M., et al. (2015). Inverse modeling of CH_4 emissions for 2010–2011 using different satellite retrieval products from GOSAT and SCIAMACHY. *Atmos. Chem. Phys.*, **15**, 113–133, doi:10.5194/acp-15-113-2015.

Andres, R.J., Boden, T.A. & Higdon, D. (2014). A new evaluation of the uncertainty associated with CDIAC estimates of fossil fuel carbon dioxide emission. *Tellus B*, **66**, doi:10.3402/tellusb.v66.23616.

Asefi-Najafabady, S., et al. (2014). A multiyear, global gridded fossil fuel CO_2 emission data product: Evaluation and analysis of results. *J. Geophys. Res. Atmos.*, **119**, 10213–10231, doi:10.1002/ 2013JD021296.

Baker, D.F., et al. (2006). TransCom 3 inversion intercomparison: Impact of transport model errors on the interannual variability of regional CO_2 fluxes, 1988–2003. *Global Biogeochem. Cycles*, **20**, GB1002, doi:10.1029/2004GB002439.

Baldocchi, D., et al. (2001). Fluxnet: a new tool to study the temporal and spatial variability of ecosystem–scale carbon dioxide, water vapor, and energy flux densities. *Bull. Amer. Meteor. Soc.*, **82**, 2415–2434.

Ballantyne, A.P., et al. (2012). Increase in observed net carbon dioxide uptake by land and oceans during the past 50 years. *Nature*, **488**, 70–73.

Basu, S., et al. (2013). Global CO_2 fluxes estimated from GOSAT retrievals of total column CO_2. *Atmos. Chem. Phys.*, **13**, 8695–8717, doi:10.5194/acp-13-8695-2013.

Basu, S., et al. (2014). The seasonal variation of the CO_2 flux over Tropical Asia estimated from GOSAT, CONTRAIL, and IASI. *Geophys. Res. Lett.*, **41**, 1809–1815, doi:10.1002/2013GL059105.

Beirle, S., et al. (2011). Megacity emissions and lifetimes of nitrogen oxides probed from space. *Science*, **333**, 1737–1739, doi:10.1126/science.1207824.

Belikov, D.A., et al. (2014). Column-averaged CO_2 concentrations in the subarctic from GOSAT retrievals and NIES transport model simulations. *Polar Science*, doi:10.1016/j.polar.2014.02.002.

Bergamaschi, P., et al. (2007). Satellite chartography of atmospheric methane from SCIAMACHY on board ENVISAT: 2. Evaluation based on inverse model simulations. *J. Geophys. Res.*, **112**, doi:10.1029/2006jd007268.

Bergamaschi, P., et al. (2013). Atmospheric CH_4 in the first decade of the 21st century: Inverse modeling analysis using SCIAMACHY satellite retrievals and NOAA surface measurements. *J. Geophys. Res.*, **118**, 7350–7369, doi:10.1002/jrgd.50480.

Bloom, A.A., et al. (2010). Large-scale controls of methanogenesis inferred from methane and gravity spaceborne data. *Science*, **327**, 322–325.

Boesch, H., et al. (2011). Global characterization of CO_2 column retrievals from shortwave-infrared satellite observations of the Orbiting Carbon Observatory-2 mission. *Remote Sens.*, **3**, 270–304.

Boreman, G.D. (1997). Basic electro-optics for electrical engineers. ISBN 0-8194-2806-X, SPIE, Washington.

Bousquet, P., et al. (2000). Regional changes in carbon dioxide fluxes of land and oceans since 1980. *Science*, **290**, 1342–1346.

Bovensmann, H., et al. (2010). A remote sensing technique for global monitoring of power plant CO_2 emissions from space and related applications. *Atmos. Meas. Tech.*, **3**, 781–811.

Bovensmann, H., et al. (2014a). Scientific and Technical Assistance for the Deployment of a flexible airborne spectrometer system during C-MAPExp. ESA Contract No 4000106993/12/NL/FF/lf, Study Final Report.

Bovensmann, H., et al. (2014b). CarbonSat Earth Explorer 8 candidate mission Level-2 and Level-1b requirements consolidation study. ESA contract no 4000105676/12/NL/AF, Study Final Report.

Brandt, A.R., et al. (2014). Methane leaks from North American natural gas systems. *Science*, **343**, 733–735, doi:10.1126/science.1247045.

Bréon, F.-M., et al. (2015). An attempt at estimating Paris area CO_2 emissions from atmospheric concentration measurements. *Atmos. Chem. Phys.*, **15**, 1707–1724, doi:10.5194/acp-15-1707-2015.

Broquet, G., et al. (2011). A European CO_2 biogenic flux inversion at mesoscale from continuous *in situ* mixing ratio measurements. *J. Geophys. Res.*, **116**, D23303, doi:10.1029/2011JD016202.

Broquet, G., et al. (2013). Regional inversion of CO_2 ecosystem fluxes from atmospheric measurements: reliability of the uncertainty estimates. *Atmos. Chem. Phys.*, 13, 9039–9056, doi:10.5194/acp-13-9039-2013.

Buchwitz, M., Rozanov, V.V. & Burrows, J. P. (2000). A near-infrared optimized DOAS method for the fast global retrieval of atmospheric CH_4, CO, CO_2, H_2O, and NO total column amounts from SCIAMACHY Envisat-1 nadir radiances. *J. Geophys. Res.*, **105**, 15231–15245, doi:10.1029/2000JD900191.

Buchwitz, M., et al. (2013a). Carbon Monitoring Satellite (CarbonSat): assessment of atmospheric CO_2 and CH_4 retrieval errors by error parameterization. *Atmos. Meas. Tech.*, **6**, 3477–3500, doi:10.5194/amt-6-3477-2013.

Buchwitz, M., et al. (2013b). Carbon Monitoring Satellite (CarbonSat): assessment of scattering related atmospheric CO_2 and CH_4 retrieval errors and first results on implications for inferring city CO_2 emissions. *Atmos. Meas. Tech. Discuss.*, **6**, 4769-4850.

Buchwitz, M., et al. (2015a). The Greenhouse Gas Climate Change Initiative (GHG-CCI): Comparison and quality assessment of near-surface-sensitive satellite-derived CO_2 and CH_4 global data sets. *Remote Sens. Environ.*, **162**, 344–362, *http://dx.doi.org/10.1016/j.rse.2013.04.024*.

Buchwitz, M., et al. (2015b). Task 6 Technical Note for ESA study contract n° 4000109818/13/NL/FF/lf: Local Scale Mission Performance Analysis - Draft Version. 10 April 2015.

Butz, A., et al. (2011). Toward accurate CO_2 and CH_4 observations from GOSAT. *Geophys. Res. Lett.*, **38**, L14 812, doi:10.1029/2011GL047888.

Cambaliza, M.O.L., et al. (2015). Quantification and source apportionment of the methane emission flux from the city of Indianapolis. *Elem. Sci. Anth.*, **3**, 000037, doi:10.12952/journal.elementa.000037.

CEOS (2014). CEOS Strategy for Carbon Observations from Space. The Committee on Earth Observation Satellites (CEOS) Response to the Group on Earth Observations (GEO) Carbon Strategy. Published September 2014. Available from *http://ceos.org/document_management/Publications/WGClimate_CEOS-Strategy-for-Carbon-Observations-from-Space_Apr2014.pdf.*

Chevallier, F., et al. (2005). Inferring CO_2 sources and sinks from satellite observations: Method and application to TOVS data, *J. Geophys. Res.*, **110**, D24309, doi:10.1029/2005JD006390.

Chevallier, F., Bréon, F.-M. & Rayner, P. J. (2007). Contribution of the Orbiting Carbon Observatory to the estimation of CO_2 sources and sinks: Theoretical study in a variational data assimilation framework, *J. Geophys. Res.*, **112**, D09307, doi:10.1029/2006JD007375.

Chevallier, F., et al. (2014a). Toward robust and consistent regional CO_2 flux estimates from *in situ* and space borne measurements of atmospheric CO_2. *Geophys. Res. Lett.*, **41**, 1065–1070, doi:10.1002/2013GL058772.

Chevallier, F., et al. (2014b). ESA Climate Change Initiative (CCI) User Requirements Document (URD) for the Essential Climate Variable (ECV) Greenhouse Gases (GHG). version 2 (28. Aug. 2014), link: *http://www.esa-ghg-cci.org/?q=webfm_send/173.*

Chimot, J., et al. (2014). LOGOFLUX - CarbonSat Earth Explorer 8 candidate mission – Inverse modelling and mission performance study. ESA contract no 400010537/12/NL/CO, Study Final Report.

Ciais, P., et al. (2005). Europe-wide reduction in primary productivity caused by the heat and drought in 2003. *Nature*, **437**, 529–533, doi:10.1038/nature039

Ciais, P., et al. (2010). *Geo Carbon Strategy. Geo Secretariat Geneva/FAO, Rome, 48 pp.* Online at *http://www.globalcarbonproject.org/global/pdf/GEO_CarbonStrategy_20101020.pdf* (accessed May 2015).

Ciais, P., et al. (2013). Carbon and other biogeochemical cycles. In: *Climate Change 2013: The physical science basis.* Contribution of Working Group I to the Fifth Assessment Report of the Intergovernmental Panel on Climate Change [Stocker, T.F., Qin, D., Plattner, G.-K., Tignor, M., Allen, S.K., Boschung, J., Nauels, A., Xia, Y., Bex, V. & Midgley, P.M. (eds.)]. Cambridge University Press, Cambridge, United Kingdom and New York, NY, USA, pp. 465–570, doi:10.1017/CBO9781107415324.015.

Ciais, P., et al. (2014). Current systematic carbon-cycle observations and the need for implementing a policy-relevant carbon observing system. *Biogeosciences*, **11**, 3547–3602, doi:10.5194/bg-11-3547-2014.

Cox, P.M., et al. (2013). Sensitivity of tropical carbon to climate change constrained by carbon dioxide variability. *Nature*, **494**, 341–344, doi:10.1038/nature11882.

Cressot, C., et al. (2014). On the consistency between global and regional methane emissions inferred from SCIAMACHY, TANSO-FTS, IASI and surface measurements. *Atmos. Chem. Phys.*, **14**, 577–592, doi:10.5194/acp-14-577-2014.

Deng, F., et al. (2014). Inferring regional sources and sinks of atmospheric CO_2 from GOSAT XCO_2 data. *Atmos. Chem. Phys.*, **14**, 3703–3727, doi:10.5194/acp-14-3703-2014

Dlugokencky, E.J., et al. (2011). Global atmospheric methane: budget, changes and dangers. *Philos Trans A Math Phys Eng Sci*, **369**, 2058–2072, doi:10.1098/rsta.2010.0341.

Duren, R. M. & Miller, C.E. (2012). Measuring the carbon emissions of megacities. *Nature Clim. Change*, **2**, 560–562, doi:10.1038/nclimate1629.

Enting, I.G., Trudinger, C.M. & Francey, R.J. (1995). A synthesis inversion of the concentration and $\delta^{13}C$ of atmospheric CO_2. *Tellus*, **47B,** 35–52.

ESA (2006). The Changing Earth: New Scientific Challenges for ESA's Living Planet Programme. ESA Publication ESA SP-1304.

ESA (2014). Good and bad news for our atmosphere. Online at *http://www.esa.int/Our_Activities/Observing_the_Earth/Space_for_our_climate/Good_and_bad_news_for_our_atmosphere.*

ESA (2015a). Earth Observation Science Strategy for ESA – A New Era for Scientific Advances and Societal Benefits, ESA SP-1329/1 (2 volumes). European Space Agency, Noordwijk, the Netherlands.

ESA (2015b). ESA's Living Planet Programme: Scientific Achievements and Future Challenges – Scientific Context of the Earth Observation Science Strategy for ESA, ESA SP-1329/2 (2 volumes), European Space Agency, Noordwijk, the Netherlands.

Frankenberg, C., et al. (2006). Satellite chartography of atmospheric methane from SCIAMACHY on board Envisat: Analysis of the years 2003 and 2004. *J. Geophys. Res.*, **111**, D07303, doi:10.1029/2005JD006235.

Frankenberg, C., Butz, A. & Toon, G.C. (2011a). Disentangling chlorophyll fluorescence from atmospheric scattering effects in O_2-A-band spectra of reflected Sun-light. *Geophys. Res. Lett.*, **38**, L03801, doi:10.1029/2010GL045896.

Frankenberg, C., et al. (2011b). New global observations of the terrestrial carbon cycle from GOSAT: Patterns of plant fluorescence with gross primary productivity. *Geophys. Res. Lett.*, **38**, L17706, doi:10.1029/2011GL048738.

Frankenberg, C., et al. (2012). Remote sensing of near-infrared chlorophyll fluorescence from space in scattering atmospheres: implications for its retrieval and interferences with atmospheric CO_2 retrievals. *Atmos. Meas. Tech.*, **5**, 2081–2094, doi:10.5194/amt-5-2081-2012.

Frankenberg, C., et al. (2014). Prospects for chlorophyll fluorescence remote sensing from the Orbiting Carbon Observatory-2. *Remote Sens. Environ.*, **147**, 1–12, doi:10.1016/j.rse.2014.02.007.

Fraser, A., et al. (2013). Estimating regional methane surface fluxes: The relative importance of surface and GOSAT mole fraction measurements. *Atm. Chem. Phys.*, **13**, 5697–5713, doi:10.5194/acp-13-5697-2013.

Friedlingstein, P., et al. (2006). Climate-carbon cycle feedback analysis: Results from the (CMIP)-M-4 model intercomparison. *J. Climate* **19**, 3337–3353.

Friedlingstein, P., et al. (2014). Uncertainties in CMIP5 climate projections and uncertainties due to carbon cycle feedbacks. *J. Climate*, **27**, 511–526; doi:10.1175/JCLI-D-12-00579.1.

Galli, A., et al. (2014). The impact of spectral resolution on satellite retrieval accuracy of CO_2 and CH_4. *Atmos. Meas. Tech.*, **7**, 1105–1119, doi:10.5194/amt-7-1105-2014.

GCOS (2010). Implementation plan for the Global Observing System for Climate in Support of the UNFCCC. (**GCOS-92, WMO/TD-No 1219**). Online at *http://www.wmo.int/pages/prog/gcos/Publications/gcos-138.pdf*

GCOS (2011). Systematic observation requirements for satellite-based data products for climate - 2011 Update - Supplemental details to the satellite-based component of the “Implementation Plan for the Global Observing System for Climate in Support of the UNFCCC (2010 Update)”. **GCOS-154**.

Gerbig C., Körner, S. & Lin, J.C. (2008). Vertical mixing in atmospheric tracer transport models: error characterization and propagation. *Atmos. Chem. Phys.*, **8**, 591–602.

Gerilowski, K., et al. (2011). MAMAP - a new spectrometer system for column-averaged methane and carbon dioxide observations from aircraft: instrument description and performance assessment. *Atmos. Meas. Tech.*, **4**, 215–243, doi:10.5194/amt-4-215-2011.

Gisi, M., et al. (2012). XCO_2-measurements with a tabletop FTS using solar absorption spectroscopy. *Atmos. Meas. Tech.*, **5**, 2969–2980, doi:10.5194/amt-5-2969-2012.

Göckede, M., et al. (2010). Sensitivity of a subregional scale atmospheric inverse CO_2 modeling framework to boundary conditions. *J. Geophys. Res.*, **115**, D24112. doi:10.1029/2010JD014443.

Guan, D., et al. (2012). The gigatonne gap in China’s carbon dioxide inventories. *Nature Clim. Change*, **2**, 672–675, doi:10.1038/nclimate1560.

Guerlet S., et al. (2013). Reduced carbon uptake during the 2010 Northern Hemisphere summer from GOSAT. *Geophys. Res. Lett.*, **40**, 2378–2383, doi:10.1002/grl.50402.

Gurney, K.R., et al. (2002). Towards robust regional estimates of CO_2 sources and sinks using atmospheric transport models. *Nature*, **415**, 626–630, doi:10.1038/415626a.

Hansen, M.C., et al. (2013). High-resolution global maps of 21st-century forest cover change. *Science*, **342**, 850–853, doi:10.1126/science.1244693.

Hasekamp, O.H. & Butz, A. (2008). Efficient calculation of intensity and polarization spectra in vertically inhomogeneous scattering and absorbing atmospheres. *J. Geophys. Res.* **113**, D20309.

Hayman, G.D., et al. (2014). Comparison of the HadGEM2 climate-chemistry model against in-situ and SCIAMACHY atmospheric methane data. *Atmos. Chem. Phys. Discuss.*, **14**, 12967–13020, doi:10.5194/acpd-14-12967-2014.

Heymann, J., et al. (2012). SCIAMACHY WFM-DOAS XCO_2: reduction of scattering related errors. *Atmos. Meas. Tech.*, **5**, 2375–2390, doi:10.5194/amt-5-2375-2012.

Houweling, S., et al. (2012). Iconic CO_2 time series at risk, *Science*, **337**, 1038–1040, doi:10.1126/science.337.6098.1038-b.

Houweling, S., Krol, M. & Bergamaschi, P. (2014). A multi-year methane inversion using SCIAMACHY, accounting for systematic errors using TCCON measurements. *Atmos. Chem. Phys.*, 14, 3991–4012, doi:10.5194/acp-14-3991-2014.

Houweling, S., et al. (2015). An inter-comparison of inverse models for estimating sources and sinks of CO_2 using GOSAT measurements. *J. Geophys. Res. Atmos.*, accepted, doi: 10.1002/2014JD022962.

Humpage, N., et al. (2014). GreenHouse Observations of the Stratosphere and Troposphere (GHOST): a novel shortwave infrared spectrometer developed for the Global Hawk unmanned aerial vehicle. *Proc. SPIE*, **9242**, Remote Sensing of Clouds and the Atmosphere XIX and Optics in Atmospheric Propagation and Adaptive Systems XVII, 92420P, doi:10.1117/12.2067330.

Hungershoefer et al. (2010). Evaluation of various observing systems for the global monitoring of CO_2 surface fluxes. *Atmos. Chem. Phys.*, **10**, 10503–10520, doi:10.5194/acp-10-10503-2010.

IPCC (2006). IPCC guidelines for national greenhouse gas inventories. Prepared by the National Greenhouse Gas Inventories Programme, Eggleston H.S., Buendia L., Miwa K., Ngara T. and Tanabe K. (eds). Published by IGES, Japan.

IPCC (2013). Summary for Policymakers. In: *Climate Change 2013: The Physical Science Basis*. Contribution of Working Group I to the Fifth Assessment Report of the Intergovernmental Panel on Climate Change (Stocker, T.F., D. Qin, G.-K. Plattner, M. Tignor, S.K. Allen, J. Boschung, A. Nauels, Y. Xia, V. Bex and P.M. Midgley (eds.), Cambridge University Press, Cambridge, United Kingdom and New York, NY, USA.

Joiner, J., et al. (2011). First observations of global and seasonal terrestrial chlorophyll fluorescence from space. *Biogeosciences*, **8**, 637–651, doi:10.5194/bg-8-637-2011.

Joiner, J., et al. (2013). Global monitoring of terrestrial chlorophyll fluorescence from moderate-spectral-resolution near-infrared satellite measurements: methodology, simulations, and application to GOME-2. *Atmos. Meas. Tech.*, **6**, 2803–2823, doi:10.5194/amt-6-2803-2013.

Jones, C.D., et al. (2013). Twenty-first-century compatible CO_2 emissions and airborne fraction simulated by CMIP5 Earth system models under four representative concentration path-ways. *J. Climate*, **26**, 4398–4413, doi:10.1175/JCLI-D-12-00554.1.

Jung, M., et al. (2011). Global patterns of land-atmosphere fluxes of carbon dioxide, latent heat, and sensible heat derived from eddy covariance, satellite, and meteorological observations. *J. Geophys. Res.*, **116**, G00J07, doi:10.1029/2010JG001566.

Karion, A., et al. (2010). AirCore: An innovative atmospheric sampling system. *J. Atmos. Oceanic Technol.*, **27**, 1839–1853, doi:10.1175/2010JTECHA1448.1.

Karion, A., et al. (2013). Methane emissions estimate from airborne measurements over a western United States natural gas field. *Geophys. Res. Lett.*, **40**, 4393–4397, doi:10.1002/grl.50811.

Keeling, C.D. (1960). The concentration and isotopic abundances of carbon dioxide in the atmosphere. *Tellus*, **12**, 200–203.

Keeling, R. F., and Severinghaus, J. (2000), Atmospheric oxygen measurements and the carbon cycle. In: *The Carbon Cycle*, T. M. L. Wigley and D. S. Schimel, Editors, Global Change Institute, **6**, 134–140, Cambridge University Press (2000).

Khvorostyanov, D., et al. (2008). Vulnerability of east Siberia's frozen carbon stores to future warming. *Geophys. Res. Lett.*, **35**, L10703, doi:10.1029/2008GL033639.

King, A.W., et al. (2007). What Is the Carbon Cycle and Why Care? In: *The First State of the Carbon Cycle Report (SOCCR): The North American Carbon Budget and Implications for the Global Carbon Cycle*. A Report by the U.S. Climate Change Science Program and the Subcommittee on Global Change Research [King, A.W., Dilling, L., Zimmerman, G.P., Fairman, D.M., Houghton, R.A., Marland, G., Rose, A.Z. & Wilbanks, T.J. (eds.)]. National Oceanic and Atmospheric Administration, National Climatic Data Center, Asheville, NC, USA, 15–20.

Kirschke, S., et al. (2013). Three decades of global methane sources and sinks. *Nature Geosci.*, **6**, 813–823, doi:10.1038/ngeo1955.

Kort, E.A., et al. (2012). Space-based observations of megacity carbon dioxide. *Geophys. Res. Lett.*, **39**, L17806, doi:10.1029/2012GL052738.

Kort, E.A., et al. (2014). Four corners: The largest US methane anomaly viewed from space. *Geophys. Res. Lett.*, **41**, 2014GL061503, doi:10.1002/2014GL061503.

Koven, C.D., et al. (2011). Permafrost carbon-climate feedbacks accelerate global warming. *Proc. Natl. Acad. Sci. U.S.A.*, **108**, 14769–14774, doi:10.1073/pnas.1103910108

Krings, T., et al. (2011). MAMAP – a new spectrometer system for column-averaged methane and carbon dioxide observations from aircraft: retrieval algorithm and first inversions for point source emission rates. *Atmos. Meas. Tech.*, **4**, 1735–1758, doi:10.5194/amt-4-1735-2011.

Krings, T., et al. (2013). Quantification of methane emission rates from coal mine ventilation shafts using airborne remote sensing data. *Atmos. Meas. Tech.*, **6**, 151–166, doi:10.5194/amt-6-151-2013

Kurz, W.A., et al. (2008). Mountain pine beetle and forest carbon feedback to climate change. *Nature*, **452**, 987–990, doi:10.1038/nature06777.

Le Quéré, C., et al. (2014). Global carbon budget 2013. *Earth Syst. Sci. Data*, **6**, 235–263, doi:10.5194/essd-6-235-2014.

Long, D.A. & Hodges, J.T. (2012). On spectroscopic models of the O2 A-band and their impact upon atmospheric retrievals. *J. Geophys. Res.*, **117**, D12309, doi:10.1029/2012JD017807.

MACC-II (2014). Monitoring Atmospheric Composition and Climate - Interim Implementation (MACC-II), Final project report. Funded as part of the European Community's Seventh Framework Programme (FP7 THEME [SPA.2011.1.5-02]) under grant agreement 283576. Online at *http://www.copernicus-atmosphere.eu/documents/maccii/general/MACCII_FinalReport.pdf*.

Maksyutov, S., et al. (2013). Regional CO_2 flux estimates for 2009–2010 based on GOSAT and ground-based CO_2 observations. *Atmos. Chem. Phys.*, **13**, 9351–9373, doi:10.5194/acp-13-9351-2013.

Massart, S., et al. (2014). Assimilation of atmospheric methane products into the MACCII system: from SCIAMACHY to TANSO and IASI. *Atmos. Chem. Phys.*, **14**, 6139–6158, doi:10.5194/acp-14-6139-2014.

Meirink, J., et al. (2008). Four-dimensional variational data assimilation for inverse modeling of atmospheric methane emissions: Analysis of SCIAMACHY observations. *J. Geophys. Res.*, **113**, D17301, doi:10.1029/2007jd009740.

Melton, J.R., et al. (2013). Present state of global wetland extent and wetland methane modelling: conclusions from a model inter-comparison project (WETCHIMP). *Biogeosciences*, **10**, 753–788, doi:10.5194/bg-10-753-2013.

Michalak, A.M., Hirsch, A. & Bruhwiler, L. (2005). Maximum likelihood estimation of covariance parameters for Bayesian atmospheric trace gas surface flux inversions. *J. Geophys. Res.*, **110**, D24107, doi:10.1029/2005JD005970.

Miller, C.E., et al. (2007). Precision requirements for space-based XCO_2 data. *J. Geophys. Res.*, **112**, D10314, doi:10.1029/2006JD007659

Miller, S.M., et al. (2013). Anthropogenic emissions of methane in the United States. *Proc. Natl. Acad. Sci. U.S.A.*, **110**, 20018–20022, doi:10.1073/pnas.1314392110.

Monteil, G., et al. (2013). Comparison of CH_4 inversions based on 15 months of GOSAT and SCIAMACHY observations. *J. Geophys. Res.*, **118**, 11807–11823, doi:10.1002/2013JD019760.

Montzka, S.A., et al. (2011). Small interannual variability of global atmospheric hydroxyl. *Science*, **331**, 67–69, doi:10.1126/science.1197640.

Nguyen, H., et al. (2014). A method for colocating satellite XCO_2 data to ground-based data and its application to ACOS-GOSAT and TCCON. *Atmos. Meas. Tech.*, **7**, 2631–2644, doi:10.5194/amt-7-2631-2014.

Nisbet, E. & Weiss, R. (2010). Top-down versus bottom-up. *Science*, **328**, 1241–1243, doi:10.1126/science.1189936.

O'Dell, C.W., (2010). Acceleration of multiple-scattering, hyperspectral radiative transfer calculations via low-streams interpolation. *J. Geophys. Res.*, **115**, D10 206, doi:10.1029/2009JD012803.

O'Dell, C.W., et al. (2012). The ACOS CO_2 retrieval algorithm – Part 1: Description and validation against synthetic observations. *Atmos. Meas. Tech.*, **5**, 99–121, doi:10.5194/amt-5-99-2012.

Oshchepkov, S., Bril, A. & Yokota, T. (2008). PPDF-based method to account for atmospheric light scattering in observations of carbon dioxide from space. *J. Geophys. Res.*, **113**, D23210, doi:10.1029/2008JD010061.

Ostler, A., et al. (2014). Multistation intercomparison of column-averaged methane from NDACC and TCCON: impact of dynamical variability. *Atmos. Meas. Tech.*, **7**, 4081–4101, doi:10.5194/amt-7-4081-2014.

Parazoo, N.C., et al. (2013). Interpreting seasonal changes in the carbon balance of southern Amazonia using measurements of XCO_2 and chlorophyll fluorescence from GOSAT. *Geophys. Res. Lett.*, **40**, 2829–2833, doi:10.1002/grl.50452.

Park, G.H., (2010). Variability of global net sea-air CO_2 fluxes over the last three decades using empirical relationships. *Tellus Ser. B*, **62**, 352–368.

Patra, P.K., et al. (2011). TransCom model simulations of CH_4 and related species: linking transport, surface flux and chemical loss with CH_4 variability in the troposphere and lower stratosphere. *Atmos. Chem. Phys.*, **11**, 12813–12837, doi:10.5194/acp-11-12813-2011.

Patra, P.K., et al. (2014). Observational evidence for interhemispheric hydroxyl-radical parity. *Nature*, **513**, 219–223, doi:10.1038/nature13721.

Peters, W., Miller, J.B. & Withaker, J. (2005). An ensemble data assimilation system to estimate CO_2 surface fluxes from atmospheric trace gas observations. *J. Geophys. Res.*, **110**, D24304, doi:10.1029/2005JD006157.

Peters, G.P., et al. (2012). Rapid growth in CO_2 emissions after the 2008-2009 global financial crisis. *Nature Clim. Change*, **2**, 2–4, doi:10.1038/nclimate1332.

Peylin, P., et al. (2013). Global atmospheric carbon budget: results from an ensemble of atmospheric CO_2 inversions. *Biogeosciences*, **10**, 6699–6720, doi:10.5194/bg-10-6699-2013.

Pfeil, B., et al. (2013). A uniform, quality controlled Surface Ocean CO_2 Atlas (SOCAT). *Earth Syst. Sci. Data*, **5**, 125-143, doi:10.5194/essd-5-125–2013.

Piao, S., et al. (2013). Evaluation of terrestrial carbon cycle models for their sensitivity to climate variability and the observed rise in atmospheric CO_2 abundance. *Glob. Chang. Biol.*, doi:10.1111/gcb.12187.

Pütz, S., et al. (2014). Long-term carbon loss in fragmented Neotropical forests. *Nat. Commun.*, **5**, 5037, doi:10.1038/ncomms6037.

Randerson, J.T., et al. (2009). Systematic assessment of terrestrial biogeochemistry in coupled climate-carbon models. *Glob. Chang. Biol.*, **15**, 2462–2484, doi:10.1111/j.1365-2486.2009.01912.x.

Raupach, M.R., et al. (2007). Global and regional drivers of accelerating CO_2 emissions. *Proc. Natl. Acad. Sci. U.S.A.*, **104**, 10288–10293, doi:10.1073/pnas.0700609104.

Rayner, P.J. & O'Brien, D. M. (2001). The utility of remotely sensed CO_2 concentration data in surface source inversions. *Geophys. Res. Lett.*, **28**, 175–178.

Rayner, P., et al, (2005). Two decades of terrestrial carbon fluxes from a carbon cycle data assimilation system (CCDAS). *Glob. Biogeochem. Cycles*, **19**, GB2026, doi:10.1029/2004GB002254.

Reichstein, M., et al. (2013). Climate extremes and the carbon cycle, *Nature*, **500**, 287–295, doi:10.1038/nature12350.

Reuter, M., et al. (2010). A method for improved SCIAMACHY CO_2 retrieval in the presence of optically thin clouds, *Atmos. Meas. Tech.*, **3**, 209–232, doi:10.5194/amt-3-209-2010.

Reuter, M., et al. (2011). Retrieval of atmospheric CO_2 with enhanced accuracy and precision from SCIAMACHY: Validation with FTS measurements and comparison with model results. *J. Geophys. Res.*, **116**, D04301, doi:10.1029/2010JD015047.

Reuter, M., et al. (2012). A joint effort to deliver satellite retrieved atmospheric CO_2 concentrations for surface flux inversions: the ensemble median algorithm EMMA. *Atmos. Chem. Phys. Disc.*, **12**, 23195–23217.

Reuter, M., et al. (2014a). Decreasing emissions of NOx relative to CO_2 in East Asia inferred from satellite observations. *Nature Geosci*, **7**, 792–795, doi:10.1038/ngeo2257.

Reuter, M., et al. (2014b). Satellite-inferred European carbon sink larger than expected. *Atmos. Chem. Phys.*, **14**, 13739–13753, doi:10.5194/acp-14-13739-2014.

Rigby, M., Manning, A.J., & Prinn, R.G. (2011). Inversion of long-lived trace gas emissions using combined Eulerian and Lagrangian chemical transport models. *Atmos. Chem. Phys.*, **11**, 9887–9898, doi:10.5194/acp-11-9887-2011.

Ringeval, B., et al. (2014). Methane emissions from floodplains in the Amazon basin: Challenges in developing a process-based model for global applications. *Biogeosciences*, **11**, 1519–1558, doi:10.5194/bg-11-1519-2014.

Rödenbeck, C., et al. (2009). A two-step scheme for high-resolution regional atmospheric trace gas inversions based on independent models, *Atmos. Chem. Phys.*, **9**, 5331–5342, doi:10.5194/acp-9-5331-2009.

Rodgers, C.D. (2000). Inverse methods for atmospheric sounding: Theory and practice. World Scientific, Singapore.

Schepers, D., et al. (2012). Methane retrievals from Greenhouse Gases Observing Satellite (GOSAT) shortwave infrared measurements: Performance comparison of proxy and physics retrieval algorithms. *J. Geophys. Res.*, **117**, D10307, doi:10.1029/2012JD017549.

Schimel, D., et al. (2015). Observing terrestrial ecosystems and the carbon cycle from space. *Glob. Chang. Biol.*, **21**, 1762–1776, doi:10.1111/gcb.12822.

Schneising, O., et al. (2013). Anthropogenic carbon dioxide source areas observed from space: assessment of regional enhancements and trends. *Atmos. Chem. Phys.*, **13**, 2445–2454, doi:10.5194/acp-13-2445-2013.

Schneising, O., et al. (2014a). Terrestrial carbon sink observed from space: variation of growth rates and seasonal cycle amplitudes in response to interannual surface temperature variability. *Atmos. Chem. Phys.*, **14**, 133–141, doi:10.5194/acp-14-133-2014.

Schneising, O., et al. (2014b). Remote sensing of fugitive methane emissions from oil and gas production in North American tight geologic formations. *Earth's Future*, **2**, 548–558, doi:10.1002/2014EF000265.

Scholze, M., et al. (2009). Prognosing terrestrial carbon cycling with uncertainties: Results from a Carbon Cycle Data Assimilation System (CCDAS). IOP Conference Series: Earth and Environmental Science, 6, 042028, doi:10.1088/1755-1307/6/4/042028

Schuh, A.E., et al. (2010). A regional high-resolution carbon flux inversion of North America for 2004. *Biogeosciences*, **7**, 1625–1644. doi:10.5194/bg-7-1625-2010.

Séférian, R., et al. (2013). Skill assessment of three earth system models with common marine biogeochemistry. *Clim. Dyn.*, **40**, 2549–2573, doi:10.1007/s00382-012-1362-8.

Seibert, P. & Frank, A. (2004). Source-receptor matrix calculation with a Lagrangian particle dispersion model in backward mode. *Atmos. Chem. Phys.*, **4**, 51–63.

Shindell, D.T., et al. (2013). Interactive ozone and methane chemistry in GISS-E2 historical and future climate simulations. *Atmos. Chem. Phys.*, **13**, 2653–2689, doi:10.5194/acp-13-2653-2013.

Sierk, B., et al. (2014). The CarbonSat candidate mission: Imaging greenhouse gas concentrations from space. *Proc. SPIE*, **9218**, doi:10.1117/12.2061930.

Thompson, D.R, et al. (2012). Atmospheric validation of high accuracy CO_2 absorption coefficients for the OCO-2 mission. *J. Quant. Spectr. Rad. Trans.*, **113**, 2265–2276, doi:10.1016/j.jqsrt.2012.05.021.

Turnbull, J., et al. (2015). Towards quantification and source sector identification of fossil fuel CO_2 emissions from an urban area: Results from the INFLUX experiment. *J. Geophys. Res.* **120**, 292–312, doi:10.1002/2014JD022555.

United Nations (2012). United Nations Department of Economic and Social Affairs World Urbanization Prospects, the 2011 Revision; available at *http://esa.un.org/unpd/wup/index.htm*.

Wang, R., et al. (2013a). High-resolution mapping of combustion processes and implications for CO_2 emissions. *Atmos. Chem. Phys.*, **13**, 5189–5203, doi:10.5194/acp-13-5189-2013.

Wang, W., et al. (2013b). Variations in atmospheric CO_2 growth rates coupled with tropical temperature. *Proc. Natl. Acad. Sci. U.S.A.*, **110**, 13061–13066, doi:10.1073/pnas.1219683110.

Wofsy, S.C., et al. (2011). HIAPER Pole-to-Pole Observations (HIPPO): climatically important atmospheric gases and fine-grained, global-scale measurements of aerosols. *Phil. Trans. R. Soc. Lond. A*, **369**, 2073–2086, doi:10.1098/rsta.2010.0313.

Wunch, D., et al. (2009). Emissions of greenhouse gases from a North American megacity. *Geophys. Res. Lett.*, **36**, L15810, doi:10.1029/2009GL039825.

Wunch, D., et al. (2011a). A method for evaluating bias in global measurements of CO_2 total columns from space. *Atmos. Chem. Phys.*, **11**, 12317–12337, doi:10.5194/acp-11-12317-2011.

Wunch, D., et al. (2011b). The total carbon column observing network. *Phil. Trans. R. Soc. Lond. A.*, **369**, 2087–2112, doi:10.1098/rsta.2010.0240.

Yoshida, Y., et al. (2011). Retrieval algorithm for CO_2 and CH_4 column abundances from short-wavelength infrared spectral observations by the Greenhouse gases observing satellite. *Atmos. Meas. Tech.*, **4**, 717–734, doi:10.5194/amt-4-717-2011.

→ ACRONYMS

Acronyms

ACT	Across Track
ACTM	Atmospheric Chemistry and Transport Model
AG	Aktien Gesellschaft
AGILE	Astro-rivelatore Gamma a Immagini Leggero
AIGGS	Airborne Imaging Greenhouse Gas Spectrometer
AIRS	Atmospheric Infrared Sounder
AIT	Assembly Integration and Testing
ALD	Atomic Layer Deposition
ALT	Along Track
AM	Acquisition Mode
AOCS	Attitude and Orbit Control System
AOD	Aerosol Optical Depth
ARA	Absolute Radiometric Accuracy
AVIRIS	Airborne Visible/Infrared Spectrometer
BRDF	Bidirectional Reflectance Distribution Function
BSDF	Bidirectional Scatter Distribution Function
CAMS	Copernicus Atmosphere Monitoring Service
CCD	Charge Coupled Device
CCDAS	Carbon Cycle Data Assimilation System
CCDB	Characterisation and Calibration Database
CCSDS	Consultative Committee for Space Data Systems
CDHS	Command and Data Handling Subsystem
CDR	Critical Design Review
CEOS	Committee on Earth Observation Satellites
CFRP	Carbon Fibre Reinforced Plastic
CH_4	methane
CO_2	carbon dioxide
COD	Cloud Optical Depth
CoM	Centre of Mass
CORECI	Compression Recording Ciphering Unit
COP	Community of Practice
CSS	Coarse Sun Sensor
CTH	Cloud Top Height
CWP	Cloud Water Path
DDA	Data Download Assembly
DEM	Digital Elevation Model
DOP	Degree of Polarisation
DRAMA	Debris Risk Assessment and Mitigation Analysis
EC	European Commission
ECMWF	European Centre for Medium-Range Weather Forecasts
EEM	Electrical Engineering Model
EEMCS	Earth Explorer Mission Control System
EMS	Estrack Management and Scheduling System
EOL	End of Life
EPA	Environmental Protection Agency
ESOC	European Space Operations Centre
ESRA	Effective Spectral Radiometric Accuracy
EU	European Union
FAR	Flight Acceptance Review
FCL	Fold-back Current Limiters
FCU	Flight Calibration Unit
FDIR	Failure Detection Isolation and Recovery
FEE	Front End Electronics
FLEX	Fluorescence Explorer
FOS	Flight Operations Segment
FOV	Field of View
FP	Full Physics
FPGA	Field-Programmable Gate Array
FTS	Fourier Transform Spectrometer
FWC	Full-Well Capacity
FWHM	Full Width at Half Maximum
GaA	Gallium Arsenide
GCOS	Global Climate Observing System
GEO	Group on Earth Observations
GEOSS	Global Earth Observation System of Systems
GFRP	Glass-Fibre Reinforced Plastic
GHGIS	Greenhouse Gas Imaging Spectrometer
GM	Geometry Module
GNSS	Global Navigation Satellite System
GOSAT	Greenhouse gases Observing Satellite
GPP	Gross Primary Production
GS	Ground Segment
HKTM	Housekeeping/Telemetry
HSS	High Spatial Sampling
IASI	Infrared Atmospheric Sounding Interferometer
ICOS	Integrated Carbon Observation System
ICU	Instrument Control Unit
IEA	International Energy Agency
IM	Init Mode
ILS	Instrument Line Shape
IPCC	Intergovernmental Panel on Climate Change
ISM	Intermediate Safe Mode
ISRF	Instrument Spectral Response Function

IWGGMS	International Workshop on Greenhouse-Gas Measurements from Space
L1M	Observing system simulation module up to Level-1 data
L2M	Level-1 to Level-2 processing module
LCL	Latching Current Limiters
LEO	Low Earth Orbit
LEOP	Launch and Early Orbit Phase
LES	Large-Eddy-Simulation
LOS	Line of Sight
LTDN	Local Time of Descending Node
LVA	Launch Vehicle Adapter
MAMAP	Methane Airborne Mapper
MCS	Mission Control System
MCT	Mercury-Cadmium-Telluride
MIB	Main Instrument Baseplate
MLD	Mechanics and Lamps Drive
MLI	Multi-Layer Insulation
MPS	Mission-Planning System
NACP	North American Carbon Program
NAND	NOT + AND
NDVI	Normalised Difference Vegetation Index
NEE	Net Ecosystem Exchange
NGP	Next-Generation Panchromatic
NIR	Near-infrared
NM	Normal Mode
NU	Non Uniformity
OBC	Onboard Computer
OBDH	Onboard Data Handling
OBSW	Onboard Software
OCM	Orbit Control Mode
OCO	Orbiting Carbon Observatory
OCO-2	Orbiting Carbon Observatory-2
OECD	Organisation for Economic Cooperation and Development
OEM	Optical Engineering Model
OGSE	Optical Ground Support Equipment
OH	hydroxyl radical
OHB	Otto Hydraulik Bremen
OMI	Ozone Monitoring Instrument
OPS	Orbit Position
OSSE	Observing System Simulation Experiment
PCDU	Power Conditioning and Distribution Unit
PCR	Preliminary Concept Review
PDGS	Payload Data Ground Segment
PDHT	Payload Data Handling and Transmission
PDHU	Payload Data Handling Unit
PDR	Preliminary Design Review
PEM	Proximity Electronics Modules
PFM	Proto-Flight Model
PMDM	Processor Module and Detection Management
ppb	parts per billion
ppm	parts per million
PRNU	Photo Response Non Uniformity
PS	Polarisation Sensitivity
PSF	Point-Spread Function
PSLV	Polar Satellite Launch Vehicle
RAAN	Right Ascension of the Ascending Node
RC	Repeat Cycle
RCP	Representative Concentration Pathways
RIU	Remote Interface Unit
RTU	Remote Terminal Unit
RxRA	Relative Spatial Radiometric Accuracy
RλRA	Relative Spectral Radiometric Accuracy
SADM	Solar Array Driving Mechanism
SARA	Re-entry Survival and Risk Analysis
SCARAB	Space Craft Atmospheric Re-entry and Aero–thermal Break up
SEDF	System Energy Distribution Function
SEM	Scanning Electron Microscope
SEOSAT	Spanish Earth Observation Satellite
SGM	Scene Generator Module
SH	Slit Homogeniser
SiC	Silicon Carbide
SIE	System Integrated Energy
SIF	Solar-Induced (vegetation chlorophyll) Fluorescence
SM	Structural Model
SNR	Signal-to-Noise Ratio
SpW	Space Wire
SSD_{ACT}	Spatial Sampling Distance Across-Track
SSD_{ALT}	Spatial Sampling Distance Along-Track
SSI	Spectral Sampling Interval
SSLI	Single Layer Insulation
SSMM	Solid-State Mass Memory
SSO	Sun Synchronous Orbit
SRR	System Requirements Review
SW	Software
SWIR	Shortwave-infrared
SZA	Solar Zenith Angle
TC	Tele Command
TCCON	Total Carbon Column Observing Network
TES	Tropospheric Emission Spectrometer
TM	Telemetry
TMA	Three-Mirror Anastigmat
TRL	Technology Readiness Level
TT&C	Telemetry, Tracking and Command
UNFCCC	United Nations Framework Convention on Climate Change

USM	Ultimate Safe Mode
VAE	Video Acquisition Electronics
VE	Video Electronics
VIS	Visible
WMO	World Meteorological Organization
XCH_4	methane dry air mole fraction
XCO_2	carbon dioxide dry air mole fraction

ESA Member States

Austria
Belgium
Czech Republic
Denmark
Estonia
Finland
France
Germany
Greece
Hungary
Ireland
Italy
Luxembourg
Netherlands
Norway
Poland
Portugal
Romania
Spain
Sweden
Switzerland
United Kingdom

An ESA Communications Production